Hyperspectral Coherent Anti-Stokes Raman Scattering (CARS) Imaging

Von der Fakultät für Mathematik und Physik der Universität Stuttgart zur Erlangung der Würde eines Doktors der Naturwissenschaften (Dr. rer. nat.) genehmigte Abhandlung

Vorgelegt von

Dipl. Phys. Stefan Gomes da Costa

aus Saarbrücken

Hauptberichter: Prof. Dr. Jörg Wrachtrup
Mitberichter: Prof. Dr. Martin Dressel

Tag der mündlichen Prüfung: 23.05.2019

Durchgeführt am 3. Physikalischen Institut der Universiät Stuttgart in der Arbeitsgruppe von Dr. Andreas Volkmer

2019

Contents

Contents iii

1. Deutsche Zusammenfassung 1

2. Introduction 7

3. Theoretical Background 11

3.1. Supercontinuum Generation Processes 11

3.1.1. Self- and Cross-Phase Modulation 13

3.1.2. Soliton Generation 13

3.1.3. Spontaneous Four-Wave Mixing 14

3.1.4. Spontaneous Raman Scattering 15

3.2. Supercontinuum Generation in Photonic Crystal Fibers 16

3.3. CARS Fundamentals 17

3.3.1. CARS Signal Generation in Forward- and Epi-Direction 19

3.3.2. Multiplex CARS Spectroscopy 22

3.3.3. Interferometric CARS Spectroscopy 24

3.3.4. Time-Resolved Broadband Multiplex CARS Spectroscopy . . . 26

3.4. Sum Frequency Generation 27

3.4.1. Second Harmonic Generation 28

3.5. Two-Photon Induced Fluorescence 29

3.6. UV-VIS Absorption Spectroscopy 29

4. Experimental Methods 31

4.1. Generation and Characterization of ps-Supercontinuum Pulses 31

4.2. Hyperspectral CARS Imaging Setup 34

4.3. Setup for Interferometric Hyperspectral CARS Imaging with Broadband Correlated Photon Pairs 37

4.4. 2D CARS Microspectroscopy Setup . . . 41
4.5. Spontaneous Raman Microspectroscopy . . . 44
4.6. UV-VIS Absorption Spectroscopy . . . 45
4.7. Sample Preparations . . . 45
4.7.1. Pollen Samples . . . 45
4.7.2. Prebiotic Broth Samples . . . 45
4.7.3. Solvent Samples . . . 46
4.7.4. Index-Matched PMMA-Wedge Samples . . . 46
4.8. Data Analysis . . . 46
4.8.1. SC Spectra Analysis . . . 47
4.8.2. CARS Spectra Analysis . . . 47
4.8.3. E-CARS Spectra Analysis . . . 48
4.8.4. Interferometric CARS Spectra Analysis . . . 49
4.8.5. 2D CARS Spectra Analysis . . . 49
4.8.6. Spontaneous Raman Spectra Analysis . . . 50
4.8.7. 2PF Spectra Analysis . . . 50

5. Simulation of CARS Supercontinuum Generation 51
5.1. Simulations of Supercontinuum Generation . . . 52
5.1.1. Supercontinuum Generation with few-ps Pulses . . . 54
5.1.2. Supercontinuum Generation with fs Pulses . . . 60
5.1.3. Supercontinuum Generation with Longer ps-Pulses . . . 62
5.1.4. Comparison of SC Simulations for Different Seed Pulse Lengths 66
5.2. Simulations of Broadband CARS Generation . . . 67
5.2.1. Comparison of CARS generation with SC generated with different pulse lengths . . . 68
5.3. Summary and Conclusions . . . 75

6. Picosecond-Hyperspectral CARS Imaging 77
6.1. Concept of ps-Hyperspectral CARS . . . 77
6.2. Chemical Analysis of a Miller-Type Complex Prebiotic Broth . . . 80
6.2.1. Spontaneous Raman Spectroscopy . . . 81
6.2.2. CARS Spectroscopy . . . 82
6.2.3. UVVIS Absorption Spectroscopy . . . 84
6.2.4. 2PF and SHG Spectroscopy . . . 86
6.2.5. Discussion . . . 86
6.2.6. Summary and Conclusions . . . 88
6.3. Application to 2D Chemical Imaging of Single Cyclamen Pollen Grains 89
6.3.1. Multivariate Analysis . . . 90

6.3.2. Univariate Analysis . . . 92
6.3.3. Summary and Conclusions . . . 93
6.4. Application to 3D Hyperspectral CARS and 2PF Imaging of Single Daisy Pollen Grains . . . 95
6.4.1. Summary, Conclusions, and Outlook . . . 98

7. Interferometric Hyperspectral CARS Imaging with a Broadband Spontaneous FWM Source 99
7.1. The Broadband Interferometric CARS Idea . . . 100
7.2. Performance of the FWM Source of Broadband Phase-Correlated Photon Pairs . . . 102
7.3. Implementation of Interferometric Hyperspectral CARS . . . 104
7.3.1. Broadband Interferometric CARS Spectroscopy . . . 105
7.3.2. Interferometric Hyperspectral CARS Imaging . . . 108
7.4. Summary, Conclusions and Outlook . . . 110

8. Two-Dimensional CARS Microspectroscopy 111
8.1. Characterization of the Laser Pulses, Used for 2D-CARS Microscopy 113
8.2. 2D-CARS of Toluene . . . 114
8.3. Raman Free Induction Decay in Toluene . . . 114
8.4. Summary, Conclusions and Outlook . . . 117

9. Epi-Detected Hyperspectral CARS Imaging 119
9.1. Characterization of an Index-Matched PMMA Wedge Sample . . . 121
9.1.1. Refractive index matching . . . 121
9.1.2. Wedge Height Profile Measurements . . . 122
9.2. Forward-Detected CARS of Index Matched PMMA . . . 123
9.3. Epi-Detected CARS of Index Matched PMMA . . . 124
9.4. Forward- and Epi-Detected CARS Spectra for Varying PMMA Wedge Thickness . . . 125
9.5. Summary, Conclusions and Outlook . . . 131

A. Appendix 133
A.1. Pulse Length Dependence of Simulated Supercontinuum Generation . 133
A.2. Two Photon Induced Auto Fluorescence of Single Daisy Pollen Grain 135

Acknowledgments 136

Bibliography 137

List of Figures **148**

List of Symbols **159**

Statement of Authorship **165**

Curriculum Vitae **167**

Publication List to Date **168**

1 Deutsche Zusammenfassung

Optische Analysen mikroskopischer Proben blicken auf eine lange Historie zurück, in der viele verschiedene Mikroskopietechniken über die Jahre hinweg entwickelt wurden. Viele der optischen Mikroskopie-Methoden ermöglichen eine zerstörungsfreie und nicht-invasive Untersuchung der Proben. Sind bei dieser Untersuchung nicht nur rein morphologische Informationen erwünscht, können durch die Kombination mit optischen Spektroskopietechniken zusätzliche chemische Informationen über die Probe gewonnen werden. Die sensitivste unter den chemisch-spezifischen, optischen Mikroskopiemethoden basiert auf der Fluoreszenzspektroskopie, für die die chemisch-spezifische Fluoreszenzmarkierung der Proben genutzt wird. Im Gegensatz dazu ermöglichen Schwingunsspektroskopien eine markierungsfreie Untersuchung der Proben, unter denen die Raman-Spektroskopie zu den vielseitigsten Methoden zur Bestimmung von intrinsischen, molekularen Strukturinformationen der Probe zählt. Zusätzlich zu einer hohen chemischen Spezifizität bietet die Raman-Spektroskopie unter Verwendung eines konfokalen Mikroskops eine hohe räumliche Auflösung. Da jedoch der Raman-Effekt sehr schwach ist, werden häufig lange Integrationszeiten benötigt. Zudem ist das Raman-Signal oft von Fluoreszenz der Probe überdeckt. Über die kohärente anti-Stokes Raman-Streuung (engl.: Coherent anti-Stokes Raman scattering (CARS)) können diese Limitierungen unter Verwendung eines zweiten Anregungsfeldes umgangen werden, da eine kohärente Anregung der molekularen Schwingungen erfolgt, und diese im Folgenden von einem dritten Feld abgefragt wird. Die resultierende CARS-Emission wird auf der anti-Stokes-Seite der Anregungswellenlängen erzeugt, wobei der Einfluss des Ein-Photon-induzierten Fluoreszenzhintergrundes – im Vergleich zu der spontanen Raman Detektion – vermieden wird. Zusätzlich dazu führt die kohärente Verstärkung zu einer Messsensitivität, die um drei Größenordnungen höher liegt. Außerdem führt die Multi-Photonen-Eigenschaft zu einem intrinsischen, drei-dimensionalen Auflösungsvermögen in der optischen Mikroskopie.

Die erste, durch Professor Xie und Kollegen in 1999 [1] präsentierte, Umsetzung von CARS in einem Mikroskopie-Aufbau hat ein neues Interesse an der CARS-Methode

als ein leistungsfähiges, nichtinvasives, optisches Werkzeug für die schnelle, markierungsfreie, chemische Bildgebung geweckt. Die Methode basiert auf einem intrinsischen Schwingungskontrast der Probe und erlaubt einen Einblick in die molekulare Zusammensetzung mikroskopischer Proben.

Über die Detektion einzelner CARS-Resonanzen hinaus wird eine experimentelle Realisierung der Messung eines zusammenhängenden Raman-Spektralbereichs von über 4000 cm^{-1} für jeden einzelnen Bildpunkt benötigt. In dieser Doktorarbeit wurde ein neues Konzept der hyperspektralen CARS-Bildgebung eingeführt, welche auf der Erzeugung breitbandiger Stokes-Pulse mit einer, für eine effiziente CARS-Anregung adäquaten, spektralen Breite und Energiedichte in einer photonischen-Krsitallfaser (engl.: Photonic Crystal Fiber (PCF)) basiert. Für die erfolgreiche Umsetzung dieses Konzepts mussten zunächst folgende Fragen beantwortet werden: Welche PCF-erzeugten Superkontinuumspulse (SC) ermöglichen eine hyperspektrale CARS-Erzeugung mit hoher spektraler Auflösung und mit hohem Signal-zu-Rausch-Verhältnis? Was ist außerdem die beste experimentelle Lösung für die direkte Messung der Amplitude und der Phase eines stark fokussierten, breitbandigen elektromagnetischen Feldes?

Da die hyperspektrale CARS Erzeugung von der Interaktion einzelner Paare von schmalbandigen Pump und breitbandigen Stokes-Pulsen in der Probe abhängt, war es wichtig, die breitbandige CARS Generierung für einzelne Pulse zu untersuchen, was experimentell nicht möglich ist. In Kapitel 5 wurde daher zunächst die hyperspektrale CARS Erzeugung mit ps-induzierten SC-Pulsen simuliert, um damit die idealen Stokes-Pulse für das gewählte PCF-Design zu bestimmen.

Durch die Simulation der Phase und Amplitude des breitbandigen, PCF-erzeugten SC sowie durch die anschließende äquivalente Simulation für das mit diesen SC-Feldern erzeugte, breitbandige, komplexe CARS Feld wurden einzelne, breitbandige CARS-Pulse charakterisiert, wozu es bisher keine Veröffentlichungen gibt. Anregungspulslängen im fs- und ps-Bereich wurden untersucht, wodurch nicht komprimierbare, einzelne SC-Pulse erzeugt wurden, die den gesamten Raman-Spektralbereich abdecken, der für die anschließende hyperspektrale CARS-Erzeugung benötigt wird. In Anbetracht des abgedeckten Raman-Spektralbereichs, des CARS Signal-zu-Rausch-Verhältnisses (engl.: signal-to-noise-ratio (SNR)), der einfacheren experimentellen Umsetzung und der spektralen Auflösung mit einer spektralen Bandbreite, die mit typischen Schwingungsresonanzen übereinstimmen, stellte sich ein $2,94$ ps Puls als bester Anregungspuls heraus. Auf den Simulationsergebnissen basierend wurde das Konzept für eine ps-hyperspektrale CARS-Bildgebung mit $2,94$ ps Anregungspulsen entwickelt und ein experimenteller Aufbau realisiert, welcher in Kapitel 6 im Detail beschrieben wird.

Anschließend wurde eine pikosekunden-hyperspektrale CARS-Bildgebung erfolgreich an zwei exemplarischen Proben angewandt und charakterisiert. Die Messungen beider Proben profitierten stark von der Vermeidung des intrinsischen Fluoreszenzhintergrundes.

Zunächst wurden Ursuppenproben, die von einem Miller-Urey-Experiment (MU) stammen, untersucht, um ein weiteres Verständnis ihrer komplexen und unbekannten, molekularen Zusammensetzung und chemischen Struktur auf eine nicht-invasive Weise zu erlangen. In Abhängigkeit der Anfangsbedingungen der MU-Experimente wurden Moleküle mit einer höheren Anzahl aromatischer, beziehungsweise einer höheren Anzahl von Nitril und aliphatischen C-H Verbindungen durch breitbandige CARS-Spektroskopie identifiziert. Aufgrund des starken Fluoreszenzhintergrundes konnte hier nicht mit spontaner Raman-Spektroskopie gemessen werden. Die Zuordnung der charakteristischen Peaks zu den aromatischen C_xN_y Ringstrukturen deuten auf die Präsenz von Nukleinsäuren hin, was durch ergänzende UVVIS-Absorptionspsektroskopie untermauert wurde.

In der zweiten Anwendung des neuen Konzepts wurde die ps-hyperspektrale CARS-Bildgebung zur experimentellen, chemischen 2D- und 3D-Kartierung der chemischen und strukturellen Eigenschaften von Molekülen innerhalb eines einzelnen Pollenkorns demonstriert. Hierbei wurde der Vorteil der kohärenten Verstärkung der intrinsischen Raman-Antwort der Probe durch hyperspektrales CARS ausgenutzt, um eine schnelle, markierungsfreie Bildgebung einer biologischen Probe einer Pflanzenzelle mit unbekannter Zusammensetzung zu erzeugen. Mit einer sub-Mikrometer-Auflösung wurde der spektrale Fingerabdruck der zahlreichen, unterschiedlichen, biologischen Komponenten in der intrazellulären Struktur enthüllt. Die beiden gleichzeitigen, quantitativen und volumetrischen 3D-hyperspektrale CARS- und 2PF-Bildgebungen eines gesamten, einzelnen Gänseblümchen-Pollenkorns wurde erfolgreich demonstriert, wobei insgesamt 950400 Spektren in 127 Minuten aufgenommen wurden. Die multivariate Analyse des aufgenommenen hyperspektralen Datensatzes erlaubt die Auswertung der Daten ohne vorherige Kenntnisse der Probe. Als Ergebnis wurden das Pollenplasma, beide Pollenkerne und die Exine anhand ihrer jeweils charakteristischen spektralen Signaturen von Proteinen, Nukleinsäuren sowie eines phenolisches Biopolymers visualisiert.

Die hyperspektrale CARS-Bildgebung ist eine kohärente Methode, die eine kohärente Verstärkung des in der Probe erzeugten CARS-Feldes durch die Interferenz mit einem externen, lokalen Oszillator- (LO-) Feld ermöglicht. In Kapitel 7 wurde ein neuer Ansatz für eine interferometrische, hyperspektrale CARS-Bildgebung realisiert, bei der breitbandige, phasen-korrelierte, sogenannte Signal- und Idler-Photonenpaare, in einer PCF erzeugt wurden, die durch pikosekunden-gepumpte,

breitbandige, spontane, Vier-Wellen-Mischung (engl.: Four-Wave-Mixing (FWM)) erzeugt und für den interferometrischen CARS-Prozess das LO- und das Stokes-Feld bereitgestellt wurden. Die zeitliche Verzögerung zwischen dem LO- und dem CARS-Feld der Probe ermöglichte die volle Kontrolle über deren Phasenbeziehung und stellte somit den vielfältigsten Ansatz für interferometrische, hyperspektrale CARS-Bildgebung dar. Dieser direkte, experimentelle Zugang zur Phase und Amplitude des CARS-Feldes ermöglichte die direkte Bestimmung des komplexen Schwingungsverhaltens der nichtlinearen Suszeptibilität dritter Ordnung $\chi^{(3)}(\nu)$ der Probe. Im Gegensatz dazu musste zur standard-hyperspektralen CARS-Bildgebung die Phase nachträglich zur Messung bestimmt werden. Der experimentelle Nachweis dieses neuen Konzeptes der interferometrischen, hyperspektralen CARS-Bildgebung wurde an einem einzelnen, mikroskopischen Benzaldehyd-Tropfen durchgeführt.

Nach der exklusiven Anwendung der hyperspektralen CARS-Bildgebung in der Frequenzdomäne wurde in Kapitel 8 die Zeitdomäne hinzugefügt. Die Charakteristik von CARS als eine Raman-Pump-Probe-Technik wurde hierbei ausgenutzt, wobei der Abfragepuls zu dem zeitlich überlappten Paar von Pump- und Stokes-Pulsen verzögert ist. Dadurch sollte die Implementierung von zeitaufgelösten, multiplex-(2D-) CARS die Messung der Dephasierungszeiten von allen spektral aufgelösten Raman-Kohärenzen gleichzeitig ermöglichen. Hier wurde 2D-CARS mit einem ps- und einem nah-transform-limitierten, wenige Schwingungen zählenden, fs-Puls erfolgreich an einer reinen Toluol Test-Probe in einem sub-Femtoliter Probenvolumen angewendet. Die freien Raman-Induktionszerfallskonstanten (engl.: Raman free induction decay (RFID)) von zahlreichen Schwingungsmoden von Toluol wurden durch die Analyse ihrer zeitgleich aufgenommen CARS-Intensitätszeitprofile extrahiert. Unter anderem waren wir in der Lage, zum ersten Mal die Schwingungsmoden bei 1000 cm^{-1} und 1019 cm^{-1} in zeitaufgelöster 2D-CARS Mikrospektroskopie spektral aufzulösen.

Für die Anwendung von CARS in den Lebenswissenschaften ist es oft aufgrund von Streuung und Absorption der Anregungsfelder in dicken Proben nicht möglich, in Transmission zu messen. Daher ist es häufig unerlässlich, das erzeugte CARS in einer epi-Detektionsgeometrie zu sammeln. In den meisten vorhergehenden Studien zu epi-detektierter CARS-Mikroskopie trägt die Rückreflektion des vorwärtsgestreuten CARS (F-CARS) der Probe den größten Anteil zum epi-detektierten CARS-Signal bei. Für eine komplette, experimentelle Charakterisierung und ein besseres Verständnis des intrinsisch rückgestreuten CARS (engl.: epi-scattered CARS (E-CARS)) muss das von der Probe rückreflektierte F-CARS getrennt oder besser vermieden werden. In Kapitel 9 wurde für die erste, systematische und quantitative, experimentelle Studie intrinsischer breitbandiger E-CARS-Emission eine sehr dünne

PMMA-Probe mit sich kontinuierlich ändernder Dicke eingeführt. Reine, breitbandige E-CARS Spektren wurden aufgenommen, wobei simultan das resonante und nichtresonante E-CARS von einer mikroskopischen Probe gemessen wurde, was mit konventioneller F-CARS-Mikrospektroskopie nicht möglich war. Die Tatsache, dass das gesamte, breitbandige E-CARS Spektrum gemessen wurde, ermöglicht die Beurteilung des Ursprungs verschiedener E-CARS-Signalbeiträge und somit deren Vergleich mit vorhergehenden Simulationen. Zum ersten Mal wurde hier das theoretisch vorhergesagte, oszillatorische Verhalten des E-CARS-Signals in Abhängigkeit der Probendicke für das gesamte Spektrum experimentell und quantitativ nachgewiesen.

2 Introduction

The optical analysis of microscopic samples has a long history, and many different microscopy techniques evolved through the years. While many of the optical microscopy methods provide destruction-free and noninvasive investigation of the samples, if not only morphological information is desired, its combination with optical spectroscopy techniques provide additional chemical information of the sample. Among the chemical specific optical spectroscopies, the most sensitive technique is based on fluorescence spectroscopy, which takes advantage of chemically specific labeling of the sample with fluorophores. In contrast, vibrational spectroscopies allow for its label-free investigation, among which Raman spectroscopy is one of the most versatile methods for the extraction of intrinsic molecular structure information about the sample. In addition to high chemical specificity, it provides high spatial resolution when performed in a confocal microscope. However, as the spontaneous Raman effect is weak, often long integration times are needed, and its signal may often be overwhelmed by fluorescence in various samples. Coherent anti-Stokes Raman scattering (CARS) circumvents these limitations by adding a second excitation field, coherently exciting the molecular vibrations, which are probed by a third field. The resulting CARS emission is generated on the anti-Stokes side of the excitation wavelengths, avoiding the impact of one-photon induced fluorescence background, when compared to spontaneous Raman detection. Moreover, its coherent amplification provides about three orders of magnitude higher detection sensitivity, and its multi-photon nature provides intrinsic three-dimensional sectioning capability in optical microscopy.

The first implementation of CARS in a microscopy setup reported by Xie and coworkers in 1999 [1] has started a new interest in the coherent Raman technique as a powerful noninvasive optical tool for fast label-free chemical imaging based on the intrinsic vibrational contrast of the sample and providing insights of the molecular composition within microscopic samples.

Beyond single-resonance CARS detection, an experimental realization of probing the contiguous Raman range over 4000 cm^{-1} for each image pixel is required. In this

thesis, a novel concept of hyperspectral CARS imaging is introduced, which relies on the generation of broadband Stokes pulses in a photonic-crystal fiber (PCF) with a spectral width and energy density which are adequate for efficient CARS excitation. For the successful realization of this concept, first the following questions had to be answered: What PCF-generated supercontinuum (SC) pulse allows hyperspectral CARS generation with both high spectral resolution and high signal-to-noise ratio? Furthermore, what is the best experimental solution for the direct measurement of both amplitude and phase of a broadband field under tightly focused excitation laser beam conditions?

As the hyperspectral CARS generation is dependent on the interaction of a single pair of a narrowband pump and a broadband Stokes pulse in the sample, it is important to investigate the generation of the broadband CARS field on a single-pulse level, which cannot be done experimentally. In chapter 5 the hyperspectral CARS generation with ps-seeded SC pulses is therefore simulated to identify the ideal Stokes pulse for a given PCF design.

By simulating the phase and amplitude for the broadband PCF seeded SC, and consecutively for the broadband complex CARS field generated with these single SC fields, single-pulse broadband CARS spectra are characterized, which has not been reported in the literature yet. Seed pulse lengths in the fs- and ps-regime are investigated, obtaining non-compressible single SC spectra covering the full Raman shift range needed for subsequent hyperspectral CARS generation. Considering the spectral resolution, with a bandwidth matching that of a typical vibrational resonance, the covered spectral Raman-shift range, the CARS signal-to-noise ratio (SNR), and the simplest experimental implementation, the use of a single laser oscillator, providing 2.94-ps seed-pulses proved to be the best choice.

Based on the simulation results, the concept of all-ps hyperspectral CARS imaging with 2.94-ps pulses was developed and an experimental setup was subsequently realized, which are described in detail in chapter 6. Picosecond Hyperspectral CARS imaging is then successfully demonstrated and characterized by investigating two exemplary samples, which both strongly benefit from avoiding the intrinsic fluorescence background.

First, samples of primordial broth from a Miller-Urey (MU) experiment are studied in order to gain more insight into their complex and unknown molecular composition and chemical structure in a non-invasive way. Depending on the initial conditions in the MU experiment, molecules with a higher degree of aromaticity, or a higher amount of nitriles and aliphatic C-H compounds, were identified by broadband CARS spectroscopy, which could not be detected by conventional Raman spectroscopy because of the presence of a strong fluorescence background. The

assignment of the characteristic peaks to aromatic C_xN_y ring structures indicates the presence of nucleic acids, which find supporting evidence in the corresponding UVVIS absorption spectra.

In the second demonstration of the novel concept, the all-ps hyperspectral CARS imaging is then experimentally applied to the 2D and 3D mapping of chemical and structural properties of molecules inside a single pollen grain. Here, the advantage of the coherent enhancement of the samples intrinsic Raman response in hyperspectral CARS is exploited, performing fast and label-free imaging of a biologically relevant example of a plant cell with unknown composition. The spectral fingerprints of the various biological constituents within their sub-cellular structures are revealed within a sub-micron focus spot. Simultaneous 3D hyperspectral CARS and 2PF volumetric and quantitative imaging of an entire single daisy pollen grain was successfully demonstrated, where in total 950400 spectra were acquired within 127 minutes. The multivariate analysis of the recorded hyperspectral data set has enabled an evaluation without a priori knowledge of the sample. As a result, the exine, the pollen plasma, and both pollen nuclei, were visualized based on their characteristic spectral Raman signatures of phenolic biopolymers, proteins, and nucleic acids, respectively.

Hyperspectral CARS imaging is a coherent technique where a coherent enhancement of the CARS field generated in the sample is possible by interference with an external local oscillator (LO) field. In chapter 7, a new approach to interferometric hyperspectral CARS imaging is realized, where broadband phase-correlated signal and idler photon pairs are produced in a PCF by picosecond-seeded broadband spontaneous FWM, which provide the LO field and the Stokes fields, respectively. The temporal delay between the LO field and the CARS field from the sample enables the full control over their phase relation, and hence provides the most general approach to interferometric hyperspectral CARS imaging. This direct experimental access to the phase and amplitude of the CARS field allows the extraction of the complex vibrational response of the samples third order nonlinear susceptibility $\chi^{(3)}(\nu)$, which is in contrast to the standard hyperspectral CARS imaging approach, where the phase needs to be estimated posterior to the measurements. The proof of this novel concept of interferometric hyperspectral CARS imaging is experimentally demonstrated for a single microscopic droplet of benzaldehyde.

After performing hyperspectral CARS imaging exclusively in the frequency domain, in chapter 8 the time domain is added. By exploiting the characteristic of CARS being a Raman pump-probe technique, where the probe pulse is delayed with respect to the pair of temporally overlapped pump and Stokes pulses, the implementation of time-resolved multiplex (2D) CARS enables the measurement of the dephasing

times of all spectrally resolved Raman coherences simultaneously. Here, 2D-CARS microspectroscopy with a ps- and a near transform-limited few-cycle fs-pulse has been successfully applied to a neat toluene test sample within a sub-femtoliter probe volume. The Raman free induction decay (RFID) constants of various vibrational modes of toluene were extracted from the analysis of their simultaneously recorded CARS intensity time-profiles. As such, for the first time we were able to spectrally separate the 1000 cm^{-1} and the 1019 cm^{-1} modes in time resolved 2D-CARS microspectroscopy.

For the application of CARS microscopy in the life sciences, it is often not possible to measure in transmission due to scattering and absorption of the excitation fields inside a thick sample. Therefore it is often indispensable to collect the generated CARS in a epi-detection geometry. In most previous studies on epi-detected CARS microscopy, the back-reflection of forward scattered CARS (F-CARS) from the sample is giving the strongest epi-detected CARS signal contribution. For a complete experimental characterization and better understanding of intrinsic epi-scattered CARS (E-CARS), the back-reflection of the F-CARS from the sample needs to be separated or better eliminated. In chapter 9, a very thin PMMA polymer sample of continuously varying thickness was introduced for the first systematic and quantitative experimental study of intrinsic broadband E-CARS emission. Pure broadband E-CARS spectra were measured, providing simultaneously both resonant and non-resonant E-CARS from a microscopic sample, which could not be measured by conventional F-CARS microspectroscopy. The fact, that the full broadband E-CARS spectrum is measured allows the evaluation of the origin of different E-CARS signal contributions and therefore their comparison with previous simulations. For the first time, the theoretically predicted oscillatory behavior of pure E-CARS signal in dependence of the sample thickness was experimentally and quantitatively verified for the full spectrum.

3 Theoretical Background

In this chapter, the required theoretical background for understanding the main work of this thesis is shortly given. First, the various nonlinear interactions that lead to spectral pulse broadening in supercontinuum generation (SCG), are described in section 3.1. Among them are discussed the processes of spontaneous Raman scattering and spontaneous FWM, which are of further interest as diagnostic tools and a source of broadband phase-correlated photons, respectively. Subsequently the theory of SCG in photonic crystal fiber (PCF) is described in section 3.2, followed by section 3.3, containing the theoretical description of CARS spectroscopy in forward- and epi-direction, broadband CARS spectroscopy, interferometric CARS detection, and time resolved CARS spectroscopy. Finally three short sections 3.4, 3.5, and 3.6 describe the processes of sum frequency generation (SFG), two photon induced fluorescence (2PF), and UVVIS absorption spectroscopy, respectively.

3.1. Supercontinuum Generation Processes

For the simultaneous generation of CARS over a wide spectral range, a broadband source is needed. Additionally, a spatial coherence of that broadband light source similar to that of laser light is needed, which can be tightly focused to a diffraction limited spot with a high NA objective lens. Furthermore this broadband light should be continuous and broad enough to simultaneously cover both, the fingerprint region and the *C-H* stretching vibration region of molecular Raman resonances. By exploiting SCG in a solid-core PCF with a high non-linearity such required broadband pulses for broadband CARS generation are provided.

Supercontinuum (SC) generation (SCG) is an accumulation of nonlinear wavelength conversion processes that significantly broaden the spectrum of typically short laser pulses. The heart of the understanding of this behavior, is to investigate the dispersion properties of the nonlinear medium, in which the SC is generated. The material

dispersion D is given in first approximation by [2]

$$D(\lambda) = -|\beta_2| \, 2\pi c/\lambda^2 \tag{3.1}$$

with the group velocity dispersion (GVD) $|\beta_2|$, the speed of light in vacuum c, and the wavelength λ of the incident electrical field. The dispersion of a bulk material is directly connected to the absorption of the material by the Kramers-Kronig relation in all linear and most non-linear cases [3]. Considering light in the near infrared regime, a transparent bulk material shows normal dispersion, which means that the blue components of an incident field experience a higher phase velocity than the red components.

In PCFs a waveguide dispersion, which is due to the geometry of the photonic structure of the materials with different refractive indexes, adds to the common material dispersion D. Photonic crystal fibers have been proven to be a versatile highly nonlinear medium, due to the tunability of their waveguide dispersion, such as their hole and pitch parameters and of their PCF nonlinear interaction length. The core diameter of a typical PCF used for SC generation lies in the range from two to three times of the recommended seed wavelength, providing single mode operation and guiding for all SC wavelengths.

Benchmark lengths are the dispersion length L_D and the nonlinear length L_{NL} of the PCF, which are defined in equations (3.2) and (3.3), respectively [2, p. 52]:

$$L_D = \frac{{T_0}^2}{|\beta_2|} \tag{3.2}$$

$$L_{NL} = \frac{1}{\gamma P_0} \tag{3.3}$$

Here T_0 is the input laser pulse length, γ is the nonlinear coefficient of the PCF, and P_0 is the optical peak power of the incident pulse. For dispersion and nonlinear processes to take effect on the traveling pulse inside the PCF, the fiber length needs to be in the same order of magnitude as the dispersion length and nonlinear length, respectively.

Many different processes are involved in SCG. The lowest-order nonlinear effect that can occur in an optical fiber is originating from the third order susceptibility $\chi^{(3)}$ [2, p. 14], as due to symmetry constrictions $\chi^{(2)}$ effects are prohibited for cylindrically symmetrical optical fibers.

3.1.1. Self- and Cross-Phase Modulation

Self-phase modulation (SPM) is a consequence of the nonlinear refraction of light, which is dependent on the intensity $|E|^2$ of an incident optical pulse with electrical field strength E that propagates through a nonlinear $\chi^{(3)}$-active medium.
In its simplest form the total refractive index $\tilde{n}$ of this nonlinear material is then given by [2, p.14]

$$\tilde{n}(\omega, |E|^2) = n(\omega) + n_2 \ |E|^2 \tag{3.4}$$

with $n(\omega)$ being the linear refractive index, and n_2 being the nonlinear-index coefficient [2, p.15]:

$$n_2 = \frac{3}{8n} Re(\chi^{(3)}_{1111}). \tag{3.5}$$

$\chi^{(3)}$ is the third order susceptibility tensor element describing the nonlinear response of the material. In the case of a strong optical field and a high $\chi^{(3)}$ value, the refractive index considerably differs from the value of the linear refractive index n. Now when a short laser pulse propagates in an optical fiber at its leading edge the increasing pulse intensity causes an increase in the refractive index $\tilde{n}$, whereas at its trailing edge the opposite is the case. As a result, a continuously increasing refractive index causes a red shift of the pulse spectral components at the leading edge of the pulse. At its trailing edge the decreasing refractive index causes a blue shift of the pulses spectral components. This effect is called self-phase modulation (SPM), and its inverse wavelength shifts result in a spectral broadening of the propagating pulse. If this refractive index modulation acts on another copropagating weaker pulse, such as a soliton, this effect is called cross-phase modulation (XPM).

3.1.2. Soliton Generation

Another kind of generation of new wavelengths happens through soliton generation. Solitons are generated, when the pump wavelength resides in the anomalous dispersion regime of the PCF [2], where its anomalous dispersion is compensated by SPM. This way a dynamically stable wave packet propagates through the fiber, which is called a soliton. This equilibrium of SPM and dispersion is usually power dependent, so that solitons can serve as pulse source where the wavelength is easily tunable by a variation of the input seed power [4, 5]. Even if they are typically initiated by vacuum fluctuations their form and spectral position are purely dominated by the fiber parameters [2].

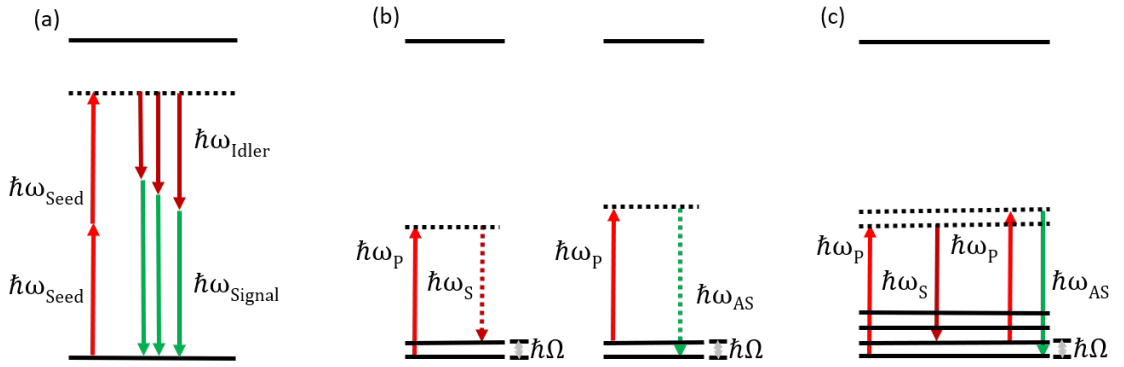

Figure 3.1.: Schematic representation of energy level diagrams for (a) spontaneous FWM process, (b) for the processes of Stokes (left panel) and anti-Stokes (right panel) spontaneous Raman scattering, and (c) the narrowband CARS process. Solid horizontal lines represent the electronic and vibrational states. Dashed horizontal lines represent virtual states. $\hbar\Omega$ represents the energy of an exemplary vibrational resonance.

3.1.3. Spontaneous Four-Wave Mixing

Four-wave mixing (FWM) is the most general term for frequency mixing in a $\chi^{(3)}$-active medium [6]. For example, SPM is only a special cases of FWM where all four frequencies are degenerate. Here mainly the case of spontaneous FWM will be discussed, where two fields are degenerated, and the other two fields are not.

Within a non-resonant $\chi^{(3)}$ medium, vacuum fluctuations in the presence of a strong laser pulse can lead to a spontaneous FWM process, where two photons of the energy $\hbar\omega_P$ of the laser pulse are converted into an idler and a signal photon, having a lower energy $\hbar\omega_{idler}$ and a higher energy $\hbar\omega_{signal}$, respectively, as depicted in figure 3.1 (a). The wavelengths of the four waves are related according to energy conservation [3]:

$$2\,\omega_{Seed} = \omega_{Signal} + \omega_{Idler} \tag{3.6}$$

with the seed, the signal and the idler frequencies ω_{Seed}, ω_{Signal} and ω_{Idler} respectively. Even if the signal and idler waves are randomly generated due to vacuum fluctuations, not only energy but also momentum is conserved, which reveals itself in the phase relationship between the four waves involved [2]:

$$2\,\phi_{Seed} = \phi_{Signal} + \phi_{Idler}. \tag{3.7}$$

where ϕ_{Seed}, ϕ_{Signal} and ϕ_{Idler} are the phases of the seed, the signal and the idler waves respectively.

One prerequisite for this process to happen is minimizing the effective phase mismatch $\kappa = |\Delta\mathbf{k}_{FWM}| + \Delta k_{NL}$. The wave vector mismatch due to material dispersion for the signal wave is given by $\Delta\mathbf{k}_{FWM} = \mathbf{k}_{Signal} - (2\ \mathbf{k}_{Seed} - \mathbf{k}_{Idler})$, where $\mathbf{k}_{Seed}$, $\mathbf{k}_{Signal}$, $\mathbf{k}_{Idler}$ are the wave vectors of the respective fields. The nonlinear contributions of SPM and XPM to the phase mismatch are represented by $\Delta k_{NL} = 2\gamma P_0$. For the case where the two initial photons are taken from the same pulse, which is the case considered here, the FWM gain as a function of κ is then given by [2, p. 373]:

$$g_{FWM} = \sqrt{(\gamma P_0)^2 - (\frac{\kappa}{2})^2}. \tag{3.8}$$

The spontaneous FWM signal and idler sidebands are maximized at the frequencies [2, p.383]

$$\Omega_{Signal,Max} = \omega_{Seed} + \sqrt{2\gamma P_0 / |\beta_2|} \tag{3.9}$$

$$\Omega_{Idler,Max} = \omega_{Seed} - \sqrt{2\gamma P_0 / |\beta_2|} \tag{3.10}$$

where the phase-matching is fulfilled ($\kappa \approx 0$).

3.1.4. Spontaneous Raman Scattering

Spontaneous Raman scattering is a form of inelastic light scattering on molecules or solid matter. Raman scattering can occur when the molecular vibration results in a change of the polarizability of the respective molecular bonds. Figure 3.1 (b) shows on the left panel the energy level diagram of the Stokes Raman scattering process, where excitation by a pump photon with energy $\hbar\omega_P$ and the spontaneous emission of the Stokes Raman photon with energy $\hbar\omega_S$ occurs, leaving the sample at an excited vibrational state with energy $\hbar\Omega$. On the right panel of figure 3.1 (b) the anti-Stokes Raman scattering process is shown, where the pump photon excites the sample, which already resides in an excited vibrational state with energy $\hbar\Omega$, to a virtual state, and an anti-Stokes Raman photon with higher energy $\hbar\omega_{AS}$ is emitted, leaving the sample at the vibrational ground state.

The intensity ratio between the anti-Stokes Raman signal ($I_{anti-Stokes}$) and the Stokes Raman signal (I_{Stokes}) depends on the population of the ground and the excited vibrational states, respectively, and is proportional to the temperature dependent Boltzmann factor [7]:

$$\frac{I_{anti-Stokes}}{I_{Stokes}} \propto e^{-\hbar\Omega/k_B T_{sample}}. \tag{3.11}$$

Here $\hbar$ is the reduced Planck constant, k_B is the Boltzmann constant and T_{sample} is the temperature of the sample. This means that at room temperature the Raman peak intensities in the so called fingerprint region (500 cm^{-1} − 1800 cm^{-1}) on the anti-Stokes side are 100 to 1000 times weaker than those on the Stokes side.

3.2. Supercontinuum Generation in Photonic Crystal Fibers

In PCFs the air hole structure surrounding the fiber core determines the waveguide dispersion properties and therefore the overall dispersion. The important parameters here, are the distance between the air holes as well as their sizes. If the polarization of the field of the propagating pulses is to be maintained throughout the fiber length, a symmetry break of the air-hole-pattern is introduced causing birefringence in the fiber. The great advantage of using solid core PCFs for SCG is the ease to choose the interaction length, simply by choosing the fiber length. Another advantage is that the mode profile at the exit facet of the fiber is very close to a perfect gaussian profile throughout all wavelengths.
For the simulation of the supercontinuum generated in a nonlinear PCF, the generalized nonlinear Schrödinger equation (GNLSE) needs to be solved, according to Dudley et al. [8]

$$\frac{\partial \tilde{A}'}{\partial z} = i\frac{\gamma\omega}{\omega_0} exp(-\hat{L}z)\, \mathfrak{F}\left\{ A(z,T) \int_{\infty}^{\infty} R(T') \left|A(z,T-T')\right|^2 dT' \right\}, \tag{3.12}$$

which describes the propagation of light in a PCF. Here $\hat{L}$ is the complex linear operator

$$\hat{L} = i(\beta(\omega) - \beta(\omega_0) - \beta_1(\omega_0)\left[\omega - \omega_0\right]) - \alpha(\omega)/2. \tag{3.13}$$

$R(T')$ is the Raman response of the nonlinear medium, and γ is its nonlinear coefficient. ω_0 is the optical seed center frequency, A is the field amplitude of the pulse in the fiber, $\tilde{A}'$ is the complex spectral envelope, T is the time in the conmoving frame $T = t - \beta_1 z$, T' is integration variable equivalent to T, $\mathfrak{F}$ is the symbol for the

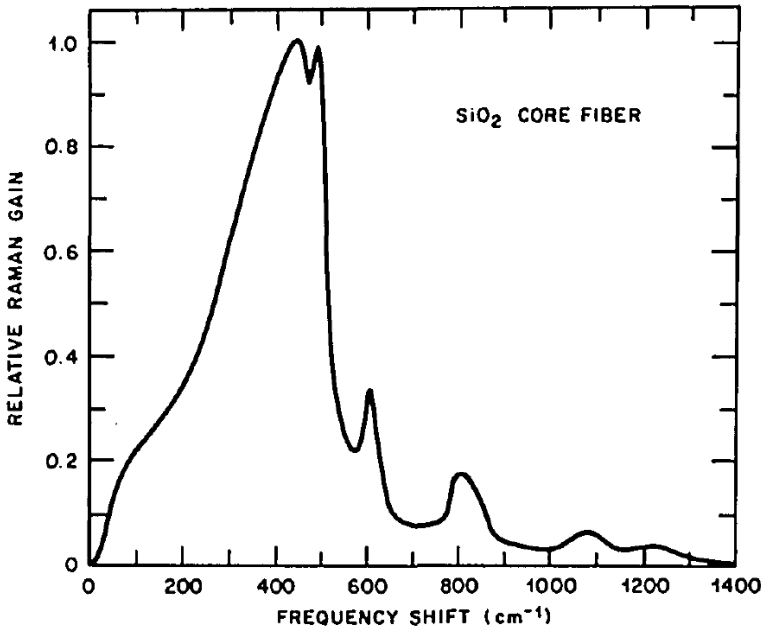

Figure 3.2.: Raman gain of fused silica, taken from Stolen et al. [9]

Fourier transformation, and z is the propagation length. The Raman response R of the fused silica PCF in the frequency domain is displayed in figure 3.2. β represents the effective refractive index, β_1 is the inverse group velocity, and α the attenuation in the PCF.
For the input pulse, a hyperbolic-secant pulse amplitude profile is assumed, which is described in the time domain by

$$A = A_T \cdot sech(t/T_0) \tag{3.14}$$

with the amplitude A_T, the time t and the temporal width T_0. The full width at half maximum (FWHM) of the incident pulse intensity profile is then given by $T_{FWHM} = 2(ln(1+\sqrt{2})) \cdot T_0 \approx 1.76 \cdot T_0$. In the course of this thesis the pulse length always refers to T_{FWHM} represented by the symbol T unless stated otherwise.
So, when the parameters of the PCF and of the incident pulse are known, then through the simulation information about the amplitude and phase of the generated SC can be extracted on a single pulse level.

3.3. CARS Fundamentals

Coherent anti-Stokes Raman scattering (CARS) is another special case of FWM, which was first described by Maker and Terhune in 1965 [10]. In CARS, three fields

of the FWM process are provided by the incident pump, Stokes, and probe pulses, and a fourth field is generated. Whenever the frequency difference between the pump and the Stokes field matches a vibrational resonance of the sample, the CARS field is enhanced. In the case of CARS, FWM is a parametric process [2], where first a coherence in the sample is created by the pump and the Stokes fields. Subsequently this coherence is probed by the probe field, which in the most common degenerate case, is provided by another pump photon, and an CARS field is emitted, compare figure 3.1 (c). According to energy conservation, the CARS field is emitted at the anti-Stokes frequency

$$\omega_{AS} = 2\,\omega_P - \omega_S \tag{3.15}$$

where the frequencies of the pump and the Stokes fields are ω_P and ω_S respectively. The corresponding phase relationship between these fields follows from the momentum conservation, and is given by

$$\phi_{AS} = 2\,\phi_P - \phi_S \tag{3.16}$$

where ϕ_{AS}, ϕ_P, and ϕ_{AS} are the phases of the CARS, the Pump, and the Stokes field, respectively.

The detected CARS signal intensity is proportional to the modulus square of the third order non-linear polarization $P^{(3)}_{CARS}$ induced in the sample [11]

$$I_{CARS}(\omega_{AS}) \propto \left|\mathbf{P}^{(3)}_{CARS}(\omega_{AS})\right|^2, \tag{3.17}$$

with

$$\mathbf{P}^{(3)}_{CARS}(\omega_{AS}) = \chi^{(3)}(\omega_P - \omega_S)\,\mathbf{E}_P(\omega_P)^2\,\mathbf{E}_S(\omega_S). \tag{3.18}$$

Here, $\mathbf{E}_P$ is the pump electric field, and $\mathbf{E}_S$ is the Stokes electric field, and $\chi^{(3)}(\omega_P - \omega_S)$ is the third order non-linear susceptibility of the sample, which is a complex tensor with 81 tensor components [3]. Here only the tensor element $\chi^{(3)}_{1111}$ is considered, where all four involved electric fields are linear polarized along the same direction. From equations (3.17) and (3.18) then follows:

$$I_{CARS}(\omega_{AS}) \propto \left|\chi^{(3)}(\omega_P - \omega_S)\right|^2. \tag{3.19}$$

$\chi^{(3)}$ can be separated into two parts, which is a resonant $\chi_r^{(3)}$ and a non-resonant $\chi_{NR}^{(3)}$ part. For a Raman active resonance r the amplitude of complex $\chi^{(3)}$ is then expressed by [11]

$$\chi_{1111}^{(3)} = \frac{A_{r,1111}}{\delta_r - i\Gamma_r} \tag{3.20}$$

with the amplitude $A_{r,1111}$, the detuning $\delta_r = \Omega_r - (\omega_P - \omega_S)$ from the Raman resonance at frequency Ω_r and the half-width at half maximum Γ_r. The purely real non-resonant (NR) part $\chi_{NR}^{(3)}$ can be considered as frequency independent. The modulus square of $\chi^{(3)}$ is then described as

$$\left|\chi^{(3)}(\omega_P - \omega_S)\right|^2 = \left|\chi_r^{(3)} + \chi_{NR}^{(3)}\right|^2 = (\chi_{NR}^{(3)})^2 + \left|\chi_r^{(3)}\right|^2 + 2\chi_{NR}^{(3)} Re(\chi_r^{(3)}). \tag{3.21}$$

Due to this coherent mixing of the resonant and NR parts of $\chi^{(3)}$, the measured CARS intensities consist of three contributions which are the so called NR-background $(\chi_{NR}^{(3)})^2$, a purely resonant part $\left|\chi_r^{(3)}\right|^2$, and a mixing term of both $2\chi_{NR}^{(3)} Re(\chi_r^{(3)})$, as depicted in figure 3.3 for a single Lorentzian vibrational resonance. The advantage of the non-resonant CARS field, is that it acts as a local oscillator field, which can enhance the resonant CARS field above the noise, as manifested in the mixing term of equation (3.21).
The spontaneous Raman scattering signal I_{Stokes} is proportional to the imaginary part of $\chi^{(3)}$ [13]

$$I_{Stokes}(\omega - \omega_P) \propto Im(\chi_r^{(3)}(\omega_P - \omega_S)). \tag{3.22}$$

3.3.1. CARS Signal Generation in Forward- and Epi-Direction

For CARS, the condition for wave vector matching here is given by [11]

$$|\Delta\mathbf{k}_{CARS}| \cdot l \ll \pi \tag{3.23}$$

where l is the interaction length, and $|\Delta\mathbf{k}_{CARS}|$ is the wave vector mismatch for CARS due to material dispersion, given by

$$\Delta\mathbf{k}_{CARS} = \mathbf{k}_{AS} - (2\,\mathbf{k}_P - \mathbf{k}_S) \tag{3.24}$$

$\mathbf{k}_{AS}$, $\mathbf{k}_P$ and $\mathbf{k}_S$ are the wave vectors of the CARS, the pump and the Stokes fields, respectively. For tightly focused laser beams in the sample, the interaction length l

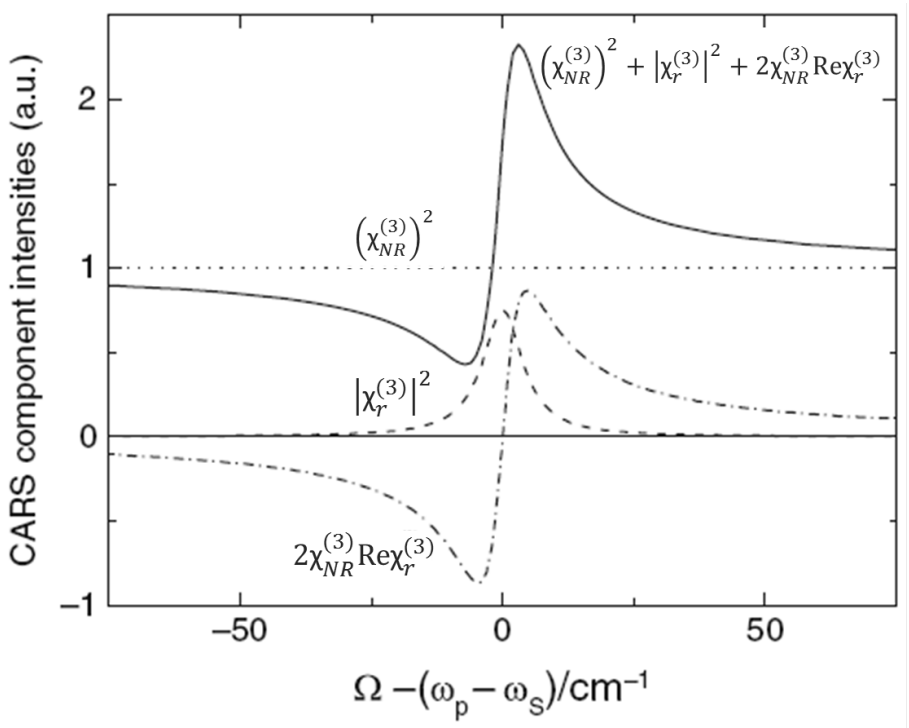

Figure 3.3.: Formation of the dispersive CARS line shape and its single contributions for a simulated Lorentzian Raman resonance according to equation (3.21) ($\Gamma_r = 4.6\ cm^{-1}$, $A_{r,1111} = 4\ cm^{-1}$). The total CARS signal proportional to $\left|\chi^{(3)}\right|^2$ (solid line) is composed of the non-resonant contribution $(\chi_{NR}^{(3)})^2$ (dotted line), the resonant part $\left|\chi_r^{(3)}\right|^2$ (dashed line), and the mixing term of both $2\chi_{NR}^{(3)}Re(\chi_r^{(3)})$ (dash-dotted line). Figure taken from reference [12]

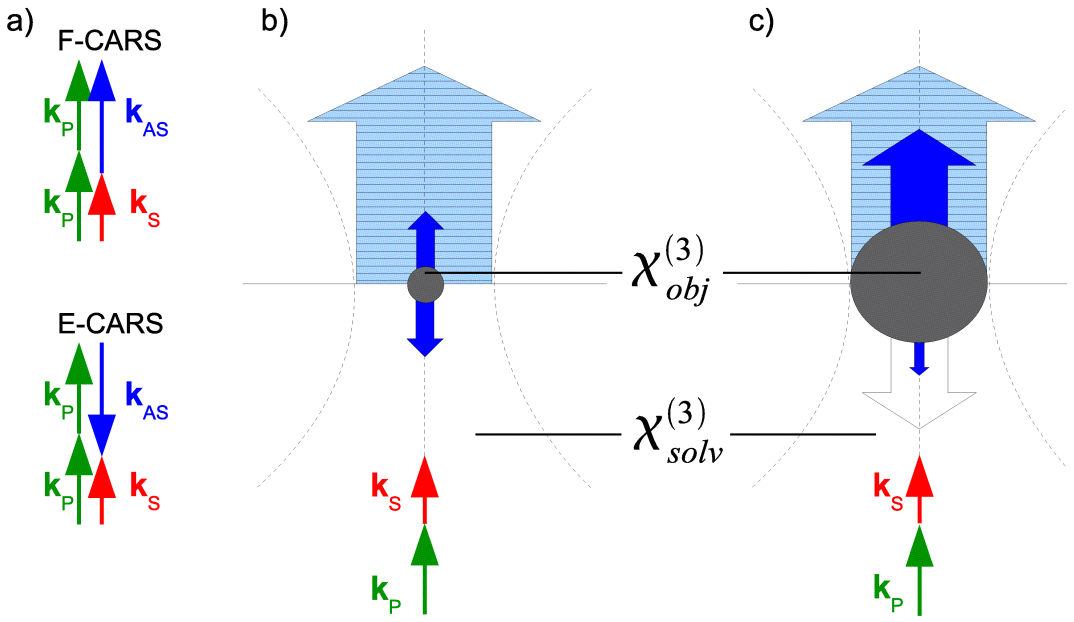

Figure 3.4.: a) Wave vectors in the focus center for forward- and epi-detected CARS microscopies. A schematic representation of the CARS emission from (b) a microscopic sphere with diameter $D_{obj} \ll \lambda_P/2$ (blue arrows), the surrounding bulk medium (light blue arrows), and (c) a sphere with a diameter $D_{obj} \approx \lambda_P/2$ is shown. Additionally in (c), the solvents F-CARS emission back-reflected at the objects surface is shown (white arrow). $\chi^{(3)}_{obj}$ and $\chi^{(3)}_{solv}$ are the third order susceptibilities for the object and the surrounding solvent, respectively. The figure is adapted from reference [11].

is directly given by the focal volume for the case when the objects are bigger than the focal volume, and by the object size for objects smaller than the focal volume. Since the wave vector mismatch is a vector quantity, it depends not only on the direction of the incident pump, Stokes, and probe fields, but also on the direction in which the CARS emission is collected [14]. For a typical geometry used in CARS microscopy all wave vectors are shown in figure 3.4 (a). The CARS emission in the forward direction (F-CARS) from the sample in the center of the focal volume can be considered parallel to the wave vectors of the incident co-propagating pump and Stokes fields. Since $\mathbf{k}_{AS} \approx 2\ \mathbf{k}_P - \mathbf{k}_S$, the wave vector mismatch in F-CARS is $|\Delta\mathbf{k}_{CARS}| \approx 0$. For CARS in the epi-direction (E-CARS), the wave vector of the CARS emission is considered anti parallel with $\mathbf{k}_{AS} \approx -(2\ \mathbf{k}_P - \mathbf{k}_S)$ resulting in a considerable wave vector mismatch of $|\Delta\mathbf{k}_{CARS}| \approx 2|\mathbf{k}_{AS}| = 4\pi n/\lambda_{AS}$, where n is the linear refractive index of the scattering object. Therefore, in epi-direction the condition for the wave vector matching (equation (3.23)) is only achieved for very small interaction lengths, which is only given for objects in the range of and smaller than the CARS wavelength. As a result, samples with a thickness along the

optical axis much smaller than the CARS wavelength λ_{AS} generate similar CARS in forward- and epi-directions (figure 3.4 (b)). On the other hand, the CARS emission in epi-direction of bulk material, for example of the surrounding solvent, is almost fully canceled out in figure 3.4 (b) and (c).
Since F-CARS generated in bulk medium and back-reflected on for example an interface of a macroscopic object, into the epi-direction (see white arrow in figure 3.4 (c)), can contribute to the detected E-CARS signal, refractive index matching is required to ensure pure E-CARS detection.

3.3.2. Multiplex CARS Spectroscopy

In order to coherently excite more than one vibrational resonance simultaneously, a spectrally broad pulse is used as the Stokes pulse in the CARS process. In contrast to the narrowband case, described in equation (3.18), the frequency dependence of the third order polarization $\mathbf{P}^{(3)}_{CARS}$ for parallel-polarized fields is then given by [15]

$$\mathbf{P}^{(3)}_{CARS}(\omega_{AS}) = \int_{-\infty}^{+\infty} d\omega_P \int_{-\infty}^{+\infty} d\omega_S \int_{-\infty}^{+\infty} d\omega_{P'} \chi^{(3)}_{1111}(-\omega_{AS};\omega_P,-\omega_S,\omega_{P'}) \\ E_P(\omega_P)E_S(\omega_S)E_P(\omega_{P'})\delta(\omega_P-\omega_S+\omega_{P'}-\omega_{AS}). \tag{3.25}$$

Here, the excitation process with the pump and Stokes fields has the character of a cross-correlation, whereas the probing represents a convolution [16].
In the case where a narrowband pulse and a broadband pulse are interacting in the sample, their respective roles as pump, Stokes, and probe fields determine different CARS generation schemes. In the most common scheme for broadband multiplex CARS, shown in figure 3.5 (a), referred to in the following sections as CARS scheme A, the pump photon is provided by the narrowband pulse, the Stokes photon is taken from the broadband pulse, and the nonlinear excitation is probed with the narrowband pulse [15, 17]. In this scheme, the excitation bandwidth is governed directly by the bandwidth of the Stokes pulse spectrum, as in the cross-correlation of the narrowband pump pulse with the broadband Stokes pulse mainly the shape of the broadband pulse is preserved.
Another possibility for CARS generation with a pair of a broadband and a narrowband pulses is scheme B shown in figure 3.5 (b). Here, the pump and Stokes photons originate from different frequency components within the bandwidth of the broadband pulse and the probe field originates from the narrowband pulse. The nonlinear vibrational excitation is now given by the auto-correlation of the broadband pulse with itself. The result is that low vibrational frequencies are excited

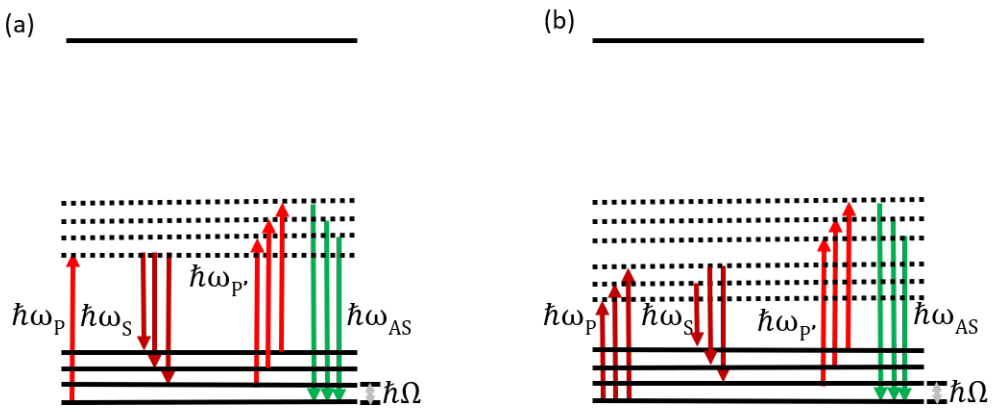

Figure 3.5.: Different possibilities of multiplex CARS excitation. (a) Scheme A: The broadband pulse is acting as the Stokes field only, and the narrowband pulse provides the pump and probe fields. (b) Scheme B: The broadband pulse is acting as both the pump and Stokes fields and the narrowband pulse acts as the probe field only.

much more effectively than higher ones. A third scheme C is when pump, Stokes, and probe photons all originate from the same broadband pulse. In this scheme no spectral resolution is directly provided. In order to obtain spectral resolution a narrow spectral feature needs to be experimentally defined. Therefore we disregard this scheme for further considerations.

All possibilities of CARS interaction of the broadband and the narrowband pulses in the sample can in principal occur at the same time and contribute to the measured CARS spectrum. Only the relative contributions of the different CARS schemes can be adjusted by the relative intensities of the broadband and narrowband pulses. If the power of the narrowband pulse is high in comparison to the broadband pulse then scheme A is favored. When the intensity of the broadband pulse is increased, in comparison to the narrowband pulse, the relative contributions to the CARS signal of scheme B dominates until it approaches the situation described in scheme C, where the role of the narrowband pulse is negligible. Also the relative spectral phase between the broadband and the narrowband fields plays an important role for the different contributions, as the coherence requirements for the different schemes are tremendously diverse. Assuming a constant phase for the narrowband field in scheme A, the relative spectral phase of the broadband field is not important, as every single frequency component of the Stokes continuum generates a CARS signal at a unique spectral position. When the CARS signal is detected in a spectrally resolved manner, different spectral components do not interfere with each other on the detector. Therefore, in scheme A, both, a spectrally coherent and an incoherent broadband Stokes pulse lead to the same CARS spectrum. As a consequence a

spectrally incoherent broadband SC pulse generated in a PCF can be used, and it is not necessary to use a fully coherent transform-limited pulse. The spectral phase of the broadband pulse starts to play a role, when it has more than one possibility for generating the CARS field at a given spectral position. This can be easily seen, when looking at scheme B a bit more in detail, where pump and Stokes fields are taken from the same broadband pulse. There are many possible combinations to generate a spectral component at a certain frequency. Now if those different combinations do not posses the same phase, they do not constructively interfere on the detector. In this scenario, the excitation process for the CARS generation depends on the coherence of individual frequency components within the broadband pulse. Furthermore, now there are many different possible frequency combinations to generate the same CARS frequency. Hence also the relative spectral phase differences between those pairs are relevant. In the case of using an incoherent broadband pulse, these combinations have different phases and therefore destructively interfere on the detector.

3.3.3. Interferometric CARS Spectroscopy

In order to realize interferometric detection of CARS, a local oscillator (LO) field at the frequencies of the CARS field with a fixed phase relation to the CARS field is required. By comparing the frequency and phase relationship of CARS (equations (3.15) and (3.16), respectively) with those of spontaneous FWM (equations (3.6) and (3.7), respectively), we see that the above two requirements for a LO field are fulfilled as long as first the same pump field $E_P(\omega_P, \phi_P)$ is used to seed the spontaneous FWM source as well as to pump the CARS process in the sample, second, the idler field $E_{Idler}(\omega_{Idler}, \phi_{Idler})$ generated in the FWM source is used as the Stokes field $E_{Stokes}(\omega_{Stokes}, \phi_{Stokes})$ in the CARS process in the sample, such that $\omega_{Idler} = \omega_S$ and $\phi_{Idler} = \phi_S$, and third, the signal field $E_{Signal}(\omega_{Signal}, \phi_{Signal})$ generated in the FWM source is used as the LO field for the interferometric detection of the CARS field $E_{CARS}(\omega_{CARS}, \phi_{CARS})$, such that $\omega_{Signal} = \omega_{CARS}$ and $\Delta\phi = \phi_{CARS} - \phi_{Signal} = const.$

For example, in the absence of vibrational resonances, the CARS field $E_{CARS}(\omega_{AS}, \phi_{AS})$ generated with the idler field as the Stokes field $E_S(\omega_S, \phi_S)$ and a replica of the seed pulse as the pump and probe fields $E_P(\omega_P, \phi_P)$ is now an exact replica of the signal field $E_{Signal}(\omega_{Signal}, \phi_{Signal})$ from the spontaneous FWM process. Keeping in mind the phase relation of the signal and idler fields, given in equation (3.7), the CARS field and the signal field have the same phase after compensating for the phase accumulation due to material dispersion in an uncommon beam path.

Therefore, the broadband signal field can be considered as a perfect local oscillator for an hyperspectral interferometric CARS experiment.

The detected interferometric CARS signal $S(\nu_{AS}, \Delta\phi)$, where $\nu_{AS} = 10^2\,\pi\,c\,\omega_{AS}$ is then proportional to the presented sum following Potma et al. [18]:

$$\begin{aligned} &S(\nu_{AS}, \Delta\phi) \propto |E_{Signal}|^2 + |E_{CARS}|^2 \\ &+2E_{Signal}{E_P}^2 E_S\{[\chi^{(3)}_{NR} + Re(\chi^{(3)}_r(\nu_{AS}))]cos\Delta\phi + [Im(\chi^{(3)}_r(\nu_{AS}))]\ sin\Delta\phi\}, \end{aligned} \tag{3.26}$$

where the first summand is the modulus square of the local oscillator field here provided by the spontaneous FWM signal field, the second summand being the modulus square of the normal CARS field generated in the sample, and the third summand being the mixing term, where the cosine dependence of the phase difference $\Delta\phi$ describes the real part of $\chi^{(3)}_r(\nu_{AS})$ and the NR contribution $\chi^{(3)}_{NR}$, and the imaginary part of $\chi^{(3)}_r(\nu_{AS})$ being described by the sine dependence of $\Delta\phi$.

In order to directly extract the amplitude and phase of the CARS field generated in the sample from the optically heterodyne detected CARS signal $S(\nu_{AS}, \Delta\phi)$, the dual-quadrature spectral interferometry (DQSI) procedure [19] is applied:

$$\begin{aligned} &|E_{CARS}(\nu_{AS})| \propto \tfrac{1}{4|E_{Signal}(\nu_{AS})|}\cdot \\ &\sqrt{(S(\nu_{AS}, \Delta\phi = 0) - S(\nu_{AS}, \Delta\phi = \pi))^2 + \left(S\left(\nu_{AS}, \Delta\phi = \tfrac{\pi}{2}\right) - S\left(\nu_{AS}, \Delta\phi = \tfrac{-\pi}{2}\right)\right)^2} \end{aligned} \tag{3.27}$$

where

$$\phi_{AS} = arctan\left(\frac{S(\nu_{AS}, \Delta\phi = \frac{\pi}{2}) - S(\nu_{AS}, \Delta\phi = \frac{-\pi}{2})}{S(\nu_{AS}, \Delta\phi = 0) - S(\nu_{AS}, \Delta\phi = \pi)}\right). \tag{3.28}$$

Here, four interferometric CARS spectra at phase differences of $\Delta\phi = 0, \frac{\pi}{2}, -\frac{\pi}{2}$ and π need to be recorded. Consequently, with the control of $\Delta\phi$ between the CARS field and the local oscillator field, it is possible to experimentally extract the full information of the complex CARS field of the sample [19, 20].

In practice, the CARS field generated in a microscopic object in the sample is much weaker then the local oscillator field, such that $|E_{Signal}(\nu_{AS})| \gg |E_{CARS}(\nu_{AS})|$. As mentioned above we can also express the local oscillator field amplitude by $|E_{Signal}(\nu_{AS})| \propto |E_P^2 E_S|\chi^{(3)}_{NR}$. As a result the real and imaginary parts of the complex $\chi^{(3)}(\nu_{AS})$ of the sample can be extracted in a simplified way by reducing the required number of measurements to two interferometric CARS spectra $S(\nu_{AS}, \Delta\phi)$

at two different phase differences and to the independent measurement of the signal pulse spectrum proportional to $|E_{Signal}(\nu_{AS})|^2$, according to equation (3.29):

$$\frac{S(\nu_{AS},\Delta\phi) - k_{SR}|E_{Signal}(\nu_{AS})|^2}{k_{SR}|E_{Signal}(\nu_{AS})|^2} \propto \begin{cases} \left(const + Re\left(\chi_r^{(3)}(\nu_P - \nu_S)\right)\right), \Delta\phi = 0 \\ Im\left(\chi_r^{(3)}(\nu_P - \nu_S)\right), \Delta\phi = \frac{\pi}{2}. \end{cases} \tag{3.29}$$

Here, k_{SR} represents the proportionality factor that includes the experimental detection efficiency of the system. For the case of identical non-resonant CARS and local oscillator field amplitudes, the constant on the right side of equation (3.29) is one.

3.3.4. Time-Resolved Broadband Multiplex CARS Spectroscopy

In the previous description of CARS signal generation the pump, Stokes, and probe fields were all simultaneously incident in the sample. Here, the idea of time-resolved broadband multiplex CARS spectroscopy is to introduce a controllable time delay on the probe pulse in CARS scheme A (see figure 3.5), such that the pump and Stokes fields are simultaneously incident in the sample while the probe pulse is delayed. In this way the dephasing of molecular vibration coherences can be experimentally investigated, which in the case of time resolved Raman spectroscopy, is called Raman free induction decay (RFID) [21, 22]. The time-resolved CARS signal is then given by [22, 23]:

$$I_{CARS}(\Delta\tau_{Pr}) \propto \int_{-\infty}^{+\infty} dt \left| P_{CARS}^{(3)}(\Delta\tau_{Pr}, t)\right|^2 \tag{3.30}$$

where $\Delta\tau_{Pr}$ describes the time delay between the probe field $E_{P'}$ and the pair of temporally overlapping pump and Stokes fields, E_P and E_S, respectively. The time dependent third order polarization denotes as:

$$\begin{aligned} P_{CARS}^{(3)}(\Delta\tau_{Pr}, t, \omega_{AS}) = -E_{P'} \int_{-\infty}^{+\infty} dt_2 E_P(t + \Delta\tau_{Pr} - t_2) \\ \times E_S^*(t + \Delta\tau_{Pr} - t_2) exp[i(\omega_P - \omega_S)t_2]\alpha_P(t_2), \end{aligned} \tag{3.31}$$

where $\alpha_P(t_2)$ describes the samples linear polarizability in the time domain for the case of parallel linear polarizations of all fields involved:

$$\alpha_P(t_2) = A_{NR}\delta(t_2) + \sum_r A_r^{aniso} exp(-i\Omega_r t_2) \times \left[\left(\rho_r^{-1} - \frac{4}{3}\right) exp\left(\frac{-t_2}{T_{2,r}}\right) + \frac{4}{3} exp(-t_2(T_{2,r}^{-1} + T_{or,r}^{-1}))\right]. \tag{3.32}$$

Here, A_{NR} is the amplitude of the the non-resonant sample response described by the delta function. A_r^{aniso} is the amplitude, ρ_r is the depolarization ratio, $T_{2,r}$ is the dephasing time, Ω_r is the center frequency, and $T_{or,r}$ is the rotational correlation time of the vibrational resonance r. When investigating the decay of a single spectrally isolated vibrational resonance, the time resolved CARS intensity profile for times larger than the instrument system response can be modeled with a single exponential decay function:

$$I_{CARS}(\nu_{AS}, \Delta\tau_{Pr}) = y_0 + I_{CARS}(\nu_{AS}, 0)\, e^{-\Delta\tau_{Pr}/(2\,T_{2,r})} \tag{3.33}$$

Here, y_0 is the CARS signal intensity background and $I_{CARS}(\nu_{AS}, 0)$ is the CARS intensity of the vibrational resonance at zero time delay. The dephasing time $T_{2,r}$ of the coherence of a vibrational resonance r is directly connected to its spectral bandwidth $\Gamma_r = (10^2\pi c T_{2,r})^{-1}$ in units of cm^{-1} via the Fourier transform.

3.4. Sum Frequency Generation

SFG is used to characterize the spontaneous broadband FWM source and is therefore described here for the case, where SFG between the broadband signal and idler fields occurs. The corresponding energy level diagram for the SFG is depicted in figure 7.1 (b). The energy and momentum conservations result in the following relations for the SFG frequency ω_{SFG} and phase ϕ_{SFG} of

$$\omega_{SFG} = \omega_{Signal} + \omega_{Idler}, \tag{3.34}$$

and

$$\phi_{SFG} = \phi_{Signal} + \phi_{Idler}, \tag{3.35}$$

respectively.

In the SFG of broadband signal and idler fields generated by spontaneous FWM, a coherent and an incoherent SFG process occur. The coherent SFG generation occurs when the sum frequency of the interacting signal and idler photons matches twice the frequency of the initial seed photons used in the spontaneous FWM process, such that $\omega_{SFG} = \omega_{Signal} + \omega_{Idler} = 2\omega_{Seed}$, and when also the sum phase fulfills $\phi_{SFG} = \phi_{Signal} + \phi_{Idler} = 2\phi_{Seed}$. In this way, a coherent SFG peak at $2\omega_{Seed}$ with a narrow bandwidth, similar to that of the seed pulse is generated. The incoherent SFG generation takes place if this strict conditions are not fulfilled. Here, an arbitrary photon of the broadband signal field interacts with an arbitrary photon of the broadband idler field, whose phases are uncorrelated. In this way, a broadband SFG field is generated with a bandwidth similar to that of the broadband signal and idler fields.
The SFG intensity spectrum $I_{SFG}(\omega_{SFG})$ for broadband phase-correlated photon pairs is described here [3]:

$$I_{SFG}(\omega_{SFG}) \propto |P^{(2)}(\omega_{SFG})|^2 \tag{3.36}$$

with the second-order nonlinear polarization $P^{(2)}(2\omega_{SFG})$, given by

$$\begin{aligned} P^{(2)}(\omega_{SFG}) = \int d\omega_{Signal} \int d\omega_{Idler} E_{Signal}(\omega_{Signal}) E_{Idler}(\omega_{Idler}) \\ \times F_{\Delta k}(\omega_{Signal}, \omega_{Idler}) \chi^{(2)}(-\omega_{SFG}; \omega_{Signal}, \omega_{Idler}) \delta(\omega_{Idler} + \omega_{Signal} - \omega_{SFG}). \end{aligned} \tag{3.37}$$

This expression represents an extension [24] from a theoretical model reported in [25]. Here, $F_{\Delta k}(\omega_{Signal}, \omega_{Idler})$ is the phase matching function, and $\chi^{(2)}(-\omega_{SFG}; \omega_{Signal}, \omega_{Idler})$ is the second order non-linear susceptibility of the sample.
The ratio between the coherent and incoherent SFG peak depends on the coherence of the broadband signal and idler fields at the sample position. To maximize this ratio, the phase relation between the two fields (see equation (3.7)) needs to be preserved. Therefore, the phase difference accumulated on their beam paths to the sample needs to be compensated. The intensity of the coherent SFG peak is inversely proportional to the spectral bandwidth of the spontaneous FWM side lobes [25, 26].

3.4.1. Second Harmonic Generation

Second harmonic generation is a degenerate case of SFG, where both incident fields are identical ($\omega_{Signal} = \omega_{Idler}$). Or in other words, SHG is the doubling of the

incident pump laser frequency ω_P on a non-linear $\chi^{(2)}$-active medium, as for example a BBO crystal. The SHG signal intensity is then given by [3]:

$$I_{SHG}(2\omega_P) \propto |P^{(2)}(2\omega_P)|^2 \tag{3.38}$$

with the second-order nonlinear polarization for narrowband pump fields $E_P(\omega_P)$ given by:

$$P^{(2)}(2\omega_P) = \chi^{(2)}(2\omega_P)E_P^2(\omega_P). \tag{3.39}$$

3.5. Two-Photon Induced Fluorescence

Two-photon induced fluorescence (2PF) is the instantaneous absorption of two photons, resulting in the population of an electronic state of a fluorescent molecule and in the subsequent spontaneous fluorescence emission of a photon [23]. The two-photon induced time averaged photon flux of the fluorescence I_{2PF} upon excitation with a train of pulses with length T_0, and repetition rate f_{rep} is given by [27]:

$$I_{2PF} \propto \delta_{2PF} \frac{P_P^2}{T_0 f_{rep}}, \tag{3.40}$$

where δ_{2PF} is the two photon absorption cross section of the fluorescent molecule at the two photon excitation wavelength, and P_P is the time averaged excitation power.

3.6. UV-VIS Absorption Spectroscopy

The absorbance of a material is defined by the Beer-Lambert law [28, p.20]

$$A_{UVVIS}(\lambda) = \log \frac{I_0(\lambda)}{I_1(\lambda)} = \epsilon_0(\lambda) \cdot c_{con} \cdot d, \tag{3.41}$$

where I_0 is the incident intensity, I_1 is the transmitted intensity, $\epsilon_0(\lambda)$ is the extinction coefficient at the wavelength λ, d is the thickness, and c_{con} is the molar concentration of the molecular sample.

4 Experimental Methods

In this chapter the experimental details of the used measurement setups, the preparation and characterization of investigated samples and the applied data analysis are described. First, the setup for supercontinuum generation and characterization is described in section 4.1. This is followed by the description of the home-built hyperspectral CARS imaging setup in section 4.2 most extensively used throughout this thesis, and which served as the starting point for all other advanced instrumentation developed for the epi-CARS experiments, the interferometric hyperspectral CARS imaging with a broadband spontaneous FWM source in section 4.3, and 2D-CARS experiments in section 4.4. Conventional spontaneous Raman and UVVIS absorption experiments are described in sections 4.5 and 4.6, respectively.
Subsequently, the preparations and characterizations of all samples are described in section 4.7. In the last section 4.8 of this chapter, the different steps for the used analysis of the recorded CARS, SHG and 2PF data are explained.

4.1. Generation and Characterization of ps-Supercontinuum Pulses

In this thesis different goals for supercontinuum (SC) generation are presented. For hyperspectral CARS imaging, a very broad SC is required as the Stokes pulse, whose SC generation is described and characterized in chapter 5. For the interferometric hyperspectral CARS imaging experiments, a correlation between the Stokes and signal continuum fields is a prerequisite, which are both generated in a broadband spontaneous FWM source, described and characterized in section 7.2.
The setup for the generation and characterization of all SC pulses is sketched in figure 4.1. In brief, the emission from a mode-locked Ti:sapphire laser oscillator (Mira 900-P, Coherent Inc.) providing a pulse train of 2.94-ps sech^2 pulses at a repetition rate of 76 MHz and a wavelength chosen between 796 and 808 nm (according to the respective application) passes through a Faraday isolator FI (12105, EOT Inc.), a 90/10 beam splitter $BS1$ (BS1-800-10-1012-45P, CVI Melles Griot, further

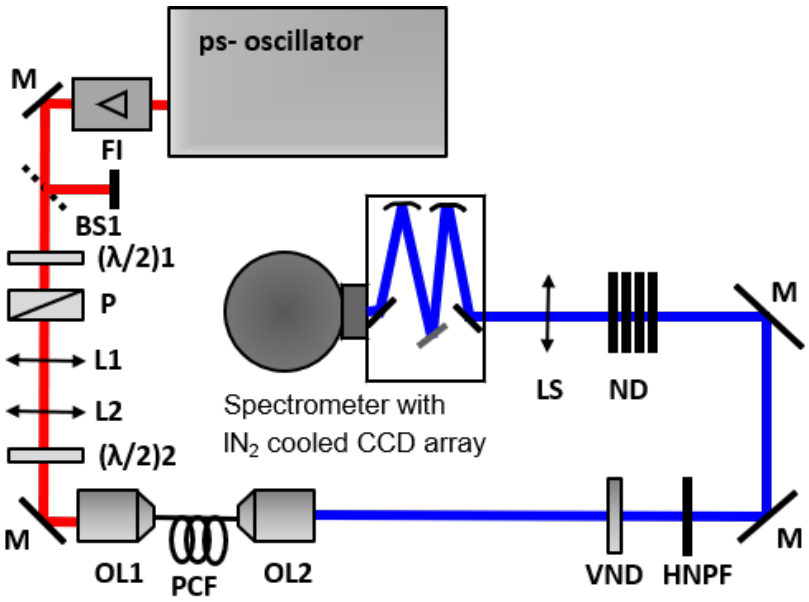

Figure 4.1.: Schematic representation of the setup for SCG and characterization. FI: Faraday isolator, M: steering mirrors, BS1: beam splitter, $(\lambda/2)1$ and $(\lambda/2)2$: lambda-half wave plate, P: polarizer, $L1$ - $L4$ and LS: lenses, $OL1$ and $OL2$: objective lenses, VND: variable neutral density filter, $HNPF$: holographic notch filter, ND: neutral density filters.

described in section 4.2), followed by a combination of $\frac{\lambda}{2}$-plate $(\lambda/2)1$ (WPA1312, CASIX), and a Glan-Taylor polarizing beam splitter P (GL10-B, Thorlabs), used for variable power adjustment. The beam is controlled in diameter and collimation by a telescope consisting of lenses L_1 and L_2 (both 75 mm, both LBF254-075-B, Thorlabs Inc.), an additional $\frac{\lambda}{2}$-plate $(\lambda/2)2$ ($\lambda/2$ 808nm, Foctek Photonics Inc.) is used for adjusting the seed laser polarization, before the 40× objective lens $OL1$ (M-40x, Newport) is used to optimally couple the beam into a nonlinear photonic crystal fiber (PCF: FemtoWHITE800 or NLPM800, both NKT Photonics A/S).

A schematics of the PCF structure is shown in figure 4.2 (a). The FemtoWHITE800 is a 12 cm long end sealed nonlinear PCF with a core diameter of 1.8 μm, a mode field diameter of (1.6 ± 0.3) μm, numerical aperture (NA) of 0.38 at 780 nm, a nonlinear coefficient of $\gamma \approx 95 \frac{1}{W \cdot km}$, and zero dispersion wavelengths (ZDW) at ≈ 750 and ≈ 1260 nm, which comes in an aluminum housing [29].

For fulfilling the phase matching conditions for spontaneous FWM and thus for the efficient generation of broadband spontaneous FWM side lobes in the PCF, the dispersion curve of the PCF should be very flat, lying around zero, and the seed wavelength should be chosen in the anomalous regime of the dispersion curve, very close to the ZDW. The PCF NLPM800 has a core diameter of 1.8 μm, a mode field diameter of 1.6 μm, NA of 0.38 at 780 nm and a nonlinear coefficient of $\gamma \approx 97 \frac{1}{W \cdot km}$,

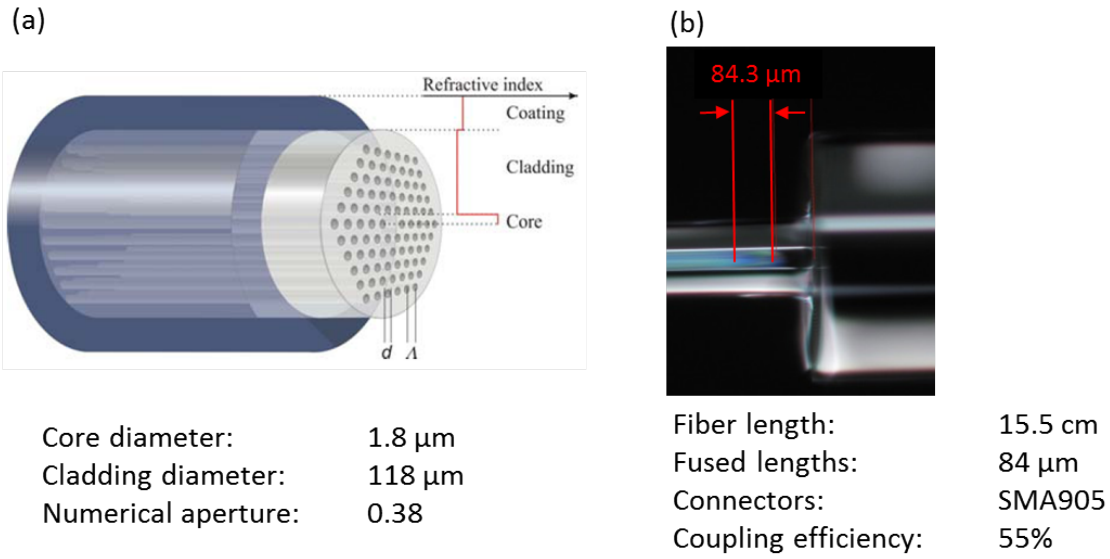

Figure 4.2.: (a) Schematics of the nonlinear PCFs [30] used for broadband SCG in hyperspectral CARS imaging and as a broadband spontaneous FWM source [30], (b) microscope image of the custom-made end piece of the PCF NLPM800 after fusing and end-sealing [31].

with ZDWs at 800 and 1085 nm [30, 32], and is provided without housing and end sealing. Here, the wavelength of the 2.37 ps Ti:sapphire ($sech^2$) seed pulses is tuned to 798 nm in order to seed this PCF close to its actual ZDW identified to be at 797.5 nm. The dispersion of the PCF has a maximum of only about 20 $ps/(km \cdot nm)$ around 940 nm and a maximum slope of 100 $(ps/(km \cdot nm))/(100\ nm)$ in the relevant range between 660 nm and 1060 nm.

In order to facilitate stable and durable operation, the PCF NLPM800 should also be end-sealed and ideally be in a protective housing. Due to the lack of the possibility to buy such fibers, we explored different ways to get the PCF that fit our needs. Initially one of the ways was to seal and connectorize the fiber by ourselves with the help and facilities of Prof. Amiel Ishaaya at Ben-Gurion University in Israel. The final design used for the experiments presented in chapter 7 has been customized in collaboration with the group of Dr. Thomas Schreiber at the Fraunhofer Institute of Applied Optics and Precision Engineering (IOF) in Jena. After end-sealing, the here used NLPM800 is 15.5 cm long, with a fused length of 84 μm, as shown in figure 4.2 (b).

After the PCF, the SC and residual laser seed beams are collimated with a 20× objective lens $OL2$ (M-20x, Newport). For achieving high in- and out-coupling efficiencies, the NA of the fiber has to be matched by that of the coupling optics. In the present experiments, where high peak intensities up to a maximum of $10^{10}\ W/cm^2$ are obtained in the focus of $OL1$, it is crucial to minimize the in-coupling losses in

order to avoid damage of the PCF. Here, overall in- and out-coupling efficiencies η between 45% (for the PCF femtoWHITE800) and 55% (for the PCF NLPM800) are achieved, as determined by the ratio between optical powers measured just before and after the in- and out-coupling objective lenses with a thermal power meter sensor (S302C, Thorlabs Inc.).
The collimated emission from the PCF is attenuated with a variable neutral density filter VND (54-082, Edmund optics) and a stack of neutral density filters ND by 6 to 9 orders of magnitude before being focused with an achromatic 50 mm lens LS (PCX FL 50, Newport Inc.) onto the entrance slit of an imaging spectrometer with 150 mm focal length (SP150, Acton Research). The SC spectra are recorded with a lN_2-cooled CCD camera (Spec10, Roper Scientific). Using a 600 g/mm grating in the spectrometer, spectra with overlapping spectral regions are recorded at spectral center wavelengths of 650, 800 and 950 nm. At each spectral center wavelength, 100 spectra with 10 ms acquisition time are recorded, followed by averaging and stitching, in order to obtain a continuous spectrum of the full SC.
For the SC characterization experiments using the NLPM800, the remaining out-coupled seed pulse is spectrally blocked with a holographic notch filter HNPF (HNPF-800, Kaiser Optics) placed in between the VND filter and the ND filters.

4.2. Hyperspectral CARS Imaging Setup

All nonlinear optical experiments were carried out using a home-built multiplex-CARS microspectrometer, sketched in figure 4.3, consisting of a single ps-laser source, a SC generation unit, an inverted microscope (IX71, Olympus), and an imaging spectrometer in the forward- and epi-detection geometry. In brief, the emission from a mode-locked Ti:sapphire laser oscillator (Mira 900-P, Coherent Inc.) providing a pulse train of 2.94-ps sech^2-pulses at a repetition rate of 76 MHz and at a wavelength of 808 nm passes through a Faraday isolator FI (12105, EOT Inc.) and is then first split into two parts at beam splitter $BS1$ in a ratio 10/90 (BS1-800-10-1012-45P, CVI Melles Griot) or 30/70 (0164-845-01C, Coherent Inc.). The smaller fraction of the beam serves as the pump pulses for CARS, SHG and 2PF excitation, while the bigger fraction is seeding a photonic crystal fiber (PCF: femtoWHITE800, NKT Photonics A/S) generating a picosecond supercontinuum, the long-wavelength part of which is used as Stokes-pulses for CARS, after passing a sequence of a $\frac{\lambda}{2}$-plate (WPA1312, CASIX), a Glan-Taylor polarizing beam splitter P (GL10-B, Thorlabs), and a telescope, consisting of lenses $L1$ and $L2$ (both LBF254-075-B, Thorlabs Inc.). The $\frac{\lambda}{2}$-plate in combination with the polarizing beam splitter is used as an variable power adjustment, controlling the seed power before focused

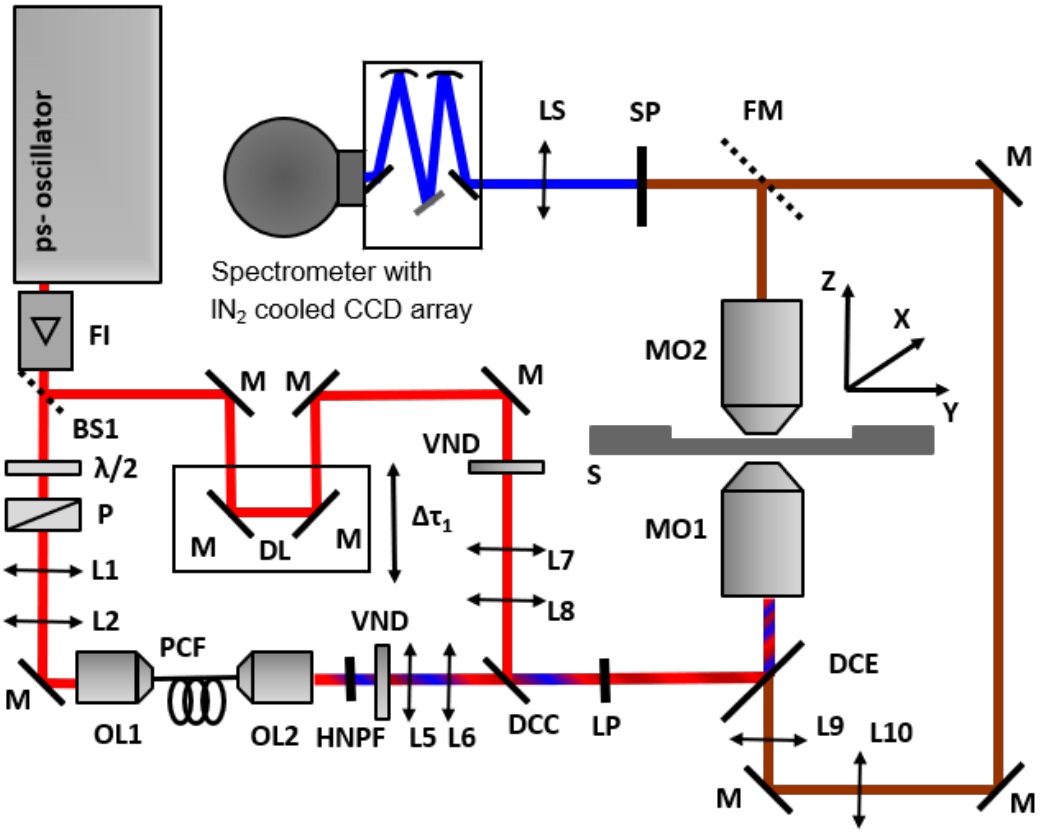

Figure 4.3.: Schematic representation of the home-built multiplex-CARS microspectrometer setup. FI: Faraday isolator, $BS1$: beam splitter, $\lambda/2$: half wave plate, P: polarizing beam splitter, $L1$-$L10$ and LS: lenses, M: steering mirrors, $OL1$ and $OL2$: objective lenses, VND: variable neutral density filter, $HNPF$: holographic notch filter, DCC and DCE: dichroic mirrors, DL: delay line, LP: long-pass filter, $MO1$ and $MO2$: microscope objective lenses, S: sample scanning stage including sample holder, SP: short-pass filters, FM: flip mirror. The multicolored line represents the spatially and temporally overlapped pump, Stokes and signal beams.

onto the PCF end facet with an objective lens $OL1$ (M-40x, Newport). The exiting light from the PCF is collimated with a second objective lens $OL2$ (M-20x, Newport), and the residual seed pulses are spectrally blocked with a holographic notch filter $HNPF$ (HNPF-800, Kaiser Optics). After each beam passing a variable neutral density filter VND (54-082, Edmund optics), the Stokes and pump beams are separately controlled in size and collimation by the telescopes consisting of lenses $L5$ (75 mm) and $L6$ (300 mm) lens, and $L7$ (75 mm) and $L8$ (250 mm) lens, respectively. Next, both collimated beams are recombined and made collinear, on a dichroic mirror DCC (zq 800 rdc, Chroma Technology). The temporal overlap of the pulses from both beams is controlled by the time delay $\Delta\tau_1$ of the pump pulses with a retro-reflector (PS975-B, Thorlabs) on a motorized translation-stage DL (M-410.DG, Physik Instrumente). Before the microscope, the low wavelength part of the beams is spectrally blocked with a long pass filter LP (FEL800, Thorlabs). Inside the microscope the beams are directed upwards with a dichroic mirror DCE (795DCSPXR, Chroma) before collinearly focused into the sample using a 1.2 NA water immersion microscope objective $MO1$ (UPLSAPO IR 60XW, Olympus). While in the SHG and 2PF experiments only the pump beam is used for sample excitation and the Stokes beam is blocked, both the spatial and temporal overlap of pump and Stokes pulses in the focus are satisfied in the CARS experiments. All pulses have the same linear polarization. If not stated otherwise, the averaged pump and Stokes powers in the focus for the CARS experiments amount to 60 mW and 13 mW, respectively. The generated CARS, SHG and 2PF emissions are either par-focally collected in the forward-direction with an identical microscope objective $MO2$ or in the epi-direction with the same microscope objective $MO1$ as used for the excitation.

In the E-CARS detection path, the CARS emission passes through the dichroic mirror DCE in transmission, is focused with the inbuilt tube lens $L9$ (150 mm) of the $IX71$ Olympus microscope and is consecutively collimated with a parfocal lens $L10$ (Achr100F, Coherent Inc.) before the beam is directed towards the spectrometer, which is also used for the F-CARS detection. For the consecutive recording of forward- and epi-CARS data, a flip mirror FM (FM90, Thorlabs Inc.) is used to switch between the two detection paths. In this way, the experimental conditions for the CARS signal generation and detection are kept as similar as possible for both detection configurations.

The CARS signal is spectrally isolated from the excitation pulses with two short-pass filters SP (RU785SP, Semrock and FES800, Thorlabs Inc.). For SHG and 2PF experiments, the separation from the excitation pulses is done with one short-pass filter SP (RU785SP, Semrock). Spectrally resolved detection is performed by focus-

ing the emission with a 50 mm achromatic lens LS (PCX FL 50, Newport Inc.) on the entrance slit of an imaging spectrometer, consisting of a 150-mm monochromator (SP150, Acton Research) equipped with a 600 g/mm grating and a liquid-N_2 cooled CCD-array detector (Spec10, Roper Scientific) with 1340 lateral pixels. The resulting spectral pixel resolution amounts to typically 4 cm^{-1}.
Nonlinear imaging is performed by scanning the sample with a piezo-electric translation stage S (P517.3CL, Physik Instrumente) with a maximum travel range of $(100 \times 100 \times 20)$ μm in x-, y-, and z-directions, respectively. The experiment control of scanning and synchronized hyperspectral imaging data acquisition is performed by a software written in-house by Alexander Kovalev.
For all experiments performed in the E-CARS detection, as presented in chapter 9, the measurements conditions were as follows: The average laser power at the sample position were set to 36 mW for the pump and 18 mW for the Stokes beam. For the long range scan, described in section 9.4, the sample is scanned in x-direction taking spectra in forward- and epi-direction with a 10 ms and 1000 ms pixel integration times, respectively, and a 150-nm step size along the x-axis. In epi CARS detection an additional scan is acquired with longer pixel integration times of 20 s but with a shorter scan range and a step size of 85 nm.

4.3. Setup for Interferometric Hyperspectral CARS Imaging with Broadband Correlated Photon Pairs

For the realization of interferometric hyperspectral CARS imaging an additional local oscillator field needs to be introduced into the setup, which interferes with the CARS field from the sample on the detector. It is therefore necessary to extend the setup according to the requirements for the generation and the control of an additional third phase coherent field as well as for the interferometric stability of the setup. Consequently three major changes are performed to the setup shown in figure 4.3: first, full spatial and temporal control over the short-wavelength part of the SC pulses generated in the PCF by spontaneous FWM, which from hereon are called the signal pulses, is established. Second, the dispersion of both the broadband spontaneous FWM signal and idler pulses introduced by optical components in the system is compensated. And third, the interferometric stability is realized by a mostly common path for all beams. The setup for the interferometric hyperspectral CARS imaging, depicted in figure 4.4, then consists of five main parts: the single picosecond seed laser oscillator, second, the broadband spontaneous FWM source,

a beam control section including two interferometers and the dispersion control segment, the microscope, and the detection system.

The emission from a mode-locked Ti:sapphire laser oscillator (Mira 900-P, Coherent Inc.) providing a pulse train of 2.94-ps sech^2-pulses at a repetition rate of 76 MHz and a wavelength of 800 nm passes through a Faraday isolator FI (12105, EOT Inc.) and is split into the seed pulse and the pump pulse just before the PCF (NLPM800, NKT Photonics A/S) with a 30/70-beam splitter $BS1$ (0164-845-01C, Coherent Inc.). The larger fraction is used to seed the spontaneous FWM generation in the custom-made end-sealed and connectorized PCF NLPM800, the optical layout of which is described in section 4.1. The smaller fraction acts as the pump pulses for CARS signal generation in the sample, which are directed into a delay line $DL1$ (M-410.DG, Physik Instrumente) to control the time delay $\Delta\tau_1$ between the pump and SC pulses.

The spontaneous FWM signal and idler continuum pulses coming out of the PCF are collimated with an off-axis parabolic mirror $OAPM$ (MPD00M9-P01, Thorlabs Inc.), which minimizes dispersion and avoids chromatic aberrations in comparison to a lens based objective. The collimated beams are then recombined on a holographic notch filter for 800 nm $HNPF$ (800 HNPF, Kaiser Optics) under a small angle.

Subsequently, all collinear beams are then directed to the dispersion compensation part of the setup. In order to preserve the phase of all generated frequency components in the broadband spontaneous FWM pulses at the focus position in the sample, the normal dispersion accumulated throughout the optical path of the setup, up to the sample needs to be pre-compensated. In order to keep this dispersion low enough, only low-GDD steering mirrors (OA095 and OA093, Femtolasers) are used throughout the beam path before the microscope. In our setup, the dispersion compensation is achieved with purely passive components [33, 34], consisting of two pairs of negative dispersion mirrors $DCMP$ (GSM209, Femtolasers). Here, a fixed amount of negative GDD of $(-45 \pm 10)\ fs^2$ onto the pulse at each bounce on the mirror is imprinted. Because of the stepwise adjustment of the dispersion by choosing an appropriate number of bounces, a pair of thin glass wedges DGL (OA924, Femtolasers) is introduced into the beam path just before the negative dispersion mirrors. The glass wedges allow for a continuous fine adjustment of the GDD by adding or reducing the amount of glass in a continuous way without beam displacement. The total amount of bounces for the experiments presented in this thesis was 60, unless stated otherwise, according to a dispersion compensation of $GDD = (-2700 \pm 600)\ fs^2$.

Subsequently the beam is expanded with an all refractive beam telescope consisting of two parabolic low-GDD mirrors $PM1$ and $PM2$ (OA056 and OA823, Femtolasers)

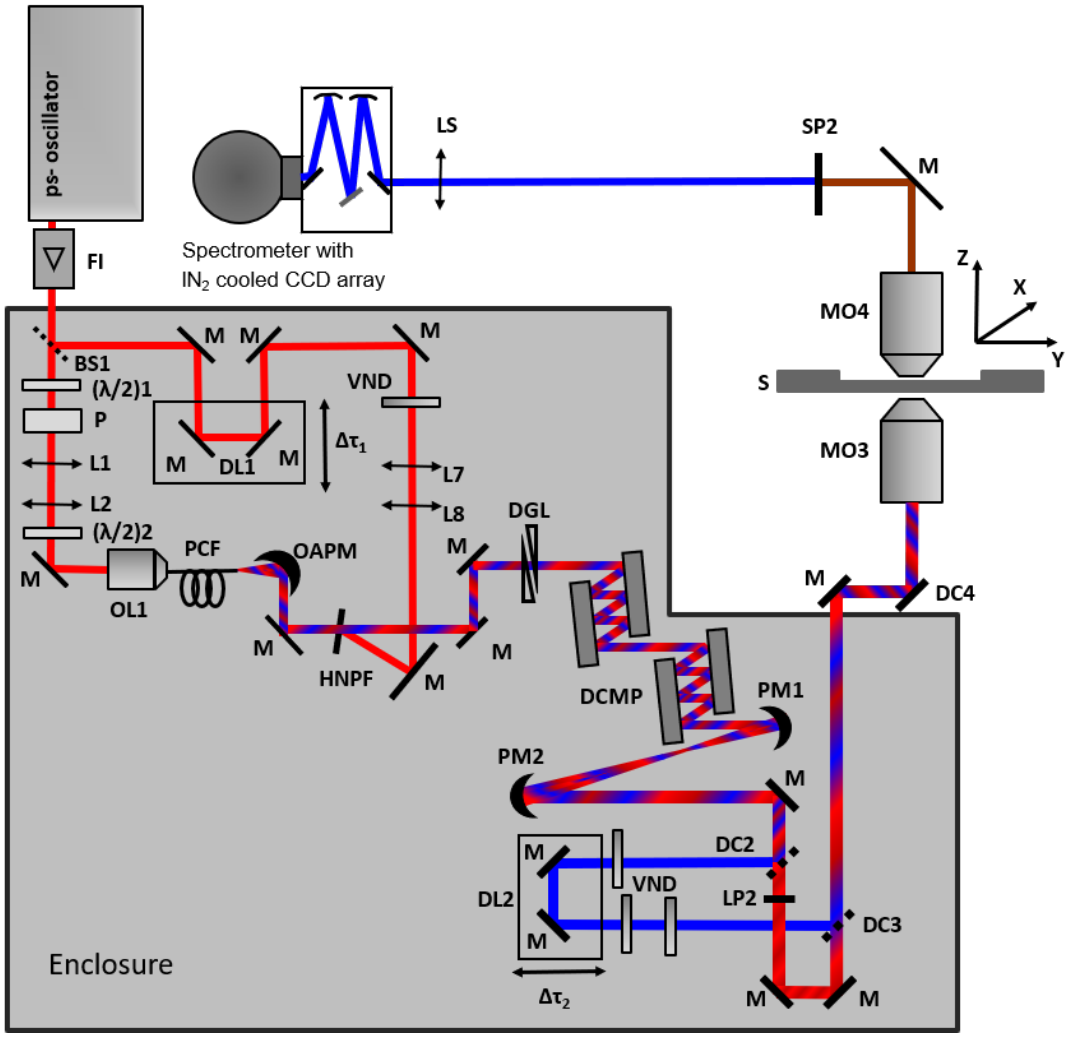

Figure 4.4.: Schematic representation of the home-built setup for interferometric hyperspectral CARS imaging with broadband correlated photon pairs. FI: Faraday isolator, $BS1$: beam splitter, $(\lambda/2)1$ and $(\lambda/2)2$: half wave plates, P: polarizing beam splitter, $L1$-$L8$ and LS: lenses, M: steering mirrors, $OL1$: objective lens, $OAMP$: off-axis parabolic mirror, $HNPF$: holographic notch filter, $DL1$ and $DL2$: delay lines, VND: variable neutral density filters, DGL: dispersive glass wedges, $DCMP$: dispersion compensation mirror pairs, $PM1$ and $PM2$: parabolic mirrors, $DC2$ and $DC3$: dichroic mirror, $SP1$ and $SP2$: short-pass filters, $MO3$ and $MO4$: microscope objective lenses, S: sample scanning stage including sample holder. The multi-colored line represents the spatially and temporally overlapped pump, Stokes and signal beams.

with focal lengths of 150 mm and 300 mm, respectively, resulting in a collimated beam diameter that matches the back-aperture of the objective lens.

To control the phase of the signal field relative to the idler and pump fields, the collinear beams are split into two parts with a dichroic beam splitter $DC2$ (770DCXXR, Chroma). The signal beam passes through three variable neutral density filters VND (100FS04DV.4, Newport Inc.), enabling the reduction of the signal beam intensity to the CARS intensity generated by the pump and the idler fields in the sample. Next, the signal pulses are delayed by $\Delta\tau_2$ relative to the pair of pump and idler pulses by using a second delay line $DL2$, consisting of two low-GDD mirrors on a manual translation stage equipped with a micrometer screw and additional with a Piezo-electric actuator (PC4FL, Thorlabs) with a travel range of 4.6 μm, controlled by a 50 V laboratory voltage DC source. The signal beam is then recombined with the pump and idler beams, which have passed through a long pass filter $LP2$ (RU785LP, Semrock) removing residual components of the signal field, at a dichroic mirror $DC3$ (795DCSPXR, Chroma). The polarizations of the fields are linear and oriented parallel to the x-axis.

Inside the microscope the beams are directed upwards with a custom-made dichroic mirror $DC4$ (OA073, Femtolasers) and collinearly focused into the sample using a 0.95 NA water immersion objective $MO3$ (W N-Achroplan 40X, Zeiss), used without immersion water. If not stated otherwise, the average pump and Stokes powers in the focus amounts to 60 mW and 13 mW, respectively. CARS imaging is performed by scanning the sample with a Piezo-electric translation stage S (P517.3CL, Physik Instrumente) with maximum travel ranges of $(100 \times 100 \times 20)$ μm in x-, y-, and z-directions, respectively. The CARS emission generated in the sample and the signal pulses transmitted through the sample are par-focally collected in the forward-direction with a 0.9 NA water immersion objective $MO4$ (LUMPLFLN 60×W, Olympus) and spectrally isolated from the pump and idler pulses with two short-pass filters $SP2$ (RU785SP, Semrock and FES800, Thorlabs Inc.). Spectrally resolved detection is performed by focusing the emission with a 50 mm achromatic lens LS (PCX FL 50, Newport Inc.) on the entrance slit of an imaging spectrometer, consisting of a 150-mm monochromator (SP150, Acton Research) equipped with a liquid-N_2 cooled CCD-array detector (Spec10, Roper Scientific). The contribution of the local oscillator field to the intensity of the CARS emission generated in the sample is adjusted by the VND filters previously described.

In order to provide interferometric stability, especially in the non-common optical pathways, only very rigid mechanical components are used throughout the setup. Additionally, air fluctuations, which are the main source of phase fluctuations in our setup, are minimized by building an enclosure around most of the beam paths

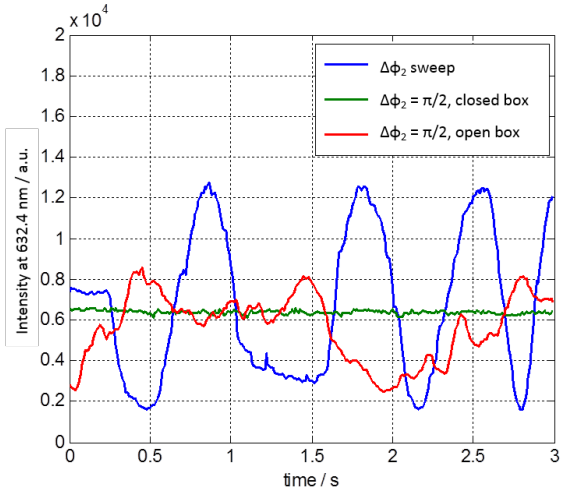

Figure 4.5.: Recorded interferometric signal stability of the second interferometer defined by $DC2$ and $DC3$, see figure 4.4 using a 633-nm reference laser, while performing a continuous sweep of $\Delta\phi_2$ (blue curve), at a fixed $\Delta\phi_2 = \frac{\pi}{2}$ with the box open (red curve), and at a fixed $\Delta\phi_2 = \frac{\pi}{2}$ with a closed box (green curve).

between the laser source and the microscope. The results of the interferometric stability tests obtained by monitoring the detected interference signal of a 633 nm reference laser, sent through both arms of the second interferometer defined by $DC2$ and $DC3$ beam splitter, shown in figure 4.4, as a function of time delay $\Delta\tau_2$ ($\Delta\phi = \frac{2\pi c}{\lambda}\Delta\tau_2$) are shown in figure 4.5. The blue curve presents the interference signal while sweeping the phase difference $\Delta\phi_2$. The visibility of the interference amounts to approximately 80 %. Fixing the phase difference to $\frac{\pi}{2}$, where the interferometric sensitivity is highest, the interference signal fluctuates by more than 50 % (red curve) when the box is open, which is equivalent to phase fluctuations of more than $\frac{\pi}{2}$. In contrast, when the same experiment is performed with the box closed, the interference signal is stable within 5 % (green curve). In conclusion, it can be stated that a sufficient passive interferometric stability over tens of seconds is achieved by simply enclosing the setup. An active stabilization is therefore not necessary for the experiments shown in the following chapters.

4.4. 2D CARS Microspectroscopy Setup

The setup for the time resolved broadband multiplex CARS measurements is shown in figure 4.6, where according to scheme B depicted in figure 3.5 (b), an ultra-broadband few-cycle laser pulse is providing the pump and Stokes fields, and a narrowband ps pulse is providing the probe field for the CARS process.

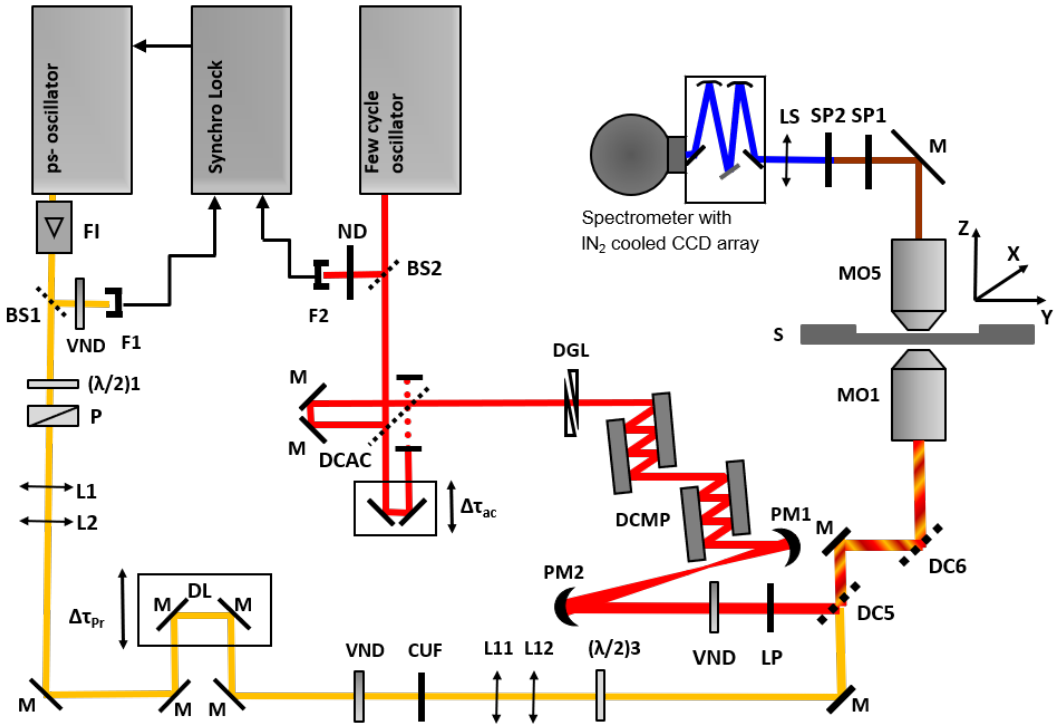

Figure 4.6.: Schematic representation of the home-built setup for 2D CARS microspectroscopy with a ps- and a few-cycle fs-pulse. FI: Faraday isolator, $BS1$ and $BS2$: beam splitters, $F1$ and $F2$: optical fibers, $(\lambda/2)1$ and $(\lambda/2)3$: half wave plates, P: polarizing beam splitter, $L1$-$L12$ and LS: lenses, M: steering mirrors, DL: delay line, VND: variable neutral density filter, CUF: laser clean up filter, $DCAC$: dichroic mirror in auto-correlator, DGL: dispersive glass wedges, $DCMP$: dispersion compensation mirror pairs, $PM1$ and $PM2$: parabolic mirrors, LP: long pass filter, $DC5$ and $DC6$: dichroic mirrors, $MO1$ and $MO5$: microscope objective lenses, S: sample scanning stage including sample holder, $SP1$ and $SP2$: short pass filters. The multi-colored line represents the spatially and temporally overlapped pump, Stokes and probe beams.

The two different pulse trains are generated in two different laser oscillators having nominally the same repetition rate of 76 MHz. In order to synchronize the exact repetition rates, an active synchronization of the cavity length of both oscillators is necessary. This is realized by tuning the cavity length of one oscillator in combination with an electronic synchronization device 'Synchro Lock 900' (Coherent Inc.), which detects the repetition rates of both laser oscillators precisely and then feedback controls the cavity length . Here, the signal from the few-cycle laser oscillator provides the master repetition rate, to which the repetition rate of the ps-laser oscillator is slaved.

In brief, the emission from the picosecond mode-locked Ti:sapphire laser oscillator (Mira 900-P, Coherent Inc.) providing a train of 2.94-ps sech^2 pulses at a repetition rate of 76 MHz and a wavelength of 800 nm passes through a Faraday isolator FI (12105, EOT Inc.) and a 90/10 beam splitter (BS1-800-10-1012-45P, CVI Melles Griot). The smaller fraction of the beam is directed through a VND filter and coupled into an optical fiber $F1$, which is connected to the Synchro Lock. The main fraction of the beam passes through a sequence of a $\frac{\lambda}{2}$-plate $(\lambda/2)1$ (WPA1312, CASIX), a Glan-Taylor polarizing beam splitter P (GL10-B, Thorlabs), a telescope consistent of lenses L1 and L2 (LBF254-075-B and LBF254-200-B, Thorlabs Inc.), a delay line DL (M-410.DG, Physik Instrumente) defining the probe pulse time delay $\Delta\tau_{Pr}$, a variable neutral density filter VND (100FS04DV.4, Newport Inc.), a laser clean up filter CUF (F94-808, Semrock), a second telescope consisting of lenses $L11$ and $L12$ (PCX FL 100, Coherent and AC254-100-B, Thorlabs) for collimating this beam and adjusting its beam size to match the back-aperture of the microscope objective $MO1$, and a $\frac{\lambda}{2}$-plate $(\lambda/2)3$ (WPA1312, CASIX) before combining with the few-cycle pulse train.

The emission from the second mode-locked Ti:sapphire laser oscillator (Rainbow HP, Femtolasers) providing a train of sub 7-fs sech^2 pulses at a repetition rate of 76 MHz and a center wavelength of 808 nm passes through a 5/95 beam splitter $BS2$ (OA041, Femtolasers), where the bigger fraction is directed through a neutral density filter ND and is coupled into an optical fiber $F2$, which is connected to the Synchro Lock module. The smaller fraction passes through a home-built interferometric auto-correlator (IAC) described in detail in reference [34], followed by a pair of dispersive glass wedges DGL (OA124, Femtolasers), two pairs of dispersion compensating mirrors $DCMP$ (GSM209, Femtolasers), which allow passive pre-compensation of material dispersion in the optical pathway up to the sample as described in section 4.3 in detail. Thereafter, the beam passes an all reflective telescope, consisting of two parabolic mirrors $PM1$ and $PM2$ (OA055 f=150 mm and OA056 f=300 mm, both Femtolasers), a variable neutral density filter VND and a

long pass filter LP (FEL800, Thorlabs) before combined and made collinear with the probe beam of the ps-pulses on a dichroic mirror $DC5$ (795DCSPXR, Chroma). Inside the microscope the beams are directed upwards with a dichroic mirror $DC6$ (OA073, Femtolasers) and collinear focused into the sample, using a 1.2 NA water immersion objective $MO1$ (UPLSAPO IR 60XW, Olympus). The sample is mounted on a Piezo-electric translation stage S (P517.3CL, Physik Instrumente) with maximum travel ranges of $(100 \times 100 \times 20)$ μm in x-, y-, and z-directions, respectively. The CARS emission generated in the sample is par-focally collected in the forward-direction with a 0.9 NA water immersion objective $MO5$ (LUMPLFLN 60XW, Olympus) and subsequently spectrally isolated from the excitation pulses with two short-pass filters $SP1$ and $SP2$ (RU785SP, Semrock and FES800, Thorlabs Inc.). Spectrally resolved detection is performed by focusing the emission with a 50 mm achromatic lens LS (PCX FL 50, Newport Inc.) on the entrance slit of an imaging spectrometer, consisting of a 150-mm monochromator (SP150, Acton Research) equipped with a 600 g/mm grating and a liquid-N_2 cooled CCD-array detector (Spec10, Roper Scientific) with 1340 lateral pixels, resulting in a spectral pixel resolution of typically 4 cm^{-1}. 2D CARS microspectroscopy is performed by synchronizing hyperspectral image data acquisition with the control of time delay $\Delta\tau_{Pr}$ between the few-cycle and the ps-pulses by using a software written in-house by Alexander Kovalev.

While the fs-pulses where characterized through SHG IAC experiments using the setup shown in figure 4.6, the temporal profile of the ps-pulse was characterized through an intensity auto-correlation measurement. Here, one part of the pulse is time-delayed and the spatially recombined pulses are subsequently focused on a 1 mm BBO-crystal while recording the SFG signal filtered from the excitation pulses by three color glass filters (BG39, Thorlabs Inc.) with a photo diode detector (DET36 A/M, Thorlabs Inc.) as a function of time-delay. Except for the IAC measurements, only one arm of the interferometer was used and the other one was blocked with a beam stop (see figure 4.6).

4.5. Spontaneous Raman Microspectroscopy

Spontaneous Raman-microspectroscopy measurements were carried out with a confocal Raman microscope (alpha300RA+, WITec GmbH) equipped with a 532-nm laser and a 300-mm imaging spectrometer (UHTS300, WITec GmbH) with an EM-CCD camera (Newton 970, Andor Inc.). For all measurements, unless stated otherwise, 33 mW of the linearly along the x-direction polarized laser is focused onto the sample with a 100 $\times$, 0.9 NA objective (CF Plan, Nikon), providing a lateral spatial

resolution of $\approx 300\ nm$. A 50-μm core diameter optical fiber is used for the collection of the light which results in a spectral resolution of typically $(2.4 \pm 0.4)\ cm^{-1}$ using the 600 g/mm grating in the UHTS300. No spectral intensity correction is performed on the spontaneous Raman spectra.

4.6. UV-VIS Absorption Spectroscopy

Electronic absorption spectroscopy of the primordial broth sample solutions was performed in fused silica cuvettes of 10 mm path length, using an UV-VIS spectrometer (Perkin Elmer, Lambda 16) with a scan speed of 240 nm/min, a scan step size of 0.8 nm, a slit setting of 1 nm, and a scan range from 900 to 190 nm, if not stated otherwise.

4.7. Sample Preparations

4.7.1. Pollen Samples

Cyclamen pollen samples were extracted from living flowers obtained from the daily market of Stuttgart. Daisy blossoms were cut from the lawn behind the laboratory building. By tipping on the stamen, extracted from the blossom, the pollen were placed onto a 150-μm thick BK7 cover slip (#1, Carl-Roth), immersed in 10 μl deionized water and covered by a second cover slip separated by a 100-μm thick double sided adhesive tape (Doppelband 05538, tesa SE) as a spacer. Single pollen grains sitting on the glass surface were chosen for non-linear microspectroscopy.

4.7.2. Prebiotic Broth Samples

As detailed in reference [35], two distinct prebiotic broth samples extracted from Miller experiments with discharges into the gaseous phase and onto the liquid surface, from hereon designated as sample $A1-$ and sample $B2+$, respectively [35], were compared by optical spectroscopies. Both sample volumes of 40 ml were lyophilized immediately after extraction, each resulting in a dry weight of $(26.34 \pm 8.94)\ mg$. The lyophilized samples were re-suspended in 1 ml deionized water. Subsequently, solid particles in the suspensions were size-separated and removed by using a 0.22-μm syringe filter (P666.1, Carl Roth). Prior to nonlinear optical spectroscopy experiments, a volume of 10 μl of the resulting sample solution was placed between two cover slips (#1, Carl-Roth) separated by a 100-μm spacer (Doppelband 05538, tesa SE). Prior to UV-VIS absorption measurements, fractions of the sample-B2+ and

the sample-A1- solutions were 200-fold and 252-fold diluted with deionized water, respectively.

4.7.3. Solvent Samples

Neat benzaldehyde and toluene were prepared by placing 10 μl of the liquid between to cover slips (#1, Carl-Roth) separated by a 100-μm spacer (Doppelband 05538, tesa SE).

4.7.4. Index-Matched PMMA-Wedge Samples

An 8 μl droplet of e-beam resist (AR-P671) containing the exclusive polymer poly(methyl methacrylate) (PMMA) is drop-cast onto a cover slip (#1, Carl-Roth) spreading over typically 5 mm. After evaporation of the solvent, a thin film of solid PMMA remains on the cover-slip, with a maximum thickness of a few μm and a wedge like thickness profile at the edges. Height profiles of the PMMA wedges are measured with a profilometer as described in section 9.1.2. Prior to the spectroscopic experiments, Zinc iodide water solutions of defined concentrations, used for matching the refractive index of the PMMA droplet, is put on top of the PMMA film, which is then and covered with a second cover slip separated from the first one by a $100 - \mu m$ spacer (Doppelband 05538, tesa SE).

For preparing a 80 % ZnI_2 stock solution, 2 g of ZnI_2 (98 %, Alfa Aesar) and 2.5 mg of $Na_2S_2O_4$ are dissolved in 500 μl of deionized water. The $Na_2S_2O_4$ hereby served as an oxygen scavenger to prevent the zinc iodide solution to degrade due to oxidation. In order to find the appropriate concentration of zinc iodide to match the index of refraction of the PMMA, the stock solution is diluted with deionized water with the same concentration of $Na_2S_2O_4$ to ZnI_2 concentrations of 57 %, 60 %, **61 %**, 62 %, 63 % and 67 % by weight. In the first step, index matching is evaluated by visual inspection of the reflections at the interface between the drop-cast PMMA and the zinc iodine solution. In a second step, the degrees of reflection of a 532 nm laser beam at that interface are compared qualitatively to each other. The best index matching is achieved with the 61 % zinc iodide water solution, which corresponds to a refractive index of 1.49 [36] at 589 nm.

4.8. Data Analysis

If not stated otherwise, all data analysis was implemented in Matlab (R2010a, Mathworks) [37].

4.8.1. SC Spectra Analysis

SC spectra were corrected for dark-counts and etaloning as follows: A measured dark-count spectrum with no light incident on the CCD-detector is subtracted form the SC spectrum. Etaloning correction is achieved by fitting the slowly varying envelope at the spectral position were etaloning is observed with a smooth spline. The SC spectrum is subtracted by this smooth fit curve. Finally the initial SC spectrum is divided by that etaloning difference spectrum.

4.8.2. CARS Spectra Analysis

The CARS spectra analysis is performed according to the procedure described by Gregor Hehl [38]. At first all raw CARS spectra are dark-count corrected, and cosmic rays are removed. In addition, each CARS spectrum is corrected for broad-band, intra-Stokes CARS contributions [38] according to scheme C (compare section 3.3.2), that are independently recorded by temporally offsetting the pump and Stokes pulses. If necessary, an etaloning correction is performed. CARS spectra are recorded inside the sample and a reference sample of pure non-resonant $\chi^{(3)}$-response in the spectral region of interest, for example water or glass, under identical experimental conditions. The sample CARS spectrum $I_{CARS,sample}(\nu_{AS})$ is then normalized by the non-resonant reference CARS spectrum $I_{CARS,ref}(\nu_{AS})$ according to equation (4.1).

$$S_{CARS}(\nu_{AS}) = \frac{I_{CARS,sample}(\nu_{AS})}{I_{CARS,ref}(\nu_{AS})} \tag{4.1}$$

The normalized CARS spectrum is then automatically corrected for varying spectral sensitivity of the excitation source and the detection system [11].

Subsequently, for each normalized CARS spectrum, its corresponding vibrational phase spectrum is retrieved by applying the maximum entropy method (MEM) [39] with squeezing, including an 8th order polynomial error-phase estimation within a subset of vibrationally non-resonant spectral regions in the recovered MEM-phase spectrum and its subsequent subtraction [40]. Next, the imaginary part of the corresponding complex , third-order susceptibility spectrum, $Im(\chi^{(3)}(\nu_{AS}))$, is reconstructed according to equation (4.2), resulting in the full characterization of the samples spectral Raman response.

$$Im(\chi^{(3)}(\nu_{AS})) = \sqrt{S_{CARS}(\nu_{AS})} \cdot \sin\phi_{AS}(\nu_{AS}) \tag{4.2}$$

where $\phi_{AS}(\nu_{AS})$ is the phase of the CARS field retrieved from the normalized CARS spectrum S_{CARS} (see equation 4.1). Finally, the $Im(\chi^{(3)}(\nu_{AS}))$ spectrum is treated exactly as a linear combination of the spontaneous Raman spectra of all contributing molecular vibrations within the sample focal volume, under the assumption that the vibrational spectra of each compound do not change upon mixing. Hence, for example, the contribution of water in the sample spectra can be subtracted by the weighted contribution of a pure $Im(\chi^{(3)}(\nu_{AS}))$ spectrum of water at its dominant $O\text{-}H$ vibrational mode at 3426 cm^{-1}. All the above mentioned analysis steps have been performed by adapting a Matlab script initially written by Gregor Hehl [38]. The $Im(\chi^{(3)}(x, y, z, \nu_{AS}))$ spectra for each (x, y, z) sample position, form then a 4D hyperspectral data cube, which is further evaluated with conventional univariate and multivariate data analysis tools [41].

4.8.3. E-CARS Spectra Analysis

While all forward-detected CARS spectra are analyzed as previously described in section 4.8.2, the epi-detected CARS spectra cannot be analyzed in the same manner. The intrinsic weak E-CARS signal in the NR spectral region only allows to record a NR-reference CARS spectrum with a very low signal-to-noise ratio (SNR). Consequently, normalization of any sample E-CARS spectrum $I_{CARS,Sample}$ with such a reference E-CARS spectrum $I_{CARS,ref}$, according to equation (4.1), leads to a problem in the subsequent MEM-phase retrieval procedure [38]. Therefore a different approach for the analysis of epi-detected CARS spectra is introduced. Because of the negligible NR-signal level in E-CARS spectra coherent mixing of resonant and non-resonant $\chi^{(3)}$ contributions are much less pronounced [38]. Instead of normalizing E-CARS spectra, the CARS spectrum is now background corrected by subtracting a spectrum, recorded for all beams incident on the same sample position but with no time overlap between the pump and the Stokes-pulses. This way, all effects caused by the individual pulses are present, but no E-CARS signal is generated.

In figure 4.7, the epi-detected CARS spectrum of the PMMA wedge sample is shown along with background and no-time-overlap- (nto)-spectra. The strong signal in the low wavenumber region originates mostly from the tail of the epi-scattered pump laser spectrum. This contribution can be almost completely removed from the PMMA E-CARS spectrum by a simple subtraction of the independently measured nto spectrum. As shown for this specific example in figure 9.4, the result mimics the spontaneous Raman spectrum. The observed peaks around 600 cm^{-1}, 800 cm^{-1}, and 1000 cm^{-1} in the epi-detected nto spectrum focused into PMMA

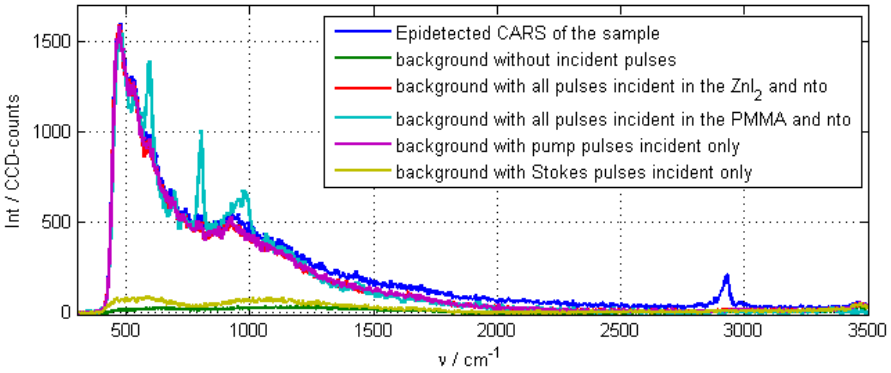

Figure 4.7.: Correction procedure for recorded sample E-CARS spectra. Dark-count corrected E-CARS spectrum of PMMA (blue curve), the epi-detected background spectrum when both beams are blocked before the microscope (green curve), with all pulses incident on the ZnI_2 but having no time overlap (nto) (red curve), with all pulses incident on the $PMMA$ but having no time overlap (nto) (cyan curve), the pump pulses incident only (magenta curve), and the Stokes pulses incident only (yellow curve).

originate from the spontaneous anti-Stokes Raman scattering of the PMMA. This spontaneous Raman contributions are removed by subtracting a linear combination of the nto-spectrum recorded in the ZnI_2 and the one recorded in the PMMA with a scaling factor proportional to the wedge height profile.

4.8.4. Interferometric CARS Spectra Analysis

All recorded spectra are first dark-count corrected by subtracting the average signal in the spectral regions, where the detection filters block any incident light on the CCD-detector. Each interferometric CARS spectrum $I_{CARS,sample}(\nu_{AS}, \Delta\phi)$ is scaled individually to an average pure signal spectrum proportional to $|E_{Signal}(\nu_{AS})|^2$ that is independently measured under identical experimental conditions in a NR region of the sample. With the experimental scaling factor k_{SR} known the real and imaginary parts of the samples $\chi^{(3)}$ response are then extracted according to equation 3.29.

4.8.5. 2D CARS Spectra Analysis

In the 2D-CARS measurements, F-CARS spectra of the sample are recorded as a function of time delay $\Delta\tau_{Pr}$ between the pair of temporally overlapped pump and Stokes pulses and the probe pulse. All recorded spectra were first dark-count corrected by subtracting the signal averaged over the first 20 pixels of the spectrum, where no light is incident on the CCD-camera. In contrast to the previous sections, no reference CARS spectrum is recorded since no phase retrieval is performed here.

Time profiles of the CARS signal were extracted from the 2D-CARS spectral data set at different vibrational frequencies and fitted to a mono-exponential RFID model function according to equation (3.33) within the time delay range starting from $\Delta\tau_{Pr} = 2.4\ ps$ up to $\Delta\tau_{Pr} = 8\ ps$, or until the noise becomes dominant for those resonances with shorter dephasing times or lower intensities.

4.8.6. Spontaneous Raman Spectra Analysis

Recorded spontaneous Raman spectra where background corrected by first subtracting a glass substrate spectrum, recorded under identical conditions at a different lateral position of the sample, where no sample of interest was present. Secondly a refined background subtraction is applied, using the average background subtraction algorithm from WITec Project 2.1 [42], with average filter size 4, selecting regions without Raman bands and interpolating in between those regions.

4.8.7. 2PF Spectra Analysis

Subsequent to cosmic ray removal and dark-count subtraction, the 2PF spectra of the primordial broth samples are corrected for the spectral sensitivity of the CCD-camera, the spectral reflectivity of the diffraction grating, the spectral transmission of the collecting objective (compare section 4.2 for experimental details), and the re-absorption of the sample. The corrected 2PF spectrum $Fl_{corr}(\lambda)$ is obtained from the measured 2PF spectrum $Fl(\lambda)$ according to [43]:

$$Fl_{corr}(\lambda) \propto Fl(\lambda) 10^{A_{UVVIS}(\lambda)} \tag{4.3}$$

with the absorbance of the material A_{UVVIS} defined in equation (3.41).

5 Simulation of CARS Supercontinuum Generation

For hyperspectral CARS imaging, a broadband coherent light source is needed, which is often provided by generating a supercontinuum (SC) in a photonic-crystal fiber (PCF) [44–46]. Understanding the temporal and spectral properties of supercontinuum generation (SCG) is desired for different wavelengths, average powers, and lengths of the seeding laser pulse, and for the different type and lengths of the employed PCF.

Where SCG is used to produce broadband compressible pulses for the generation of ultra-short laser pulses, the spectral broadening mechanism should be governed by SPM and soliton generation [47, 48] in order to keep good coherence properties. In our application of the SC pulses in hyperspectral CARS imaging, where a narrow pulse is used for both the seed pulse for SCG and for the pump pulse in the CARS generation process in the sample, it is of major importance to maintain the narrow-band character of the seed pulse by reducing SPM in the PCF as much as possible. Only then it is possible to exploit the correlations between broadband spontaneous FWM generated sidebands in the PCF, as will be required for the studies discussed in chapter 7.

In this case, SCG is governed by noise-seeded processes like spontaneous four-wave mixing, and spontaneous Raman scattering, see sections 3.1.3 and 3.1.4, respectively, and the temporal and spectral profiles of the generated SC strongly differ from pulse to pulse [49]. The experimental characterization of such single SC pulses at a repetition rate of about 80 MHz is very challenging [50] or for certain cases even currently technically impossible. Therefore, in order to investigate the optical field of a single SC pulse in both the frequency- and time-domains, simulations of the SCG process in a PCF are performed.

As each broadband CARS signal generation is dependent on the phase and amplitude of the actual SC pulse used in the CARS process, it is also important to investigate the generation of the broadband CARS field on a single pulse level. By simulating

the phase and amplitude for the broadband CARS field, generated with a single SC field, a single broadband CARS spectrum can be characterized, which up to date has not been reported in the literature yet.
In this chapter, the SC generation for different powers and pulse lengths in the fs- and ps-regime is investigated, as well as its consequences for the subsequent broadband CARS signal generation. The investigation of the phase and amplitude characteristics of broadband CARS will be addressed. Considering this more complete simulation approach, the optimal pulses lengths for seeding SCG and its use in hyperspectral CARS imaging are identified.

5.1. Simulations of Supercontinuum Generation

The key input parameters for the SCG simulation in the PCF according to the GNLSE equation (3.12) are the dispersion properties of the fiber. The dispersion curve for the PCF (FemtoWHITE800, NKT Photonics) used in this thesis is shown in figure 5.1. The dispersion curve for the wavelength region from 605 nm to 1060 nm and the second zero dispersion wavelength (ZDW) at 1260 nm were provided by NKT [51]. In order to cover the full SC region of interest, this curve was extrapolated with a polynomial of order 18 to 400 nm on the short wavelength side and to 1600 nm on the long wavelength side. The dispersion shows two zero crossings at the specified ZDWs at (750 $\pm$15) nm and (1260 $\pm$20) nm. Outside of these two ZDWs, the PCF shows normal dispersion, meaning that the red wavelength components travel faster than the blue wavelength components. In between the two ZDWs the PCF exhibits an anomalous dispersion regime where the group velocity for the blue components is higher than for the red components. Typically a flat dispersion curve close to zero around the seed wavelength is desired for SCG applications. Another PCF parameter for simulations is the nonlinear coefficient $\gamma = 95\ (Wkm)^{-1}$, which is taken from the NKT data sheet [51]. Because of the small attenuation for this PCF and the short simulated fiber length of 12 cm, the fiber attenuation is disregarded here.
SC simulations were performed for the seed wavelength $\lambda_{Seed} = 808\ nm$ and the pulse length of $T_{Seed} = 2.94\ ps\ (sech^2)$, as used in the actual experiment (see figure 4.1). For comparison, the same simulation were carried out for the seed pulse lengths 123 $fs\ (sech^2)$ and 88 $ps\ (sech^2)$. Average input seed powers given in this simulations refer to an experimental pulse repetition repetition rate of 76 MHz.
The input pulse is modeled with a $(sech^2)$ temporal profile onto which amplitude noise and phase noise is added by multiplying the pulse amplitude profile with normal distributed random values, and the phase profile with uniformly distributed

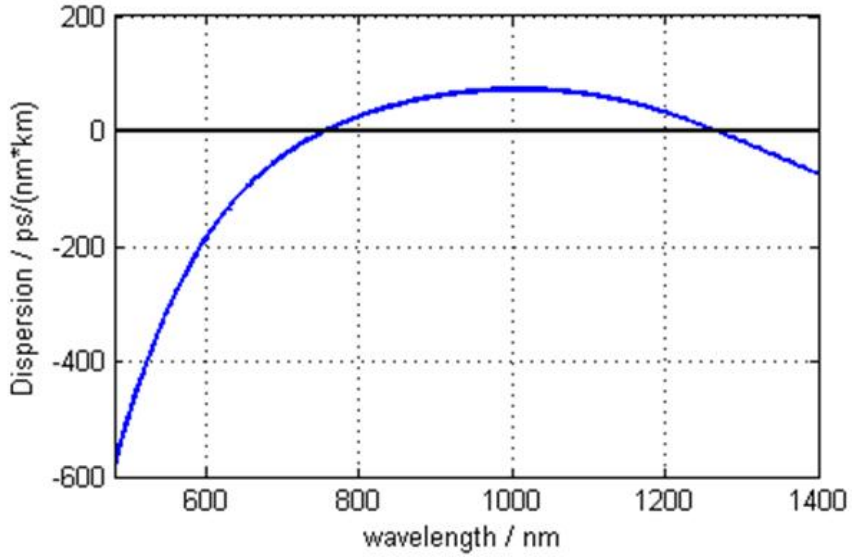

Figure 5.1.: Dispersion curve of the PCF FemtoWHITE800 [29, 51] extrapolated with a 18th order polynomial fit to the manufacturers data.

random values, which are both scaled to match the Poisson noise distribution according to Li et al. [52].

According to reference [8], the resolution of the temporal grid in solving the GNLSE has tight limitations by being fine enough to include all essential frequency components after the Fourier-transform and by not generating negative frequencies by being too fine. In our case, a time window of $T_{width} = 50\ ps$, a minimum wavelength of $\lambda_{min} = 450\ nm$, and a number of grid points of 2^{15} where chosen. The temporal grid step size dT is limited to $1.347\ fs < dT < 1.693\ fs$. For the 88 ps-simulation, $T_{width} = 800\ ps$ and a number of grid points of 2^{19}. The simulation is performed with the Matlab differential equation solver "ode45". The solver takes predefined steps in the parameter space, whose size is reduced whenever the deviations excel the given relative tolerance of 10^{-4} or the absolute tolerance of 10^{-10}.

To model the Raman response in fused silica after Stolen et al. [9] (see figure 3.2), many studies of SC simulations in PCFs use a single broad Lorentzian line. This is a valid approximation, especially when spectrally broad fs-pulses are used for seeding the SCG. In contrast, using few-ps seed-pulses for the SCG, where the spectral bandwidth is similar to that of the vibrational bands of the Raman-response of the fused silica fiber, a more complex model consisting of a linear combination of 13 Lorentzian lines is used [53], resembling the details of the vibrational spectrum of fused silica. Here, the Raman response is modeled with a linear combination of Lorentzian lines best matching the Raman spectrum of fused silica.

5.1.1. Supercontinuum Generation with few-ps Pulses

The bandwidth of the vibrational resonances of biological molecules is typically a few wavenumbers. For an efficient CARS excitation, narrowband pulses with a spectral bandwidth smaller than the vibrational bandwidth of interest, but still being in the same order of magnitude, is required, which corresponds to a transform-limited pulse length of a few picoseconds. In this section, the feasibility and the advantages of the simultaneous use of few-ps pulses for both the narrowband CARS excitation in the sample and the seeding of SCG in the PCF are examined.
In figure 5.2, the simulated SC intensity generated in the PCF femtoWHITE800 after seeding with a 2.94 ps ($sech^2$) pulse, centered at 808 nm with 550 mW average power, is displayed as a function of propagation distance inside the PCF. The 2.94 ps ($sech^2$) seed pulse has a corresponding spectral bandwidth of 3.57 cm^{-1}. The generated SC intensity is color coded using a logarithmic scale, where blue and red are low and high intensities, respectively, spanning over more than 10 orders of magnitude.
In the spectral domain, up to the first 4 cm of propagation in the fiber, no considerable generation of new wavelength components is observed. Only a reduction in the intensity of the seed pulse in combination with its weak broadening is noticed. After 4 cm, there is an onset of symmetric spectral sidebands around the seed pulse wavelength. The first pair of spectral sidebands originates from spontaneous Raman scattering, while the second pair is due to spontaneous FWM. The following spectral sidebands are due to second order processes of the aforementioned ones. Each of those sidebands consists of individual stochastic peak features. The intensities of a sideband at a given wavelength increases and decreases in an oscillatory manner throughout the propagation inside the fiber, and their overall net intensities increase. The oscillatory behavior can be assigned to soliton effects taking place in the anomalous dispersion regime of the PCF [49]. Due to all the different SCG processes, at the end of the fiber there is considerable intensity spread over several hundreds of nanometers, which is a stochastically modulated. At the beginning of the PCF, the intensity of the generated spectral components, which are not in the direct vicinity of the seed pulse, are several orders of magnitudes lower than the seed pulse itself. Later these components increase in intensity by some orders of magnitude. Towards the end of the fiber, the remaining central part of the broadened seed pulse is also much lower in intensity but still one to two orders of magnitude stronger than the broadband continuum.
Simultaneous with the onset of the sidebands in the spectral domain, an onset of sidebands in the temporal domain (see the right panel of figure 5.2) is seen. There is a build-up of stochastic features spread symmetrically in time with the propagation

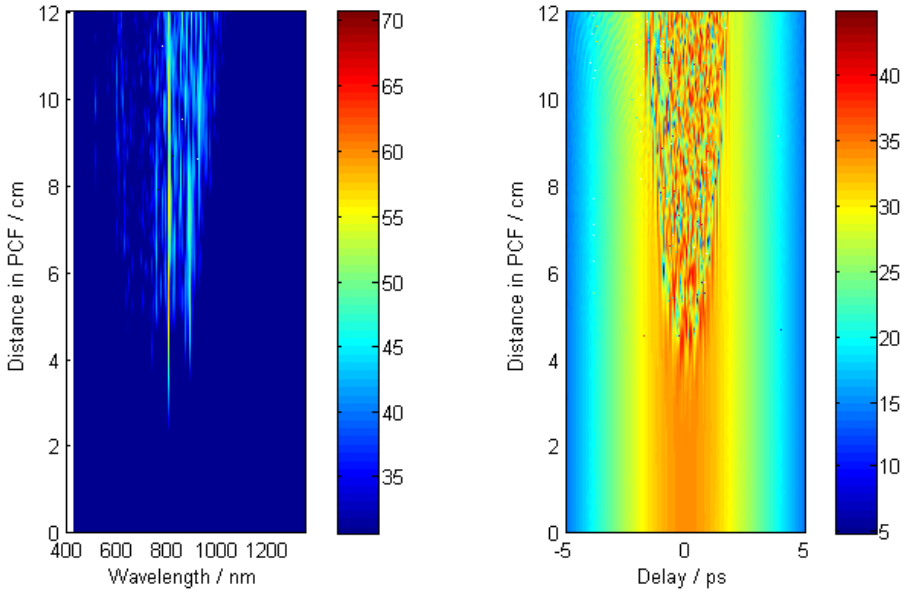

Figure 5.2.: Simulation of SC generation along the length of the PCF in the frequency- (left) and time-domains (right) for a single 2.94-ps ($sech^2$) seed pulse at 808 nm with an average input power of 550 mW. The intensity is color-coded on a logarithmic scale in dB.

length in the PCF. This means that the SCG starts spreading from the most intense part of the seed pulse towards the less intense front and tails of the pulse.

After having simulated the build-up of a stochastic SC pulse inside a ps-seeded PCF, we are now interested in its stochastic field, amplitude and phase at the exit of the PCF.

Figure 5.3 compares the spectral phase (a), the amplitudes ((b) and (d)), and the intensity profiles ((c) and (e)) in both the spectral and the temporal domains for a simulated single SC pulse at the end of a 12 cm fiber (blue curves) with the respective profiles of the seed pulse at the beginning of the fiber (green curves). The spectral amplitude and intensity profiles are represented on a logarithmic scale, revealing also weak spectral components far away from the seed wavelength. A stochastic structure is observed over a wavelength range of many hundreds of nanometers. In the direct vicinity of λ_{Seed}, the spectral phase shows a deterministic rise over several optical cycles symmetrical towards higher and lower wavelengths. Further away from λ_{Seed}, the spectral phase spreads over several hundreds of optical cycles throughout the full generated SC bandwidth. The phase spectrum of the initial pulse outside the seed spectral bandwidth shows a stochastic noise. Because the corresponding spectral field amplitudes are negligible outside the seed spectral bandwidth, the phase in this spectral region can be ignored.

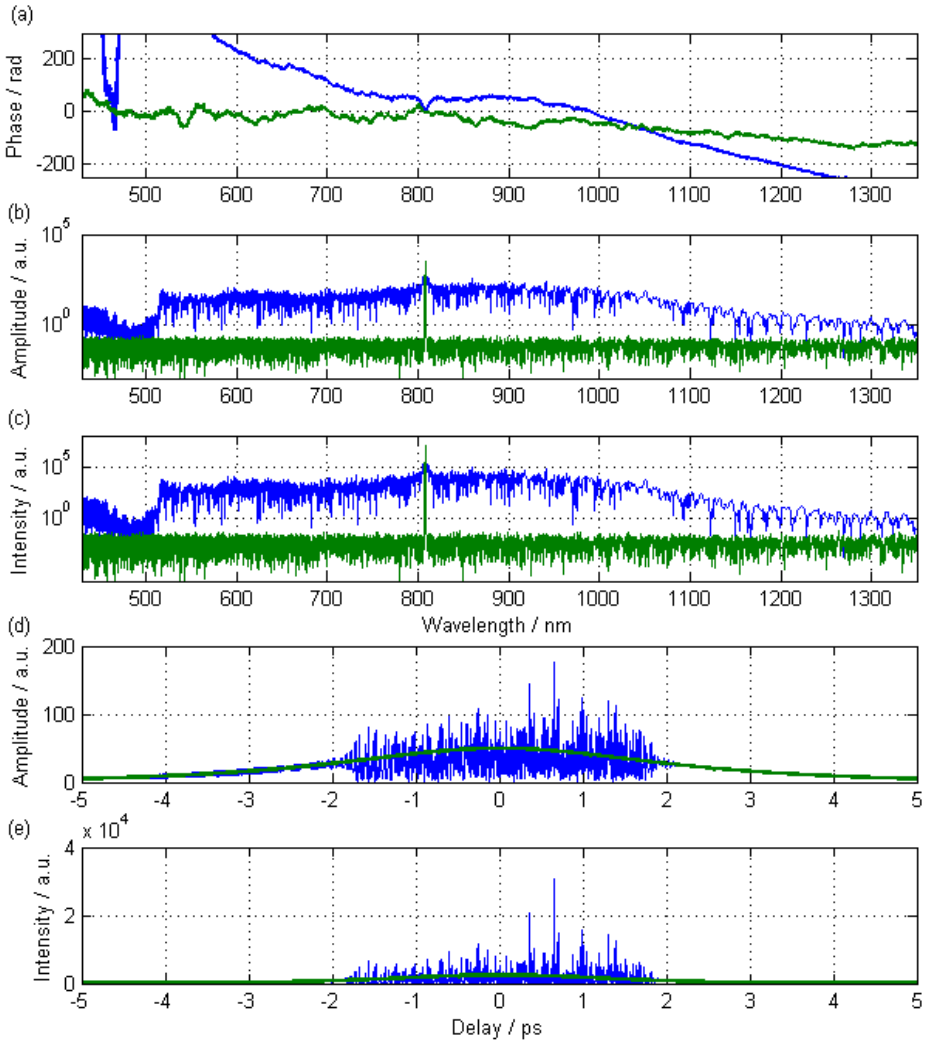

Figure 5.3.: Simulated spectral (a) to (c) and temporal (d) and (e) profiles of phase (a), amplitude (b and d), and intensity (c and e) for a single 2.94 ps ($sech^2$) seed pulse (green curves) at 808 nm with an average input power of 550 mW, and for a typical single SC pulse (blue curves) simulated at the output of the 12 cm long PCF (compare figure 5.2).

In the temporal domain, the 2.94-ps ($sech^2$) seed pulse (with noise) initially launched into the fiber generates a train of stochastic short pulses at the end of the fiber, which are distributed around the seed pulse envelope. They can easily reach six times the peak intensity of the initial seed pulse and can be only a few femtoseconds short. In contrast to the spectral domain, the pulse does not broaden in the temporal domain, but rather maintains a temporal envelope in the range of a few picoseconds, similar to that of the original seed pulse. This is because of the combination of the low dispersion in the employed PCF and the narrow bandwidth of the seed pulse. In contrast to a broadband transform-limited pulse, where the phase is constant throughout the pulse spectrum, here, the stochastic phase of the broadband SC pulse does not allow for compressing the train of very short pulses within the seed pulse envelope to a pulse length of few femtoseconds according to the SC bandwidth.

Next, the dependence of the generated SC spectra at the exit of a 12 cm PCF on the input seed power is investigated in more detail. Simulated SC spectra are directly compared with those recorded in the experiment. The experimental conditions are provided in detail in section 4.1. At low power, SPM causes the first broadening of the seed pulses spectrum (see section 3.1.1). This is highlighted in the figures 5.4 (a), (c), (e), and (g), where simulated and experimental SC spectra are shown in the region around the seed wavelength for increasing average seed powers. The shown simulated and experimental spectra are averages over 300 and 76000000 single spectra, respectively. The characteristic SPM broadening [2, p. 79 ff] starts with the splitting of the seed pulse spectrum (figure 5.4 (a)) into two peaks (figure 5.4 (c)), whose separation increases with increasing seed power. The spectral region between those two outer peaks is repeatedly filled with pairs of peaks of lower intensities (figure 5.4 (e) and (g)), resulting in an approximately flat spectral plateau. Due to spontaneous Raman scattering in fused silica, an imbalance between the two outermost peaks builds up with increasing seed power [2, p. 274 ff] and [54], meaning that the red side peak becomes stronger than the blue side peak. Above a certain seed power level, other processes start to contribute to the SCG. As a consequence, the pure SPM broadening with the described peak structure starts to wash out into a broader SC. All of the described power dependent phenomena are seen in both, the experimental and the simulated SC spectra, which qualitatively match each other. Please note here the different scaling of the y-axes in the sub-figures for better clarity, which also shows that similar relative intensities in experimental and simulated SC spectra are obtained. The imbalance in intensity between the red and blue sides of the SC pulse spectrum is much more pronounced in the experimental spectra. Also, the intensities of the outer SPM peaks decrease stronger with increasing seed power in the simulated spectra (figure 5.4 (g)).

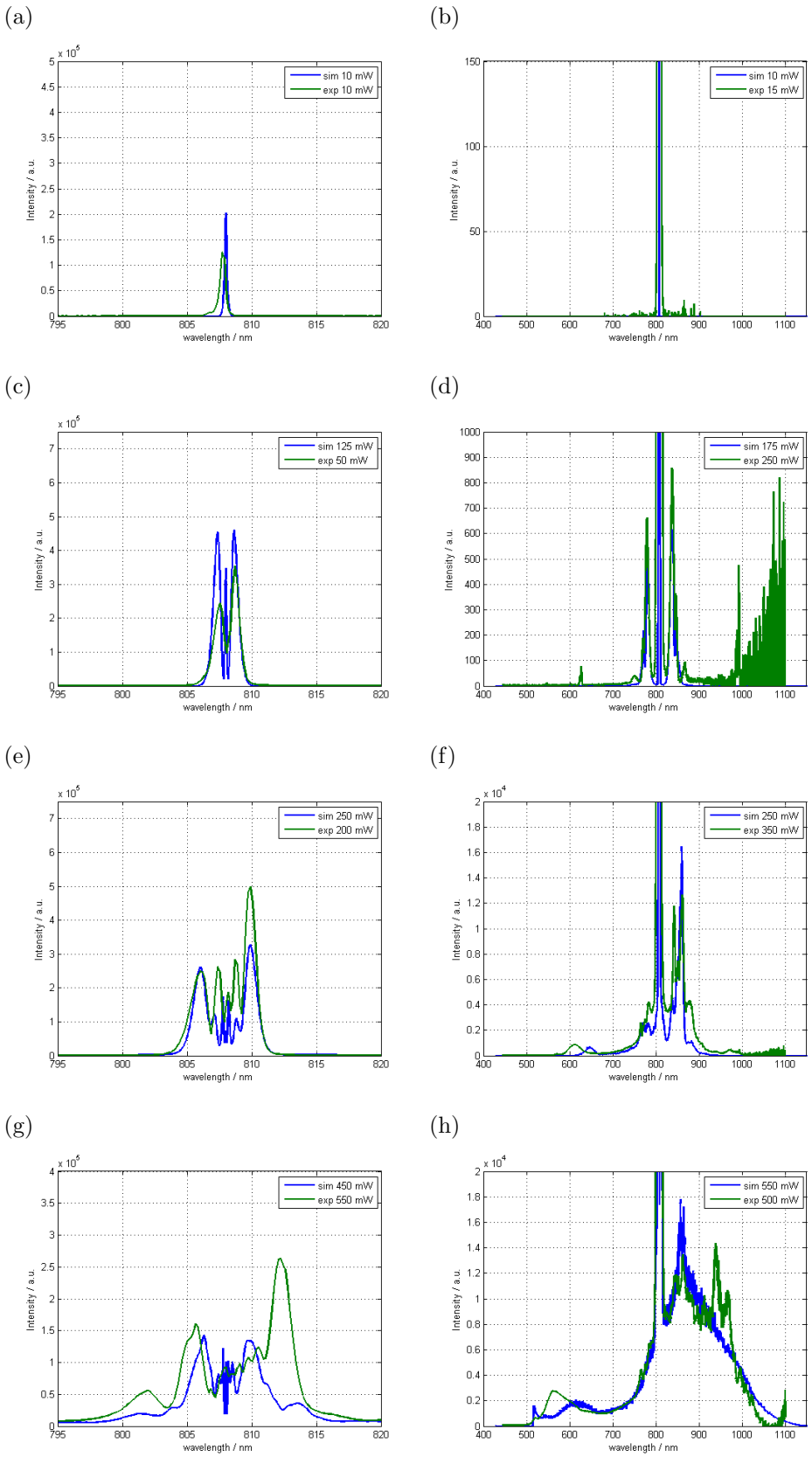

Figure 5.4.: Comparison of SC spectra obtained from simulations (blue curves) and experimental measurements (green curves) at four different seed power regimes in the vicinity of the seed wavelength (a, c, e and g) and over the full spectral range of SC generation (b, d, f and h). See text for experimental and simulation details.

While for low powers the SPM is the main process for spectral broadening, at higher seed powers, additional processes start dominating the SCG. With further increase of seed power the intensity of the SPM-broadened seed pulse spectrum reduces, and especially the outer SPM peaks start to merge with new frequency components generated further away from the seed wavelength. In figure 5.4 (b), (d), (f), and (h), experimental and simulated averaged SC spectra for different seed powers are shown now over the full spectral range of the SC. While at a very low average seed power the pulse spectrum is almost unchanged after passing the fiber (figure 5.4 (b)), by increasing the seed power the appearance of two strong side peaks at 780 nm and 838 nm are seen (figure 5.4 (d)), which are assigned to the Stokes- and anti-Stokes-Raman scattering, respectively, of silica resonances at a Raman-shift of $\pm$ 440 cm^{-1} (compare figure 3.2). Both Raman shifted peaks show a shoulder on the side of higher Raman shift wavenumbers, which resembles the spectral details of the Raman response of fused silica. The small additional peaks at 860 nm and 767 nm are due to spontaneous FWM, which are starting to become measurable at the displayed power regime shown in figure 5.4 (f). Except for those FWM peaks, the experimental and simulated spectra match perfectly.

In figure 5.4 (d), from around 1000 nm towards higher wavelengths, the experimental SC spectrum exhibits strongly increased noise, which is a consequence of the correction for the wavelength dependent detection efficiency of the CCD camera (see section 4.8.1). Towards the near-IR region, the correction values are quite high and strongly amplify the noise on the low SC signal. For increasing seed power, the FWM peaks become much stronger than the Raman peaks, as can be seen in figure 5.4 (f). In this power regime, already higher orders of FWM occur, which give rise to additional spectral components further away from the seed wavelength. In both experimental and simulated SC spectra, the FWM mixing peaks have grown stronger than the Raman peaks, additional shoulders to the FWM peaks at 870.5 nm and 753.8 nm (corresponding to 889 cm^{-1}) show up, a weak and broad peak much further in the blue at 620 nm appears, and the wavelength regions in between this peak and the seed wavelength starts uniformly filling up.

For even higher seed powers (compare figure 5.4 (h)), all of the aforementioned nonlinear processes start to grow and interfere with each other. As a result, even more new spectral components are generated such that the previously well defined spectral features are washed out over a broad spectral range. Even in this seed power regime, there is a strong imbalance towards the red side of the seed wavelength. Here, the match between experiment and simulation is also very good except for two additional peaks at 940 and 967 nm observed in the experimental SC spectrum. The latter could neither be assigned to a specific process of SCG nor to a property of the PCF.

This sharp edge at 510 nm in the simulated SC spectra, is attributed to the high error sensitivity in the extrapolation of the manufacturers PCF dispersion curve below 600 nm (see discussion of figure 5.1).

It should be noted that the seed power dependence of the simulated SC spectrum does not match perfectly in a quantitative manner with the experimental SC spectrum. The main source for this discrepancy is assigned to the exact form of the PCF dispersion curve, on which the SCG is very sensitive. The dispersion curve used in the simulation is an exemplary curve for the specified fiber, which might slightly deviate from the actual dispersion curve of the PCF used in the experiment. Additionally, for the determination of the dispersion parameters used in the simulation, it had to be extrapolated and fitted with an analytic expression. These approximations represent other sources of uncertainty, which are not very important for the SC simulation in the low seed power regime, where spectral broadening is mainly governed by SPM. But for high seed powers, when many different processes contribute to and dominate the spectral broadening, small deviations in the dispersion curve far away from the seed wavelength can lead to strong discrepancies between simulation and experiment.

In summary, the results of the SC simulations in show a stochastic amplitude distribution but also a stochastic phase distribution throughout the bandwidth of each single SC pulse, which is in agreement with experiments reported in reference [50]. Furthermore, a good match between simulated and experimental spectra is observed, so that the simulated SC spectra resemble those spectral features and their seed power dependencies observed in the experiment. Therefore, we will use theses simulated complex SC fields for the subsequent simulation of complex broadband CARS fields, as will be discussed in section 5.2.

5.1.2. Supercontinuum Generation with fs Pulses

As mentioned before, the contribution of different processes to SCG varies strongly according to the seed pulse lengths. Therefore, in order to evaluate if a much shorter pulse length is more favorable for SCG its corresponding simulations with fs-pulses are investigated next. In figure 5.5, the evolution of the simulated SCG along the PCF is displayed for seeding with a single 123 fs ($sech^2$) pulse centered at 808 nm with an average power of 100 mW. Except for the seed pulse properties, all simulation input parameters are identical to those detailed before in section 5.1.1. The average power was chosen such that a spectral density in the red part of the SC at the end of the PCF is generated, which is similar to that obtained with few-ps pulses (see figure 5.3 (c)).

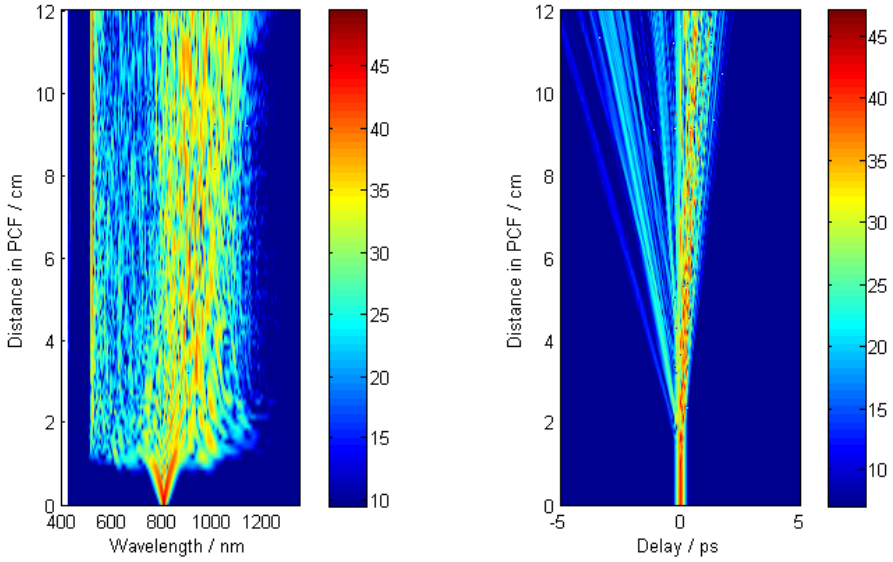

Figure 5.5.: Simulation of SC generation along the length of the PCF in the frequency- (left) and time-domain (right) for a single 123 fs ($sech^2$) seed pulse at 808 nm with an average input power of 100 mW. The intensity is color-coded on a logarithmic scale in dB.

In the spectral-domain (figure 5.5, left panel), in contrast to seeding the PCF with few-ps pulses, the SCG with the 123-fs seed pulses starts right from the beginning of the fiber. Within the first centimeter a strong SPM broadening over many tens of nanometers is seen, which is followed by a broadband stochastic distribution of new wavelength components over the whole considered spectral range. Here again, the sharp edge close to 500 nm, below which no spectral components are generated, is attributed to errors made in the extrapolation of the PCF dispersion curve used for the simulation. Because of spontaneous Raman scattering in fused silica, the spectral weight of the SC lies more on the red side of the seed wavelength.

In the time domain (figure 5.5, right panel), the evolution of the simulated SCG reveals formation of many orders of solitons at relatively low power and their temporal walk off from the time zero defined by the seed pulse. The temporal profile of the seed pulse itself continuously slowly broadens and also shifts by a couple of hundreds of femtoseconds towards positive time delays, while propagating through the fiber.

Figure 5.6 takes a closer look at the complex field of a simulated SC pulse that exits the 12 cm long PCF (blue curves), which clearly differ from that of the ps-seeded SC pulse (compare 5.3). For comparison, the 123 fs seed pulse before the fiber (green curves) is also shown. It has a considerable spectral width over tens of nanometers. The spectral phase, amplitude, and intensity of the simulated SC field

are stochastically distributed within the full spectral SC range, which are similar to those obtained with a few-ps seeded SC pulse (see figure 5.3) and previously discussed in section 5.1.1. However, the absence of any signature of the seed pulse strongly differs from the ps case. All spectral components of the initial fs-seed pulse have been converted into the broad continuum with an almost constant spectral density throughout the whole spectrum.

In the temporal domain (figures 5.6 (d) and (e)), sharp and strong peaks spread over several picoseconds of positive time delay are observed in the single simulated SC field (blue curves). In contrast to the ps case the temporal distribution of these sub-pulses exceeds the temporal envelope of the fs-seed pulse. The latter could be caused by those sharp features in the spectral domain, whose transform-limited temporal width is much longer than the short fs-seed pulse. Furthermore, the shift of sub-pulses towards positive time delays is caused by chirp of both the fs-seeded pulse, while traveling through the fiber, and of the different spectral SC components, which are already formed in the first centimeters of the fiber.

5.1.3. Supercontinuum Generation with Longer ps-Pulses

In this section, the same simulation of SCG is performed for a much longer seed pulse of 88 ps ($sech^2$). Here, the seed peak power is chosen to be similar to that of the 2.94 ps seed pulse discussed in section 5.1.1, which corresponds to an average power of 22400 mW for a pulse repetition rate of 76 MHz. As seen in the spectral domain (figure 5.7 left panel), after 1 cm propagation inside the fiber there is an onset of spontaneous FWM side lobes placed symmetrically around the seed pulse wavelength, which consist of a stochastic distribution of sub-peaks. After one more centimeter, a set of second-order spontaneous FWM side lobes emerges further away from the seed wavelength. Shortly thereafter more side lobes appear, creating a broad SC with a stochastic peak structure spreading over the full spectral region. The intensity and bandwidth of this SC pulse increase while further propagating through the PCF.

In the temporal domain (figure 5.7 right panel), the simulated evolution of the SCG while propagating through the PCF looks very similar to that obtained for a 2.94 ps ($sech^2$) seed pulse (see figure 5.2, right panel). After a couple of centimeters into the PCF, stochastic features around the center of the seed pulse start to appear, whose onset seems to start at a fiber distance, where the first spectral FWM side-lobes have increased to considerable intensity. Please note that here the intensity scaling is different from that used in figure 5.2, and that the temporal axis covers a much larger range. As can be seen in figure 5.7 (right panel), the sub-peaks are

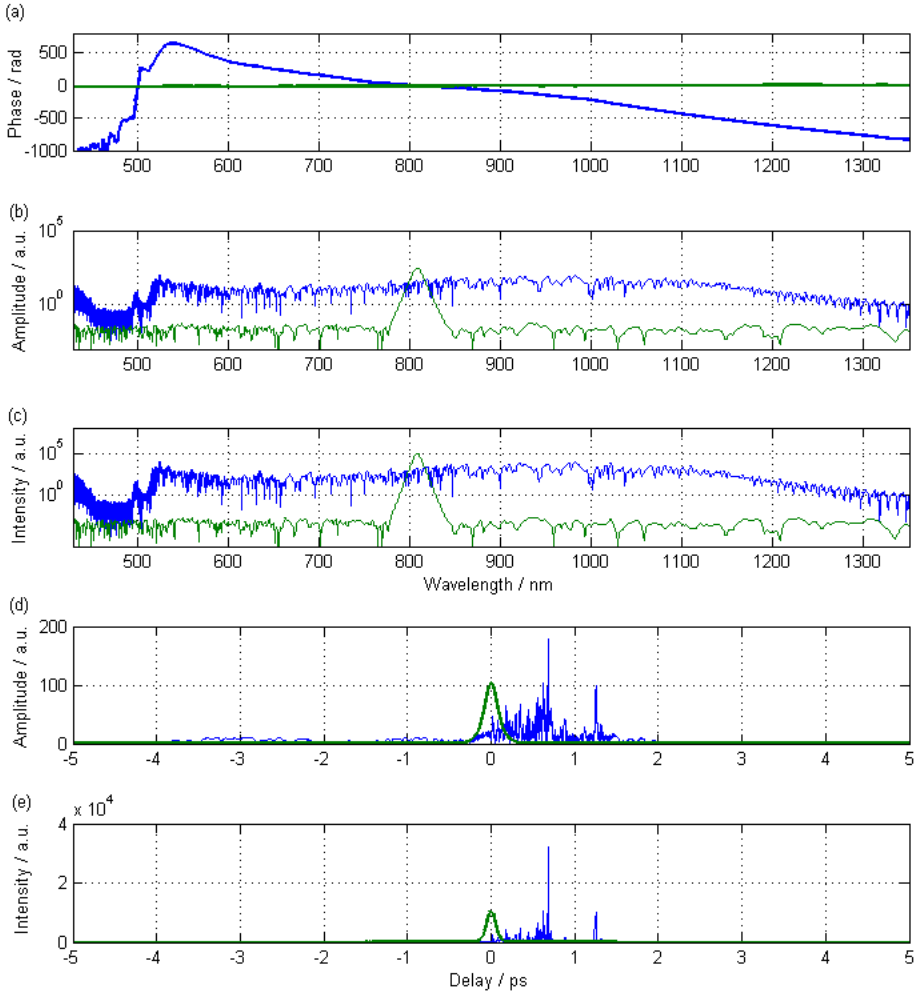

Figure 5.6.: Simulated spectral (a-c) and temporal (d and e) profiles of phase (a), amplitude (b and d) and intensity (c and e) for a single 123-fs ($sech^2$) seed pulse (green curves) at 808 nm with an average input power of 100 mW, and for a typical single SC pulse (blue curves) simulated at the end of a 12 cm PCF (compare figure 5.5).

distributed over much larger time delays spanning more than 100 ps, but staying within the order of magnitude of the temporal bandwidth of the initial seed pulse.

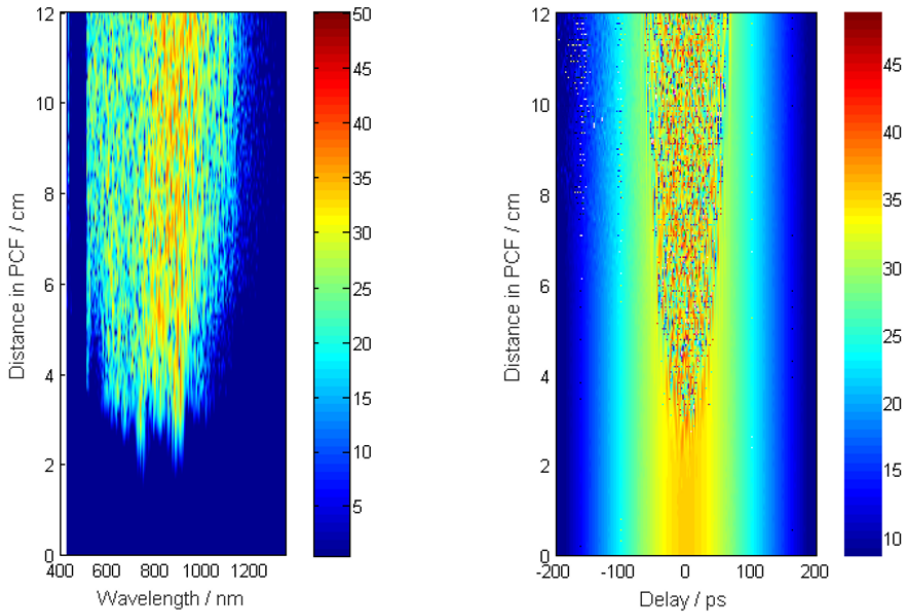

Figure 5.7.: Simulation of SC generation along the length of the PCF in the frequency- (left panel) and time-domain (right panel) for a single 88 ps ($sech^2$) seed pulse at 808 nm with an average input power of 22400 mW. The intensity is color-coded on a logarithmic scale in dB.

Having a closer look on the complex field of a single SC pulse at the exit of the 12 cm PCF (figure 5.8), it is directly evident that the resulting field looks alike that of the simulated SC using a 2.94 ps seed pulse (compare figure 5.3). The increased spectral resolution in the phase, amplitude, and intensity spectrum, shown in figures 5.8 (a), (b), and (c), respectively, has a pure technical reason. It stems from the need for a much bigger time window of $T = 800$ ps when simulating the SC field with a 88-ps seed pulse using the same temporal resolution as in the previous cases. Due to the higher spectral resolution, the spectrum in figure 5.8 (c) seems to be smoother than the SC generated with the shorter pulses.

In the temporal domain, shown in figures 5.8 (d) and (e) the simulated SC pulse at the end of the fiber consists of a distribution of sub-peaks spanning over 100 ps around the center of the initial seed pulse envelope, that can be up to ten times more intense than the seed pulse.

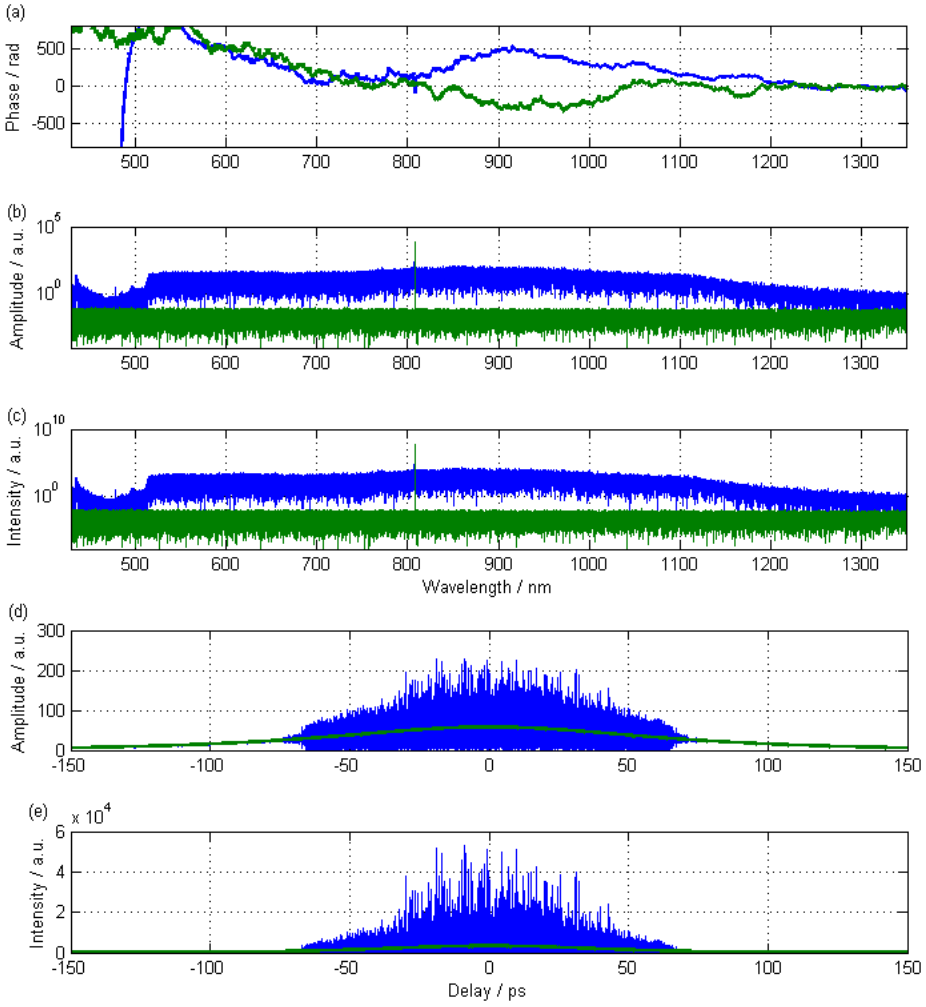

Figure 5.8.: Simulated spectral (a)-(c) and temporal (d) and (e) profiles of phase (a), amplitude (b) and (d), and intensity (c) and (e) for a single 88 ps ($sech^2$) seed pulse (green curves) at 808 nm with an average input power of 22400 mW, and for a typical single SC pulse (blue curves) simulated at the end of a 12 cm PCF (compare 5.7).

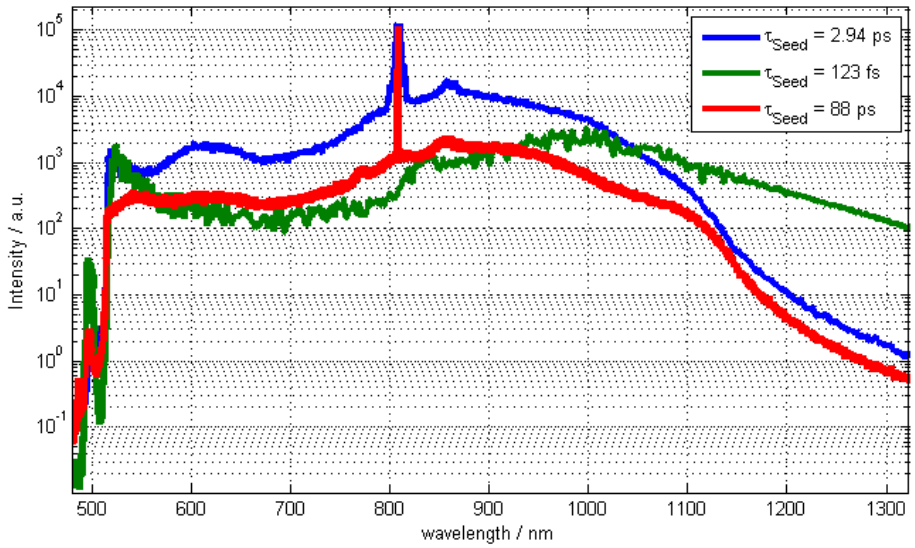

Figure 5.9.: Simulated average supercontinuum spectra for seed pulse lengths of 2.94 ps, 123 fs, and 88 ps, and seed peak powers of 9428 W, 2170 W, and 2952 W, respectively. See text for further simulation details.

5.1.4. Comparison of SC Simulations for Different Seed Pulse Lengths

Figure 5.9 compares simulated SC spectra for the three different seed pulse lengths introduced in the previous sections, where averaged seed powers are chosen to result in similar spectral densities on the Stokes part of the supercontinuum. The spectra shown here are averaged over 150 single simulated SC spectra in order to better reveal the overall shape of the generated SC spectrum rather than the stochastic features of the single pulse spectra. Note that in the actual experiment the stochastic single pulse features are completely smoothed out because many thousands of pulses are averaged. Averaged seed powers were 100 mW, 550 mW, and 22400 mW for pulse lengths of 123 fs, 2.94 ps, and 88 ps resulting in 9428 W, 2170 W, and 2952 W, respectively. The peak powers of all three simulated seed pulses for SCG therefore reside in the same order of magnitude. This can explain why for all three pulse lengths SC spectra with similar bandwidths are generated even though the seed pulse lengths span almost three orders of magnitude.

The shapes of the Stokes parts of the SC spectra for the 2.94 ps and 88 ps seed pulses are very similar with their spectral densities reaching a maximum between 850 nm and 900 nm and both decreasing continuously towards higher wavelengths. These intensities drop by approximately one order of magnitude from their maxima in the near-IR to their respective values at 1100 nm. Together with the pump wavelength

of 808 nm , the application of such Stokes pulses for CARS generation results in an accessible Raman shift range of interest of up to 3285 cm^{-1}. In contrast, the Stokes part of the fs-seeded SC spectrum exhibits a smaller spectral change of its spectral density.
In summary, all SC simulations for the three different seed pulse lengths generate a broad SC spectrum at the end of the 12 cm long PCF, with the spectral envelope spanning over several hundred of nanometers. In all three cases, the generated SC provides a Stokes continuum with a relatively flat profile covering the full spectral CARS range of interest. Next, the CARS simulations with all three SC pulses will be performed to investigate the impact of the single pulse SC fields on the generation of the respective CARS fields.

5.2. Simulations of Broadband CARS Generation

In the next step, the simulated SC spectra are further used in CARS generation simulations. Because for the CARS excitation only the Stokes part of the SC is needed, all spectral components on the short wavelength side of the seed pulse as well as the seed pulse itself are cut off, which is analogous to spectral filtering each SC pulse as performed in the actual experiment (see setup in figure 4.3). The simulation of single CARS pulses is then performed in the frequency domain by first calculating the complex CARS field according to equation (3.25). For each of the single simulated Stokes fields, a purely non-resonant CARS spectrum and one for the vibrational response of neat benzaldehyde are computed. Here, either only a constant $\chi^{(3)}_{NR} = 1$ or in addition a linear combination model for the 10 strongest bands of benzaldehyde are used. The Lorentzian line shape parameters (according to equation (3.20)) used in the simulations are listed in table 5.1. The resonance frequencies Ω_r and the widths Γ_r are extracted from the measured spontaneous Raman spectrum of benzaldehyde. The amplitudes A_r are taken from reference [55]. As in the experiment, the pump and probe pulses used for the simulations of CARS generation are 2.94 ps and 88 ps, which are identical with the seed pulses used for the respective SCG simulations. For the CARS simulations, the experimental situation is mimicked by treating the simulated SC pulse with the transmission curves of the long-pass filter, dichroic filters, and of the objective lens used in the experiment. Due to this major alteration of the simulated SC pulse, the temporal resolution of the resulting simulated Stokes pulse is considerably reduced due to the reduction in its spectral bandwidth. Also, its intensity is decreased.
Because the numerical integration of the nested integral in equation 3.25 over a very broad spectral range with the required high resolution is extremely computational

Table 5.1.: Lorentzian line shape parameters used to model the non-linear resonant Raman response of benzaldehyde

r	Ω_r [cm^{-1}]	A_r	Γ_r [cm^{-1}]
1	617	12	10
2	831	17	10
3	1003	95	5
4	1025	12	8
5	1169	14	14.5
6	1207	30	10
7	1587	10	8
8	1599	46	10
9	1701	36	15
10	3068	16	15

demanding [56], the simulation of CARS generation therefore is limited here to the dominant CARS generation process according to the CARS scheme A (see section 3.3.2).

To illustrate the simulation procedure of CARS generation, figure 5.10 shows an example of a single CARS pulse together with the pump and Stokes input pulses used in the simulation. For comparison, the corresponding averages over 150 simulated Stokes and CARS pulses are also shown. The intensity-spectra of the single CARS pulse are magnified by seven orders of magnitude for better visibility. In the CARS intensity spectrum it can be nicely seen that the spectral shape of the NR regions resembles the transformation of the spectral shape of the Stokes spectrum onto the anti-Stokes side of the pump wavelength. The comparison of the intensity spectra of the CARS intensity with that of the input Stokes intensity reveal the mirror transformation of the stochastic spectral features from the Stokes continuum to the CARS continuum. Only after averaging over many pulses, the characteristic CARS line shapes of the individual benzaldehyde resonances can be observed.

5.2.1. Comparison of CARS generation with SC generated with different pulse lengths

In figure 5.11, the simulated CARS phase and intensity spectra using the 2.94 ps seeded Stokes pulse and the 2.94 ps pump/probe pulse with an average power of 20 mW are shown together with the corresponding temporal profile of this CARS

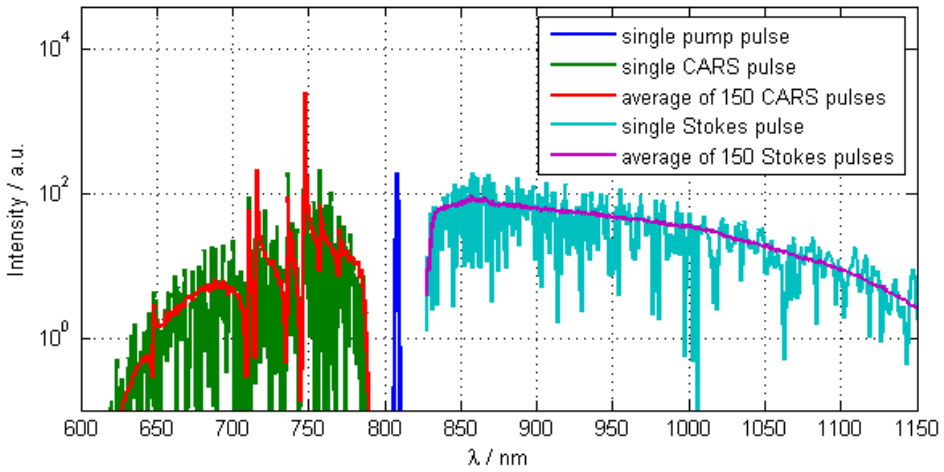

Figure 5.10.: Intensity spectra of simulated Stokes, pump, and CARS pulses using a 2.94-ps ($sech^2$) seed-, pump-, and probe-pulse. In green and cyan single pulse spectra are shown. In red and purple spectra averaged over 150 pulses are shown. The pump pulse is represented by the blue curve.

pulse.

In figures 5.11 (b) and (c), the spectra averaged over 150 single pulses are additionally shown in red, which much closer resemble the experimentally measured spectra. In the actual CARS experiments, integration times of 1 to 100 ms are typically used for acquiring a single CARS spectrum. With a pulse repetition rate of 76 MHz of the laser system, this leads to an averaging over 152000 pulses for an integration time of 2 ms. Although, due to computational limitations, only 150 pulses are averaged in the CARS simulation, resembling an effective experimental integration time of 1.97μs, the stochastic noise originating from SCG is already drastically reduced, whereas for the single simulated CARS pulse the strongly stochastic nature of the SC pulse is dominating. Below 350 cm^{-1}, the SC pulse was cut off by the dichroic filter as described above, and therefore no CARS field is generated here. The averaged CARS intensity slowly decreases towards larger wavenumbers and vanishes at about 4000 cm^{-1}. In figure 5.11 (a), a strong variation of the spectral phase in the single simulated CARS pulse is observed, which follows the spectral phase of the single simulated SC pulse, shown in figure 5.3 (a). Since in the actual experiment, the detection of a CARS intensity spectrum accumulates many subsequent pulses, the phase information becomes irrelevant.

In the temporal domain, the single simulated CARS pulse mirrors the strongly stochastic distribution of short sub-pulses that have already been observed in its simulated SC input pulse (see figure 5.3 (e)). The time profile averaged over the 150 single CARS pulses shows a temporal width of about 2 ps, which is consistent

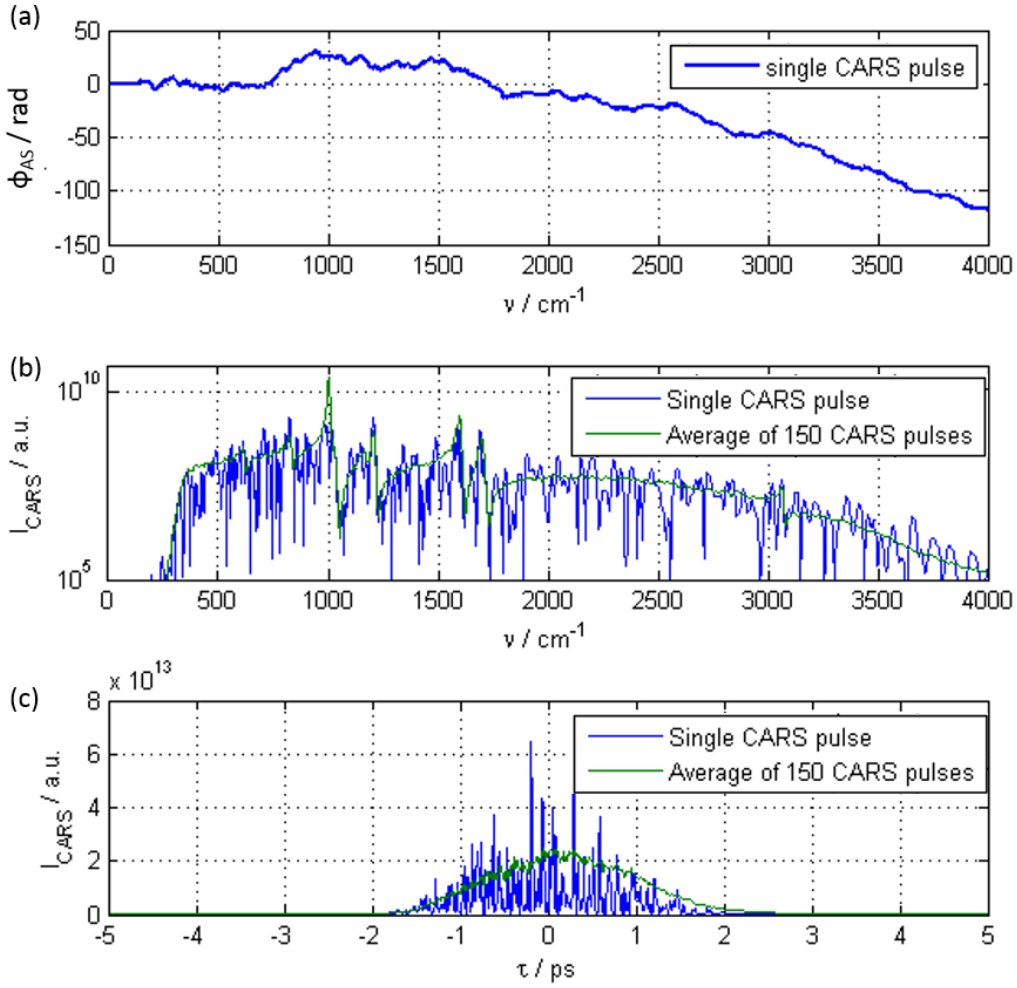

Figure 5.11.: Simulated spectral ((a) and (b)), and temporal (c) profiles of CARS (a) phase-, (b) and (c) intensity generated with a 2.94-ps pump/probe pulse and a 2.94-ps seeded Stokes continuum pulse. In blue, single CARS pulse profiles are shown, while in green averages over 150 single CARS pulses are shown.

with the width of the temporal envelope of the single input Stokes and pump/probe pulses. The stochastic sub-pulses in the single CARS profile have a temporal width in the order of 20 to 30 fs (FWHM), and their maxima amount to more than double the maximum of the averaged CARS profile.

Similar CARS generation simulations are performed with the simulated SC pulses generated with much shorter 123-fs and much longer 88-ps seed pulses and with simulated average powers of the pump/probe pulse of 20 mW, the results of which are displayed in figures 5.12 and 5.13, respectively. In both cases, very similar characteristics of the simulated CARS pulses are observed. As for the CARS pulse simulated with a 2.94-ps seeded Stokes continuum pulse (see figure 5.11), the single CARS intensity spectra are characterized by stochastic peaks distributed over the full bandwidth of the CARS pulses, which can be much stronger than their average signal levels. Again, after averaging over 150 single CARS spectra, the signatures of the vibrational resonances are clearly seen and easily distinguished from the noise peaks. The average spectra have their maxima close to the filter edge and from thereon decrease towards higher wavenumbers, still maintaining considerable intensity at 4000 cm^{-1}.

Despite these similarities, it is evident that the single CARS spectral and temporal profiles simulated with the 123-fs seeded Stokes continuum pulse and with a 2.94-ps pump/probe pulse show differences. Compared to figure 5.11 (b), the stochastic spectral peaks in figure 5.12 (b) are much broader and more spectrally dispersed. The dispersive line shapes of the vibrational resonances are therefore not easily distinguishable from the stochastic noise peaks, which have similar spectral widths at the single CARS pulse level. The stochastic noise variation originating from the 123-fs seeded SCG is even smaller, and in principal averaging over only a few hundred single CARS pulses is enough to almost completely eliminate the stochastic noise.

The single CARS phase spectra shown in figure 5.12 (a) exhibit a four-times stronger change in total phase difference between the low and high wavenumber regions, when compared to the corresponding total phase difference observed in figure 5.11 (a). This larger phase difference for the simulated CARS pulse with a 123-fs seeded Stokes pulse is consistent with a larger phase variation already observed for the 123-fs seeded SC pulse (compare figures 5.3 and 5.6), which stems from the earlier onset of SCG and its concommitent effect of material dispersion in the PCF (see section 5.1.2).

The time domain profile of the single CARS pulse, shown in figure 5.12 (c), reveals the temporal distribution of stochastic sub-pulses over a width of about 0.9 ps (FWHM), which resembles the distribution of stochastic features in the 123-fs

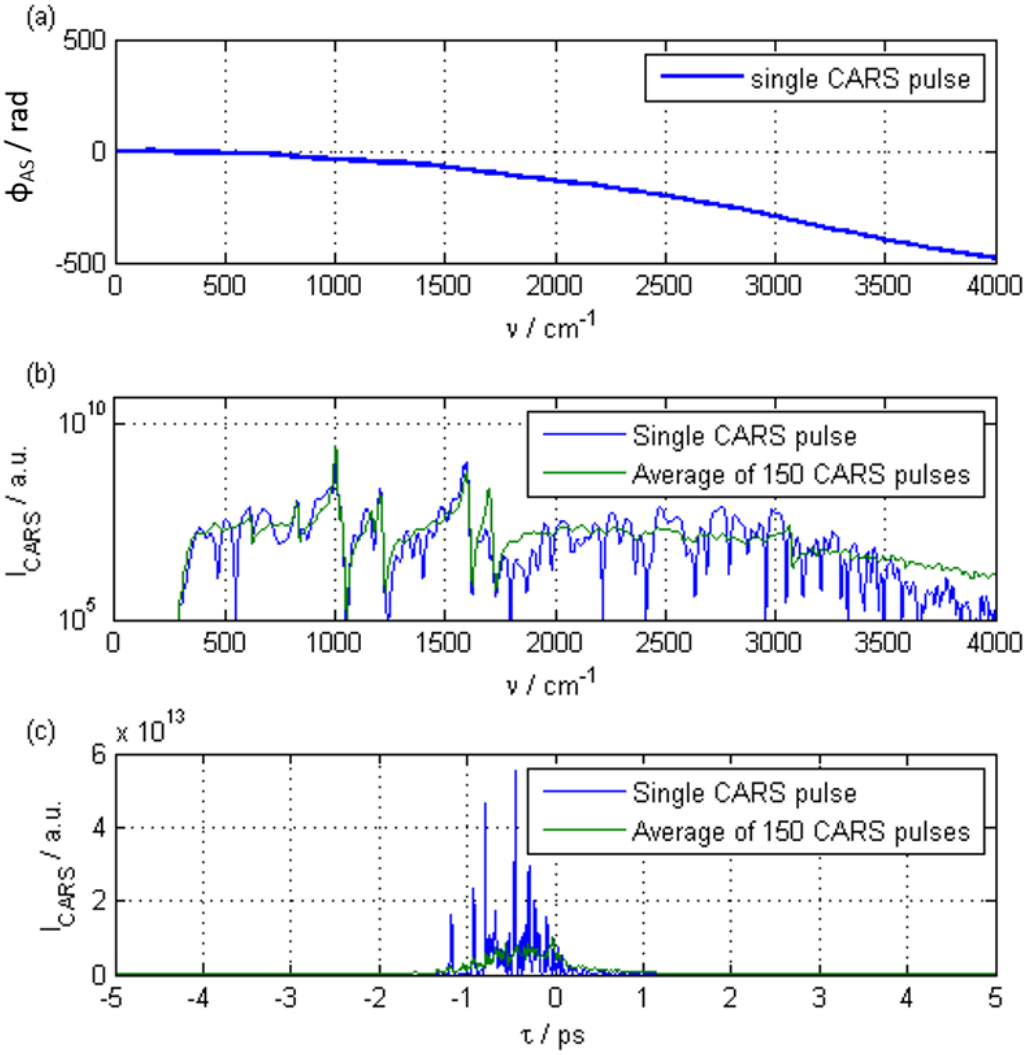

Figure 5.12.: Simulated spectral (a) and (b), and temporal (c) profiles of CARS (a) phase-, (b) and (c) intensity generated with a 2.94-ps pump/probe pulse and a 123-fs seeded Stokes continuum pulse. In blue, single CARS pulse profiles are shown, while in green averages over 150 single CARS pulses are shown.

seeded SC pulse already discussed in section 5.1.2.

For the CARS pulse using an 88-*ps* seeded Stokes continuum pulse and an 88-*ps* pump/probe pulse, the most pronounced differences are the following: Compared to the previous two cases, the absolute CARS intensity is four orders of magnitude lower due to the lower pump/probe peak power on which the CARS depends quadratically (see equations (3.18) and (3.19)) In addition the stochastic peaks in the single CARS intensity spectrum (see figure 5.13 (b)) is spectrally narrower, which originates from the much narrower pump/probe and seed pulses in combination with a narrower spectral grid because of the extended temporal window used in the simulation of the 88-*ps* seeded Stokes continuum pulse. The single simulated CARS phase spectrum shown in figure 5.13 (a) is noisier then in the previous two cases, but it shows much smaller phase variations throughout the phase spectrum, which again resembles the shape of the respective 88-*ps* seeded SC phase spectrum (see figure 5.8).

The time domain profile of the single CARS pulse, shown in figure 5.13 (c), reveals the temporal distribution of stochastic sub-pulses over a width of about 50 *ps* (FWHM), which resembles the distribution of stochastic features in the 88-*ps* seeded SC pulse already discussed in section 5.1.3.

Next, the normalized CARS spectra obtained from the three different simulation cases are compared. To eliminate the effect of the different spectral shapes of the three simulated SC pulses used for CARS excitation, as in the experimental data analysis, the raw CARS spectra are divided by corresponding reference CARS spectra simulated with only non-resonant contributions according to equation (4.1). For each case, a CARS reference spectrum was obtained by averaging over 150 different single simulated CARS pulses and by subsequent smoothing for the further reduction of noise. The resulting normalized CARS spectra simulated for all three cases are displayed in figure 5.14.

The comparison of the noise standard deviation relative to the normalized averaged CARS mean intensity in the non-resonant spectral region from 2200 cm^{-1} to 2600 cm^{-1} with values of 15 %, 11 %, and 30 % for the 123 fs, 2.94 ps, and 88 ps seeded Stokes continuum input pulses, respectively, shows that after averaging the shorter seed pulses exhibit a two to three times reduced relative noise level in comparison to that of the 88-*ps* pulse. Please note, when single CARS spectra are compared where the relative noise level amounts to a 85 %, 73 %, and 80 % for the 123 fs, 2.94 ps, and 88 ps pulses, respectively, very similar relative noise levels are observed that seem to be independent on the SC seed pulse length. Therefore, as in the experiment always several pulses are averaged, using shorter pulses is recommended.

Furthermore, by comparing the spectral resolution achieved with the three different

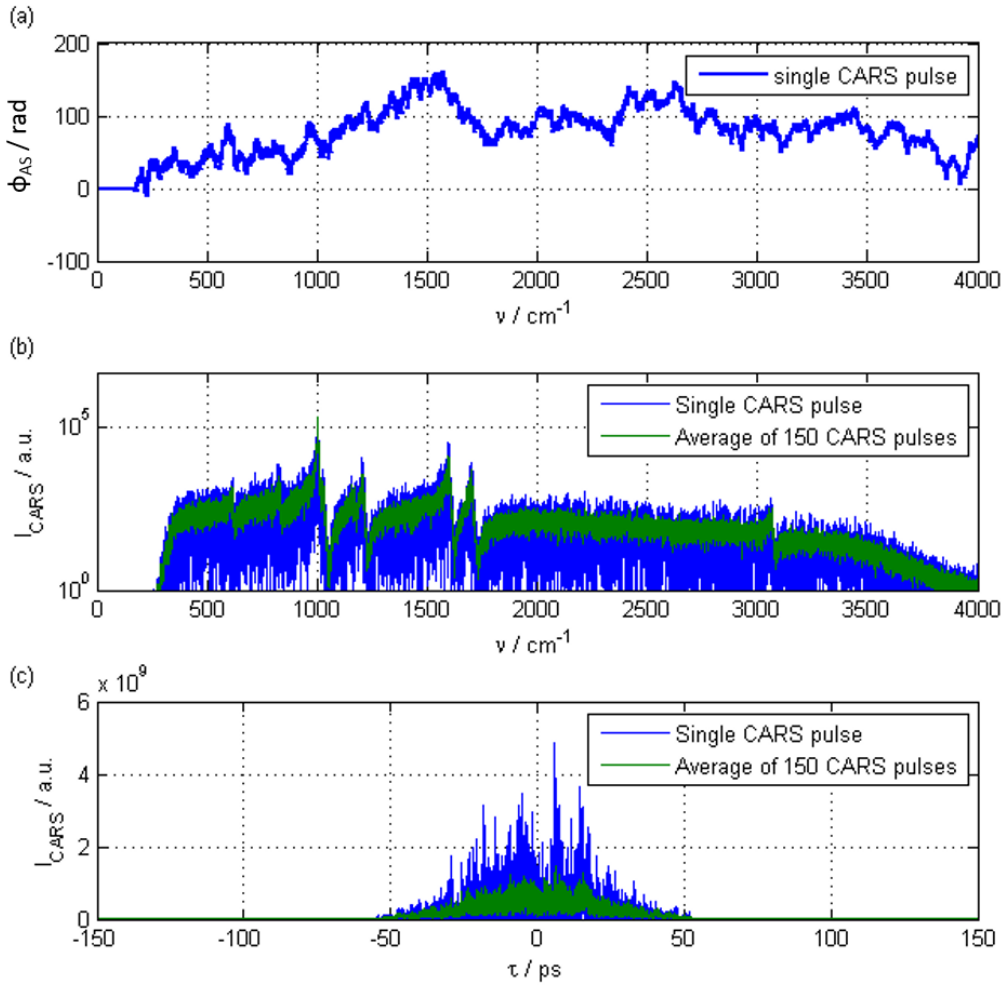

Figure 5.13.: Simulated spectral (a) and (b), and temporal (c) profiles of CARS (a) phase-, (b) and (c) intensity generated with a 88-ps pump/probe pulse and a 88-ps seeded Stokes continuum pulse. In blue, single CARS pulse profiles are shown, while in green averages over 150 single CARS pulses are shown.

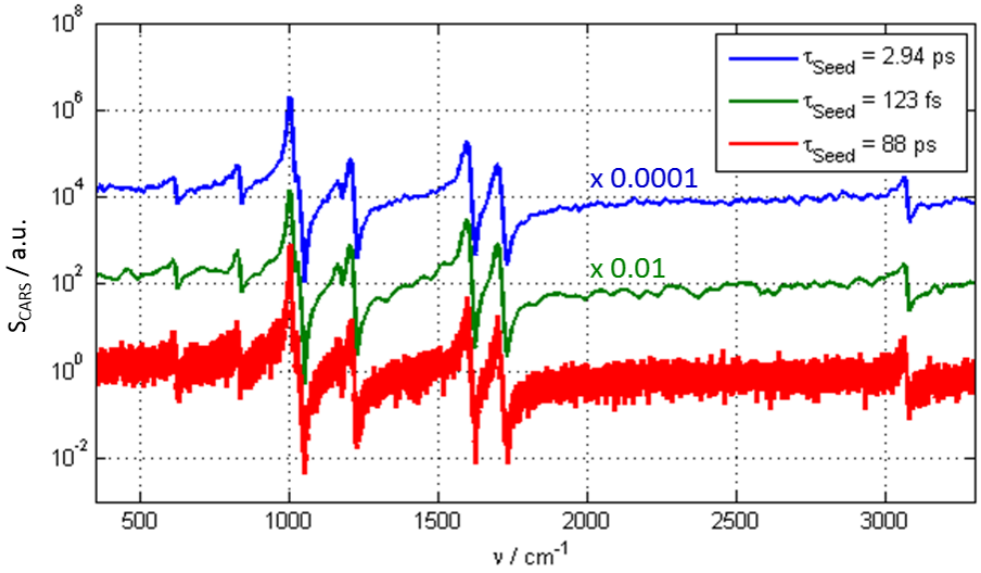

Figure 5.14.: Simulated normalized CARS spectra averaged over 150 single pulses generated with Stokes SC pulses seeded with 123 fs, 2.94 ps and 88 ps ($sech^2$) pulses. Please note the logarithmic intensity offset between spectra by 2 orders of magnitude.

Stokes SC pulses, the CARS spectrum simulated with the 88-ps pump/probe pulses and the 88-ps seeded Stokes SC pulses, providing an intrinsic transform-limited spectral bandwidth of about 0.12 cm^{-1}, has the best spectral resolution. In contrast the transform-limited bandwidth of the 2.94-ps seed pulse amounts to about 3.5 cm^{-1}. However, no major spectral degradation of the vibrational resonance features in the corresponding simulated CARS spectra are observed. For the 123-fs seed pulse, the transform-limited spectral bandwidth amounts to 85 cm^{-1}, which exceeds the typical line width of a vibrational resonance (see table 5.1). Since a 2.94-ps pump/probe pulse in combination with the 123-fs seeded Stokes continuum pulse is simulated here, again no degradation of spectral resolution in the green curve of figure 5.14 is observed. This observation is in agreement with the fact that the pump/probe pulse determines the spectral resolution in the CARS process in scheme A.

5.3. Summary and Conclusions

Often, smooth experimental SC spectra generated in a PCF are presented in the literature, which are averaged over many thousands of single SC pulse spectra.These averaged SC spectra only reflect the spectral envelope controlled by the gain curve for the specific PCF and the parameters of the seed pulse used. However, to investigate the CARS process, which relies on the spatial and temporal overlap of single pump,

probe, and Stokes pulses those averaged pulses are not sufficient to characterize the complex field of a single CARS pulse. Here, SC pulses generated in a nonlinear PCF were simulated and subsequently investigated on a single pulse level for varying seed pulse lengths of 123 fs, 2.94 ps and 88 ps. For all investigated pulse lengths, non-compressible single SC were obtained with strong phase noise and stochastic amplitude profiles. After averaging over many single simulated SC pulses rather smooth spectra covering the full Raman shift range needed for subsequent broadband CARS generation are obtained for all investigated seed pulse lengths.
For the first time, broadband complex CARS fields were simulated and investigated for single pulses using the simulated single SC pulses. For all three seed pulse lengths, CARS bandwidths covering 4000 cm^{-1} were obtained, indicating that broadband CARS generation can be achieved with SC seed pulse lengths that vary over at least three orders of magnitude. The spectral resolution of the CARS spectra was best for the 88-ps pulses, but the spectral resolution of the CARS spectra for the 123-fs and 2.94-ps pulses proved to be fully sufficient, as it is determined only by the bandwidth of the pump/probe pulse used in the CARS process according to scheme A, By using a 2.94-ps probe pulse, whose bandwidth is comparable to typical bandwidths of vibrational resonances, the spectral resolution is not deteriorated. The simulated CARS spectra differed in the exhibited signal-to-noise ratio (SNR), which was best for the case of the 2.94-ps seed pulses and sligthly worse for the case of the 123-fs pulses. Because of the major experimental advantage, that only a single picosecond pulsed laser source is needed for the realization of broadband CARS spectroscopy with 2.94-ps pump/probe, as well as 2.94-ps seeded Stokes SC pulses, while providing high spectral resolution and best SNR, this is the preferred configuration for the subsequent hyperspectral CARS imaging experiments presented in chapters 6 and 9.

6 Picosecond-Hyperspectral CARS Imaging

Following the decision to use the 2.94 *ps*-pulses for the SCG and subsequent CARS generation motivated in chapter 5, in this chapter, first the concept of all ps-hyperspectral CARS is explained in brief. In the second part, all ps SC based broadband CARS spectroscopy is applied to the investigation of primordial broth samples in order to gain more insight into their complex and unknown molecular composition in an non-invasive way. Additionally, differences in the molecular composition between primordial broths prepared under different initial conditions are shown. The results from CARS measurements will be compared with other optical techniques providing additional information.
In the third part of this chapter, all ps SC based broadband hyperspectral CARS imaging is experimentally applied to the mapping of chemical and structural properties of molecules inside a single pollen grain. Here, the spectral fingerprints of the various biological constituents are to be revealed within a sub-micron focus spot. Furthermore, the distribution and location of each biological constituent is mapped in corresponding images, which can be related to one another.
The fourth part consists of the 3D hyperspectral CARS imaging of a single pollen grain. Here, the novel method is applied to extract volumetric and quantitative information on the dimension and amount of biological constituents based on their chemical signatures.

6.1. Concept of ps-Hyperspectral CARS

In order to generate a CARS field, it is necessary to have a pump, a probe and a Stokes field overlapping spatially and temporally on a sample. In conventional ps CARS approaches, narrowband pulses are used to excite and probe single vibrational resonances in a narrowband manner. In contrast, in the here presented ps-hyperspectral CARS approach one of the pulses is chosen to be a ps-generated

broadband SC pulse, enabling the excitation and detection of a full vibrational spectrum at once. If only the spectral domain is regarded, figure 6.1 (a) depicts the corresponding energy level diagram with narrowband pump and broadband Stokes fields with energies $\hbar\omega_P$ and $\hbar\omega_S$, respectively, which is in accordance to CARS scheme A discussed in section 3.3.2.

The high peak powers necessary for CARS are most easily generated by short laser pulses, instead of strong continuous-wave laser sources. If pulsed lasers are used, not only the overlap of all involved laser pulses in the three spatial dimensions needs to be guaranteed, but also their temporal overlap is crucial to generate CARS. Now, if ps-pulses are used as pump and probe pulses, and a fs-pulse is used as the Stokes pulse, the temporal overlap of the pulses is not matched. That means that the ps-pump/probe fields will be present in the sample at times where the fs-field has already vanished, and no CARS field is generated anymore. Figure 6.1 (b) shows a simplified time-frequency illustration of the pulses involved in this case, where the elliptical shapes depict time-frequency representations of the pump/probe, Stokes, CARS fields, and the vibrational excitation in green, red, blue, and dark red with their corresponding frequencies of ω_P, ω_S, ω_{AS}, and $\omega_P - \omega_S$, respectively. Next to the ellipse representing the coherent Raman excitation, a typical Raman spectrum is shown. Even if the higher peak intensity of the short fs-pulse compensates the worse temporal overlap by generating a more intense CARS signal, the parts of the ps-field present in the sample, where the amplitude of the short fs-pulse has already vanished, cannot contribute to the CARS signal generation. Those parts solely contribute to other nonlinear processes, which can possibly incur damage of the sample.

If instead of a fs-Stokes continuum pulse a broad ps-Stokes continuum pulse is used, the average temporal overlap with the ps pump and probe pulses is much better, as depicted in figure 6.1 (c). In this way, all temporal parts of the pulses can contribute to the CARS generation and do not contribute to unnecessary sample damage. Even if the SC pulses do not follow the ideal configuration of this simplified picture, as seen from chapter 5 the average intensity distribution within a ps-SC pulse provides a better match with the temporal duration of the ps-pump- and -probe-pulses when compared with a broad fs-pulse. Further advantages of the presented ps-hyperspectral CARS imaging concept are the use of a single ps-laser oscillator for the pump- and probe-pulses, as well as for the generation of the SC Stokes pulse (compare chapter 5), no need of additional pulse shaping of the probe pulse, and an intrinsic temporal overlap of all pulses once the optical paths are matched to each other.

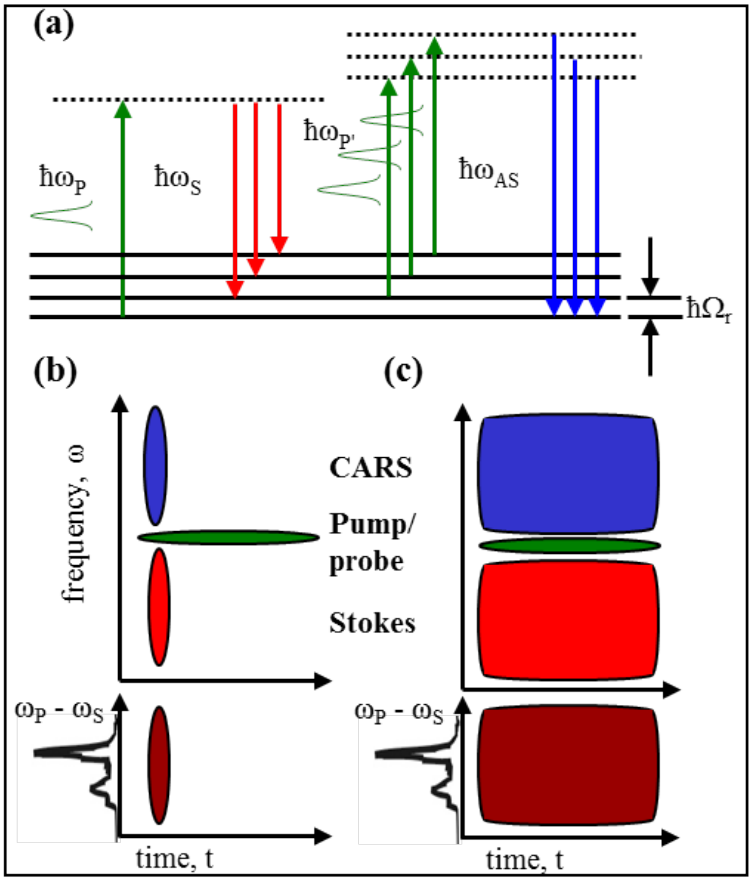

Figure 6.1.: (a) Energy level diagram for multiplex CARS according to scheme A. Time-frequency representation for (b) fs-hyperspectral CARS (blue) with a broad fs-Stokes pulse (red) and for (c) all ps-hyperspectral CARS (blue) with a ps-Stokes continuum pulse (red). In both cases transform-limited pump- and probe-pulses (green) are assumed. The induced Raman excitation (dark red) at frequency $\omega_P - \omega_S$ is also shown with a representative Raman spectrum (black curve).

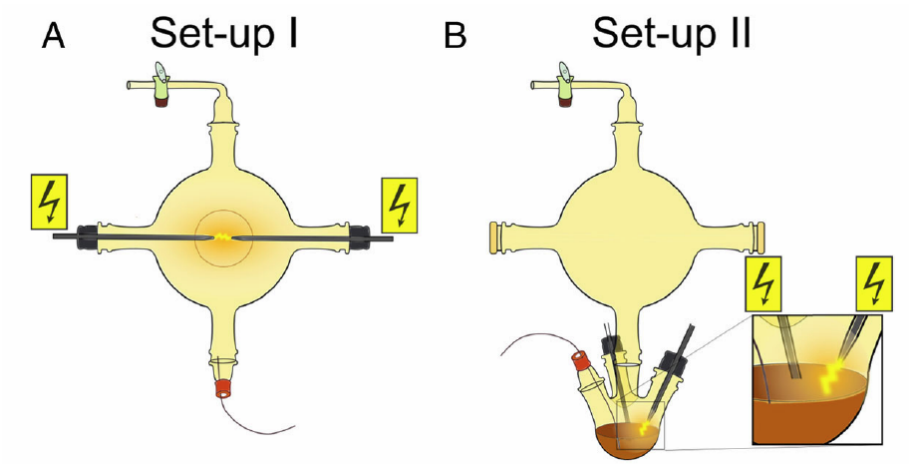

Figure 6.2.: Miller-type experimental setups for the generation of prebiotic broth samples $A1-$ and $B2+$ using the electrical discharge (A) in the gaseous phase and (B) onto the water surface. Taken from Scherer et al. [35].

6.2. Chemical Analysis of a Miller-Type Complex Prebiotic Broth

The ground-breaking experiments of Miller and Urey in the 1950s [57, 58], trying to generate complex molecules from very simple compounds and electrical discharges in a model system resembling what was believed to be the chemical atmosphere of the early earth, attracted a lot of attention. Even many complex molecules have been detected and have extensively been investigated by chemical analytical means, there is still an active interest in the understanding of the mechanisms and of the chemical dynamics behind their formation. Mass spectroscopy is one of the state of the art tools for investigating such primordial broth samples, as it can also be applied to the online-monitoring of the formation process [59]. Additionally, it was found that the chemical composition of the primordial broth is very sensitive to the experimental electrical discharge geometry. Depending whether the electrical discharge, providing the energy for the formation of the complex molecules, is applied in the gaseous phase or onto the liquid surface, as shown in the setups I and II in figure 6.2 (a) and (b), respectively, the composition of molecules in the primordial broths differ considerably [35]. Due to their complexities, a single analytical method cannot detect and identify all formed molecules. Therefore, it is advantageous to apply complementary spectroscopic methods based on non-invasive techniques for their investigation, revealing information on different levels, such as the molecular bonding, functional groups, and the involved atomic species.

Among the non-invasive vibrational spectroscopies, CARS spectroscopy is a very promising choice as it circumvents several limitations encountered in infrared ab-

sorption and spontaneous Raman scattering spectroscopies, which are perturbed by the high absorption of water, and the presence of an auto-fluorescence background masking the weak Raman bands of primordial broth, respectively. CARS spectroscopy, usually using excitation pulses in the near-infrared range, and detecting on the blue side of the excitation wavelength, is less sensitive to fluorescence background since the fluorescence is usually emitted on the red side of the excitation wavelength. Together with its high detection sensitivity, CARS spectroscopy is hence a promising tool for the investigation of this complex prebiotic broth solution.

In the following sections, results for the two different primordial broth samples designated as sample $A1-$ and sample $B2+$ (see section 4.7.2)from spontaneous Raman experiments, from CARS, and other multi-photon induced spectroscopies, and from UVVIS absorption experiments will be described and discussed. A short summary concludes this section.

6.2.1. Spontaneous Raman Spectroscopy

For the investigation of the vibrational signatures of primordial broth solutions, we first apply spontaneous Raman spectroscopy. Normalized spontaneous Raman spectra from sample $A1-$ (black curve) and sample $B2+$ (red curve) are shown in figure 6.3. The acquired spectra of both samples show a strong fluorescence background throughout the whole measured spectral range, already at low excitation powers. Sample $A1-$ exhibits a 30-times increased fluorescence intensity compared to sample $B2+$, which is in accordance with the higher absorption of this sample at the excitation wavelength of 532 nm (see figure 6.5 and further discussed in section 6.2.3). Unfortunately, this auto-fluorescence of the investigated solutions, which will be characterized in more detail in section 6.2.4, is masking the Raman-features in both samples. Even the attempt to bleach the fluorescence was not solving this problem.

In the spectra shown in figure 6.3, even the strong water bands centered at around 3400 cm^{-1} can barely be observed above the fluorescence background. In order to observe the weak Raman bands of the chemical components of interest at their low concentrations in the aqueous solutions, one way to avoid the fluorescence background is, for example, the detection of Raman scattering on the anti-Stokes side of the excitation wavelength. Another way is the excitation at longer wavelengths further into the red, where no fluorescence is excited. In our proposed CARS scheme, both approaches are fulfilled, and therefore it is very promising for achieving high quality vibrational spectra of primordial broth.

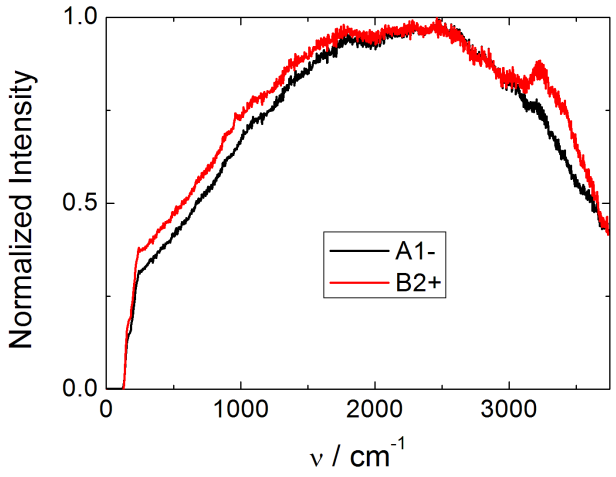

Figure 6.3.: Spontaneous Raman spectra of primordial broth solutions $A1-$ (black) and $B2+$ (red) obtained with a confocal Raman microscope under 532 nm cw-excitation wavelength and a few mW incident power at the sample. The acquisition time per spectrum was 100 ms. Shown are averages over 1000 spectra.

6.2.2. CARS Spectroscopy

Figure 6.4 (a) displays the normalized CARS spectra according to equation (4.1) of pure water and of the primordial broth sample $B2+$. The corresponding reconstructed $Im(\chi^{(3)}(\nu))$ spectra are shown in figure 6.4 (b). Figure 6.4 (c) compares the reconstructed $Im(\chi^{(3)}(\nu))$ spectra of samples $A1-$ and $B2+$ after the subtraction of the weighted $Im(\chi^{(3)}(\nu))$ spectrum of pure water. The normalized CARS spectra of sample $B2+$ resembles mostly the spectrum of pure water with only small distinct spectral differences at around 1000 cm^{-1} and in the C-H-stretching vibration region (see inset). The most dominant differences in the O-H stretching vibration region of water ranging from below 3000 cm^{-1} to over 4000 cm^{-1} are not considered here, as the interest of this studies lies in the chemical compounds of the solute and not of the solvent. In the $Im(\chi^{(3)}(\nu))$ spectra displayed in figure 6.4 (b), only small amplitude differences between the pure water spectrum and the spectrum of sample $B2-$ are visible. The inset shows again the amplified C-H-stretching vibration region, where distinct vibrational bands of the primordial broth solutions can be observed. After weighted subtraction with the $Im(\chi^{(3)})$-spectrum of pure water, the reconstructed $Im(\chi^{(3)}(\nu))$ spectra of both samples, displayed in figure 6.4 (c), clearly reveal the vibrational signatures of the solutes under investigation with very distinct spectral features between the sample $A1-$ and sample $B2+$.

The strongest spectral features of the sample $A1-$ are the peaks in the C-H-stretching vibration region, which are present in most organic compounds. The most intense peak appears at 2940 cm^{-1} with shoulders at 2890 cm^{-1} and 2970 cm^{-1}

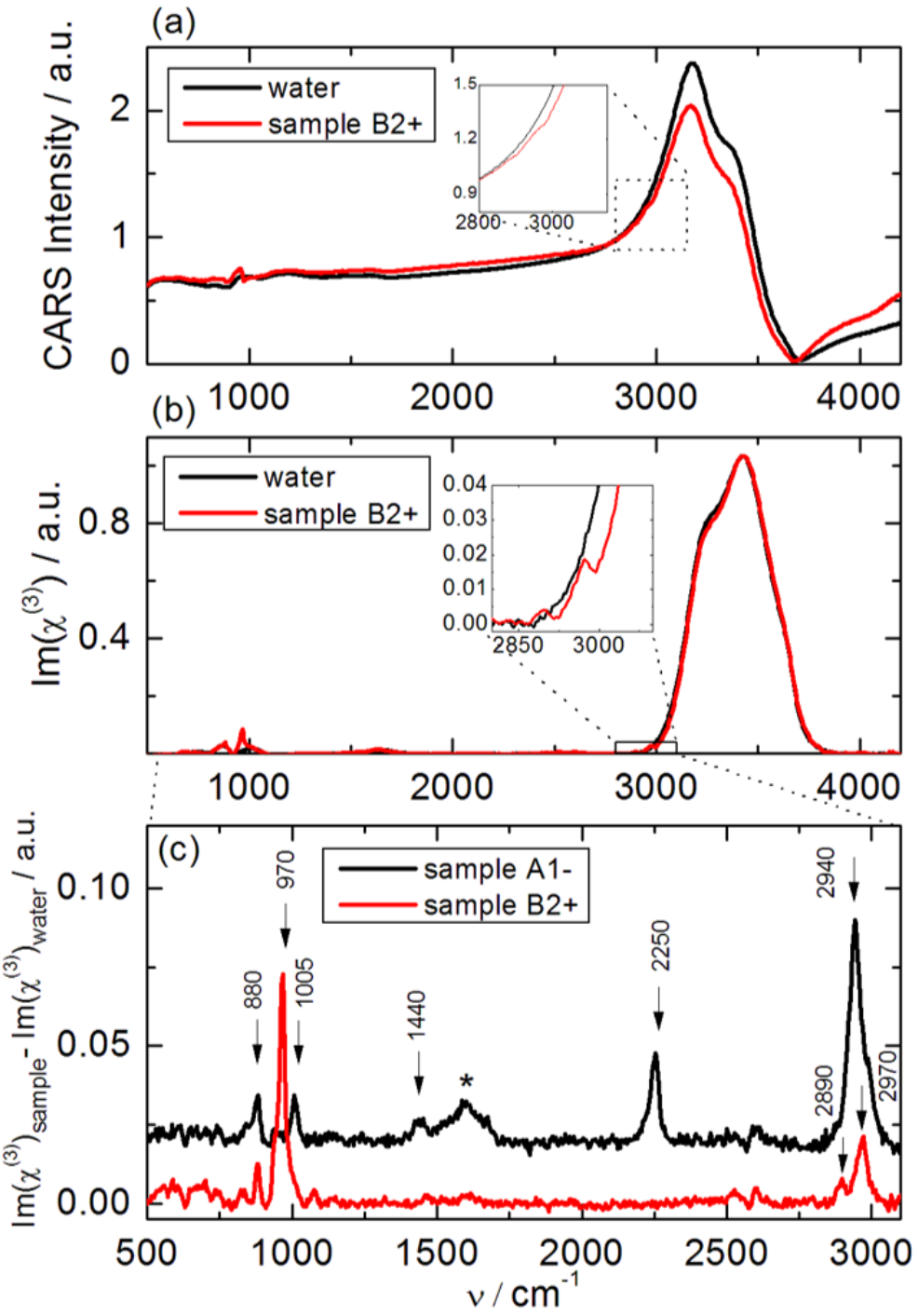

Figure 6.4.: (a) Normalized CARS spectra of water (black curve) and of aqueous solutions of primordial broth sample $B2+$ (red curve) after dividing by a non-resonant reference spectrum (compare euqation 4.1). (b) Reconstructed $Im(\chi^{(3)}(\nu))$-spectra of water (black curve) and sample $B2+$ (red curve). (c) $Im(\chi^{(3)}(\nu))$ of primordial broth samples $A1-$ (black curve) and sample $B2+$ (red curve) after subtraction of the weighted $Im(\chi^{(3)}(\nu))$ spectrum of water. The spectra are offset by 0.02. See text and table 6.1 for peak assignments. Insets: zoom into the spectral region of C-H-stretching vibrations. CARS spectra of samples $A1-$ and $B2+$ where recorded with total acquisition times of 12.5 s and 50 s, respectively. The incident average laser pump and Stokes powers at the sample where 60 mW and 13 mW, respectively.

Table 6.1.: Assignment of observed vibrational bands in primordial broth samples

ν [cm^{-1}]	Assignment	Observed in sample	Reference
880	aliphatic $C-N$ stretch alternative: *C-H wag vibration*	$A1-$ and $B2+$	[60]
970	tentative: C_xN_y *ring breathing*	$B2+$	[62, 63]
1005	ring breathing of phenyl residues	$A1-$	[60]
1440	scissoring of CH_2	$A1-$	[60]
2210	$R_{aromatic}$-$C{\equiv}N$	$A1-$	[60, 61]
2250	$R_{aliphatic}$-$C{\equiv}N$	$A1-$	[60, 61]
2890	symmetric CH_3 stretching	$B2+$	[60]
2940	asymmetric CH_2 stretching	$A1-$	[60]
2970	asymmetric CH_3 stretching	$B2+$	[60]

assigned to the asymmetric CH_2 stretching, symmetric CH_3 stretching, and asymmetric CH_3 stretching modes, respectively [60]. The most unique feature of the sample $A1-$ is the characteristic band at 2250 with a shoulder at 2210 cm^{-1}, which indicate the presence of aliphatic ($R_{aliphatic}$-$C{\equiv}N$) and aromatic ($R_{aromatic}$-$C{\equiv}N$) nitriles [60, 61]. Bands in the fingerprint region are identified as the scissoring mode of the CH_2 groups at 1440 cm^{-1}, the ring breathing mode of phenyl residues at 1005 cm^{-1}, and the aliphatic C-N stretching mode at 880 cm^{-1}. Alternatively, the band at 880 cm^{-1} could also correspond to the C-H wag vibrations of NH_2-monosubstituted benzene [60]. The broad peak around 1600 cm^{-1}, marked with $'*'$, is a residue from the incomplete subtraction of the water spectrum, and therefore is not further regarded. The most distinguished features in the spectrum of the sample $B2+$ compared to that of the sample $A1-$ is the lack of any spectral signature of $C{\equiv}N$ triple bonds at 2250 cm^{-1} and the strong and sharp peak at 970 cm^{-1}, which is tentatively assigned to breathing modes of small aromatic rings containing both C and N atoms [62, 63]. Therefore, the sample $B2+$ seems to contain more aromatic molecules than the sample $A1-$, which is consistent with the lack of aliphatic CH_2 groups. Similar vibrational spectral features have been observed for tholins [61, 62]. In table 6.1, the most important peaks with their tentative assignments are summarized.

6.2.3. UVVIS Absorption Spectroscopy

For the further investigation of the origin of the observed auto-fluorescence in the primordial broth samples, UVVIS absorption spectroscopy is applied to the samples,

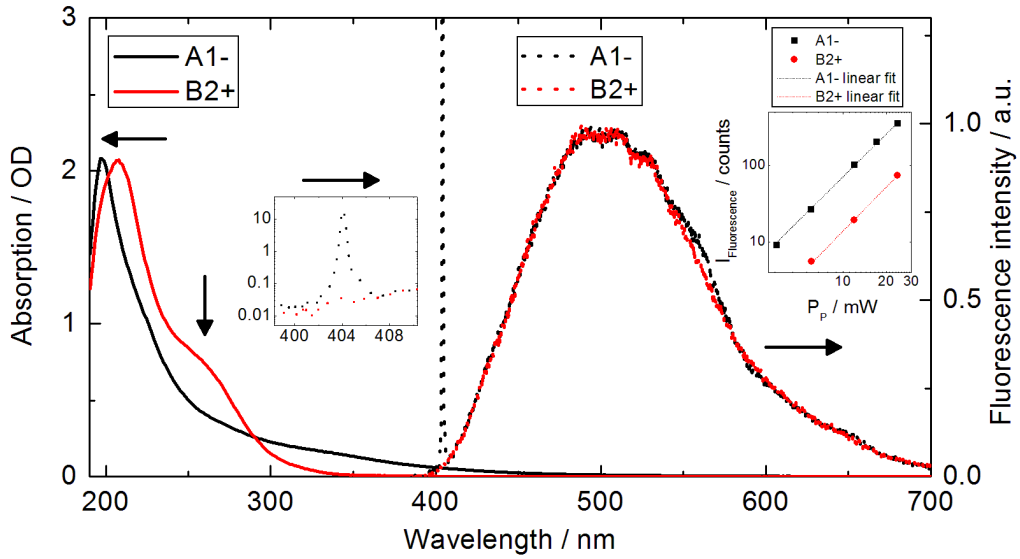

Figure 6.5.: UVVIS absorption spectra (solid lines) and normalized two-photon induced fluorescence (2PF) spectra (dotted lines) of primordial broth samples $A1-$ (black curves) and $B2+$ (red curves). Both 2PF spectra were excited with an average pump laser power before the objective lens of 60 mW, and integration times were 5 s and 2.5 s, respectively. The insets show the zoom the spectral range around 404 nm and the log-log power dependences of 2PF intensities for samples $A1-$ (black squares) and $B2+$ (red circles) together with their linear fit (dashed lines).

probing the optical absorption governed by the excitation of electronic states in the molecules. The objective here, is to answer the question, whether the strong differences in the observed auto-fluorescence intensity (compare section 6.2.1) is caused by the difference in absorption in the relevant wavelength range.

As shown in figure 6.5, UVVIS absorption spectra of both samples show a peak around 200 nm. Additionally, sample $B2+$ reveals an absorption shoulder at 260 nm, which is absent in sample $A1-$. However, the 200-nm absorption peak in the $A1-$ spectrum has a tail reaching further into the visible wavelength range.

The peak around 200 nm is attributed to an electronic absorption within a $\pi \rightarrow \pi*$ ${}^1B_{2u} \leftarrow {}^1A_{1g}$ transition [64]. The shoulder at 260 nm is associated with electronic absorption ${}^1B_{1u} \leftarrow {}^1A_{1g}$ from conjugated-π-orbitals of aromatic rings containing carbons and nitrogens [64, 65]. The long tail of the absorption band indicates a mixture of various different molecule contributions to the absorption peak and causing a higher absorption for sample $A1-$ at 532 nm. The latter can result in a much more efficient one-photon-fluorescence excitation at 532 nm in sample $A1-$. The long absorption tail therefore can explain the discrepancy in fluorescence

intensity observed for the different samples.

6.2.4. 2PF and SHG Spectroscopy

In order to investigate in more detail the auto-fluorescence observed in section 6.2.1, the two-photon induced fluorescence (2PF) of the primordial broth samples is studied. The normalized 2PF spectra of the two samples show only little spectral differences. However, the sample $A1-$ shows a 20-times increased 2PF intensity compared to that of sample $B2+$. As for the one-photon induced fluorescence excited at 532 nm (see discussion in section 6.2.1), these differences can be tentatively explained by a higher two-photon absorption cross-section for sample $A1-$ at the two-photon excitation wavelength of 808 nm. In the inset on the right side of figure 6.5, a measured dependence of the 2PF intensity on the incident pump laser power at the focus position in the sample is shown in a double-logarithmic representation for both samples. For these measurements, the fluorescence count rate spectrally integrated within a 3.7-nm interval around the peak wavelength at 500 nm is analyzed. Additionally, fit curves to the measured data are shown (black and red dashed curves) using a simplified fit model of the form $I_{Fluo} = A \cdot P_P^p$ (compare equation (3.40)). The resulting fit values are $A = 0.8965 \pm 0.0675$, $p = 1.8944 \pm 0.0311$ and $A = 0.1899 \pm 0.0251$, $p = 1.8744 \pm 0.0519$ for sample $A1-$ and sample $B2+$, respectively. The exponent p being just below two for both samples indicates that the fluorescence excitation is dominated by a two-photon process, for which an exponent of two is expected.
In the 2PF spectral data sets shown in figure 6.5, a very sharp peak at 404 nm, being an order of magnitude stronger than the 2PF signal is observed, while it is absent for the $B2+$ sample (see inset on the left side of figure 6.5). The intensity of this peak is not stable but strongly fluctuates over time throughout the measurement, which indicates that diffusion of a particle into and out of the focal spot causes this spectral feature at 404 nm.

6.2.5. Discussion

The one-photon cw-excitation at 532 nm does not hit a direct absorption peak of the primordial broth components, but lies within their long wavelength tails, which is a probable reason for the strong one-photon-induced fluorescence overwhelming their weak Raman scattering. The water bands slightly visible in the spontaneous Raman spectra of the primordial broth samples, can be compared with the water bands in the corresponding $Im(\chi^{(3)}(\nu))$ spectra before water subtraction. With this comparison, it becomes very clear that the vibrational bands much weaker than

the water band intensities cannot be observed in the spontaneous Raman spectra masked by the strong fluorescence background.

In contrast, the CARS spectra clearly allow the observation of distinct vibrational bands. Furthermore, depending on which set-up was used in the Miller-Urey-type experiment to produce the primordial broth solution, distinct vibrational features are observed, indicating their distinct chemical composition. In the set-up where the discharge happens in the gaseous phase (sample $A1-$), more nitriles and aliphatic CH_2 groups are observed. For the set-up with discharges onto the liquid surface (sample $B2+$), the lack of nitriles and aliphatic CH_2 bands and the presence of aromatic ring breathing bands for C and N moieties suggest a higher amount of aromatic molecules produced during the Miller-Urey experiment. This could be caused by the local evaporation of water and with this the abundance of oxygen in the formation process of more complex molecules [35].

The strong vibrational band observed at 970 cm^{-1} in the reconstructed $Im(\chi^{(3)}(\nu))$ spectrum of sample $B2+$ indicates that the discharge onto the water surface produces more aromatic C_xN_y-ring structures. Such rings or double rings are present for example in nucleic acids. Supporting evidence for this interpretation comes from the UVVIS absorption spectra. Based on observations by Oro et al. [65], who assigned the absorption shoulder at 260 nm to the absorption of adenine, which has a C_5N_4-double-ring structure, molecules with a similar structure are good candidates as a source of the 970 cm^{-1} band.

The stronger 2PF-intensity of sample $A1-$ compared to that of sample $B2+$ qualitatively agrees well with the stronger optical absorption observed in the UVVIS spectra, if we assume that the two-photon absorption cross-section follows the same spectral behavior as the one-photon absorption (see figure 6.5).

In parallel, mass spectroscopy measurements where performed on the same samples and executed by Scherer et al. [35]. Although, not presented in this thesis, one main result was the detection of a polymeric compound in the sample $B2+$ [35]. Nevertheless no signatures of polymeric compounds are found in the $Im(\chi^{(3)}(\nu))$ spectra reconstructed from our CARS experiments. The discrepancy between the results obtained with different methods is most probably attributed to the fact that mass spectroscopy is extremely sensitive to exactly polymeric compounds due to their higher ionization efficiencies [35], whereas CARS spectroscopy exhibits no exclusive specificity to these compounds. Nevertheless, the correlated presence of the polymers and the aromatic C_xN_y-rings detected by both complementary methods leads to the hypothesis that there might be a catalytic interaction between those molecular structures [35]. Supporting evidence for this hypothesis comes from the observation that on the other hand, the abundance of nitriles and the simultaneous

disappearance of the vibrational signature of aromatic C_xN_y ring structures observed in the $Im(\chi^{(3)}(\nu))$ spectra are correlated with the absence of the polymeric species for the corresponding samples, as revealed by mass spectroscopy.

The intense and sharp spectral feature at 404 nm is most probably due to SHG of the pump laser pulses, originating from small diffusing particles still present in the primordial broth solution. For those particles to effectively generate SHG they need to consist of non-centrosymmetric structure [3] made of molecular complexes present in the primordial broth.

6.2.6. Summary and Conclusions

Spontaneous Raman spectroscopy was tested to non-invasively characterize the primordial broth solutions, but it clearly showed to be not applicable to these samples due to their overwhelming auto-fluorescence background.

In contrast, the investigation of the primordial broth samples proves to be feasible with CARS spectroscopy, where excitation in the near-infrared wavelength range and anti-Stokes detection are exploited. Characteristic vibrational signatures for samples generated under different conditions of the Miller-Urey experiment are observed. The sample generated with discharges onto the water surface exhibits molecules with a higher degree of aromaticity, whereas the sample generated with discharges into the gaseous phase has a higher amount of nitriles and aliphatic C-H compounds. The assignment of the 970 cm^{-1} peak to aromatic C_xN_y ring structures indicates the presence of nucleic acids, which find supporting evidence in the corresponding UVVIS absorption spectra. Regarding the origin of the observed auto-fluorescence background, the correlation between the UVVIS absorption and the corresponding 2PF spectra suggests the presence of chemical components with both high one-photon and two-photon absorption cross-sections in the long wavelength tail of the electronic transitions.

The comparison with mass spectroscopy for the same samples reveal that CARS spectroscopy detected a high abundance of amides in sample $A1-$, whereas this was not observed with mass spectroscopy. On the other hand, an abundance of polymeric compounds was revealed by mass spectroscopy, which could not be detected with CARS spectroscopy. These studies show how important it is to use complementary spectroscopic methods for a thorough investigation of unknown complex samples.

Freely diffusing non-centrosymmetric particles possibly consisting of non-dissolved primordial broth crystallites, are potentially causing the observed SHG signals. These particles may consist of complex molecules formed in the primordial broth experiments and agglomerated during the lyophilization process.

After proving the feasibility of using all-ps hyperspectral CARS to the investigation of mixtures of complex molecular compositions in an unknown solution, its combination with imaging will be explored in the following section.

6.3. Application to 2D Chemical Imaging of Single Cyclamen Pollen Grains

One of the big advantages of hyperspectral CARS is the coherent enhancement of the samples intrinsic Raman response. In this section, these advantages are exploited for performing fast and label-free hyperspectral CARS imaging of a biological sample with apriori unknown composition. Single pollen grains are taken as an example for this demonstration of chemical mapping their sub-cellular structure with a high spatial resolution.

Spontaneous Raman microscopy [66], one- and two-photon induced fluorescence microscopy [67, 68] and multiplex CARS microspectroscopy [69] have been previously applied to the investigation of pollen grains. In comparison to spontaneous Raman imaging, where also the intrinsic vibrational response is probed, the higher detection sensitivity in CARS imaging enables fast chemical mapping with an intrinsic 3D-sectioning capability, while having a low level of auto-fluorescence.

Single pollen grains of cyclamen flowers suspended in water between two cover glasses are investigated with all-ps hyperspectral CARS imaging. In figure 6.6 (a), an exemplary bright field image of cyclamen pollens is shown.

A two-dimensional (2D)-hyperspectral CARS data set is acquired by sample scanning the equatorial x-y-plane of the pollen grains and recording full CARS spectra from 500 cm^{-1} to over 3715 cm^{-1} within 874 spectral pixels for each spatial pixel with a spatial pixel dwell time of 100 ms. The average pump and broadband Stokes powers on the sample are 25 mW and 13 mW, respectively.

In figure 6.6 (b) the image shows the integrated $Im(\chi^{(3)})$ amplitude in the C-H-stretching vibration region extracted from the reconstructed hyperspectral CARS data set, which resembles an image typically acquired with conventional narrowband SRS imaging [70]. The images shown in figures 6.6 (b) and (c) have the spatial dimensions of (30.3×17.2) μm^2 and (90×51) $pixels$.

In the following, the spatial differences in chemical compositions represented by spatial differences in the relative amplitude ratios of characteristic vibrational bands are analyzed with uni-variate and multivariate approaches.

6.3.1. Multivariate Analysis

The hyperspectral data set, consisting of the reconstructed $Im(\chi^{(3)})$-spectra for each image pixel, is subjected to a K-means cluster multivariate analysis [41, 71, 72], where the spectra are clustered into a predefined number of groups according to their spectral similarities. For each cluster, an average spectrum is calculated, and for the image pixels a specific cluster color is assigned. The resulting cluster map is displayed in figure 6.6 (c) together with the corresponding cluster-spectra in figures 6.6 (d) and (e). The same color is used for each cluster spectrum and for their corresponding pixels in the cluster map.

While in figure 6.6 (b) the integrated *C-H* stretch image only reveals the pollen grain wall and two intercellular structures with lower amplitude contrast, the cluster map shows the same pollen structures, but now based exclusively on the chemical information encoded in the full $Im(\chi^{(3)})$ cluster spectra, disregarding differences in the overall spectral amplitude. Now the cluster spectra together with the cluster map can be used to evaluate the molecular composition of each pollen component and to identify the individual constituents.

In figure 6.6 (e) the zoom into the fingerprint region of the $Im(\chi^{(3)})$ cluster spectra is shown in order to emphasize the spectral differences between them.

The red cluster defines the pollen cytoplasma which is rich on proteins. Characteristic spectral features are here the phenylalanine ring-breathing mode at 1004 cm^{-1}, the amide I band at about 1645 cm^{-1} with its shoulder around 1600 cm^{-1}, and the broad overlapping bands between 1200 cm^{-1} and 1400 cm^{-1} mostly assigned to the amide II mode [60], which are all indicators for proteins.

The green cluster defines the two nuclei inside a pollen grain, which represent the vegetative cell nucleus and the generative cell nucleus. The vegetative cell nucleus is usually bigger but less dense in nucleotides than the generative cell nucleus [73]. The corresponding green cluster spectrum looks very similar to the red cluster spectrum with differences present in the region above 800 cm^{-1}, where vibrational spectral bands of nucleic acids reside [60]. Another difference between red and green cluster spectra is the shoulder at 1490 cm^{-1}, which is assigned to the ring-breathing mode of the nucleotides adenine and guanine. The differences of the nuclei cluster spectrum to the blue, light blue, and yellow cluster spectra are most pronounced in the spectral region around 1600 cm^{-1}, where the amide I band resides. Also, the absence of the phenylalanine ring-breathing mode at 1004 cm^{-1} and the higher relative amplitude in the range between 1200 to 1350 cm^{-1} are characteristic for the green cluster spectrum of the nuclei.

From the cluster map it is very clear that the blue cluster represents the outer shell (exine) of the pollen grain. The most distinct vibrational signature in this cluster

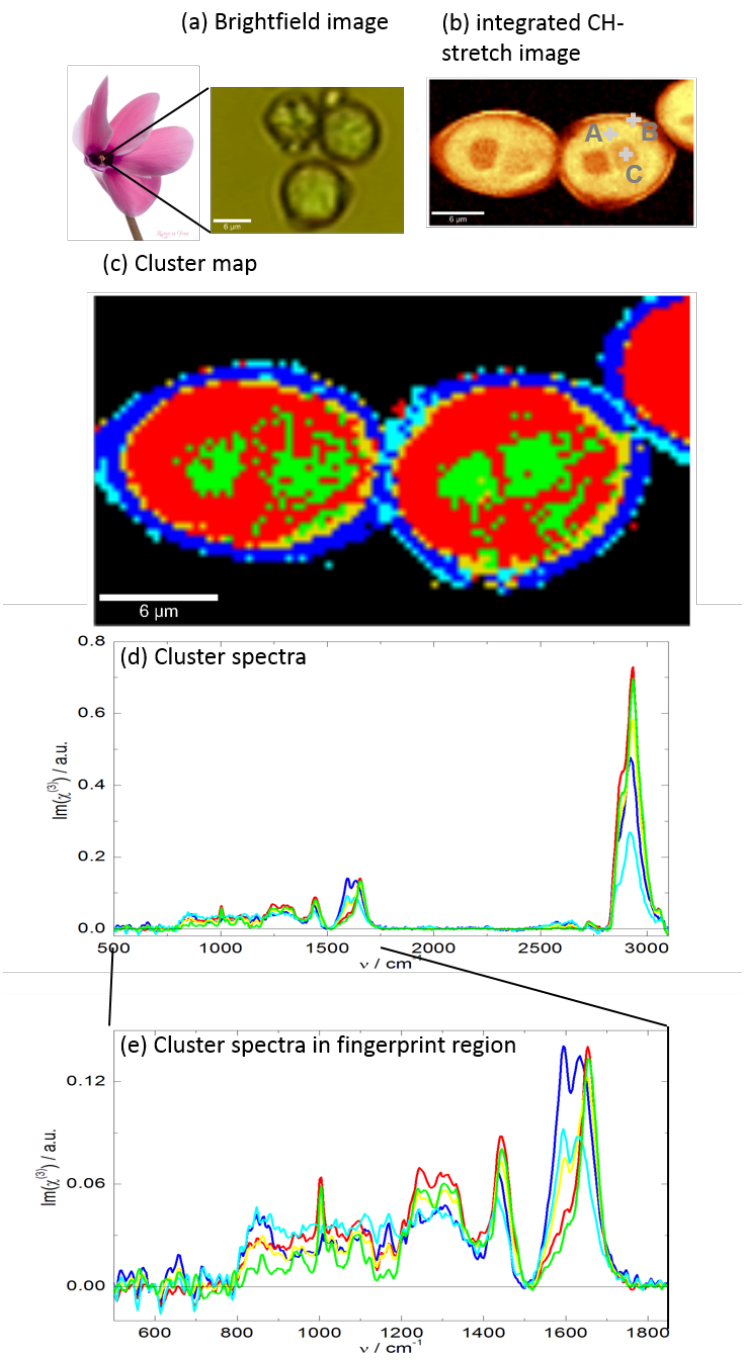

Figure 6.6.: (a) Bright-field image of cyclamen pollen grains, (b) integrated $Im(\chi^{(3)})$ amplitude image in the C-H-stretching vibrational region from 2750 to 3150 cm^{-1} of cyclamen pollen with three positions marked by the crosses in the cytoplasm, the nucleus, and the pollen shell, labeled A, B, and C, respectively, (c)K-means cluster map of the same sample region shown in (b), (d) corresponding cluster spectra with the same color code used in (c), (e) zoom into the fingerprint region of the cluster spectra shown in (d).

spectrum is the strong band at 1595 cm^{-1}, which is assigned to the phenolic ring-breathing mode of a bio-polymer, called sporopollenin, that is known to form the protective shell around the pollen grain [74].
The yellow cluster seems to be distributed along the edge between the exine (blue cluster) and the inner cytoplasm (red cluster). As the pollen grain not only exhibits an outer shell (exine) but also a thin inner shell (intine), the yellow cluster was on a first thought assigned to this inner shell. However, no reliable spectral Raman signature could be found, so that the yellow cluster spectrum is considered to represent a simple mixture of the blue and of the red cluster spectra for those image pixels, where both exine and cytoplasm are filling the focal volume.
The light blue cluster is mostly located in the pits and at the outer edges of the exine. Also here, no unique spectral features are found, so this cluster spectrum is considered to represent a mixture of exine, the surrounding water, and a bit of the pollen cytoplasma.

6.3.2. Univariate Analysis

While the cluster analysis is a great tool to separate the spectra and their corresponding spatial pixels no information about the relative amount of the different molecular components can be made. For example, mixtures of different components in the same pixel are always assigned to the strongest component. Having identified different parts of the single pollen grain, and having established characteristic spectral features for proteins, nucleic acids and the exine based on cluster analysis, next a more quantitative analysis tool is used to analyze the same hyperspectral data set. The univariate analysis uses the $Im(\chi^{(3)})$ amplitude of the vibrational bands specific for the different components to create maps that represent their relative number densities inside the focal volume. In contrast to the cluster maps with a digital definition of the cluster for each image pixel, the univariate analysis yields a continuous definition of amplitudes for each image pixel that are proportional to the relative number density of vibrational modes throughout the sample.
In figure 6.7 (a), the $Im(\chi^{(3)})$ spectra from three different positions in the single cell marked in figure 6.6 (b) by the crosses labeled A, B and C are shown. Characteristic Raman shift features used for the generation of chemical maps are marked in red, green, and blue at 1004 cm^{-1}, 1490 cm^{-1}, and 1595 cm^{-1}, respectively. The corresponding reconstructed $Im(\chi^{(3)})$-amplitude maps of the single pollen grains are shown in figure 6.7 (b) to (d), which were obtained by integrating each $Im(\chi^{(3)})$ pixel spectrum over the spectral ranges from 989 to 1020 cm^{-1}, from 1470 to 1495 cm^{-1}, and from 1572 to 1612 cm^{-1}, respectively.

For example, the maps shown in figure 6.7 (b) is a good representation for the distribution of proteins in the pollen grain based on the band at 1004 cm^{-1} assigned to the ring-breathing mode of phenylalanine. A homogeneous protein distribution within the pollen grain is found. Except for the most outer part of about 1 μm thickness, only negligible variations of the phenylalanine signature are observed.
The nucleic acids distribution in the two nucleus structures of the pollen grains [73] is shown in figure 6.7 (c), where the $Im(\chi^{(3)})$amplitude at around 1490 cm^{-1} was integrated. In figure 6.7 (d) the cell wall is visualized based on the distribution of the integrated $Im(\chi^{(3)})$ amplitude around 1595 cm^{-1}, which is assigned to a ring breathing mode of sporopollenin [74]. Especially for the pollen grain to the right, the characteristic pits in the exine are clearly visible here. In this exine there is no sign of the 1004 cm^{-1} amplitude of phenylalanine (compare figure 6.7 (b)).
In figure 6.7 (e) a red-green-blue (RGB) overlay image of the three monochrome images in figures 6.7 (b), (c), and (d) is shown where the colors of each image are added according to their respective weight. For example, for a pixel spectrum that contains amplitudes of spectral features of both, the cytoplasm (red color), and nucleic acids (green color), their mixing results in a yellow color for that image pixel in the RGB image. This is the case for the yellow pixels in figure 6.7 (e) representing the nuclei, where both features mix within the same spatial pixels.
Comparing the internal pollen grain structure revealed in the RGB-overlay image with the known structure of pollen grains [73], all major constituents of the pollen have been identified and visualized in a label free manner: the protein containing cytoplasm, the exine with the pits (allowing the pollen tube to grow), and the most characteristic feature for pollen - the two nuclei - where one is the regenerative and the other is the pollen tube nucleus respectively.

6.3.3. Summary and Conclusions

Hyperspectral CARS imaging was applied to the noninvasive investigation of individual pollen grains allowing for the visualization of the distributions of their constituents and of their dimensions based on their chemical compositions.
The analysis of the recorded hyperspectral data set with a multivariate approach, using a K-means cluster analysis, has enabled an evaluation without a priori knowledge of the pollen sample. As a result, its constituents, the exine, the pollen plasma and both pollen nuclei could be visualized, and their characteristic spectral Raman features could be identified.
The subsequent univariate analysis of the same data set has provided the additional information about the quantitative distributions of the identified chemical compo-

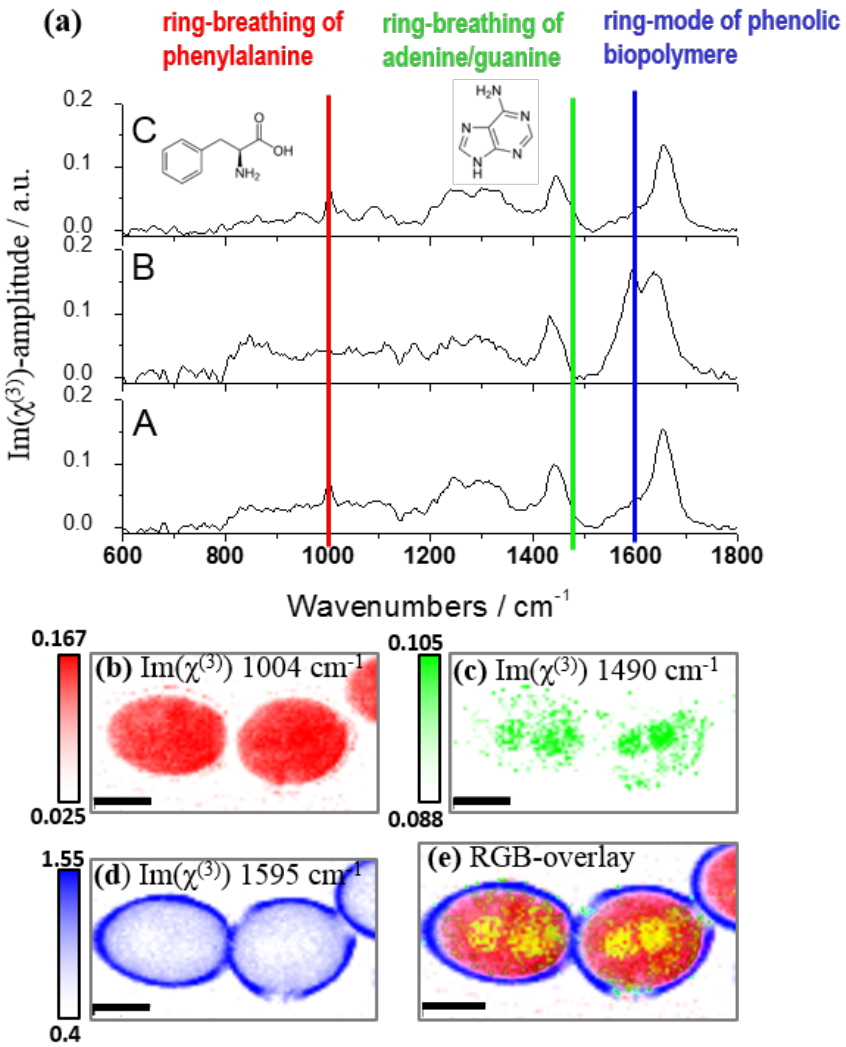

Figure 6.7.: (a) Reconstructed $Im(\chi^{(3)})$ single pixel spectra for three different image positions A, B, and C marked with crosses in figure 6.6 (b). The colored horizontal lines mark the spectral positions used for extracting the $Im(\chi^{(3)})$ amplitude maps shown in (b) to (d). Next to the red and green lines are chemical structures of exemplary molecules that exhibit the characteristic spectral features. (e) RGB overlay image of the color-coded integrated $Im(\chi^{(3)})$ amplitude maps shown in (b) to (d). The scale bar in all images is 6 μm long.

nents based on the $Im(\chi^{(3)})$ amplitudes being proportional to the relative number densities of vibrational modes. From that, the mixing and coexistence of proteins, nucleic acids, and phenolic biopolymers within a single pollen grain is visualized in a quantitative manner.

In conclusion, this application of hyperspectral CARS imaging has demonstrated its high potential for non-destructive and chemically sensitive analysis of the internal sub-structures of biological specimens.

6.4. Application to 3D Hyperspectral CARS and 2PF Imaging of Single Daisy Pollen Grains

To obtain the information about the three dimensional distribution of chemical species inside a complex sample, the intrinsic 3D sectioning capabilities [1] of hyperspectral CARS imaging is explored and volumetric chemical imaging of a single pollen grain suspended in water between two cover glasses is demonstrated next.

A Daisy pollen grain is chosen due to its craggy 3D structure, which made it a standard sample for demonstrating 3D sectioning in prior nonlinear optical imaging as for example 2PF imaging [67, 68].

The Daisy pollen is scanned in all three spatial dimensions with $100 \times 108 \times 88$ pixels in the form that consecutive 2D-images at different depths throughout the pollen are taken. A single spatial 3D-pixel here has a pixel size of 226 nm in all three dimensions. The effective pixel spectrum integration time is 3 ms. In total, 950400 spectra were acquired in 127 minutes. The average laser powers on the sample are 60 mW and 30 mW for the pump and the broadband Stokes pulses, respectively. Consecutively to the data acquisition for each 3D pixel, the $Im(\chi^{(3)})$ spectrum is reconstructed according to the previously described procedures in section 4.8.2. The 3D hyperspectral data set of the daisy pollen is analyzed in a similar way as the 2D data set of the cyclamen pollen described in section 6.3. Additionally to the Raman spectral features, the daisy pollen grains exhibit auto-fluorescence [67]. Supplementary experiments described in appendix A.2 confirmed that this observed auto-fluorescence is induced by a two-photon-excitation process. A typical measured single 2PF spectrum (green line) is shown in figure 6.8 (a), which was recorded inside the exine at the position marked by the cross and labeled A in the corresponding integrated 2PF intensity map at the equatorial plane of a single pollen grain displayed in figure 6.8 (c). The 2PF spectrum is recorded with the pump beam only incident on the sample with average power $P_P = 63\ mW$, and an integration time of 30 ms, and with a grating position centered at the wavelength 520 nm to

show the full fluorescence peak with its maximum at 510 nm. The fluorescence peak position and its spectral shape correspond to the characteristic fluorescence of FAD [75], see appendix A.2. To generate the 2PF map in figure 6.8 (c), the fluorescence was integrated within the spectral range, hatched in the spectrum shown in figure 6.8 (a).

For comparison in figure 6.8 (a), the raw CARS pixel spectra recorded at position A (black line) and at position B (blue line), inside the pollen exine and outside in water, respectively, are displayed along with a 2PF spectrum normalized to the intensity of the 2PF background present in the raw CARS pixel spectrum. The fluorescence spectrum only barely overlaps spectrally with the CARS spectrum, so that CARS and fluorescence intensities can be easily spectrally separated in the further analysis.

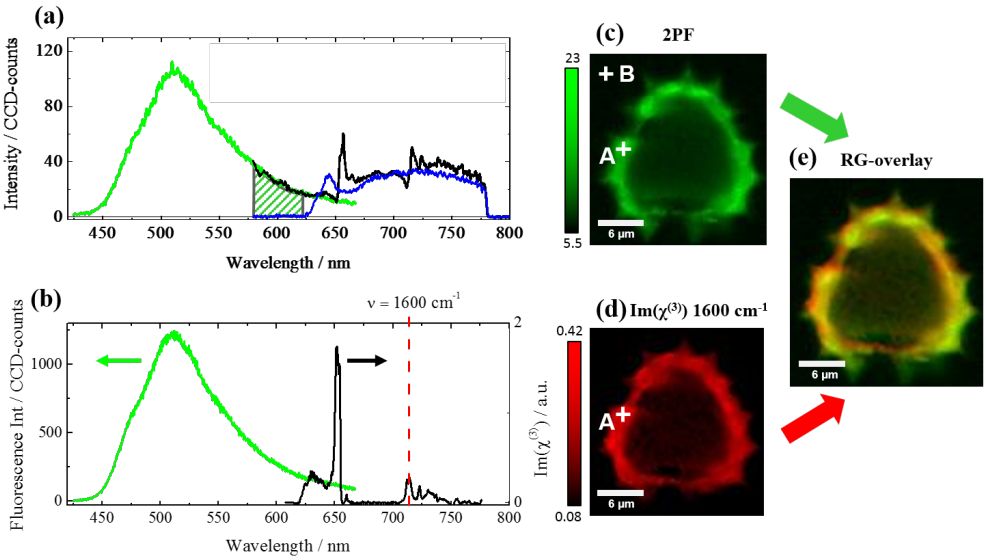

Figure 6.8.: Simultaneous hyperspectral CARS and 2PF imaging of the equatorial plane of a single daisy pollen grain. (a) Raw CARS (black curve) and 2PF (green curve) spectra of the pollen exine shell measured at the position A marked in (c). For comparison a raw CARS water spectrum (blue curve) measured at the position Bis also shown, (b) reconstructed $Im(\chi^{(3)})$ (black curve) and 2PF (green curve) spectra from the exine at position A, (c) 2PF intensity map, (d) $Im(\chi^{(3)})$-amplitude map at 1600 cm^{-1}, (e) RG-overlay image of the color-coded 2PF and $Im(\chi^{(3)})$ images.

In the further analysis, for each CARS pixel spectrum, a weighted subtraction of the pure fluorescence spectrum recorded at position A is performed, where the 2PF background contribution integrated over the hatched region is used to determine the weighting factor. This simple fluorescence background correction of each CARS pixel spectrum is allowed because due to the incoherent nature of the auto-fluorecence, there is no interference with the CARS emission on the detector.

Figure 6.8 (b) displays the reconstructed $Im(\chi^{(3)})$-amplitude spectrum for pixel A (black curve) inside the exine together with its 2PF pixel spectrum. The $Im(\chi^{(3)})$ amplitude at the spectral position marked with a red dashed line is now used to generate contrast in the image shown in figure 6.8 (d). As the 2PF image shown in figure 6.8 (c), the $Im(\chi^{(3)})$-amplitude image at 1600 cm^{-1}, reveals the same exine shell of the pollen grain. This comparison suggests that the sporopollenin itself is the cause for the auto-fluorescence in this daisy pollen grain. However, small differences in the 2PF and $Im(\chi^{(3)})$ maps are clearly seen in the RG-overlay image shown in 6.8 (e). For example, in the upper left part of the pollen there seems to be a particle exhibiting stronger fluorescence and therefore appearing greener. Also, the two lower spikes show higher fluorescence as the remaining ones. The conclusion here is that the fluorescent component in the exine is not homogeneously distributed in comparison to the sporopollenin. This information could only be extracted by doing a correlative study with both the hyperspectral CARS and the 2PF signals recorded for the same pollen simultaneously.

In figure 6.9, the results of an univariate spectra analysis of a hyperspectral CARS imaging data set for an entire single daisy pollen grain are visualized as an isosurface representation for the three characteristic spectral features of the chemical components already identified in section 6.3.2. Using the same color-code as before, the $Im(\chi^{(3)})$ amplitudes shown in blue, red, and green represent the sporopollenin in the exine, proteins in the cytoplasm, and nucleic acids in the nuclei, respectively. In addition, the 2PF intensity of flavoproteins is shown in yellow, using a high threshold for the isosurface (topmost 5 % as compared to figure 6.8 e)) in order to display the strong fluorescing particles which where present at several parts on the exine of the pollen as well as inside the pollen. The weaker auto-fluorescence originating from most parts of the shell of the pollen is therefore not explicitly shown here. The upper front quarter of the spherical pollen is cut off, providing an insight into the inner structure of the pollen.

The visualized very spiky structure of the exine is characteristic for pollen of this family of flower. The thickness of the sporopollenin shell amounts to (0.9 ± 0.3) μm. The inner part of the pollen is rather homogeneously filled with proteins rich on phenylalanine. Both nuclei are embedded in the pollen cytoplasm close to its shell and have sizes in the range from (2.5 to 4) μm in all dimensions. The fluorescing particles rich on FAD molecules have sizes in the range of a few micrometers or even below.

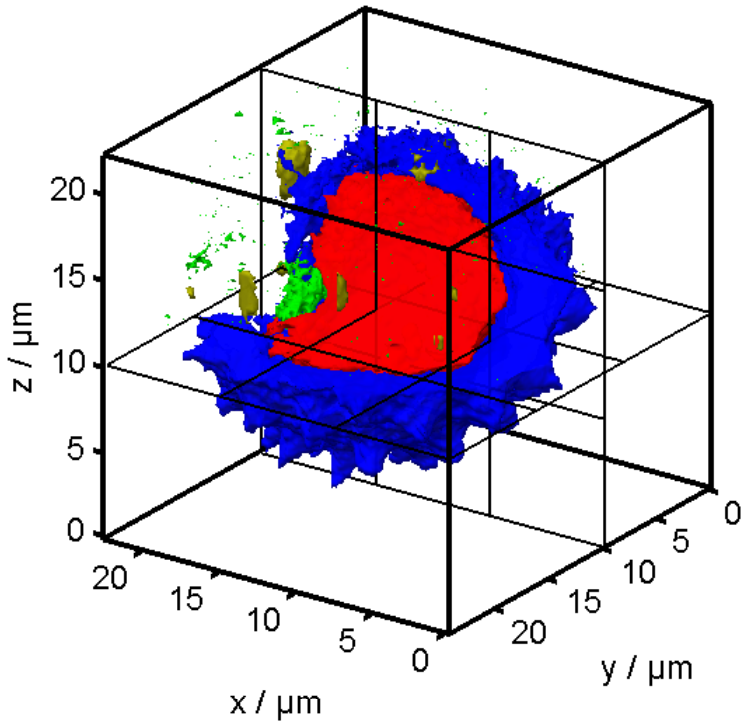

Figure 6.9.: 3D chemical map extracted from a 3D hyperspectral CARS imaging data set of a single unstained daisy pollen grain. Shown here are isosurfaces of reconstructed $Im(\chi^{(3)})$ amplitudes of characteristic Raman signatures for sporopollenin (blue), protein (red), nucleic acids (green) and of the endogenous 2PF from FAD molecules (yellow).

6.4.1. Summary, Conclusions, and Outlook

Simultaneous 3D hyperspectral CARS and 2PF volumetric imaging of an entire single daisy pollen grain was successfully demonstrated without the need for any special sample preparation. While the reconstructed $Im(\chi^{(3)})$ amplitude data set allows the extraction of the chemical information about individual pollen constituents based on their characteristic vibrational spectral features, the simultaneous detection of 2PF allows for the extraction of additional information about endogenous fluorescent species within the pollen. Based on this intrinsic multi-modal imaging capability, colocalizations of sporopollenin, and flavoproteins in the exine shell and of phenylalanine rich proteins and nucleic acids inside the nuclei of the pollen grain are observed.

Additionally, quantitative volumetric information of all identified chemical constituents of the pollen grain is provided, when proper deconvolution algorithms are applied, which offer the potential to monitor and quantify pollen developments as described by Gabarayeva and Grigorjeva [76].

7 Interferometric Hyperspectral CARS Imaging with a Broadband Spontaneous FWM Source

Hyperspectral CARS imaging being a coherent technique is accessible for coherent enhancement of the CARS field generated in the sample. This enhancement, which was first shown in 1980 [77] in the gas phase, is provided by the interference of an external local oscillator (LO) field and can be controlled through the amplitude and relative phase of this field.

In the first realization of interferometric CARS imaging, phase-preserved narrowband pump, Stokes and signal pulses were used, provided by an optical parametric oscillator OPO [18, 78]. The narrowband LO field for the interferometric CARS imaging experiment is then either generated by a separate NR-CARS process [18] or produced in the OPO as the signal beam [78]. In the first realization of broadband heterodyne detected CARS by Evans et al. [79], the generation of the required broadband LO field was again generated by a NR-CARS process in a parallel beam path. In that case, the same pulse powers and tight focusing optics are needed for the local oscillator field generation as for the CARS field generation in the sample.

In a different approach by von Vacano et al. [80], a single broadband laser pulse is phase and amplitude shaped by using a spatial light modulator. Here, a narrowband part of the pulse spectrum is consecutively used as the probe field. The LO field here is inherently present by the CARS field, generated by the parts of the broadband pulse spectrum, which are not phase controlled. The LO field can therefore not be independently controlled in this approach.

Later, Littleton et al. [81] realized a different form of hyperspectral interferometric CARS imaging using circular polarized and linear polarized fields for the narrowband pump/probe and the broadband Stokes fields, respectively. Detecting the two perpendicular polarization components of the CARS signal each in 45 degrees, relative to the polarization direction of the incoming Stokes field, and their subsequent

subtraction enable direct access to the linear vibrational response of the sample, which is comparable to its spontaneous Raman spectrum. Here, this broadband interferometric CARS imaging approach is limited to probe only a very specific combination of polarization tensor elements.
In this chapter, a new approach to interferometric hyperspectral CARS imaging is presented, where broadband signal and idler fields produced in a PCF by broadband spontaneous FWM [2, 25] are providing the local oscillator and the Stokes fields, respectively. The temporal delay between the signal field and the CARS field from the sample enables the full control over their phase relation, and hence is the most general approach to interferometric hyperspectral CARS imaging being realized. In the first section 7.1, the idea of our new approach of interferometric hyperspectral CARS imaging is outlined. In section 7.2, the generation of broadband correlated photon pairs in a spontaneous FWM source in a PCF are characterized. Subsequently our realization of interferometric hyperspectral CARS detection and imaging is shown on exemplary samples in section 7.3. Finally section 7.4 will provide a short summary, conclusion and outlook of this chapter.

7.1. The Broadband Interferometric CARS Idea

In contrast to our previous realization of picosecond hyperspectral CARS imaging, presented in chapter 6, where the goal was predominantly to generate a SC in a PCF broad and intense enough to provide a Stokes continuum pulse only, here PCF SC generation needs to be restricted to the regime dominated by spontaneous FWM. With the appropriate choice of the PCF and seed pulse parameters, two equal photons of the seed pulse combine in a nonlinear medium and are converted in a pair of signal and idler photons of higher and lower energy than the seed photons, respectively. As a result of this process, additionally to the idler continuum a signal continuum, mirrored at the seed wavelength is generated on the blue side of the seed pulse (see section 3.1.3).
For the realization of interferometric hyperspectral CARS imaging, the intrinsic phase relation between the broadband signal and idler photons provided by spontaneous FWM in a PCF is exploited. Here, the idler field provides the Stokes field and the signal field acts as a local oscillator field, interfering with the CARS field generated in the sample. To evaluate the phase relationship between the broadband signal and idler fields, provided by the spontaneous FWM source, their mutual non-linear interaction in a $\chi^{(2)}$-active medium via a SFG process is exploited. The corresponding energy level diagrams for the FWM process, the phase correlated SFG process, and the broadband interferometric CARS process are shown figure

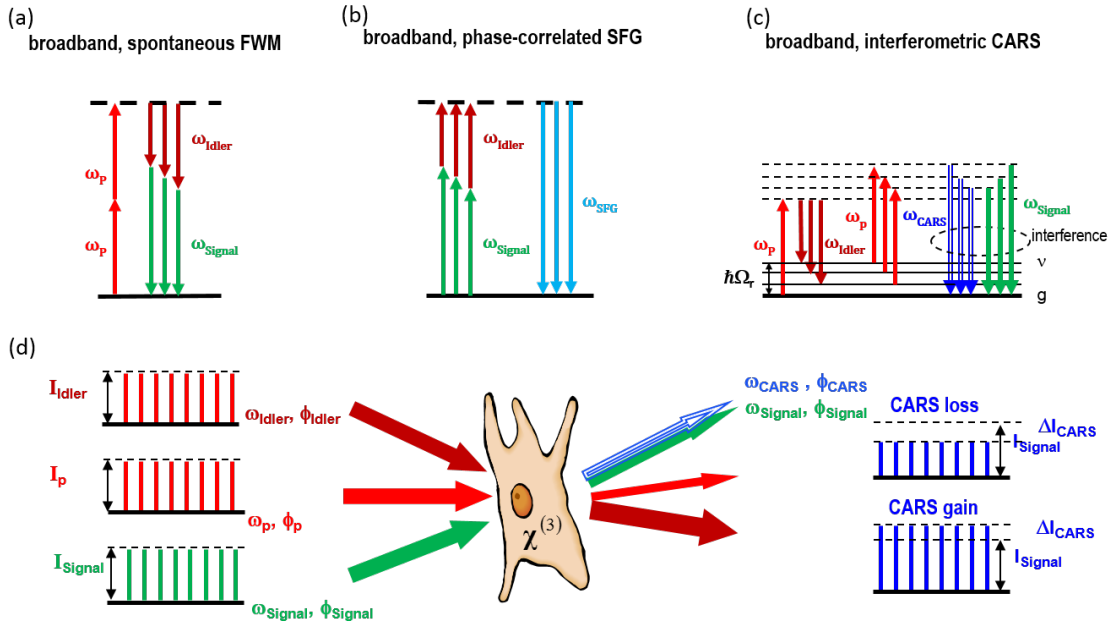

Figure 7.1.: Energy level diagrams of (a) the broadband spontaneous FWM process for random signal-idler-pairs, (b) the broadband SFG process for the phase correlated photon pairs, (c) the interferometric hyperspectral CARS process in resonance with a vibrational state at $\hbar\Omega_r$ using the same pairs of signal and idler photons generated in (a). (d) Schematic illustration of interferometric CARS occurring in a nonlinear Raman-active medium described by $\chi^{(3)}$ (e.g. a living cell)[82].

7.1 (a), (b), and (c), respectively. In figure 7.1 (d), the interaction of the three incoming, pump, signal, and idler pulse trains with the sample, characterized by $\chi^{(3)}$ is schematically illustrated for the interferometric CARS experiments [82]. The temporally and spatially overlapped pair of pump and idler pulse trains generate a CARS signal pulse train (I_{CARS}) in the sample, which interferes with the signal pulse train and experiences a gain or loss by ΔI_{CARS} depending on the phase difference $\Delta\phi = \phi_{AS} - \phi_{Signal}$. In order to enable interference, it is crucial that all spectral components of the signal continuum pulse retain a fixed phase relation to the corresponding idler continuum pulse.

The theoretical concept of interferometric hyperspectral CARS imaging is described in section 3.3.3. The experimental realization of the broadband spontaneous FWM source and of the interferometric hyperspectral CARS imaging setup are depicted in sections 4.1 and 4.3.

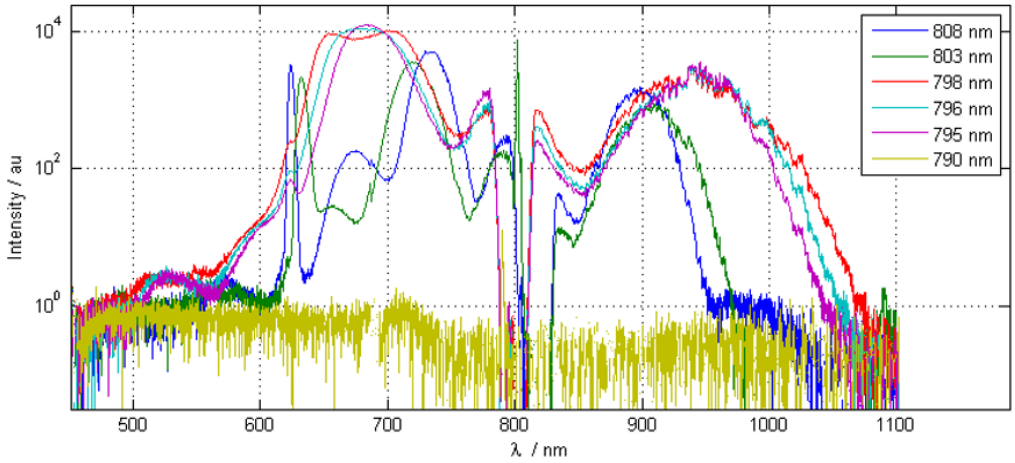

Figure 7.2.: Measured broadband FWM spectra generated in the PCF NL-PM-800 with 2.37 ps seed pulses at different seed wavelengths, and at a fixed average seed power of 364 mW. Shown are averages over 100 spectra recorded at each grating center position of 570 nm, 800 nm, and 1000 nm. The integration time for a single spectrum was 10 ms

7.2. Performance of the FWM Source of Broadband Phase-Correlated Photon Pairs

For a nonlinear PCF with a very low and flat dispersion curve, having at least one zero dispersion wavelength (ZDW), the phase-matching conditions for FWM, equations (3.9) and (3.10), can be fulfilled for a very broad spectral range, so that the broadband FWM signal and idler side lobes are generated [2]. This is the case when the PCF is seeded in the anomalous dispersion regime close to the ZDW. The optimum seed laser wavelength is identified by recording a series of spectra for different seed wavelengths at a fixed seed power of 364 mW, as shown in figure 7.2. Starting with the seed wavelength at 808 nm used in the previous CARS experiments (see chapter 6), at least three FWM lobes can be seen on the blue side of the seed wavelength. On the red side of the seed wavelength the decrease of the spectrally dependent quantum efficiency of the CCD camera towards higher wavelengths allows only to observe one FWM lobe. Tuning the seed wavelength towards the ZDW of the PCF results in merging and broadening of those FWM lobes. At 798 nm, the FWM lobes seem to be merged to one. At 796 nm and 795 nm, only one FWM side lobe is generated on each side of the seed wavelength. Seeding the fiber with shorter wavelength, inside its normal dispersion regime, results in a much weaker SC and FWM generation, which are negligible for the seed powers used. Our 2.37 ps seed pulses, tuned to 796 nm, have been identified as the best option in order to achieve a very broad contiguous spontaneous FWM generation in the NL-PM-800 used.

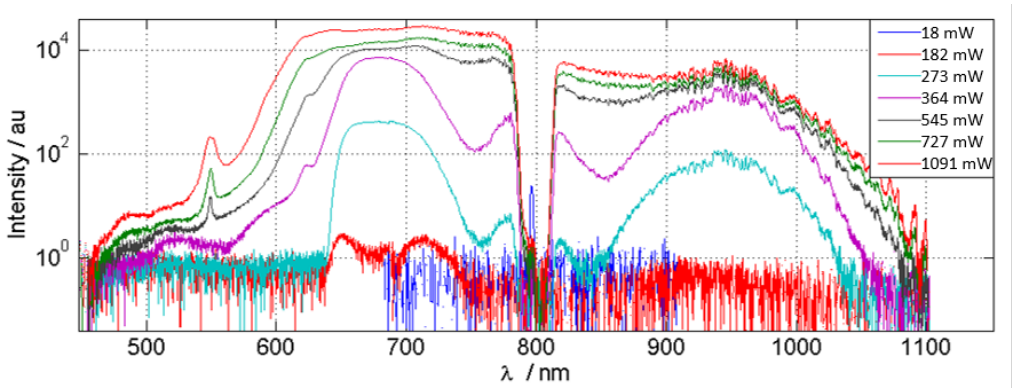

Figure 7.3.: Measured broadband spontaneous FWM spectra generated in the PCF NL-PM-800 with 2.37 *ps* seed pulses at different average powers and a fixed wavelength of 796 *nm*. The power levels given in the legends indicate the powers before the incoupling objective of the PCF. Shown are averages over 100 spectra recorded at each grating center position of 570 *nm*, 800 *nm*, and 1000 *nm*. The integration time for a single spectrum was 10 *ms*.

After choosing the optimal seed wavelength, the power regime for best spontaneous FWM generation is identified by recording a power series at a fixed seed wavelength of 796 *nm*. On the one hand, an intense idler field should be generated in order to provide a strong enough Stokes field for CARS generation in the sample. On the other hand, the seed power needs to be small enough in order to not generate too many additional non-linear signals, which would disturb the pure spontaneous FWM photon-pair correlation [83]. In the recorded power series of spontaneous FWM spectra, shown in figure 7.3, the evolution of the broadband FWM side lobes is nicely exhibited. For low average seed powers below a threshold of around 182 mW, there is basically no spontaneous FWM or other SC signals detectable. Starting at 182 mW, spontaneous FWM lobes can be observed, whose intensities increase with increasing seed power. Above 364 mW the spontaneous FWM side lobes become broader and converge to a maximum intensity plateau. The change of the spectral shape thereby indicates that additional non-linear processes contribute to this spectral broadening process. Therefore, an optimal average seed power of 364 mW is chosen for our spontaneous FWM source of broadband phase correlated photon pairs.

Very similar to a transform-limited ultra-broad (ultra short) laser pulse, the phase of all spectral components in the pair of spontaneous FWM signal and idler pulses, is preserved. This spectral coherence applies only for a specific signal photon interacting with the idler photon that was generated as its partner in the spontaneous FWM process in the first place. For all other combinations of signal and idler photons throughout the broad spectral range of the spontaneous FWM lobes, signal

and idler photons are not phase correlated and can only interact incoherently. In order to further test the bandwidth of correlated signal and idler fields generated in our spontaneous FWM source, it is not enough to measure the spectrum of the side lobes. The degree of coherence of the broadband spontaneous FWM signal and idler fields can be evaluated based on the SFG signal generated by recombination of the signal and idler fields under tight focusing conditions in a $\chi^{(2)}$-active non-linear crystal placed at the sample position. Following references [24, 25], the SFG signal is described by equations (3.36) and (3.37) with a phase according to equation (3.35). For the case of non-correlated signal and idler fields, where any spectral component of the idler can interact incoherently with any other component of the signal beam, a broad and weak SFG spectrum centered at around half the seed wavelength with a spectral width in the order of magnitude of that of the initial individual FWM lobes is generated. If phase correlated signal and idler photons coherently combine, the resulting SFG wavelength is always exactly half the seed wavelength. In other words, if the phase correlation is preserved at the sample position, a much narrower SFG spectrum, only limited by the width of the seed pulses, is obtained. In practice, both narrowband and broadband SFG spectral contributions are present, whose intensity ratio is used as an indicator for optimizing the dispersion compensation in our setup, as well as for measuring the spectral coherence of the spontaneous FWM side lobes in the first place [25, 84].

Figure 7.4 shows a measured SFG spectrum, recorded when the broadband signal and idler fields are temporally and spatially overlapped in the $\chi^{(2)}$-active crystal. This spectrum exhibits the highest ratio of coherent to incoherent SFG contributions for the best achieved combination of the coherence of the spontaneous FWM source and the best dispersion compensation, as described in 4.3. Here, the broadband incoherent SFG peak spreads out from below 390 nm up to more than 415 nm. The asymmetry is attributed to the reduced quantum efficiency of the CCD camera and the reduced transmission of the optics before the camera for wavelengths below 400 nm. The narrowband coherent SFG peak has a FWHM of only 2 nm and a much higher intensity than the broadband incoherent SFG contributions. The ratio of the narrowband to the broadband SFG peak intensities amount to 20.7.

7.3. Implementation of Interferometric Hyperspectral CARS

After all parameters have been defined and optimized, now interferometric hyperspectral CARS spectroscopy is implemented using the setup described in section

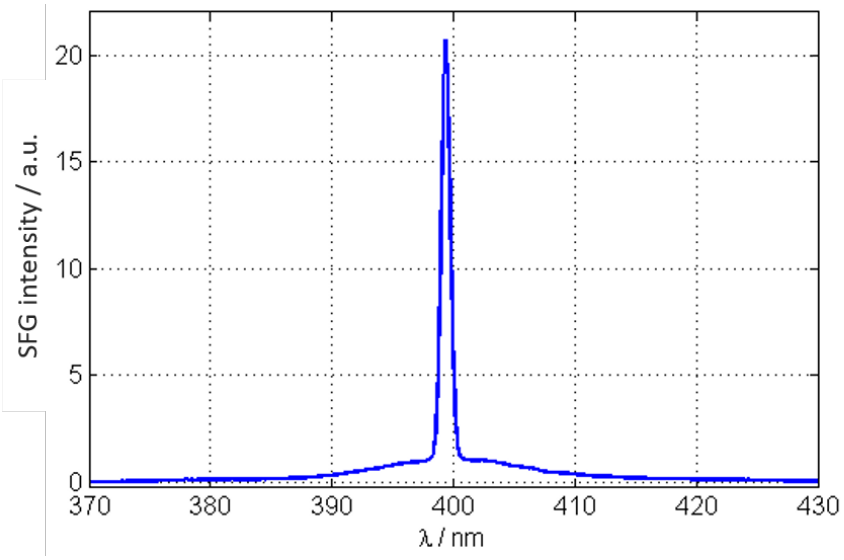

Figure 7.4.: Characterization of the broadband signal and idler pulses generated by our spontaneous FWM source by SFG spectroscopy. The SFG signal is normalized to one at the maximum of the broad incoherent contribution. The intensity ratio of the coherent to incoherent SFG peaks is 20.7 : 1. The integration time was 50 ms.

4.3. Next, the first results are presented for interferometric CARS spectroscopy and imaging applied to dedicated test samples.

7.3.1. Broadband Interferometric CARS Spectroscopy

In figure 7.5, raw spectra of interferometric CARS of neat benzaldehyde are shown for different phase differences $\Delta\phi$. Additionally, the pure signal beam spectrum (purple curve) ($\propto k_{SR} |E_{signal}|^2$) and a standard multiplex CARS spectrum (yellow curve) ($\propto |E_{CARS}|^2$) are shown for comparison. The signal spectrum expands from about 680 nm to 730 nm, corresponding to a Raman shift from 2143 cm^{-1} to 1135 cm^{-1}, respectively. In the interferometric CARS spectra, two strong vibrational resonances can be observed at around 1704 cm^{-1} and 1604 cm^{-1}, which are coherently superimposed on the broadband signal spectrum. The shape of these bands strongly depend on the phase difference $\Delta\phi$. For zero and π phase difference, the bands have a dispersive line shape. For $\Delta\phi = \frac{\pi}{2}$ the bands have a shape similar to the spontaneous Raman bands. For $\Delta\phi = -\frac{\pi}{2}$ the bands have a shape similar to the spontaneous Raman bands but with inverted amplitude. The cases resembling the spontaneous Raman bands with positive and negative amplitude correspond to the CARS gain and CARS loss processes, respectively, as depicted in figure 7.1 (d). Comparing the standard multiplex CARS spectrum with the interferometric CARS spectra for $\Delta\phi = \pm\frac{\pi}{2}$, it can be noted that the interferometric CARS spectra do not show the dispersive line shapes characteristic for vibrational CARS resonances, and

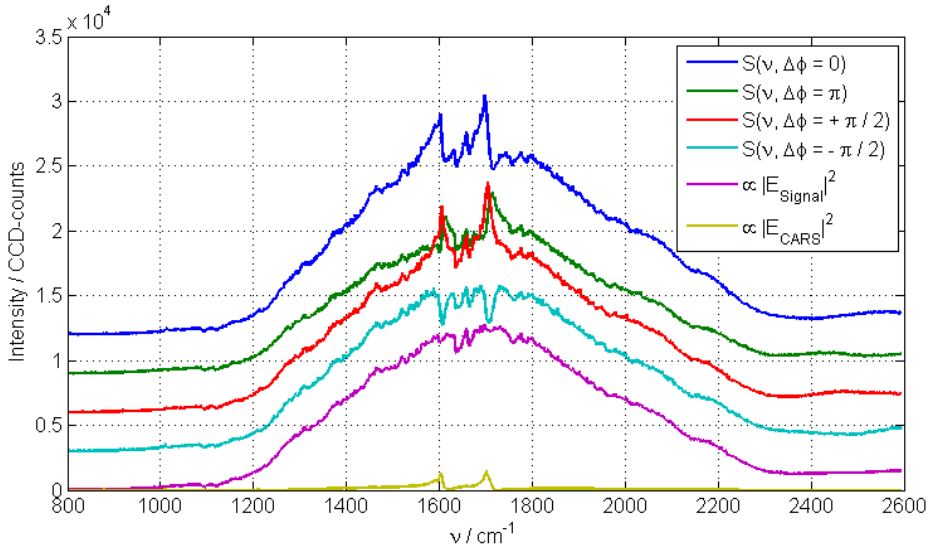

Figure 7.5.: Measured raw spectra of interferometric CARS for neat benzaldehyde at different phase differences $\Delta\phi$ between the signal and CARS fields. The interferometric CARS spectra are offset by 3000 CCD-counts each. The integration time per pixel were 50 ms. The average pump, Stokes, and signal powers at the sample position are 56.6 mW, 0.1 mW and approximately 0.0005 mW, respectively. For comparison, the corresponding standard multiplex CARS spectrum ($\propto |E_{CARS}|^2$) and the pure signal spectrum ($\propto |E_{Signal}|^2$) are also shown.

their resonance peak amplitudes are more intense, showing an amplification of the CARS fields from the sample.

In the following we will use the two interferometric CARS resonances at $\Delta\phi = 0$ and $\Delta\phi = \frac{\pi}{2}$ in combination with the signal beam spectrum in order to extract the real and imaginary spectra of the sample according to the procedure described in section 4.8.4. Figure 7.6 (a) shows the result in glass, where no vibrational resonances are observed. In the lower part of figure 7.6 (a), the corresponding phase spectrum of glass is shown, which exhibits the expected near constant phase over the whole available spectral range. The flat spectra of the extracted real and imaginary parts of $\chi^{(3)}$ extend from around 1200 cm^{-1} up to around 2300 cm^{-1}, which can be used for heterodyne detected broadband CARS measurements. This spectral range is in agreement with the observed range of the broad signal pulse spectrum (see figure 7.5). The spectral range, marked in figure 7.6 (a) can be considered as the transform-limited equivalent spectral range, within which all spectral field components have the same phase and a noteworthy amplitude. The considered range stretches over about 45 nm and would represent a Fourier-transform-limited pulse of about 29.3 fs.

In the upper part of figure 7.6 (b), the extracted real and imaginary parts of the $\chi^{(3)}$ response of neat benzaldehyde are shown. The extracted real part $Re(\chi^{(3)})$ spectrum exhibits well defined dispersive line shapes for all vibrational bands of the benzalde-

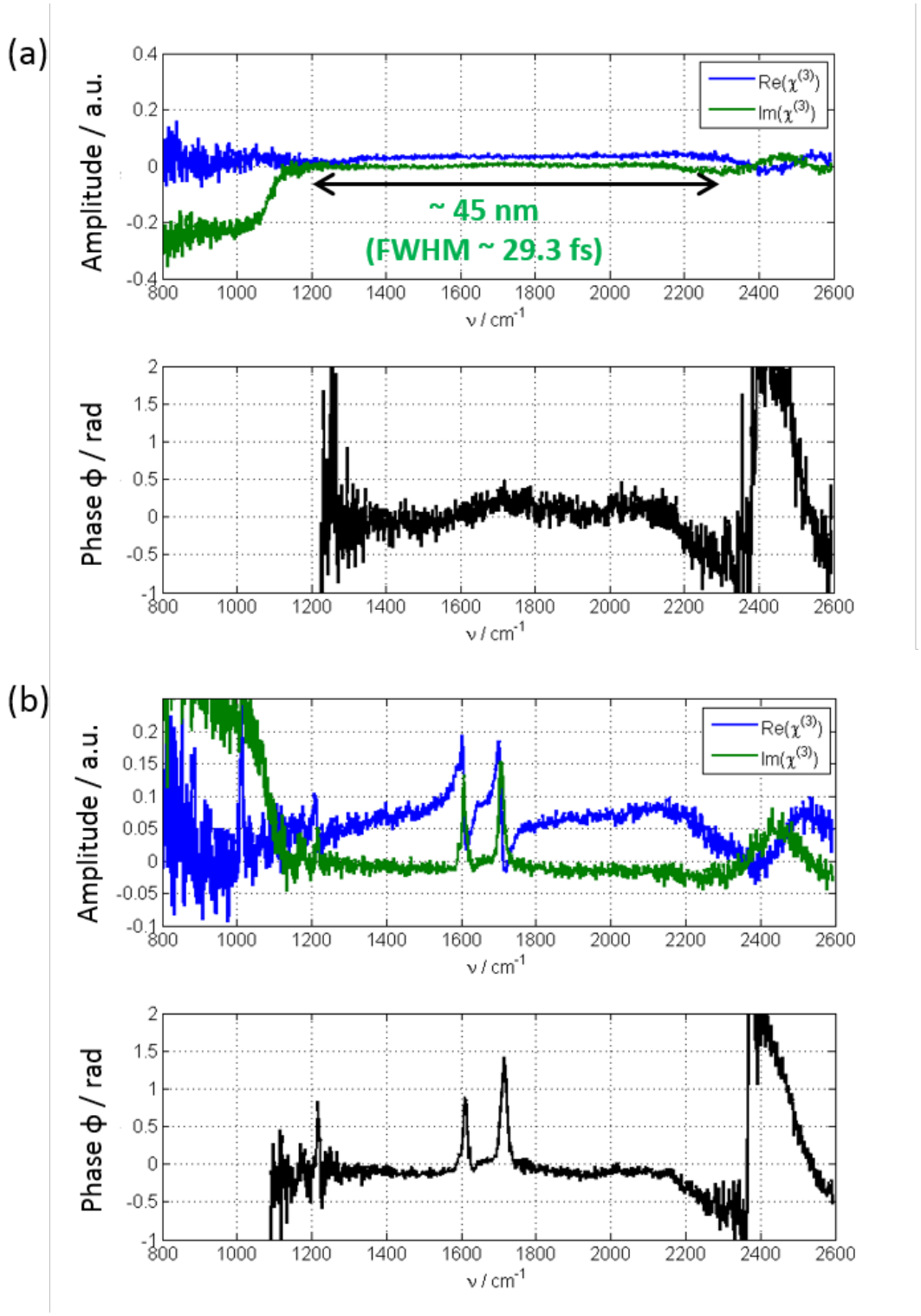

Figure 7.6.: (a) Real part $Re(\chi^{(3)})$ (blue curve), imaginary part $Im(\chi^{(3)})$ (green curve), and phase of the $\chi^{(3)}(\nu)$ spectrum (black curve) as extracted from the interferometric CARS spectra of (a) glass and (b) neat benzaldehyde. The integration time per interferometric CARS spectrum was 50 ms. The average pump, Stokes and signal powers at the position of the sample were 56.6 mW, 0.1 mW, and approximately 0.0005 mW, respectively.

hyde covered. The imaginary part $Im(\chi^{(3)})$ spectrum of all four detected vibrational resonances residing within the range from 1160 cm^{-1} up to 1704 cm^{-1} exhibit Lorentzian line shapes (similar to the spontaneous Raman spectral line shapes). In the lower part of figure 7.6 (b), the corresponding phase spectrum of neat benzaldehyde is shown, exhibiting the clear characteristic spectral phase signatures around the vibrational resonance frequencies.

7.3.2. Interferometric Hyperspectral CARS Imaging

After having successfully demonstrated the direct experimental extraction of the complex $\chi^{(3)}$ spectrum for neat benzaldehyde within a sub-femtoliter sample volume, now our novel approach of interferometric hyperspectral CARS can be combined with imaging. As a microscopic test sample, a single benzaldehyde droplet with a diameter of 12 μm at a glass surface embedded in water is chosen. The seed wavelength for the spontaneous FWM source and the pump/probe pulse in the CARS process is tuned to 800 nm, in order to cover a CARS spectral range from 940 cm^{-1} to 2034 cm^{-1}. Even the bandwidth is slightly reduced, this way more vibrational resonances of the benzaldehyde are probed in this spectral range.

Figures 7.7 (a) and (b) show images of the benzaldehyde droplet, where the extracted $Im(\chi^{(3)})$ and $Re(\chi^{(3)})$ amplitudes of the vibrational resonance at 1704 cm^{-1} (marked by an arrow in figure 7.7 (d)) of benzaldehyde were used to generate image contrast, respectively. When the imaginary part $Im(\chi^{(3)}(\nu))$ is measured, the amplitude at the maximum of the benzaldehyde band at 1704 cm^{-1} gives a positive image contrast for the benzaldehyde droplet, whereas the surrounding water has no resonance at that Raman shift, as can be seen in figure 7.7 (a). When the phase difference is changed so that the real part $Re(\chi^{(3)}(\nu))$ is measured, then the dispersive line shape of the vibrational band results in a negative amplitude at 1704 cm^{-1}, and a negative image contrast is measured within the droplet, as seen in figure 7.7 (b).

In order to directly demonstrate the influence of the phase difference between the signal and the CARS fields on the image contrast, $\Delta\phi$ is now periodically modulated while scanning the same benzaldehyde droplet. The resulting image of the droplet is shown in figure 7.7 (c), where the same amplitude at 1704 cm^{-1} is used to generate contrast. Figure 7.7 (d) and (e) display the $Im(\chi^{(3)}(\nu))$ and $Re(\chi^{(3)}(\nu))$ spectra, extracted for two representative image pixels, where the phase differences are $\Delta\phi = \frac{\pi}{2}$ and $\Delta\phi = 0$, respectively, inside the benzaldehyde droplet. The typical complex vibrational resonances of benzaldehyde are reproduced as previously shown in figure 7.6.

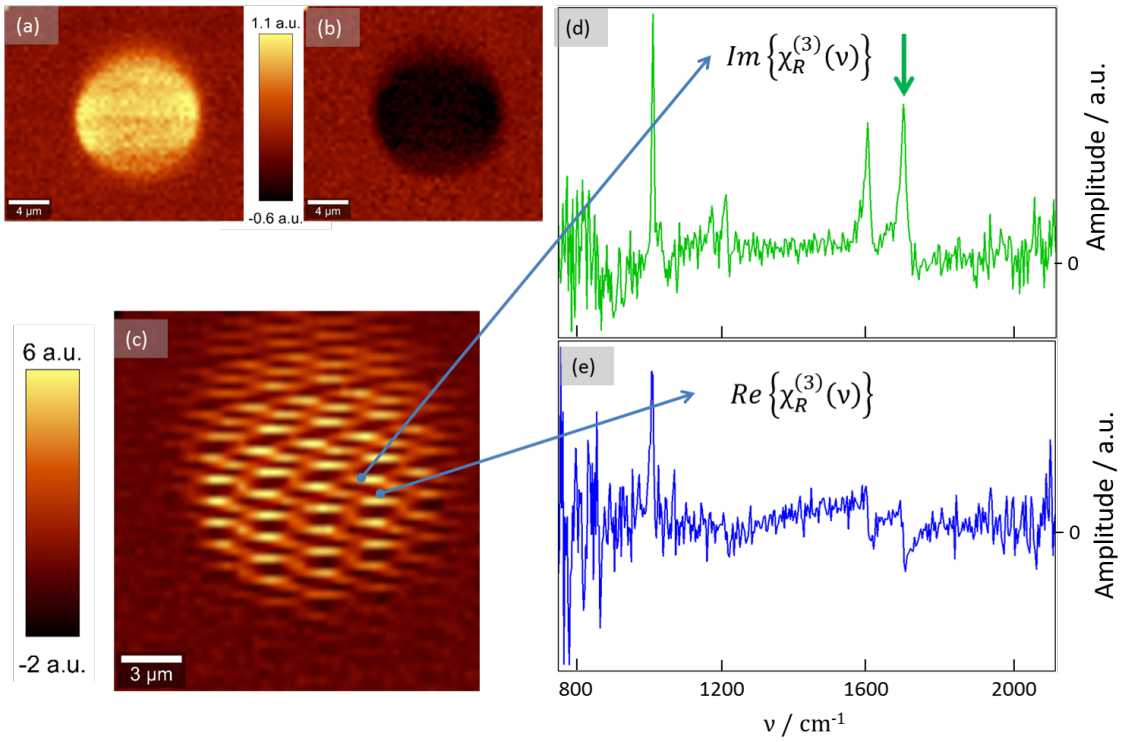

Figure 7.7.: (a) $Im(\chi^{(3)})$ and (b) $Re(\chi^{(3)})$ image of a benzaldehyde droplet embedded in water at 1704 cm^{-1} extracted from measured interformetric hyperspectral CARS data generated for a phase difference of $\Delta\phi = \frac{\pi}{2}$ and $\Delta\phi = 0$, respectively. (c) Corresponding image extracted from interferometric hyperspectral CARS data recorded while sinusoidally modulating the phase difference $\Delta\phi$ at $\approx 0.3\ Hz$ modulation frequency. Representative (d) $Im(\chi^{(3)}(\nu))$ and (e) $Re(\chi^{(3)}(\nu))$ spectra extracted from image pixels inside the benzaldehyde droplet in image (c), where $\Delta\phi = \frac{\pi}{2}$ and $\Delta\phi = 0$, respectively. Measurement parameters for (a) and (b): $26 \times 24\ \mu m^2$, 400 nm step size, 30 ms integration time per pixel spectrum, average pump, Stokes and signal powers are 59 mW , 1.5 mW and $\approx 0.005\ mW$, respectively. Measurement parameters for (c): $18.3 \times 19\ \mu m^2$, 350 nm step size, 50 ms integration time per pixel spectrum, average pump, Stokes, and signal powers are 59 mW , 1.5 mW and $\approx 0.001\ mW$, respectively.

Figure 7.7 (a) and (b) show that it is feasible to perform interferometric hyperspectral CARS imaging. As this example shows, the interferometric stability is provided throughout the 250 s total acquisition time. The visible amplitude fluctuation within the droplet anyhow are attributed to still present small phase fluctuations, in combination with not perfectly compensated intensity fluctuations of the SC.

7.4. Summary, Conclusions and Outlook

For the first time, a broadband single laser source of phase correlated photon pairs was successfully applied to achieve interferometric hyperspectral CARS imaging without any polarization restrictions and with freely tunable phase differences between all involved fields. Using picosecond pulses, the spontaneous FWM generation of broadband correlated photon pairs with a correlation bandwidth of approximately 45 nm, corresponding to a correlation time of about 30 fs, is successfully demonstrated by measuring the coherent SFG peak revealing the successful preservation of this correlation within a high NA microscopy setup by purely passive compensation of accumulated material dispersion of that setup.
We have demonstrated here the direct experimental extraction of the complex vibrational response of the third order susceptibility $\chi^{(3)}(\nu)$. This provides experimental access to both the phase and amplitude of the CARS field generated in the sample, which is in contrast to the standard hyperspectral CARS imaging approach (see chapter 6), where the phase needs to be estimated posterior to the measurements, for example, by using MEM.
For samples, which show a strong intrinsic fluorescence background that overwhelms the CARS spectrum of that sample, an amplification of the weak CARS field above the fluorescence background level is required. This amplification can be achieved by using the presented concept of interferometric hyperspectral CARS imaging.
In this chapter the proof-of-principle of interferometric hyperspectral CARS imaging with broadband correlated photons was successfully demonstrated. To reduce fluctuations due to phase noise and to enable long term measurements, for example for 3D-measurements as shown on the pollen sample in the previous chapter, active stabilization of the interferometric setup would be needed. Further future improvements of the setup will include a broader spectral CARS coverage of more than 3000 cm^{-1}, similar to that already realized for the standard hyperspectral CARS imaging case (see chapter 6). To achieve this a different fiber providing an even broader spontaneous FWM spectrum and an improved dispersion control will be needed.

8 Two-Dimensional CARS Microspectroscopy

In the previous, chapters CARS measurements were performed in the spectral domain only. Here the characteristic of CARS being a pump-probe technique is exploited by performing time-resolved multiplex CARS measurements, where the probe pulse is delayed with respect to the pair of temporally overlapped pump and Stokes pulses. In spontaneous Raman spectroscopy, the measurements of the dephasing of Raman resonances in the time-domain would require a detection system with response and dead times below 1 ps, which are not available. Therefore, the only way of measuring dephasing times of Raman coherences in the time-domain is performing a Raman pump-probe experiment.

Time-resolved CARS measurements have previously been successfully used for avoiding the non-resonant (NR)-background [85], as well as for extraction of dephasing times [21]. The instantaneous NR response of the medium causes a NR-CARS background, being only present when all pulses are simultaneously present. The Raman resonances, in contrast, have dephasing times T_2 of several hundreds of femtoseconds to a few picoseconds, and they can therefore be probed after the disappearance of the NR background.

The prerequisites for this technique are using short excitation pulses, which prepare the vibrational coherence of the sample. Consecutively the coherence of the excited vibrational states are probed by the probe pulse. For a broadband excitation, the resulting time-resolved CARS spectrum is measured spectrally resolved [86]. In more recent experiments a state-of-the-art CCD camera is used for detecting 2D-CARS [87]. With this, the dephasing of all vibrational resonances can be investigated simultaneously. The time-domain measurement of the dephasing of vibrational coherence allows for the extraction of Fourier-transform-linked parameters in the spectral domain, as for example the width of a vibrational band Γ. By simply extending the temporal measurement range, this way the need for a high spectral resolution spectrometer, which usually has a severely reduced throughput

and enables only measuring a considerably limited spectral range at once, can be circumvented.

The further major development step was performing the time-resolved CARS in a microscope [22], which was later combined with broadband excitation [88] that facilitates the spatially resolved measurement of the dephasing time of microscopic samples. Further development of this technique consisted of expanding the bandwidth of the broadband pulse, so that all vibrational resonances of a sample are measured simultaneously for each position in the sample [88, 89], introducing the 2D-representation of the temporally and spectrally resolved CARS data. In reference [89] a temporally rectangular shaped fs-pulse is used, which provides a high temporal resolution, but comes with the drawback that the laser pulse power is limited to a couple of tens of mW. For weak non-absorbing Raman scatterers it is beneficial to be able to choose also higher powers.

All of the aforementioned broadband realizations have in common, that they use the CARS scheme B, depicted in figure 3.5 (b), where the pump and Stokes fields are provided by the same very short and broad pulse and the probe pulse is provided by a longer and narrower ps pulse [88, 90, 91]. The realizations using pulses with a couple of tens of femtoseconds have the problem that their bandwidth limits the measurable CARS spectral range, and the full range of the molecular vibrations cannot be measured at once.

The spectral width of the longer but narrowband ps-pulse defines the achievable spectral resolution, and its pulse length limits the achievable temporal resolution in the 2D-CARS experiment. Moreover, vibrational modes need to be spectrally separated by the probe pulse, so that their dephasing does not interfere with neighboring bands, otherwise causing quantum beats in the time domain.

Here, we report of using a near transform-limited few-cycle pulse and a ps-pulse for the excitation and the probing, respectively, of CARS in a molecular sample inside a microscope. A high spectral resolution, separating most vibrational band signals from each other, and the availability of high power for each of the pulses, are the outstanding characteristics of the time-resolved CARS microspectroscopy realization presented in this chapter. The realization of 2D CARS microspectroscopy in the microscope enables the extraction of dephasing times for each localization within the sample and the creation of maps of the sample based on differences on the coherence lifetimes of its component's vibrational resonances.

In the first section 8.1, an evaluation of the experimental setup and excitation sources is presented. In section 8.2, the 2D-CARS experiments and results are presented and discussed, followed by the extraction and evaluation of the vibrational dephasing times in section 8.3, before summarizing in section 8.4, and giving an outlook to

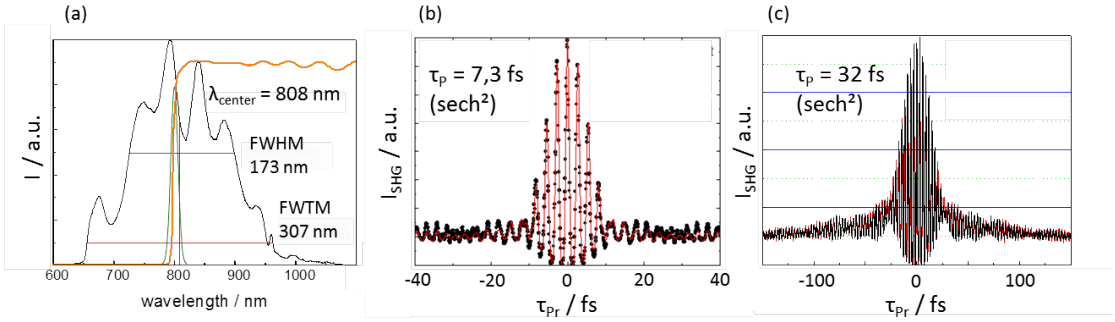

Figure 8.1.: (a) Spectrum of the few-cycle pulse (black line) centered at 808 nm, the probe pulse (green line) centered at 800 nm, and the transmission curve of the dichroic filter $DC4$ (orange line) used for spectral filtering the few-cycle pulse. (b) Interferometric SHG auto-correlation curve of the few cycle pulse in the focus of the high NA objective [34], with the measured data in black and the corresponding simulation in red. (c) Corresponding interferometric SHG auto-correlation curve (black line) of the same pulse, measured after passing through the dichroic filter $DC4$, with the corresponding simulation (red line).

potential future investigations.

8.1. Characterization of the Laser Pulses, Used for 2D-CARS Microscopy

The excitation pulses are characterized in the spectral and temporal domains by measuring the spectra and the temporal profiles, respectively. In figure 8.1 (a) the spectrum of the few-cycle pulse is shown together with the probe pulse spectrum, the latter being tuned to the center of the broadband pulse at 800 nm. The few cycle pulse spectrum spreads over 173 nm (FWHM) and over 307 nm for the full width at tenth of maximum (FWTM) around its center wavelength of 808 nm.
In figure 8.1 (b) the interferometric SHG auto-correlation of the few-cycle pulse is shown, as measured by focusing onto a non-linear crystal through the high NA objective, at the sample position (compare reference [34] for further experimental details). An in-focus temporal width of only (7.3 ± 0.3) fs $(sech)^2$ with no residual group delay dispersion (GDD) and with a residual third order dispersion (TOD) of 170 fs^3 is measured [34]. When the spectral width of the few cycle pulse is reduced to the range from 800 nm up to 1100 nm, the measured interferometric SHG auto-correlation curve becomes much temporally broader, as seen in figure 8.1 (c), resulting in an effective temporal pulse width of 32 fs $(sech)^2$. This pulse was used as the pump and Stokes pulses for the CARS excitation of vibrational resonances of the neat toluene test sample, which reside in a range between 500 cm^{-1} and

1600 cm^{-1}.
The measured pulse length of the ps pulse, which was used as the probe pulse in the CARS process, amounts to 2.9 ps assuming a transform-limited $(sech)^2$ profile.

8.2. 2D-CARS of Toluene

In figure 8.2 (b), the measured 2D-CARS spectrum of neat toluene is shown, which reveals the dependence of the 1D-CARS spectrum on the time delay τ_{Pr} between the few-cycle excitation pulse and the narrow-band probe pulse. The CARS intensity is color coded logarithmically according to the color scale bar on the right side of the figure. The lower horizontal white line indicates the zero time delay position, where the excitation and probe pulses are overlapped in time, and from which the 1D-CARS spectrum in figure 8.2 (a) is extracted. The upper white line indicates the position at 3 ps time delay, from which the second 1D-CARS spectrum, shown in figure 8.2 (a), is extracted. It can be clearly seen, that the NR-background is only present around the zero time delay position, and it falls below the detection limit after about 2 ps.
The intrinsic vibrational bands of toluene are easily identified in both 1D-CARS spectra. In the spectrum taken at $\Delta\tau_{Pr} = 0$ ps, the vibrational bands show the characteristic dispersive line profiles due to interference with the CARS field. The NR-background has a spectral shape that is typically for the multiplex CARS following scheme B, where the pump and Stokes fields are provided by the same, very short and broad pulse. The NR CARS background as well as the CARS intensity in general are strongest near to the probe wavelength and become weaker further away from the probe wavelength. The spectrum taken at $\Delta\tau_{Pr} = 3$ ps reveals vibrational bands without NR CARS background for those resonances, whose dephasing times exceed approximately 2 ps.

8.3. Raman Free Induction Decay in Toluene

As seen in the 2D-CARS spectrum of neat toluene, figure 8.2 (b), many vibrational resonances have a much longer dephasing time than the length of the probe pulse. Only at the wavenumber positions of the vibrational resonances, the CARS intensity decreases much slower, and in several cases it can still be detected after a probe delay greater than 2 ps. Other vibrational resonances, as for example those at 507 cm^{-1} and at 1200 cm^{-1}, have a dephasing time only slightly longer than the duration of the probe pulse. The arrows above and below figure 8.2 (b) indicate the wavenumber

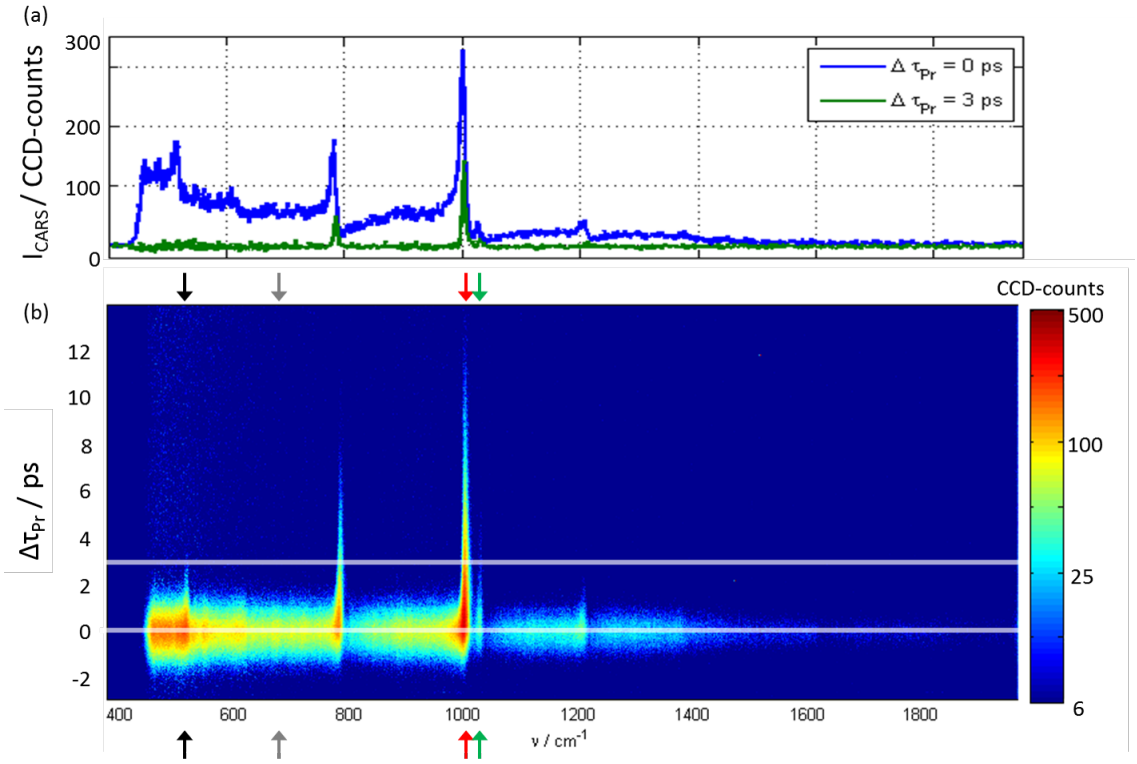

Figure 8.2.: (a) CARS-spectra of toluene measured with a few-cycle pulse providing the pump and Stokes fields and a ps-pulse providing the probe field at zero relative time delay between the fields $\Delta\tau_{Pr} = 0\ ps$ (blue line) and at $\Delta\tau_{Pr} = 3\ ps$ (green line). (b) Measured 2D-CARS spectrum of toluene with the CARS intensity being color-coded in a logarithmic scale. Measurement parameters: Average powers for the few-cycle fs- and the ps-pulses are 0.9 mW and 1.8 mW, respectively. The single spectrum integration time is 3 s. The temporal delay step size is 50 fs over a range of $\Delta\tau_{Pr}$ from $-3.36\ ps$ to $+13.44\ ps$. The white lines indicate the delay positions at which the spectra shown in (a) are extracted. The arrows indicate the spectral positions, at which the RFID curves shown in figure 8.3 are extracted.

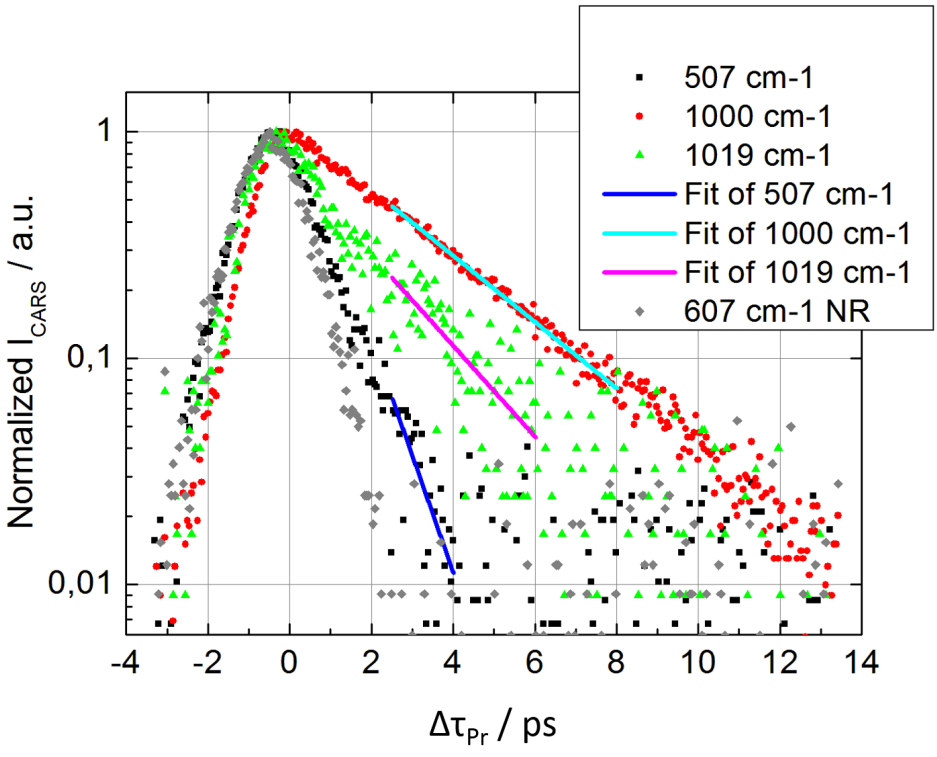

Figure 8.3.: Normalized time profiles of CARS intensities of neat toluene extracted at 507 cm^{-1} (black squares), 1000 cm^{-1} (red circles), 1019 cm^{-1} (green triangles) of toluene over the probe delay $\Delta\tau_{Pr}$, as indicated by the color-coded arrows in the 2D-CARS spectrum shown in figure 8.2 (b). The corresponding fit curves (solid lines) to a single exponential RFID model (equation (3.33)) are also shown. For comparison, the normalized CARS time profile is shown for an exemplary NR region extracted at 600 cm^{-1} (gray diamonds).

position of vibrational resonances, for which time profiles of the CARS intensities are further analyzed.

In figure 8.3, the color-coded CARS intensity profiles over time delay $\Delta\tau_{Pr}$ are shown for three selected vibrational modes of toluene, 507 cm^{-1}, 1000 cm^{-1} and 1019 cm^{-1}, together with their respective fit curves for a single exponential decay according to the RFID model (equation (3.33)), in a delay region $\tau_{Pr} > 2.5\ ps$, where the NR background is negligible, and the signal-to-noise ratio is sufficient. For comparison, the temporal CARS intensity profile is also shown at 600 cm^{-1}, which is purely non-resonant, revealing the temporal response of our 2D-CARS microspectroscopy setup.

The extracted dephasing times vary a lot. The ν_6 in-plane trigonal ring deformation mode at 1000 cm^{-1} [92–94] has the longest dephasing time. Due to the nature of its vibrational bonds, this mode is the least influenced by the local environment, and therefore exhibits the longest dephasing time (or the narrowest spectral band-

Table 8.1.: Extracted RFID time constants (T_2) and correspondent spectral bandwidth Γ for the selected vibrational resonances of neat toluene.

resonance wavenumbers Ω [cm^{-1}]	T_2 [ps] with fit error	calculated spectral bandwidth Γ [cm^{-1}] with corresponding error
507	0.84 ± 0.13	12.6 ± 4.1
770	2.05 ± 0.06	5.2 ± 0.3
1000	2.97 ± 0.05	3.6 ± 0.1
1019	2.16 ± 0.24	4.9 ± 1.1

width). The resonance at 1019 cm^{-1} is assigned to the C-H β mode [95], and is much weaker and additionally has a shorter dephasing time. Therefore the corresponding temporal CARS intensity profile is much noisier. Nevertheless also for this vibrational mode a RFID time-constant was extracted. The toluene mode at 770 cm^{-1} is attributed to the ring-breathing ν_{12} of toluene [92, 93, 96]. The mode at 507 cm^{-1} is attributed to the $a1$ fundamental vibration ν_{13} of toluene [96, 97]. The extracted RFID time-constants T_2 for all selected vibrational modes are listed in table 8.1 together with the corresponding calculated spectral vibrational bandwidth, according to $\Gamma = (10^2 \pi c T_2)^{-1}$, compare to section 3.3.4. The majority of the extracted RFID time-constants are consistent with previously reported time resolved multiplex CARS spectroscopy measurements of neat toluene. For example, McGrane et al. [98] extracted an RFID time-constant of (2.918 ± 0.047) ps for the 1002 cm^{-1} mode of toluene, which is in good agreement within the errors of our extracted RFID time-constant of (2.97 ± 0.05) ps. However,the better spectral resolution of our presented realization of time resolved multiplex CARS spectroscopy allows for the spectral separation between the very strong 1000 cm^{-1} mode and the weaker mode at 1019 cm^{-1} of toluene.

8.4. Summary, Conclusions and Outlook

2D-CARS microspectroscopy with a ps- and a near transform-limited few-cycle fs-pulse has been successfully applied to the test sample of neat toluene within a sub-femtoliter probe volume. The RFID time-constants of various vibrational modes of toluene could be extracted from the analysis of their simultaneously recorded CARS intensity time-profiles. They are in good agreement with previous works. In contrast to previous reports, where the spectral resolution is not sufficient to separate vibrational modes, and the dephasing of each of the spectrally overlapping

modes can only be extracted indirectly by evaluating the quantum beating of the respective modes [22, 88, 98, 99], this work exploits the improved spectral resolution provided by a near transform-limited 2.94 ps pulse. As a consequence, vibrational dephasing times of close-by resonances can be extracted without quantum beats. As such, for the first time we were able to spectrally separate the 1000 cm^{-1} and the 1019 cm^{-1} modes of toluene in time resolved 2D-CARS microspectroscopy, as presented in this chapter. Measuring the RFID time-constants of the vibrational modes in the time domain allows for the subsequent calculation of their spectral bandwidth Γ. The higher sensitivity provided by measuring in the time domain may offer the extraction of more accurate spectral bandwidths for narrower vibrational resonances, when compared to their direct measurement in the frequency domain.
In future studies, this can be exploited for the monitoring of small changes in the dephasing time of particular vibrational resonances in crystalline samples, which for example provide sensitivity to changes of temperature or stresses.
So far, in the above example of neat toluene, we have not exploited the intrinsic 3D-sectioning capabilities of our 2D-CARS microspectroscopy setup. In future work, our presented approach can be applied to spatially resolved measurements, where the dephasing times of all resonances can be obtained simultaneously for every position in the sample.
When tuning the probe laser to the blue edge of the few-cycle fs-pulse at 680 nm, the full bandwidth of the short excitation pulse from 680 nm up to 950 nm can be exploited. This corresponds to an accessible CARS spectral range of more than 4000 cm^{-1}. In order to implement this, future instrumental optimizations are required, which encompass the use of optimized optical filters and dichroic mirrors.

9 Epi-Detected Hyperspectral CARS Imaging

Over the years, many approaches [100–104] to increase penetration depths and imaging capabilities deep into tissue are reported, allowing for the investigation of thicker specimen in spontaneous and coherent Raman imaging techniques. Nevertheless, if living animals or humans are the target of investigation, it is not possible to measure in transmission due to scattering and absorption of the light inside a thick sample, and therefore it is indispensable to collect the generated Raman scattering in a noninvasive epi-detection configuration. In the previous chapters, only the CARS emission scattered into the forward direction has been considered. In the backward or epi-direction, due to more rigid phase matching conditions, the dependence of the CARS signal intensity on the sample size is not directly intuitive.

Epi-detected CARS microscopy has first been shown in an imaging mode by Xie and coworkers in 2001 [14, 105]. In most previous studies on epi-detected CARS microscopy the back-reflection of forward scattered CARS from the tissue is giving the strongest epi-detected CARS signal contribution. Though intrinsic epi-scattered light and the back-reflection of the forward scattered light from the sample need to be separated, calling for further investigation. When a CARS spectrum is recorded in the epi-direction, the spectral characteristics with resonant and non-resonant contributions can be used to distinguish these different contributions. The first and only direct evidence for the experimental detection of intrinsic epi-scattered CARS signal was reported by Potma and Xie [106], where characteristic interference fringes in the narrowband E-CARS signal of a single lipid membrane bilayer close to a supported lipid membrane bilayer were detected. Those observed E-CARS fringes were caused by a given and unknown variation of inter-membrane distance rather than by a well defined change of the sample size, for which an oscillatory size-dependent behavior of the E-CARS signal has previously been predicted by simulations [14].

The goal of the experiments described in this chapter is to investigate the dependence

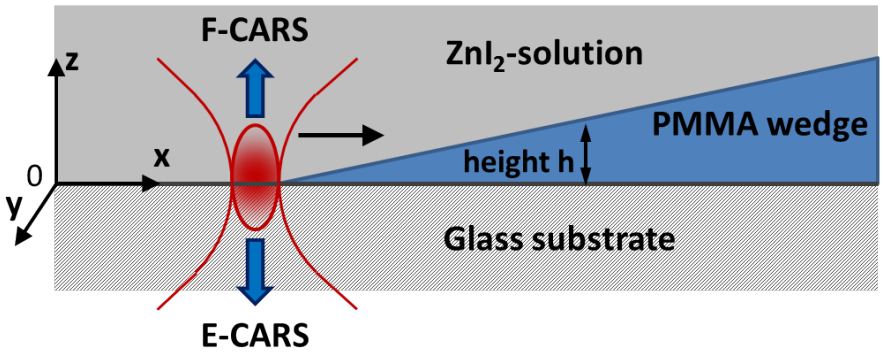

Figure 9.1.: Schematics of index-matched PMMA wedge sample system for E-CARS experiments.

of the broadband CARS spectrum intrinsically emitted in the epi-direction on the sample thickness. The sample of choice is a thin PMMA wedge on a glass cover slip, which is schematically shown in figure 9.1. To allow the comparison with previously reported E-CARS simulations [14, 56], the interface plane between the cover-glass substrate and the PMMA wedge is chosen to be in the center of the focus. Furthermore, a wedge with a gentle slope is used, such that the PMMA thickness can be considered constant within the lateral focus spot size of typically 340 nm [11]. By scanning the focus center along the x-axis, this sample permits to record both forward- and epi-detected CARS signals of one and the same specimen with a known and variable thickness under identical excitation as well as detection conditions.

In order to investigate the intrinsic epi-scattered CARS, any back-reflected forward-scattered CARS emission and back-reflected excitation light have to be avoided. The reason for back-reflections are interfaces with refractive index differences, for example between the substrate, the sample, and the surrounding medium. In several optical microscopy techniques, a good back-reflection suppression is also needed and therefore it is easy to find index-matching liquids for different materials. Unfortunately, conventional index-matching liquids are often consisting of – or at least containing – many complex molecules, which have large Raman cross-sections exhibiting many vibrational bands. Therefore, they are not usable for the planned experiments.

This chapter is organized as follows: In the first section 9.1.1 the optimization of the index-matching is described and characterized for obtaining an optimal test sample. Following in section 9.1.2 the height profile of the wedge sample is characterized with a profilometer and compared to F-CARS microscopy presented in section 9.2. The third section 9.3 presents the epi-detected CARS spectra of the index matched

PMMA wedge sample and compares them to the forward detected CARS spectra. Finally, the spectrally resolved E-CARS signal is recorded on a sample and analyzed as a function of increasing PMMA thickness in section 9.4. Section 9.5 summarizes the results of the this chapter.

9.1. Characterization of an Index-Matched PMMA Wedge Sample

For the intended experiments, a sample system is required that has a known and variable thickness, strong and clearly identifiable Raman signatures, and a refractive index, which can be matched to the underlying substrate as well as to the surrounding medium above the sample. Additionally neither the surrounding medium nor the substrate should show Raman signatures at spectral positions, where the sample has its distinct Raman bands.

9.1.1. Refractive index matching

Hendriks and Aviram [36] showed that the refractive index of aqueous zinc iodide solutions can be varied from 1.382 to 1.6190 by adjusting the zinc iodide concentration, and which in the following is used for index-matching PMMA with $n = 1.4846\ at\ 808\ nm$ [107]. The advantage of the zinc iodide solution in our case is the absence of any vibrational resonances in the spectral region of interest, which is in contrast to many other index matching liquids, that often consist of organic compounds. This is beneficial in two ways: first, one obtains a pure non-resonant reference CARS spectrum within the same sample region. Second, this CARS spectrum does not hinder the extraction of the weak vibrational signatures from the thin film. As described in section 4.7.4, the best index matching is achieved for the PMMA film in the 61 % ZnI_2 water solution, corresponding to a refractive index of $n = 1.494$ at 589 nm [36]. The observation of negligible reflection of the 808-nm pump laser at the solid-to-liquid interface of PMMA to zinc iodide solution in the microscope confirmed the very good index matching.

The refractive index of glass is $n = 1.51$ throughout the full spectral region of interest, which is very close to the refractive indices of the PMMA sample and the ZnI_2 water solution.

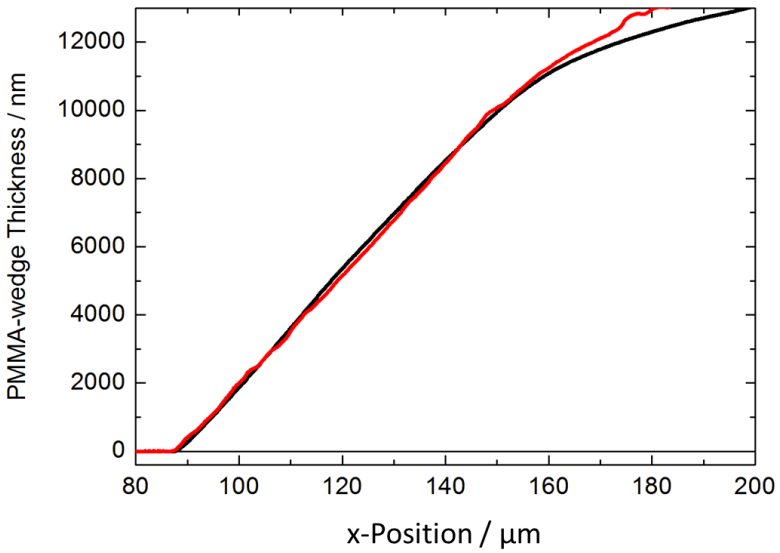

Figure 9.2.: Dektak height profiles of a PMMA wedge before (black curve) and after (red curve) being embedded in ZnI_2 solution for approximately 4 h showing a slope of $(160 \pm 12)\ nm/\mu m$.

9.1.2. Wedge Height Profile Measurements

Prior to the CARS measurements, the PMMA wedge profile is characterized using a profilometer (Dektak 150, Veeco), where a height profile along the radial x-direction (compare figure 9.1) is taken, see figure 9.2. The measurement parameters where set at: scan range $\Delta x = 200\mu m$, step size: 0.067 μm, total acquisition time: 10 s, force equivalent mass: 5 mg, stylus diameter: 12.5 μm, height range (hills & valleys): 65 μm. x-Profiles at neighboring y-positions showed same slopes of typically $(160 \pm 12)\ nm/\mu m$ for the investigated sample within the range from $x = 88\ \mu m$ to $x = 140\ \mu m$. For $x > 200\ \mu m$ the thickness reaches the maximum thickness of the tip of the PMMA droplet.

After the CARS measurement, the upper cover slip and the zinc iodide solution are carefully removed, the PMMA sample is rinsed with deionized water, and the height profile of the wedge is recorded again. Its comparison with the profile before immersing the sample in the zinc iodide solution is also shown in figure 9.2. Both profiles exhibit an almost identical height profile from which it can be concluded that the corrosive zinc iodide solution did not affect the PMMA wedge geometry during the time of approximately 4 h typically needed for performing the CARS experiments.

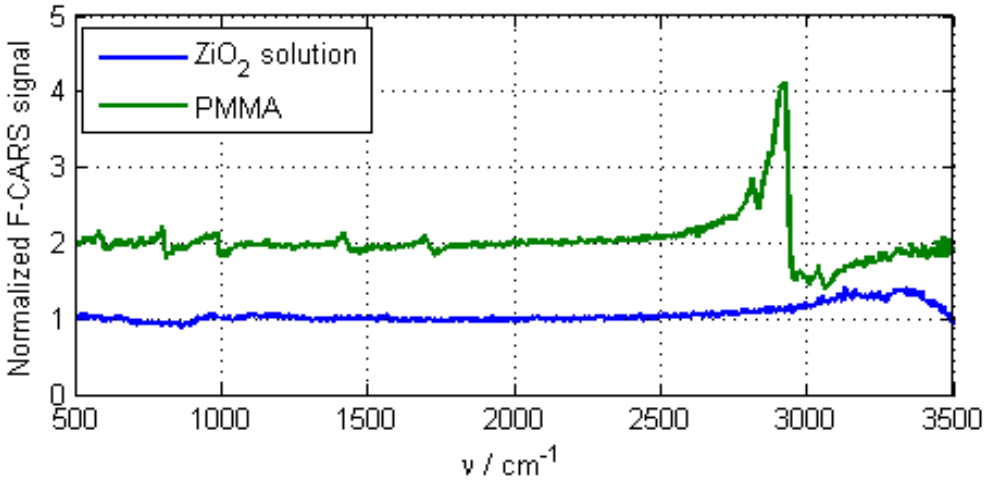

Figure 9.3.: Measured normalized F-CARS spectra of pure ZnI_2 solution (blue curve) and of PMMA (green curve, offset by 1). Both spectra were normalized by the same NR-reference CARS spectrum.

9.2. Forward-Detected CARS of Index Matched PMMA

In figure 9.3, the normalized forward detected CARS spectra recorded when focusing into PMMA at a wedge position, where the PMMA is thicker than the longitudinal extent of the focus (green curve), and when focused into the pure zinc iodide solution (blue curve) are displayed. Both spectra have been normalized by the same reference CARS spectrum recorded under identical experimental condition in glass. In the CARS spectrum of the PMMA, the characteristic resonance peaks of PMMA in the *C-H* stretching vibration region around 2924 cm^{-1} as well as in the fingerprint region, for example around 814 cm^{-1}, 1000 cm^{-1}, 1450 cm^{-1} and 1660 cm^{-1}, can be seen. These PMMA resonances nicely exhibit the dispersive CARS line shapes due to the complex mixing of the NR and resonant $\chi^{(3)}$ contributions of PMMA, compare figure 3.3. In contrast, the pure zinc iodide CARS spectrum is almost completely flat, except for a broad deviation above 2700 cm^{-1}, which is attributed to the broad *O-H* stretching vibration of water. The spectrum of the pure zinc iodide solution exhibits a strong NR CARS signal over the whole observed spectral range, which is about three times stronger than the NR CARS signal of the PMMA sample (not shown here).

9.3. Epi-Detected CARS of Index Matched PMMA

Figure 9.4 contains the epi-detected CARS spectrum (green curve) of a thin PMMA layer at a wedge thickness of 224 nm after corrections described in section 4.8.3. For comparison the spontaneous Raman spectrum of thick PMMA (black curve), the $Im(\chi^{(3)})$ spectrum of thick PMMA reconstructed from the normalized F-CARS spectrum shown in figure 9.3 (magenta curve), and the unnormalized F-CARS spectrum of pure ZnI_2 solution (blue curve) are shown. In the E-CARS spectrum, the Raman modes of PMMA are observed, most dominant in the C-H-stretching vibrational region with a strong band around 2924 cm^{-1} nicely matching with the spontaneous Raman spectrum. The Raman resonances in the fingerprint region, which are visible in the spontaneous Raman spectrum, are also present in the E-CARS spectrum, but almost completely hidden inside the noise. The elevated noise level in the E-CARS spectrum is dominated by Poisson noise due to the high nto-background signal (compare fig. 4.7).

It is evident, that the applied E-CARS spectra analysis procedure as described in section 4.8.3 is not able to eliminate a remaining broad background, which resembles almost perfectly the NR F-CARS spectrum of the pure ZnI_2 solution. As will be justified later, the broadband E-CARS background is attributed to the E-CARS signal of ZnI_2 solution generated at the interface to PMMA within the focal volume.

The reconstructed forward-detected $Im(\chi^{(3)})$ spectrum shows the same Raman peaks as the spontaneous Raman spectrum. The difference in relative peak amplitudes, especially when comparing the fingerprint region to the C-H-stretching region, originates from the uncompensated spectral detection sensitivity in the spontaneous Raman spectrum measurement. The forward-detected reconstructed $Im(\chi^{(3)})$ spectrum is intrinsically corrected for spectral detection sensitivity of the CARS system due to the normalization with the NR reference spectrum necessary in the reconstruction process (compare chapter 4.8.2). Because of the big difference in CARS signal levels between the strong F-CARS of the thick PMMA sample and the weak E-CARS of the thin PMMA sample, the integration time of the E-CARS spectrum measurement was 2000 times longer than that of the F-CARS spectrum measurement. Because the F-CARS signal of a thin PMMA layer at the same wedge thickness of 224 nm, as measured for the presented E-CARS spectrum, where forward- and epi-detected CARS signals are expected to have comparable intensities [56], comes with a much stronger background signal originating from ZnI_2 that predominantly fills the focal volume, the resonance F-CARS features are hidden in the noise. Therefore, even when the same acquisition time could be used for detecting the forward- and epi-emitted CARS spectra of a PMMA sample with

the same thickness, the F-CARS spectrum will be much noisier for samples with a thickness smaller than $\frac{\lambda_{AS}}{2n}$.

In conclusion, it can be confirmed that an intrinsic E-CARS spectrum of a very thin sample can successfully be measured in an index matched environment, which is not possible with F-CARS detection. Furthermore, the measured intrinsic E-CARS spectrum resembles almost perfectly the $Im(\chi^{(3)})$ spectrum reconstructed from the F-CARS spectrum and the spontaneous Raman spectrum of that sample.

9.4. Forward- and Epi-Detected CARS Spectra for Varying PMMA Wedge Thickness

Next, the dependence of the forward- and epi-detected CARS spectra on the thickness of the PMMA is studied. Whereas the shape of the $Im(\chi^{(3)})$ spectrum reconstructed from the F-CARS spectrum of PMMA (see figure 9.4) was found to be independent of the thickness of the PMMA, only the amplitudes of the PMMA peaks scale with the thickness for values considerably smaller then the longitudinal focal extension. This is shown for the thickness dependence of the $Im(\chi^{(3)})$-amplitude at 2924 cm^{-1} in figure 9.5. For comparison, the actual height profile of the PMMA wedge independently measured with a profilometer is also shown. Here, the $Im(\chi^{(3)})$ amplitude is scaled to overlap with the measured height profile of the wedge in the range where both curves are linear. For $x > 8$ μm, corresponding to a PMMA wedge thickness greater than approximately 800 nm, the $Im(\chi^{(3)})$ amplitude starts to saturate, when the PMMA film becomes thicker than the longitudinal extension of the focal volume. Irrespective of further increase of the PMMA thickness, the curve converges to a relatively constant level corresponding to about 1.2 μm thickness, which resembles the longitudinal length of the CARS excitation fields [11]. For a thickness considerably smaller than the focal extent in z-direction, the $Im(\chi^{(3)})$ amplitude is proportional to the wedge thickness. This experimentally confirms the theory [14]. Furthermore, we can now directly read off the PMMA thickness for a given x-position from figure 9.5. The inset in figure 9.5 shows a zoom into the tip of the PMMA wedge profile, which exhibits that the measured wedge height profile is not perfectly linear at the beginning of the PMMA wedge, probably due to the insufficient lateral resolution limit of the profilometer (compare measurement parameters in section 9.1.2). In order to minimize the error in the wedge thickness designation, especially at the tip of the PMMA wedge, a linear slope starting at zero thickness is assumed.

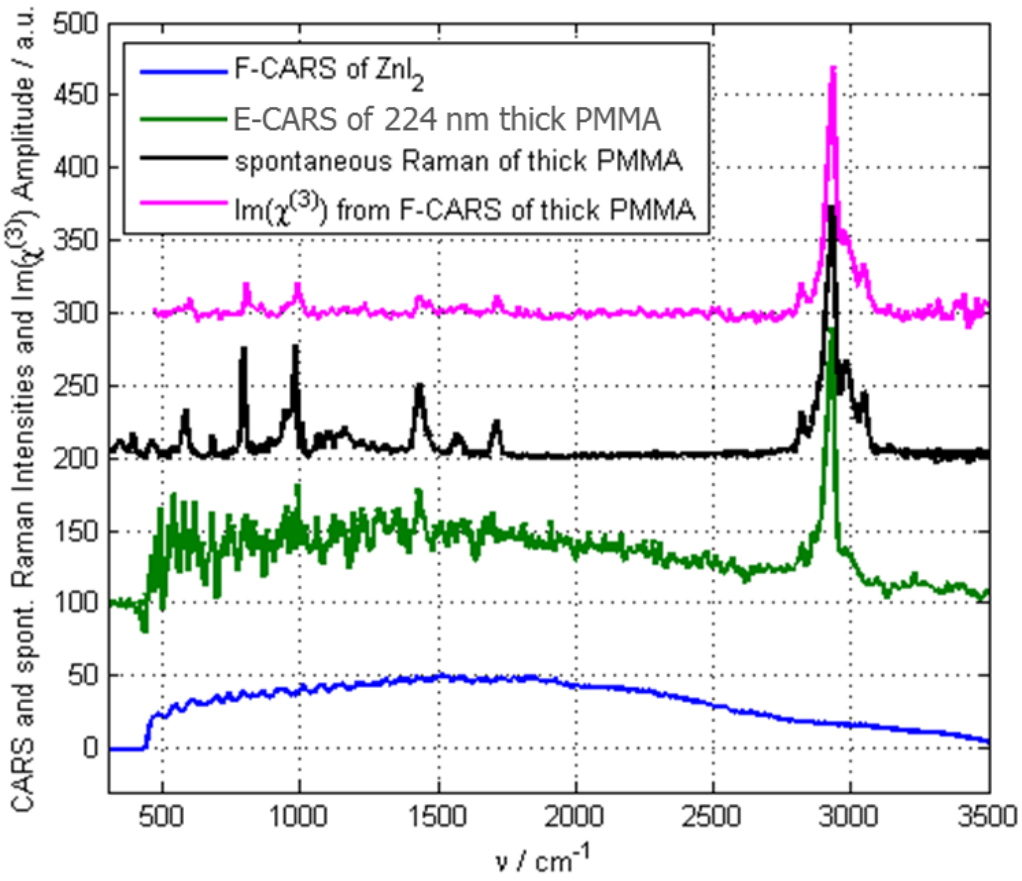

Figure 9.4.: Comparison of the E-CARS spectrum of a 224-nm thin PMMA layer (green curve), the spontaneous Raman spectrum of thick PMMA (black curve), and the $Im(\chi^{(3)})$-spectrum of thick PMMA reconstructed from the F-CARS spectrum shown in figure 9.3 (magenta curve). The spectra are scaled to the amplitude of the C-H stretching vibration at 2924 cm^{-1} and are offset by 100 arbitrary units each. Additionally, the unnormalized F-CARS raw spectrum of pure ZnI_2 solution is shown (blue curve), scaled to match the the spectral shape of the E-CARS spectrum in the NR spectral region.

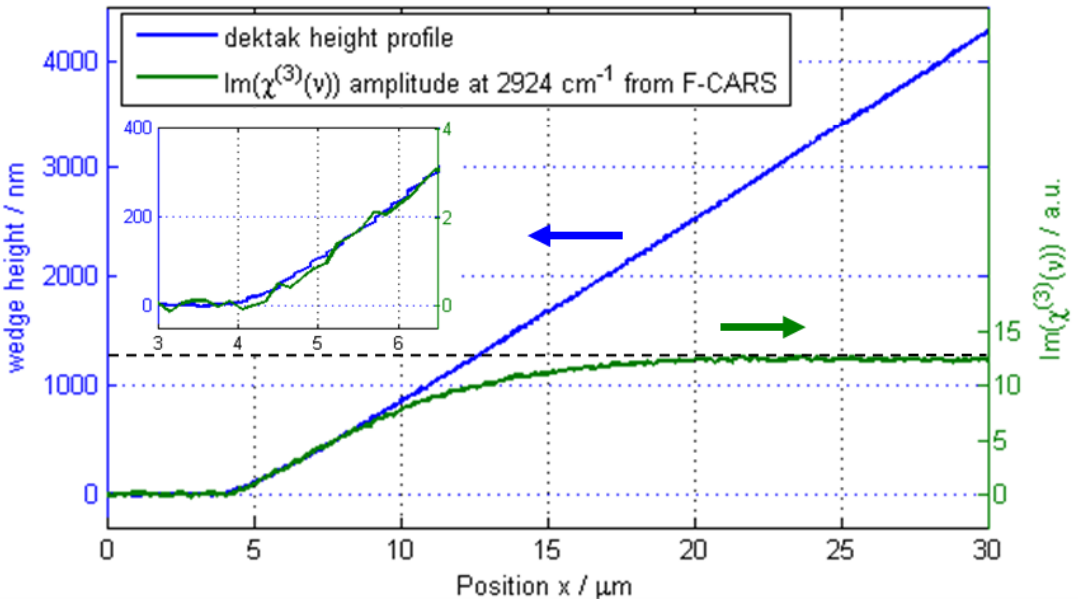

Figure 9.5.: Comparison of $Im(\chi^{(3)})$ amplitude (green curve) of PMMA at 2924 cm^{-1} reconstructed from measured F-CARS spectra with the independently recorded dektak height profile (blue curve) of the same wedge as a function of position x. The inset shows the zoom in into the thinnest part of the PMMA wedge. The horizontal dashed line indicates the saturation value of the $Im(\chi^{(3)})$ amplitude at large x-positions.

In figure 9.6, the E-CARS spectrum of a thin PMMA layer at a wedge thickness of 224 nm (red curve) is now compared with an E-CARS spectrum recorded at a wedge thickness of 352 nm (black curve). As can be seen, the latter lacks all resonant PMMA bands, even though more PMMA material resides in the sample focal volume. Only the NR background contribution seems to remain unchanged. In order to investigate the disappearance of the PMMA resonance signatures of the E-CARS emission at 325 nm thickness, E-CARS spectra are recorded while scanning the wedge through the focus position along the x-direction.

In figure 9.7 (a), a 2D representation of the measured and background corrected E-CARS spectra versus the x-position in the wedge sample is shown, where the E-CARS intensity is color-coded according to the look-up table at the right side. At low x-position values, where no PMMA is present, a broad E-CARS continuum is observed in the fingerprint region, which is assigned to the intrinsic NR E-CARS emission originating from the symmetry-break at the planar interface between the ZnI_2 solution and the glass substrate [56]. For increasing x-position, and hence for increasing PMMA wedge thickness, an oscillatory behavior of the whole spectrum is observed. Around 2924 cm^{-1}, the E-CARS peak intensity of the C-H-stretching vibrations of PMMA can be seen, which also shows periodic modulation starting

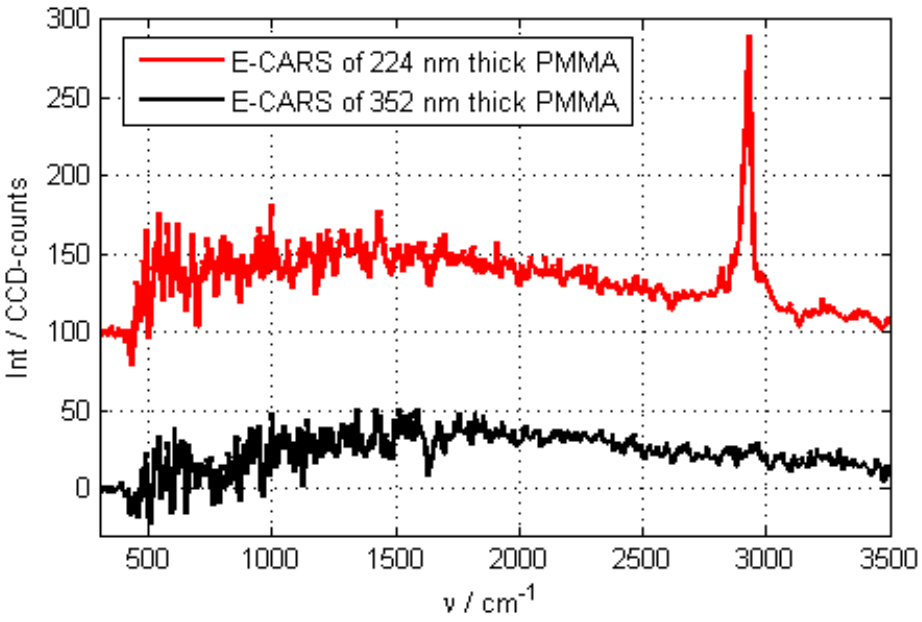

Figure 9.6.: E-CARS spectra of the 224 nm thick (red curve) and the 352 nm thick (black curve) PMMA wedge. The spectra are offset by 100 CCD-counts for better clarity.

around $x = 5\ \mu m$. In the fingerprint region oscillations of the broad NR E-CARS signal from both ZnI_2 and PMMA are mainly observed, which almost mask completely the weak vibrational signature of PMMA.

Figure 9.7 (b) shows the NR and resonant E-CARS intensity profiles extracted at 1124 cm^{-1} (blue curve) and at 2924 cm^{-1} (green curve), respectively, where the thickness axis is shown on the top of the graph as converted from the x-axis according to the previously measured wedge slope of 160 $nm/\mu m$ (compare section 9.1.2). Both E-CARS intensity profiles show oscillations with distinct periodicities. For comparison, the previously simulated E-CARS intensity at 1124 cm^{-1} (red curve) for a sphere as a function of its diameter [56] is also shown.

The zero-thickness position, i.e. the tip of the PMMA wedge, is then defined by comparing the measured E-CARS intensity profile at 1124 cm^{-1} with this previously simulated E-CARS intensity. The simulated E-CARS curve is positioned along the x-axis so that its first maximum coincides with the first maximum of the measured resonant E-CARS profile of the PMMA at 2924 cm^{-1}. The beginning of the simulated curve then defines the zero-thickness position of the PMMA wedge at $x = 3.4\ \mu m$.

In the measured NR E-CARS intensity profile at 1124 cm^{-1} the first peak is missing, when compared to the simulated E-CARS profile at the same wavenumber. This discrepancy is probably due to destructive interference of the intrinsic NR E-CARS

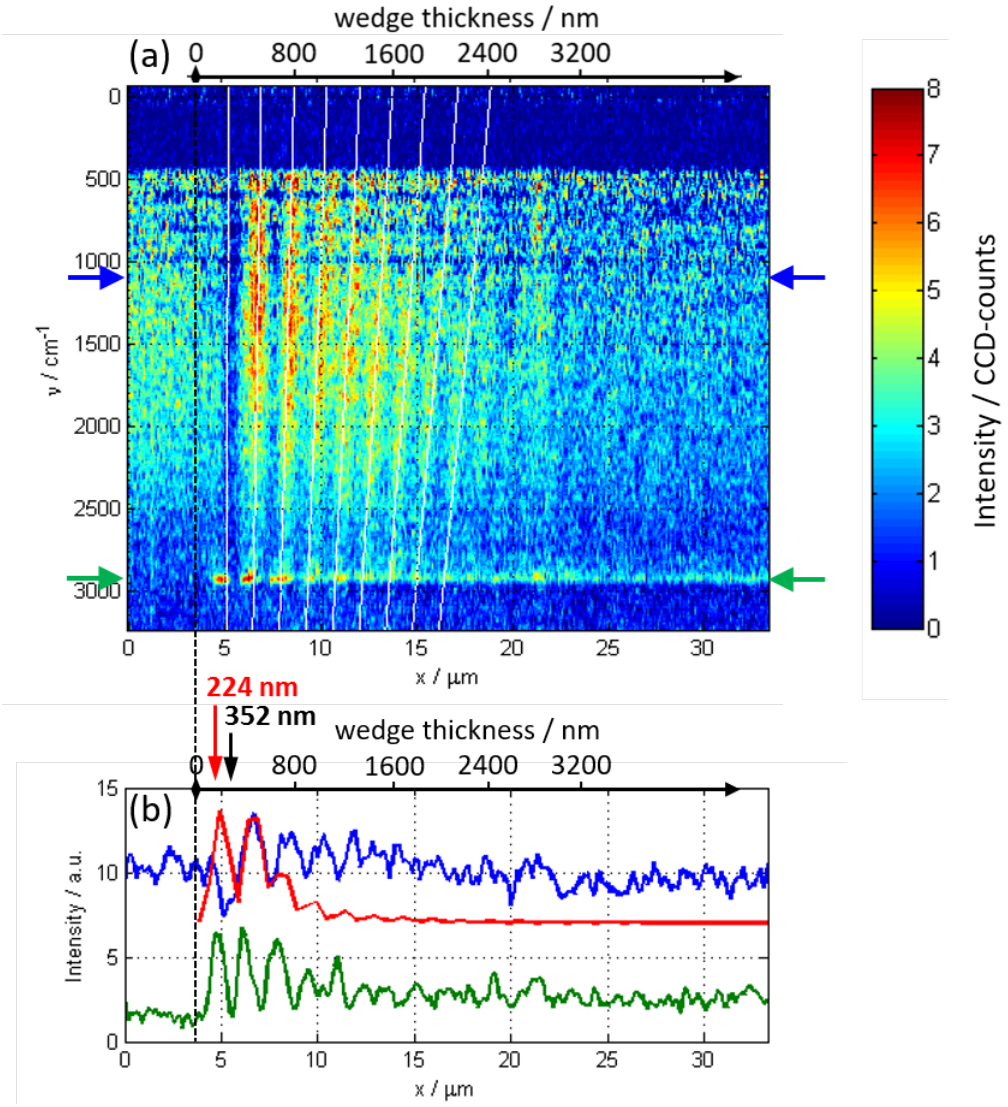

Figure 9.7.: (a) 2D representation of the measured background-corrected E-CARS spectra versus x-position (thickness) of the PMMA wedge sample. The E-CARS intensity is color-coded. The white lines are a guide to the eye representing the maxima for an oscillation with a thickness periodicity of $\frac{\lambda_{AS}}{2n}$ predicted by theory [14]. (b) E-CARS intensity profiles over the x-position (thickness) at 1124 cm^{-1} (blue curve) and 2924 cm^{-1} (green curve) extracted along the horizontal lines marked by the corresponding arrows shown in (a). For comparison, a simulated E-CARS intensity profile for a sphere (red curve) taken from reference [56] is also shown. Both E-CARS profiles at 1124 cm^{-1} are offset by 7 *a.u.* for better clarity. The vertical dashed black line marks the zero-thickness position.

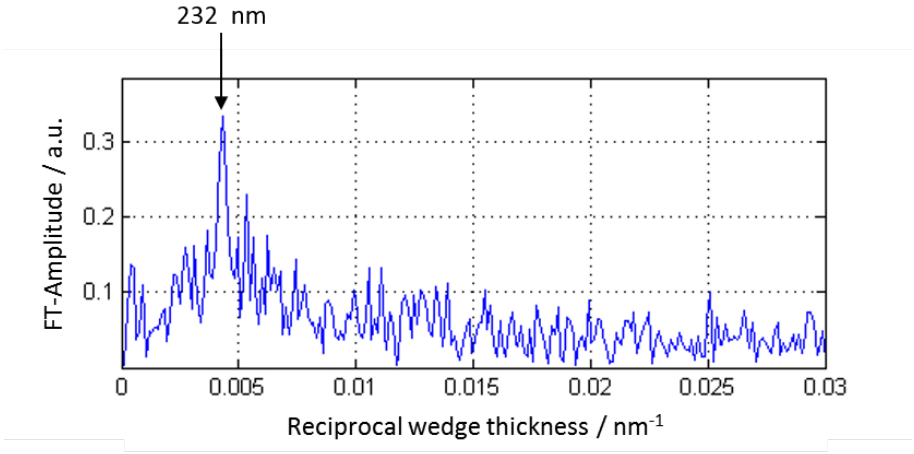

Figure 9.8.: Fourier-transform of the oscillatory part of the E-CARS intensity profile over wedge thickness at 2924 cm^{-1} shown in figure 9.7 (b). The black arrow indicates the peak corresponding to an oscillation thickness period of 232 nm.

emission originating from the PMMA tip and the NR E-CARS emission originating from the symmetry-break at the planar interface between the ZnI_2 solution and PMMA [56], which is not considered in the simulation. However, good agreement is observed for the position of the second oscillation peak and the oscillation periodicity. In contrast to the NR E-CARS thickness profile at 1124 cm^{-1}, the first oscillation peak of the E-CARS profile at 2924 cm^{-1} is present, as the NR CARS of ZnI_2 at 2924 cm^{-1} is much weaker than the resonant CARS of PMMA (compare figure 9.6) resulting in an negligible interference effect. For increasing thickness of the PMMA wedge, both the NR and resonant E-CARS intensities converge to a low but constant value, and their oscillation amplitudes are increasingly damped.

Having a closer look at the positions marked by the red and black arrows at 224 nm and 352 nm in figure 9.7 (b), respectively, the E-CARS intensity of the C-H stretching vibration is maximal at 224 nm and minimal at 352 nm, which explains the disappearance of that peak in the spectrum in figure 9.6.

In figure 9.8, the Fourier-transform of the extracted oscillation part of the measured E-CARS intensity profile at 2924 cm^{-1} is shown. This Fourier amplitude spectrum exhibits a peak corresponding to an oscillation thickness period of 232 nm.

From prior simulations, it is known that the periodicity of the E-CARS intensity strongly depends on the shape of the sample as well as on its exact axial position inside the focal volume [14, 56]. For example, the oscillation period in the size dependence of the E-CARS intensity for a sub-micron sphere is expected to be half of that of a half-sphere, which is filling one half of the the focal volume. For an E-CARS simulation for a sphere positioned in the center of the focus [14], an oscillation period of approximately $\frac{\lambda_{AS}}{2n}$ was obtained, which is in good agreement with the

oscillation period predicted for a thin slab sample as introduced in section 3.3.1. The white lines in figure 9.7 (a) are representing the theoretical maxima for such an oscillation with a thickness periodicity of $\frac{\lambda_{AS}}{2n}$. A good agreement between the measured and theoretical thickness positions of the oscillations maxima is observed throughout the whole spectrum.
The differences can be explained by the errors made in the determination of the wedge slope and in the exact definition of the zero-thickness position.

9.5. Summary, Conclusions and Outlook

In conclusion, it can be said that a suitable sample system for the first systematic and quantitative experimental study of broadband E-CARS emission was defined and successfully exploited, which has the required characteristics of strong Raman signatures in a sample of continuously increasing size within the order of magnitude of the focus dimensions, that is embedded in an index-matching liquid and a suitable substrate, both without disturbing Raman signatures.
Pure broadband E-CARS spectra are measured without major contributions from back-reflected forward-scattered CARS, providing simultaneously both resonant and NR E-CARS from a microscopic sample without disturbing strong contributions from a bulk surrounding medium. This way, the weak E-CARS spectrum of a very thin PMMA-polymer sample $\leq$ 224 nm thickness is successfully detected, which could not be achieved by conventional F-CARS microspectroscopy. It was found that the measured E-CARS spectrum of a microscopic sample is similar to its spontaneous Raman spectrum.
The fact that the full broadband E-CARS spectrum is measured allows the evaluation of the origin of different E-CARS signal contributions and therefore their comparison with simulation. For the first time, the theoretically predicted oscillatory behavior of pure E-CARS signal in dependence of the sample thickness is experimentally verified, not only for a single resonance, but for the full spectrum.
To conclude, the feasibility of intrinsic broadband E-CARS detection, when index-matching is an option, has been successfully demonstrated here. The chemical sensitivity of this novel epi-detected hyperspectral CARS imaging method opens up new prospects for the label-free and quantitative chemical characterization of complex nano materials, as for example thin polymer films, graphene, or other 2D semiconductors on non-transparent substrates, where F-CARS detection is not possible.
As another outlook, additional simulations of the broadband E-CARS fields for a wedge sample that takes into account the wedge geometry are proposed in order to

elucidate the origin of the interference effects observed in the experiment.

A Appendix

A.1. Pulse Length Dependence of Simulated Supercontinuum Generation

In figure A.1, simulations of SC spectra according to section 3.2 for the PCF FemtoWHITE800 and with the input parameters given in section 5.1 are displayed as a function of seed pulse length T_{FWHM} for same average power of 550 mW. The simulated SC spectra here are averaged over 150 single spectra in order to better reveal their spectral envelope.

For the longest seed pulse with $T_{FWHM} = 88$ ps, no SC is generated at an average power of 550 mW. Therefore, this spectrum shows only a very narrow line at the seed wavelength of 808 nm. Shorter seed pulses with $T_{FWHM} = 5$ ps already generate a quite broad SC spectrum, exhibiting a broad peak in the visible spectral region around 640 nm as well as a broad peak in the near-IR region with a very pronounced FWM peak centered at 860 nm. For increasing seed pulse lengths, the evolution of the SC generation can nicely be observed. In the visible spectral region, the broad peak shifts towards smaller wavelengths without a considerably increase in intensity, while the seed pulse length becomes shorter. The buildup of a second peak below 600 nm is most probably constrained towards lower wavelengths by the imperfections in the extrapolation of the PCF dispersion curve into the visible range. For the shortest seed pulse of 123 fs the SC spectrum extends further into the blue wavelength region by about 20 nm, but in comparison to the broadening of the peak around 640 nm, the expansion into this wavelength region seems to be constrained. A lot of intensity tends to buildup towards the low wavelength boundary.

On the near-IR side of the seed wavelength, such a limitation is not observed. The rather sharp FWM peak, strongest for the spectra of seed pulse lengths between 3 *to* 5 ps, broadens into a continuum for decreasing seed pulse lengths. Also here, the intermediate intensity of the broad continuum seems to stay rather constant, while the SC spectrum expands further into higher wavelength regions. Only for the shortest seed pulses, and hence also for the broadest generated continuum, the

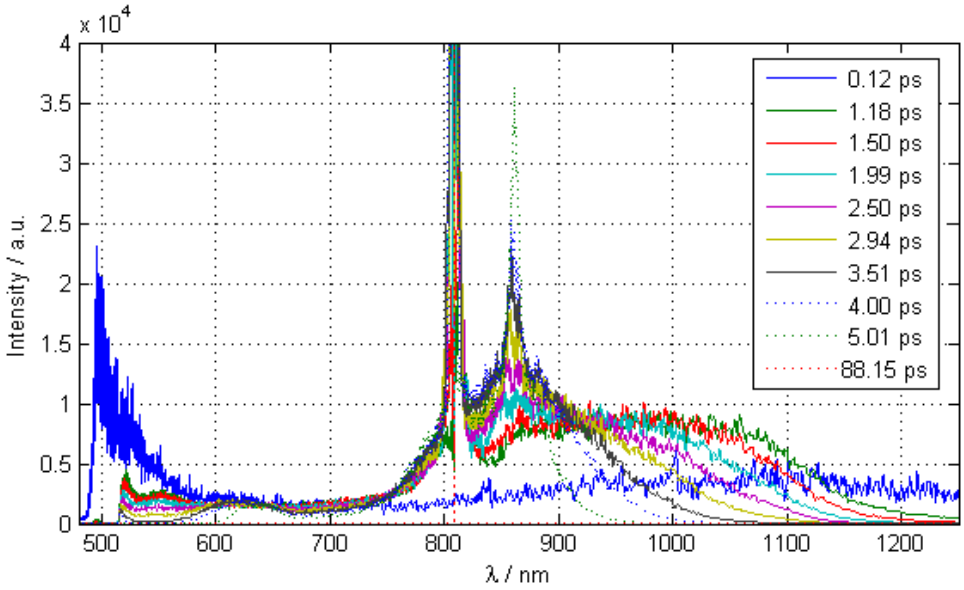

Figure A.1.: Simulated SC spectra averaged over 150 single pulse spectra for varying seed pulse length T_{FWHM} and constant average input power of 550 mW. For simulation details see section 5.1.

spectral density is considerably lower. In summary, the general trend of a broader SC spectrum expanding further into the longer wavelength range for a shorter seed pulse is obtained.

A.2. Two Photon Induced Auto Fluorescence of Single Daisy Pollen Grain

In order to further investigate the auto-fluorescence observed in the exine of a single daisy pollen grain (see figure 6.8 and discussion in section 6.4), first, the measured auto-fluorescence spectrum shown in figure A.2 (a) is compared with the 2PF spectra of two biological components (FAD and LipDH) reported in the literature [75] and reproduced in figure A.2 (b). Because a similar spectral shape and center position of 510 nm is observed in the fluorescence spectrum of FAD, the origin of the pollen auto-fluorescence in figure A.2 (a) is tentatively attributed to a flavoprotein (FAD).

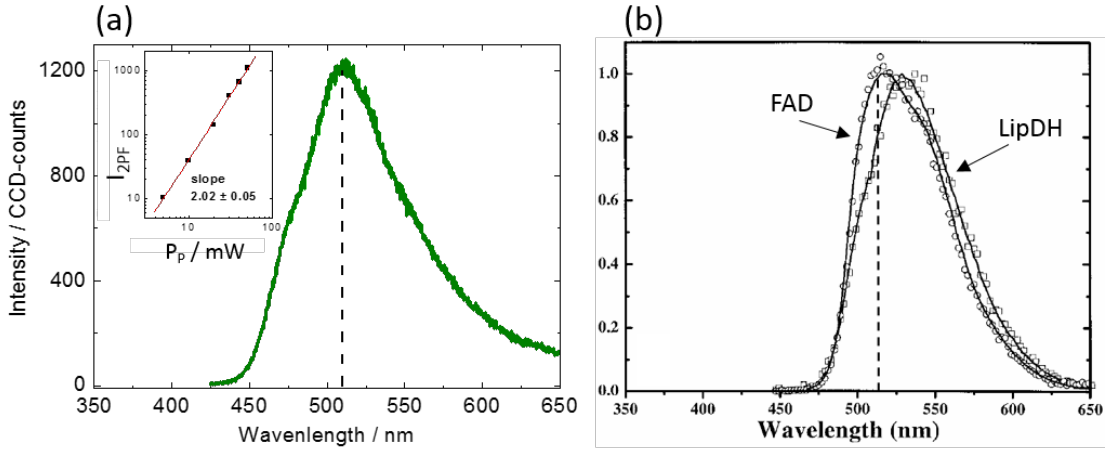

Figure A.2.: (a) Auto-fluorescence spectrum measured in the exine of a single daisy pollen grain upon 808 nm excitation. (b) 2PF spectra of FAD and LipDH adapted from reference [75]. The inset in (a) shows the dependence of the pollen auto-fluorescence intensity (black squares) on the incident average pump power in a log-log representation together with the linear fit (red curve) to the data. The horizontal dashed black lines are a guide to the eye indicating the spectral peak position at 510 nm.

Second, the dependence of the pollen auto-fluorescence intensity on the average pump pulse power P_P is measured, shown in the inset of figure A.2 (a) in a log-log plot. The linear fit to the data has a slope of 2.02 ± 0.05, and thus confirms that the observed auto-fluorescence is caused by a two-photon induced excitation process.

Acknowledgments

First of all, I thank my PhD advisor, Dr. Andreas Volkmer for guiding and supervising my PhD work. I benefited a lot from his great overview over the whole picture of the thesis topic and beyond that. His help in the design of the various setups, analyzing the data, conducting CARS simulations, and in revision of this thesis are gratefully acknowledged. His advise in argumentation lines strongly influenced me through numerous discussions.

I thank Prof. Dr. J. Wrachtrup for the possibility to do a PhD in his institute and for acting as main examiner for my PhD thesis. Furthermore, I acknowledge Prof. Dr. M. Dressel for acting as co-examiner for my PhD thesis. I wish to thank Gregor Hehl for the help in the first CARS experiments and for the development of the CARS data analysis scripts. Hui Wan I thank for the setup of the dispersion control and analysis for the SHG IAC data. Hilton B. Aguiar, and all group members I like to thank for great discussions especially about nonlinear microscopies, the nice atmosphere, and the mutual support. For fruitful discussions about broadband spontaneous FWM I thank Prof. Michael Rosenbluh, Dr. Avi Pe'er, and Dr. Rafi Vered. I would like to thank Monika Ubl for assistance in the profilometer measurements on the E-CARS sample. Thanks also go to Ralf Kamella and his team of the mechanical workshop for the production of numerous specialized parts for the various experimental setups, which were build during this thesis work.

Financial support from the European Commissions 7th Framework program within the project HEALTHF5-2008-200820 CARSEXPLORER, the European Cooperation in Science and Technology (COST) within the actions MP0603 MicroCARS and MP1102 MicroCoR, from the German Federal Ministry of Education and Research (BMBF) within the projects BMBF 13N10776 MEDICARS, BMBF 13N11074 MIKROQUANT, and BMBF 13GW0026 QuantumCARS is gratefully acknowledged.

I thank my parents, who always helped me in reaching my goals. Jota, I thank you so much for all the mental support and love you always give me, especially when I most needed it.

Bibliography

[1] A. Zumbusch, G. R. Holtom, and X. S. Xie. Three-dimensional vibrational imaging by coherent anti-Stokes Raman scattering. *Physical Review Letters*, 82(20):4142–4145, May 1999. 1, 7, 95

[2] G. P. Agrawal. *Nonlinear Fiber Optics*. Optics and Photonics. Academic Press, San Diego, fourth edition, 2006. 12, 13, 14, 15, 18, 57, 100, 102

[3] R. W. Boyd. *Nonlinear Optics*. Academic Press, Burlington, third edition, 2008. 12, 14, 18, 28, 29, 88

[4] N. Nishizawa and T. Goto. Compact system of wavelength-tunable femtosecond soliton pulse generation using optical fibers. *IEEE Photonics Technology Letters*, 11(3):325–327, Mar 1999. 13

[5] E. R. Andresen, V. Birkedal, J. Thøgersen, and S. R. Keiding. Tunable light source for coherent anti-Stokes Raman scattering microspectroscopy based on the soliton self-frequency shift. *Opt. Lett.*, 31(9):1328–1330, 2006. 13

[6] R. Engelbrecht. *Nichtlineare Faseroptik: Grundlagen und Anwendungsbeispiele*. Springer Berlin Heidelberg, 2015. 14

[7] H. Haken and H.C. Wolf. *Molekülphysik und Quantenchemie: Einführung in Die Experimentellen und Theoretischen Grundlagen*. Springer, 2003. 15

[8] J.M. Dudley and J.R. Taylor. *Supercontinuum Generation in Optical Fibers*. Cambridge University Press, 2010. 16, 53

[9] R. H. Stolen, C. Lee, and R. K. Jain. Development of the stimulated Raman-spectrum in single-mode silica fibers. *Journal of the Optical Society of America B-optical Physics*, 1(4):652–657, 1984. 17, 53, 148

[10] P. D. Maker and R. W. Terhune. Study of optical effects due to an induced polarization third order in electric field strength. *Physical Review*, 137(3A):A801–&, 1965. 17

[11] A. Volkmer. Vibrational imaging and microspectroscopies based on coherent anti-Stokes Raman scattering microscopy. *Journal of Physics D-applied Physics*, 38(5):R59–R81, Mar 2005. 18, 19, 21, 47, 120, 125, 148

[12] A. Volkmer. 6: Coherent Raman scattering microscopy. In P. Matousek and M. D. Morris, editors, *Emerging Raman Applications and Techniques in Biomedical and Pharmaceutical Fields*, pages 111 – 152. Springer, 1 edition, 2010. 20, 148

[13] R.W. Hellwarth. Third-order optical susceptibilities of liquids and solids. *Progress in Quantum Electronics*, 5:1–68, 1977. 19

[14] A. Volkmer, J.X. Cheng, and X.S. Xie. Vibrational imaging with high sensitivity via epidetected coherent anti-Stokes Raman scattering microscopy. *Physical Review Letters*, 87(2):023901, Jul 2001. 21, 119, 120, 125, 129, 130, 158

[15] J. X. Cheng, A. Volkmer, L. D. Book, and X. S. Xie. Multiplex coherent anti-stokes Raman scattering microspectroscopy and study of lipid vesicles. *Journal of Physical Chemistry B*, 106(34):8493–8498, Aug 2002. 22

[16] Jr. Camp, C. H., Y. J. Lee, J. M. Heddleston, C. M. Hartshorn, A. R. H. Walker, J. N. Rich, J. D. Lathia, and M. T. Cicerone. High-speed coherent Raman fingerprint imaging of biological tissues. *Nature Photonics*, 8(8):627–634, Aug 2014. 22

[17] M. Müller and J.M. Schins. Imaging the thermodynamic state of lipid membranes with multiplex CARS microscopy. *Journal of Physical Chemistry B*, 106(14):3715–3723, Apr 2002. 22

[18] E. O. Potma, C. L. Evans, and X. S. Xie. Heterodyne coherent anti-Stokes Raman scattering (CARS) imaging. *Opt. Lett.*, 31(2):241–243, Jan 2006. 25, 99

[19] L. Lepetit, G. Cheriaux, and M. Joffre. Linear techniques of phase measurement by femtosecond spectral interferometry for applications in spectroscopy. *Journal of the Optical Society of America B-optical Physics*, 12(12):2467–2474, Dec 1995. 25

[20] A. Wipfler, J. Rehbinder, T. Buckup, and M. Motzkus. Full characterization of the third-order nonlinear susceptibility using a single-beam coherent anti-Stokes Raman scattering setup. *Optics Letters*, 37(20):4239–4241, Oct 2012. 25

[21] A. Laurebeau and W. Kaiser. Vibrational dynamics of liquids and solids investigated by picosecond light-pulses. *Reviews of Modern Physics*, 50(3):607–665, 1978. 26, 111

[22] A. Volkmer, L. D. Book, and X. S. Xie. Time-resolved coherent anti-Stokes Raman scattering microscopy: Imaging based on Raman free induction decay. *Applied Physics Letters*, 80(9):1505–1507, 2002. 26, 112, 118

[23] S. Mukamel. *Principles of nonlinear optical spectroscopy*. Oxford series in optical and imaging sciences. Oxford University Press, 1995. 26, 29

[24] A. Volkmer. Personal communication, Dr. A. Volkmer, Universität Stuttgart, Jul 2015. 28, 104

[25] R. Vered, M. Rosenbluh, and A. Pe'er. Two-photon correlation of broadband-amplified spontaneous four-wave mixing. *Physical Review A*, 86:43837–, Oct 2012. 28, 100, 104

[26] I. Abram, R. K. Raj, J. L. Oudar, and G. Dolique. Direct observation of the second-order coherence of parametrically generated light. *Phys. Rev. Lett.*, 57:2516–2519, Nov 1986. 28

[27] C. Xu and W. W. Webb. Measurement of two-photon excitation cross sections of molecular fluorophores with data from 690 to 1050 nm. *J. Opt. Soc. Am. B*, 13(3):481–491, Mar 1996. 29

[28] Th. Dreisch and H. Konen. *Handbuch Der Physik: Licht und Materie*. Number Bd. 21. Springer-Verlag, 1929. 29

[29] NKT-Photonics. *FemtoWHITE 800 - Datasheet*. NKT Photonics, Blokken 84, 3460 Birkeroed, Denmark, fw800-110822 edition. 32, 53, 151

[30] K. P. Hansen and R. E. Kristiansen. Supercontinuum generation in photonic crystal fibers. Application note, Crystal Fibre SA, Nov 2004. 33, 149

[31] T. Schreiber. IOF Faser NKT NL-PM-800. Personal Communication, July 2014. Fraunhofer Institut fuer Angewandte Optik und Feinmechanik IOF Albert-Einstein-Strasse 7 07445 Jena Germany. 33, 149

[32] Crystal-Fiber. *Nonlinear Photonic Crystal Fiber - NL-800 Series List*. Crystal Fiber A/S, Blokken 84 - DK-3460 Birkenroed - Denmark, rev 1.5 edition, July 2006. 33

[33] G. Tempea, H. Wan, S. Gomes da Costa, H. B. De Aguiar, and A. Volkmer. Nonlinear optical microscopy with few-cycle laser pulses. In *OSA Technical Digest (online)*, pages JM2O.4–, San Jose, California, 2013. Optical Society of America. 38

[34] H. Wan. *Nonlinear optical microspectroscopy with few-cycle laser pulses*. PhD thesis, Universität Stuttgart, 2017. 38, 43, 113, 156

[35] S. Scherer, E. Wollrab, L. Codutti, T. Carlomagno, S. Gomes da Costa, A. Volkmer, A. Bronja, O. J. Schmitz, and A. Ott. Chemical analysis of a "Miller-Type" complex prebiotic broth: Part II: Gas, oil, water and the oil/water-interface. *Origins of Life and Evolution of Biospheres*, 47(4):381–403, 2016. 45, 80, 87, 153

[36] F. Hendriks and A. Aviram. Use of zinc iodide solutions in flow research. *Review of Scientific Instruments*, 53(1):75–78, 1982. 46, 121

[37] MathWorks Inc. *MATLAB R2012a (7.14.0.739)*, 2012. 46

[38] G. F. M. Hehl. *Quantitative coherent anti-Stokes Raman scattering microspectroscopy: theory and applications*. PhD thesis, Universität Stuttgart, Stuttgart, 2015. 47, 48

[39] E. M. Vartiainen. Phase retrieval approach for coherent anti-Stokes Raman scattering spectrum analysis. *J. Opt. Soc. Am. B*, 9(8):1209–1214, Aug 1992. 47

[40] E. M. Vartiainen, H. A. Rinia, M. Muller, and M. Bonn. Direct extraction of Raman line-shapes from congested CARS spectra. *Optics Express*, 14(8):3622–3630, Apr 2006. 47

[41] R. K. Reddy and R. Bhargava. 8: Chemometric methods for biomedical Raman spectroscopy and imaging. In P. Matousek and M. D. Morris, editors, *Emerging Raman Applications and Techniques in Biomedical and Pharmaceutical Fields*, pages 181 – 213. Springer, 1 edition, 2010. 48, 90

[42] WITec GmbH. *WITec Project Version 2.10 (2.10.3.3)*, 2012. 50

[43] M. Kubista, R. Sjöback, S. Eriksson, and B. Albinsson. Experimental correction for the inner-filter effect in fluorescence spectra. *Analyst*, 119:417–419, 1994. 50

[44] H. N. Paulsen, K. M. Hilligse, J. T., S. R. Keiding, and J. J. Larsen. Coherent anti-Stokes Raman scattering microscopy with a photonic crystal fiber based light source. *Opt. Lett.*, 28(13):1123–1125, Jul 2003. 51

[45] H. Kano and H. Hamaguchi. Ultrabroadband (>2500 cm^{-1}) multiplex coherent anti-Stokes Raman scattering microspectroscopy using a supercontinuum generated from a photonic crystal fiber. *Applied Physics Letters*, 86(12):121113, 2005.

[46] G. I. Petrov, R. Arora, V. V. Yakovlev, X. Wang, A. V. Sokolov, and M. O. Scully. Comparison of coherent and spontaneous Raman microspectroscopies for noninvasive detection of single bacterial endospores. *Proceedings of the National Academy of Sciences*, 104(19):7776–7779, 2007. 51

[47] F. Parmigiani, C. Finot, K. Mukasa, M. Ibsen, M. A. F. Roelens, P. Petropoulos, and D. J. Richardson. Ultra-flat SPM-broadened spectra in a highly nonlinear fiber using parabolic pulses formed in a fiber Bragg grating. *Optics Express*, 14(17):7617–7622, Aug 2006. 51

[48] J. C. Travers, J. M. Stone, A. B. Rulkov, B. A. Cumberland, A. K. George, S. V. Popov, J. C. Knight, and J. R. Taylor. Optical pulse compression in dispersion decreasing photonic crystal fiber. *Opt. Express*, 15(20):13203–13211, Oct 2007. 51

[49] J. M. Dudley, G. Genty, and S. Coen. Supercontinuum generation in photonic crystal fiber. *Reviews of Modern Physics*, 78(4):1135–1184, Oct 2006. 51, 54

[50] D. R. Solli, G. Herink, B. Jalali, and C. Ropers. Fluctuations and correlations in modulation instability. *Nature Photonics*, 6(7):463–468, Jul 2012. 51, 60

[51] Crystal-Fiber. *Nonlinear Photonic Crystal Fiber - NL-PM-750*. Crystal Fiber A/S, Blokken 84 - DK-3460 Birkenroed - Denmark, rev 1.3 edition, Nov 2003. 52, 53, 151

[52] F. Li, Q. Li, J. Yuan, and P. K. A. Wai. Highly coherent supercontinuum generation with picosecond pulses by using self-similar compression. *Opt. Express*, 22(22):27339–27354, Nov 2014. 53

[53] D. Hollenbeck and C. D. Cantrell. Multiple-vibrational-mode model for fiber-optic Raman gain spectrum and response function. *Journal of the Optical Society of America B-optical Physics*, 19(12):2886–2892, Dec 2002. 53

[54] M. Droques, B. Barviau, A. Kudlinski, M. Taki, A. Boucon, T. Sylvestre, and A. Mussot. Symmetry-breaking dynamics of the modulational instability spectrum. *Optics Letters*, 36(8):1359–1361, Apr 2011. 57

[55] SDBS No.: 672 Benzaldehyde. https://sdbs.db.aist.go.jp/sdbs/cgi-bin/landingpage?sdbsno=672, Feb 2019. 67

[56] J. X. Cheng, A. Volkmer, and X.S. Xie. Theoretical and experimental characterization of coherent anti-Stokes Raman scattering microscopy. *Journal of the Optical Society of Amreica B-Optical Physics*, 19(6):1363–1375, Jun 2002. 68, 120, 124, 127, 128, 129, 130, 158

[57] H. C. Urey. On the early chemical history of the earth and the origin of life. *Proceedings of the National Academy of Sciences of the United States of America*, 38(4):351–363, Apr 1952. 80

[58] S. L. Miller. A production of amino acids under possible primitive earth conditions. *Science*, 117(3046):528–529, 1953. 80

[59] E. Wollrab, S. Scherer, F. Aubriet, V. Carré, T. Carlomagno, L. Codutti, and A. Ott. Chemical analysis of a "Miller-Type" complex prebiotic broth: Part I: Chemical diversity, oxygen and nitrogen based polymers. *Origins of Life and Evolution of Biospheres*, 46(2):149–169, 2016. 80

[60] D. Lin-Vien, N.B. Colthup, W.G. Fateley, and J.G. Grasselli. *The Handbook of Infrared and Raman Characteristic Frequencies of Organic Molecules*. Elsevier Science, 1st edition, 1991. 84, 90

[61] H. Imanaka, B. N. Khare, J. E. Elsila, E. L. O. Bakes, C. P. McKay, D. P. Cruikshank, S. Sugita, T. Matsui, and R. N. Zare. Laboratory experiments of Titan tholin formed in cold plasma at various pressures: implications for nitrogen-containing polycyclic aromatic compounds in Titan haze. *Icarus*, 168(2):344–366, Apr 2004. 84

[62] J. M. Bernard, E. Quirico, O. Brissaud, G. Montagnac, B. Reynard, P. McMillan, P. Coll, M. J. Nguyen, F. Raulin, and B. Schmitt. Reflectance spectra and chemical structure of Titan's tholins: Application to the analysis of Cassini-Huygens observations. *Icarus*, 185(1):301–307, Nov 2006. 84

[63] E. Quirico, G. Montagnac, V. Lees, P. F. McMillan, C. Szopa, G. Cernogora, J. N. Rouzaud, P. Simon, J. M. Bernard, P. Coll, N. Fray, R. D. Minard, F. Raulin, B. Reynard, and B. Schmitt. New experimental constraints on the composition and structure of tholins. *Icarus*, 198(1):218–231, Nov 2008. 84

[64] S. Bienz, L. Bigler, and T. Fox. *Spektroskopische Methoden in der organischen Chemie*. Georg Thieme Verlag, Stuttgart, New York, 2012. 85

[65] J. Oro and A. P. Kimball. Synthesis of purines under possible primitive earth conditions .1. adenine from hydrogen cyanide. *Archives of Biochemistry and Biophysics*, 94(2):217–&, 1961. 85, 87

[66] F. Schulte. Raman-Spektroskopie als Werkzeug für die Charakterisierung und Klassifizierung von Pollen. Master thesis, Humboldt Universität zu Berlin, Berlin, 2010. 89

[67] G. J. Brakenhoff, J. Squier, T. Norris, A. C. Bliton, M. H. Wade, and B. Athey. Real-time two-photon confocal microscopy using a femtosecond, amplified Ti:sapphire system. *Journal of Microscopy*, 181(3):253–259, 1996. 89, 95

[68] J. A. Feijo and N. Moreno. Imaging plant cells by two-photon excitation. *Protoplasma*, 223(1):1–32, Mar 2004. 89, 95

[69] H. Kano and H. Hamaguchi. Vibrational imaging of a single pollen grain by ultrabroadband multiplex coherent anti-stokes Raman scattering microspectroscopy. *Chemistry Letters*, 35(10):1124–1125, Oct 2006. 89

[70] N. Patincharath, A. Kovalev, and A Volkmer. Vibrational imaging based on stimulated Raman scattering microscopy. *New Journal of Physics*, 11:033026, 03 2009. 89

[71] J. MacQueen. Some methods for classification and analysis of multivariate observations. In *Fifth Berkeley Symposium on Mathematical Statistics and Probability*, pages 281–297, Berkeley, Calif., 1967. University of California Press. 90

[72] T. Dieing, O. Hollricher, and J. Toporski. *Confocal Raman Microscopy*. Springer Berlin Heidelberg, 2011. 90

[73] B.B. Buchanan, W. Gruissem, and R.L. Jones. *Biochemistry and Molecular Biology of Plants*. Wiley, 1st edition, 2000. 90, 93

[74] N. P. Ivleva, R. Niessner, and U. Panne. Characterization and discrimination of pollen by Raman microscopy. *Analytical and Bioanalytical Chemistry*, 381(1):261–267, Jan 2005. 92, 93

[75] S.H. Huang, A.A. Heikal, and W.W. Webb. Two-photon fluorescence spectroscopy and microscopy of NAD(P)H and flavoprotein. *Biophysical Journal*, 82(5):2811–2825, May 2002. 96, 135, 158

[76] N. I. Gabarayeva and V. V. Grigorjeva. Exine development in stangeria eriopus (stangeriaceae): ultrastructure and substructure, sporopollenin accumulation, the equivocal character of the aperture, and stereology of microspore organelles. *Review of Palaeobotany ans Palynology*, 122(3-4):185–218, Nov 2002. 98

[77] Y. Yacoby, R. Fitzgibbon, and B. Lax. Coherent cancellation of background in four-wave mixing spectroscopy. *Journal of Applied Physics*, 51(6):3072–3077, 1980. 99

[78] M. Jurna, J. P. Korterik, C. Otto, and H. L. Offerhaus. Shot noise limited heterodyne detection of CARS signals. *Opt. Express*, 15(23):15207–15213, Nov 2007. 99

[79] C. L. Evans, E. O. Potma, and X. S. Xie. Coherent anti-Stokes Raman scattering spectral interferometry: determinationof the real and imaginary components of nonlinear susceptibility $\chi^{(3)}$ for vibrational microscopy. *Opt. Lett.*, 29(24):2923–2925, Dec 2004. 99

[80] B. von Vacano, T. Buckup, and M. Motzkus. Highly sensitive single-beam heterodyne coherent anti-Stokes Raman scattering. *Optics Letters*, 31(16):2495–2497, Aug 2006. 99

[81] B. Littleton, T. Kavanagh, F. Festy, and D. Richards. Spectral interferometric implementation with passive polarization optics of coherent anti-Stokes Raman scattering. *Physical Review Letters*, 111(10):103902, Sep 2013. 99

[82] A. Volkmer, A. Pe'er, and M. Rosenbluh. QuantumCARS-BIO-DISC 7: Grundlagen der hyperspektralen CARS-Bildgebung mit quanten-korrelierten Photonen. Report BMBF project 13GW0026, Universität Stuttgart, 3. Physikalisches Institut, 2016. https://doi.org/10.2314/GBV:868668613. 101, 154

[83] R. Z. Vered, Y. Shaked, Y. Ben-Or, M. Rosenbluh, and A. Pe'er. Classical-to-quantum transition with broadband four-wave mixing. *Phys. Rev. Lett.*, 114:063902, Feb 2015. 103

[84] A. Pe'er, Y. Bromberg, B. Dayan, Y. Silberberg, and A. A. Friesem. Broadband sum-frequency generation as an efficient two-photon detector for optical tomography. *Opt. Express*, 15(14):8760–8769, Jul 2007. 104

[85] F. M. Kamga and M. G. Sceats. Pulse-sequenced coherent anti-Stokes Raman scattering spectroscopy: a method for suppression of the nonresonant background. *Opt. Lett.*, 5(3):126–128, Mar 1980. 111

[86] H Hamaguchi and T L Gustafson. Ultrafast time-resolved spontaneous and coherent Raman spectroscopy: The structure and dynamics of photogenerated transient species. *Annual Review of Physical Chemistry*, 45(1):593–622, 1994. 111

[87] M. Heid, T. Chen, U. Schmitt, and W. Kiefer. Spectrally resolved fs-CARS as a probe of the vibrational dynamics of a large polyatomic molecule: magnesium octaethylporphyrin. *Chemical Physics Letters*, 334(1):119 – 126, 2001. 111

[88] Y. J. Lee and M. T. Cicerone. Vibrational dephasing time imaging by time-resolved broadband coherent anti-Stokes Raman scattering microscopy. *Applied Physics Letters*, 92(4):041108, 2008. 112, 118

[89] R. Selm, M. Winterhalder, A. Zumbusch, G. Krauss, T. Hanke, A. Sell, and A. Leitenstorfer. Ultrabroadband background-free coherent anti-Stokes Raman scattering microscopy based on a compact Er:fiber laser system. *Opt. Lett.*, 35(19):3282–3284, Oct 2010. 112

[90] D. Oron, N. Dudovich, and Y. Silberberg. Femtosecond phase-and-polarization control for background-free coherent anti-Stokes Raman spectroscopy. *Phys. Rev. Lett.*, 90:213902, May 2003. 112

[91] B. Chen and S. Lim. Optimal laser pulse shaping for interferometric multiplex coherent anti-Stokes Raman scattering microscopy. *The Journal of Physical Chemistry B*, 112(12):3653–3661, 2008. PMID: 18303885. 112

[92] K.W.F. Kohlrausch. Ramanspektrum und Benzolsymmetrie. *Naturwissenschaften*, 23(36):624–625, 1935. 116, 117

[93] F. A. Miller. Misassignment of the strong Raman band near 1000 cm-1 in some substituted benzenes, and the Herzberg versus Wilson convention for numbering the vibrations of benzene. *J. Raman Spectrosc.*, 19(3):219–221, 1988. 117

[94] H. W. Hubble, T. S. Lai, and M. A. Berg. Raman free-induction-decay measurements in low viscosity and supercooled toluene: Vibrational dephasing by shear fluctuations. *Journal of Chemical Physics*, 114(8):3662–3673, Feb 2001. 116

[95] G. Varsányi. 3 - normal vibrations of benzene and its derivatives. In G. Varsányi, editor, *Vibrational Spectra of Benzene Derivatives*, pages 141 – 393. Academic Press, 1969. 117

[96] G. Herzberg. *Infrared and Raman Spectra of Polyatomic Molecules*. Krieger Publishing Company, 1945. 117

[97] J. K. Wilmshurst and H. J. Bernstein. The iinfrared and Raman spectra of toluene, toluene-α-d3, m-xylene, and m-xylene-$\alpha\alpha$'-d6. *Can. J. Chem.*, 35(8):911–925, Aug 1957. 117

[98] S. D. McGrane, R. J.Scharff, M. Greenfield, and D. S. Moore. Coherent control of multiple vibrational excitations for optimal detection. *New Journal of Physics*, 11(10):105047, 2009. 117, 118

[99] B. D. Prince, A. Chakraborty, B. M. Prince, and H. U. Stauffer. Development of simultaneous frequency- and time-resolved coherent anti-Stokes Raman scattering for ultrafast detection of molecular Raman spectra. *The Journal of Chemical Physics*, 125(4):044502, 2006. 118

[100] K. J. I. Ember, M. A. Hoeve, S. L. McAughtrie, M. S. Bergholt, B. J. Dwyer, M. M. Stevens, K. Faulds, S. J. Forbes, and C. J. Campbell. Raman spectroscopy and regenerative medicine: a review. *npj Regenerative Medicine*, 2(1):12–, 2017. 119

[101] N. Das, Y. Dai, P. Liu, C. Hu, L. Tong, X. Chen, and Z. Smith. Raman plus x: Biomedical applications of multimodal Raman spectroscopy. *Sensors*, 17(7):1592, 2017.

[102] C.L. Evans, E.O. Potma, M. Puoris'haag, D. Cote, C.P. Lin, and X.S. Xie. Chemical imaging of tissue in vivo with video-rate coherent anti-Stokes Raman scattering microscopy. *Proceedings of the National Academy orf Sciences of the United States of America*, 102(46):16807–16812, Nov 2005.

[103] A. J. Wright, S. P. Poland, J. M. Girkin, C. W. Freudiger, C. L. Evans, and X. S. Xie. Adaptive optics for enhanced signal in CARS microscopy. *Opt. Express*, 15(26):18209–18219, 2007.

[104] T. Haohua and Boppart S. A. Coherent anti-Stokes Raman scattering microscopy: overcoming technical barriers for clinical translation. *Journal of Biophotonics*, 7(1-2):9–22, 2014. 119

[105] J.X. Cheng, A. Volkmer, L. D. Book, and X. S. Xie. An epi-detected coherent anti-Stokes Raman scattering (e-cars) microscope with high spectral resolution and high sensitivity. *The Journal of Physical Chemistry B*, 105(7):1277–1280, 2001. 119

[106] E.O. Potma and X.S. Xie. Detection of single lipid bilayers with coherent anti-Stokes Raman scattering (CARS) microscopy. *Journal of Raman Spectroscopy*, 34(9):642–650, Sep 2003. 119

[107] N. Sultanova, S. Kasarova, and I. Nikolov. Dispersion properties of optical polymers. *Acta Physica Polonica, A*, 116(4):585–587, 2009. Extracted from refractiveindex.info on 25.03.2018. 121

List of Figures

3.1. Schematic representation of energy level diagrams for (a) spontaneous FWM process, (b) for the processes of Stokes (left panel) and anti-Stokes (right panel) spontaneous Raman scattering, and (c) the narrowband CARS process. Solid horizontal lines represent the electronic and vibrational states. Dashed horizontal lines represent virtual states. $\hbar\Omega$ represents the energy of an exemplary vibrational resonance. 14

3.2. Raman gain of fused silica, taken from Stolen et al. [9] 17

3.3. Formation of the dispersive CARS line shape and its single contributions for a simulated Lorentzian Raman resonance according to equation (3.21) ($\Gamma_r = 4.6\ cm^{-1}$, $A_{r,1111} = 4\ cm^{-1}$). The total CARS signal proportional to $\left|\chi^{(3)}\right|^2$ (solid line) is composed of the non-resonant contribution $(\chi^{(3)}_{NR})^2$ (dotted line), the resonant part $\left|\chi^{(3)}_r\right|^2$ (dashed line), and the mixing term of both $2\chi^{(3)}_{NR}Re(\chi^{(3)}_r)$ (dash-dotted line). Figure taken from reference [12] 20

3.4. a) Wave vectors in the focus center for forward- and epi-detected CARS microscopies. A schematic representation of the CARS emission from (b) a microscopic sphere with diameter $D_{obj} \ll \lambda_P/2$ (blue arrows), the surrounding bulk medium (light blue arrows), and (c) a sphere with a diameter $D_{obj} \approx \lambda_P/2$ is shown. Additionally in (c), the solvents F-CARS emission back-reflected at the objects surface is shown (white arrow). $\chi^{(3)}_{obj}$ and $\chi^{(3)}_{solv}$ are the third order susceptibilities for the object and the surrounding solvent, respectively. The figure is adapted from reference [11]. 21

3.5. Different possibilities of multiplex CARS excitation. (a) Scheme A: The broadband pulse is acting as the Stokes field only, and the narrowband pulse provides the pump and probe fields. (b) Scheme B: The broadband pulse is acting as both the pump and Stokes fields and the narrowband pulse acts as the probe field only. 23

4.1. Schematic representation of the setup for SCG and characterization. FI: Faraday isolator, M: steering mirrors, BS1: beam splitter, $(\lambda/2)1$ and $(\lambda/2)2$: lambda-half wave plate, P: polarizer, $L1$ - $L4$ and LS: lenses, $OL1$ and $OL2$: objective lenses, VND: variable neutral density filter, $HNPF$: holographic notch filter, ND: neutral density filters. 32

4.2. (a) Schematics of the nonlinear PCFs [30] used for broadband SCG in hyperspectral CARS imaging and as a broadband spontaneous FWM source [30], (b) microscope image of the custom-made end piece of the PCF NLPM800 after fusing and end-sealing [31]. 33

4.3. Schematic representation of the home-built multiplex-CARS microspectrometer setup. FI: Faraday isolator, $BS1$: beam splitter, $\lambda/2$: half wave plate, P: polarizing beam splitter, $L1$-$L10$ and LS: lenses, M: steering mirrors, $OL1$ and $OL2$: objective lenses, VND: variable neutral density filter, $HNPF$: holographic notch filter, DCC and DCE: dichroic mirrors, DL: delay line, LP: long-pass filter, $MO1$ and $MO2$: microscope objective lenses, S: sample scanning stage including sample holder, SP: short-pass filters, FM: flip mirror. The multi-colored line represents the spatially and temporally overlapped pump, Stokes and signal beams. 35

4.4. Schematic representation of the home-built setup for interferometric hyperspectral CARS imaging with broadband correlated photon pairs. FI: Faraday isolator, $BS1$: beam splitter, $(\lambda/2)1$ and $(\lambda/2)2$: half wave plates, P: polarizing beam splitter, $L1$-$L8$ and LS: lenses, M: steering mirrors, $OL1$: objective lens, $OAMP$: off-axis parabolic mirror, $HNPF$: holographic notch filter, $DL1$ and $DL2$: delay lines, VND: variable neutral density filters, DGL: dispersive glass wedges, $DCMP$: dispersion compensation mirror pairs, $PM1$ and $PM2$: parabolic mirrors, $DC2$ and $DC3$: dichroic mirror, $SP1$ and $SP2$: short-pass filters, $MO3$ and $MO4$: microscope objective lenses, S: sample scanning stage including sample holder. The multi-colored line represents the spatially and temporally overlapped pump, Stokes and signal beams. 39

4.5. Recorded interferometric signal stability of the second interferometer defined by $DC2$ and $DC3$, see figure 4.4 using a 633-nm reference laser, while performing a continuous sweep of $\Delta\phi_2$ (blue curve), at a fixed $\Delta\phi_2 = \frac{\pi}{2}$ with the box open (red curve), and at a fixed $\Delta\phi_2 = \frac{\pi}{2}$ with a closed box (green curve). 41

4.6. Schematic representation of the home-built setup for 2D CARS microspectroscopy with a ps- and a few-cycle fs-pulse. FI: Faraday isolator, $BS1$ and $BS2$: beam splitters, $F1$ and $F2$: optical fibers, $(\lambda/2)1$ and $(\lambda/2)3$: half wave plates, P: polarizing beam splitter, $L1$-$L12$ and LS: lenses, M: steering mirrors, DL: delay line, VND: variable neutral density filter, CUF: laser clean up filter, $DCAC$: dichroic mirror in auto-correlator, DGL: dispersive glass wedges, $DCMP$: dispersion compensation mirror pairs, $PM1$ and $PM2$: parabolic mirrors, LP: long pass filter, $DC5$ and $DC6$: dichroic mirrors, $MO1$ and $MO5$: microscope objective lenses, S: sample scanning stage including sample holder, $SP1$ and $SP2$: short pass filters. The multi-colored line represents the spatially and temporally overlapped pump, Stokes and probe beams. 42

4.7. Correction procedure for recorded sample E-CARS spectra. Dark-count corrected E-CARS spectrum of PMMA (blue curve), the epi-detected background spectrum when both beams are blocked before the microscope (green curve), with all pulses incident on the ZnI_2 but having no time overlap (nto) (red curve), with all pulses incident on the $PMMA$ but having no time overlap (nto) (cyan curve), the pump pulses incident only (magenta curve), and the Stokes pulses incident only (yellow curve). 49

5.1. Dispersion curve of the PCF FemtoWHITE800 [29, 51] extrapolated with a 18th order polynomial fit to the manufacturers data. 53

5.2. Simulation of SC generation along the length of the PCF in the frequency- (left) and time-domains (right) for a single 2.94-ps ($sech^2$) seed pulse at 808 nm with an average input power of 550 mW. The intensity is color-coded on a logarithmic scale in dB. 55

5.3. Simulated spectral (a) to (c) and temporal (d) and (e) profiles of phase (a), amplitude (b and d), and intensity (c and e) for a single 2.94 ps ($sech^2$) seed pulse (green curves) at 808 nm with an average input power of 550 mW, and for a typical single SC pulse (blue curves) simulated at the output of the 12 cm long PCF (compare figure 5.2). 56

5.4. Comparison of SC spectra obtained from simulations (blue curves) and experimental measurements (green curves) at four different seed power regimes in the vicinity of the seed wavelength (a, c, e and g) and over the full spectral range of SC generation (b, d, f and h). See text for experimental and simulation details. 58

5.5. Simulation of SC generation along the length of the PCF in the frequency- (left) and time-domain (right) for a single 123 fs ($sech^2$) seed pulse at 808 nm with an average input power of 100 mW. The intensity is color-coded on a logarithmic scale in dB. 61

5.6. Simulated spectral (a-c) and temporal (d and e) profiles of phase (a), amplitude (b and d) and intensity (c and e) for a single 123-fs ($sech^2$) seed pulse (green curves) at 808 nm with an average input power of 100 mW, and for a typical single SC pulse (blue curves) simulated at the end of a 12 cm PCF (compare figure 5.5). 63

5.7. Simulation of SC generation along the length of the PCF in the frequency- (left panel) and time-domain (right panel) for a single 88 ps ($sech^2$) seed pulse at 808 nm with an average input power of 22400 mW. The intensity is color-coded on a logarithmic scale in dB. 64

5.8. Simulated spectral (a)-(c) and temporal (d) and (e) profiles of phase (a), amplitude (b) and (d), and intensity (c) and (e) for a single 88 ps ($sech^2$) seed pulse (green curves) at 808 nm with an average input power of 22400 mW, and for a typical single SC pulse (blue curves) simulated at the end of a 12 cm PCF (compare 5.7). 65

5.9. Simulated average supercontinuum spectra for seed pulse lengths of 2.94 ps, 123 fs, and 88 ps, and seed peak powers of 9428 W, 2170 W, and 2952 W, respectively. See text for further simulation details. . . . 66

5.10. Intensity spectra of simulated Stokes, pump, and CARS pulses using a 2.94-ps ($sech^2$) seed-, pump-, and probe-pulse. In green and cyan single pulse spectra are shown. In red and purple spectra averaged over 150 pulses are shown. The pump pulse is represented by the blue curve. 69

5.11. Simulated spectral ((a) and (b)), and temporal (c) profiles of CARS (a) phase-, (b) and (c) intensity generated with a 2.94-ps pump/probe pulse and a 2.94-ps seeded Stokes continuum pulse. In blue, single CARS pulse profiles are shown, while in green averages over 150 single CARS pulses are shown. 70

5.12. Simulated spectral (a) and (b), and temporal (c) profiles of CARS (a) phase-, (b) and (c) intensity generated with a 2.94-ps pump/probe pulse and a 123-fs seeded Stokes continuum pulse. In blue, single CARS pulse profiles are shown, while in green averages over 150 single CARS pulses are shown. 72

5.13. Simulated spectral (a) and (b), and temporal (c) profiles of CARS (a) phase-, (b) and (c) intensity generated with a 88-ps pump/probe pulse and a 88-ps seeded Stokes continuum pulse. In blue, single CARS pulse profiles are shown, while in green averages over 150 single CARS pulses are shown. 74

5.14. Simulated normalized CARS spectra averaged over 150 single pulses generated with Stokes SC pulses seeded with 123 fs, 2.94 ps and 88 ps ($sech^2$) pulses. Please note the logarithmic intensity offset between spectra by 2 orders of magnitude. 75

6.1. (a) Energy level diagram for multiplex CARS according to scheme A. Time-frequency representation for (b) fs-hyperspectral CARS (blue) with a broad fs-Stokes pulse (red) and for (c) all ps-hyperspectral CARS (blue) with a ps-Stokes continuum pulse (red). In both cases transform-limited pump- and probe-pulses (green) are assumed. The induced Raman excitation (dark red) at frequency $\omega_P - \omega_S$ is also shown with a representative Raman spectrum (black curve). 79

6.2. Miller-type experimental setups for the generation of prebiotic broth samples $A1-$ and $B2+$ using the electrical discharge (A) in the gaseous phase and (B) onto the water surface. Taken from Scherer et al. [35]. 80

6.3. Spontaneous Raman spectra of primordial broth solutions $A1-$ (black) and $B2+$ (red) obtained with a confocal Raman microscope under 532 nm cw-excitation wavelength and a few mW incident power at the sample. The acquisition time per spectrum was 100 ms. Shown are averages over 1000 spectra. 82

6.4. (a) Normalized CARS spectra of water (black curve) and of aqueous solutions of primordial broth sample $B2+$ (red curve) after dividing by a non-resonant reference spectrum (compare euqation 4.1). (b) Reconstructed $Im(\chi^{(3)}(\nu))$-spectra of water (black curve) and sample $B2+$ (red curve). (c) $Im(\chi^{(3)}(\nu))$ of primordial broth samples $A1-$ (black curve) and sample $B2+$ (red curve) after subtraction of the weighted $Im(\chi^{(3)}(\nu))$ spectrum of water. The spectra are offset by 0.02. See text and table 6.1 for peak assignments. Insets: zoom into the spectral region of C-H-stretching vibrations. CARS spectra of samples $A1-$ and $B2+$ where recorded with total acquisition times of 12.5 s and 50 s, respectively. The incident average laser pump and Stokes powers at the sample where 60 mW and 13 mW, respectively. 83

6.5. UVVIS absorption spectra (solid lines) and normalized two-photon induced fluorescence (2PF) spectra (dotted lines) of primordial broth samples $A1-$ (black curves) and $B2+$ (red curves). Both 2PF spectra were excited with an average pump laser power before the objective lens of 60 mW, and integration times were 5 s and 2.5 s, respectively. The insets show the zoom the spectral range around 404 nm and the log-log power dependences of 2PF intensities for samples $A1-$ (black squares) and $B2+$ (red circles) together with their linear fit (dashed lines). 85

6.6. (a) Bright-field image of cyclamen pollen grains, (b) integrated $Im(\chi^{(3)})$ amplitude image in the C-H-stretching vibrational region from 2750 to 3150 cm^{-1} of cyclamen pollen with three positions marked by the crosses in the cytoplasm, the nucleus, and the pollen shell, labeled A, B, and C, respectively, (c)K-means cluster map of the same sample region shown in (b), (d) corresponding cluster spectra with the same color code used in (c), (e) zoom into the fingerprint region of the cluster spectra shown in (d). 91

6.7. (a) Reconstructed $Im(\chi^{(3)})$ single pixel spectra for three different image positions A, B, and C marked with crosses in figure 6.6 (b). The colored horizontal lines mark the spectral positions used for extracting the $Im(\chi^{(3)})$ amplitude maps shown in (b) to (d). Next to the red and green lines are chemical structures of exemplary molecules that exhibit the characteristic spectral features. (e) RGB overlay image of the color-coded integrated $Im(\chi^{(3)})$ amplitude maps shown in (b) to (d). The scale bar in all images is 6 μm long. 94

6.8. Simultaneous hyperspectral CARS and 2PF imaging of the equatorial plane of a single daisy pollen grain. (a) Raw CARS (black curve) and 2PF (green curve) spectra of the pollen exine shell measured at the position A marked in (c). For comparison a raw CARS water spectrum (blue curve) measured at the position Bis also shown, (b) reconstructed $Im(\chi^{(3)})$ (black curve) and 2PF (green curve) spectra from the exine at position A, (c) 2PF intensity map, (d) $Im(\chi^{(3)})$-amplitude map at 1600 cm^{-1}, (e) RG-overlay image of the color-coded 2PF and $Im(\chi^{(3)})$ images. 96

6.9. 3D chemical map extracted from a 3D hyperspectral CARS imaging data set of a single unstained daisy pollen grain. Shown here are isosurfaces of reconstructed $Im(\chi^{(3)})$ amplitudes of characteristic Raman signatures for sporopollenin (blue), protein (red), nucleic acids (green) and of the endogenous 2PF from FAD molecules (yellow). . . 98

7.1. Energy level diagrams of (a) the broadband spontaneous FWM process for random signal-idler-pairs, (b) the broadband SFG process for the phase correlated photon pairs, (c) the interferometric hyperspectral CARS process in resonance with a vibrational state at $\hbar\Omega_r$ using the same pairs of signal and idler photons generated in (a). (d) Schematic illustration of interferometric CARS occurring in a nonlinear Raman-active medium described by $\chi^{(3)}$ (e.g. a living cell)[82]. . . 101

7.2. Measured broadband FWM spectra generated in the PCF NL-PM-800 with 2.37 ps seed pulses at different seed wavelengths, and at a fixed average seed power of 364 mW. Shown are averages over 100 spectra recorded at each grating center position of 570 nm, 800 nm, and 1000 nm. The integration time for a single spectrum was 10 ms . 102

7.3. Measured broadband spontaneous FWM spectra generated in the PCF NL-PM-800 with 2.37 ps seed pulses at different average powers and a fixed wavelength of 796 nm. The power levels given in the legends indicate the powers before the incoupling objective of the PCF. Shown are averages over 100 spectra recorded at each grating center position of 570 nm, 800 nm, and 1000 nm. The integration time for a single spectrum was 10 ms. 103

7.4. Characterization of the broadband signal and idler pulses generated by our spontaneous FWM source by SFG spectroscopy. The SFG signal is normalized to one at the maximum of the broad incoherent contribution. The intensity ratio of the coherent to incoherent SFG peaks is 20.7 : 1. The integration time was 50 ms. 105

7.5. Measured raw spectra of interferometric CARS for neat benzaldehyde at different phase differences $\Delta\phi$ between the signal and CARS fields. The interferometric CARS spectra are offset by 3000 CCD-counts each. The integration time per pixel were 50 ms. The average pump, Stokes, and signal powers at the sample position are 56.6 mW, 0.1 mW and approximately 0.0005 mW, respectively. For comparison, the corresponding standard multiplex CARS spectrum ($\propto |E_{CARS}|^2$) and the pure signal spectrum ($\propto |E_{Signal}|^2$) are also shown. 106

7.6. (a) Real part $Re(\chi^{(3)})$ (blue curve), imaginary part $Im(\chi^{(3)})$ (green curve), and phase of the $\chi^{(3)}(\nu)$ spectrum (black curve) as extracted from the interferometric CARS spectra of (a) glass and (b) neat benzaldehyde. The integration time per interferometric CARS spectrum was 50 ms. The average pump, Stokes and signal powers at the position of the sample were 56.6 mW, 0.1 mW, and approximately 0.0005 mW, respectively. 107

7.7. (a) $Im(\chi^{(3)})$ and (b) $Re(\chi^{(3)})$ image of a benzaldehyde droplet embedded in water at 1704 cm^{-1} extracted from measured interformetric hyperspectral CARS data generated for a phase difference of $\Delta\phi = \frac{\pi}{2}$ and $\Delta\phi = 0$, respectively. (c) Corresponding image extracted from interferometric hyperspectral CARS data recorded while sinusoidally modulating the phase difference $\Delta\phi$ at $\approx$ 0.3 Hz modulation frequency. Representative (d) $Im(\chi^{(3)}(\nu))$ and (e) $Re(\chi^{(3)}(\nu))$ spectra extracted from image pixels inside the benzaldehyde droplet in image (c), where $\Delta\phi = \frac{\pi}{2}$ and $\Delta\phi = 0$, respectively. Measurement parameters for (a) and (b): $26 \times 24\ \mu m^2$, 400 nm step size, 30 ms integration time per pixel spectrum, average pump, Stokes and signal powers are 59 mW , 1.5 mW and $\approx$ 0.005 mW, respectively. Measurement parameters for (c): $18.3 \times 19\ \mu m^2$, 350 nm step size, 50 ms integration time per pixel spectrum, average pump, Stokes, and signal powers are 59 mW , 1.5 mW and $\approx$ 0.001 mW, respectively. 109

8.1. (a) Spectrum of the few-cycle pulse (black line) centered at 808 nm, the probe pulse (green line) centered at 800 nm, and the transmission curve of the dichroic filter $DC4$ (orange line) used for spectral filtering the few-cycle pulse. (b) Interferometric SHG auto-correlation curve of the few cycle pulse in the focus of the high NA objective [34], with the measured data in black and the corresponding simulation in red. (c) Corresponding interferometric SHG auto-correlation curve (black line) of the same pulse, measured after passing through the dichroic filter $DC4$, with the corresponding simulation (red line). 113

8.2. (a) CARS-spectra of toluene measured with a few-cycle pulse providing the pump and Stokes fields and a ps-pulse providing the probe field at zero relative time delay between the fields $\Delta\tau_{Pr} = 0\ ps$ (blue line) and at $\Delta\tau_{Pr} = 3\ ps$ (green line). (b) Measured 2D-CARS spectrum of toluene with the CARS intensity being color-coded in a logarithmic scale. Measurement parameters: Average powers for the few-cycle fs- and the ps-pulses are 0.9 mW and 1.8 mW, respectively. The single spectrum integration time is 3 s. The temporal delay step size is 50 fs over a range of $\Delta\tau_{Pr}$ from $-3.36\ ps$ to $+13.44\ ps$. The white lines indicate the delay positions at which the spectra shown in (a) are extracted. The arrows indicate the spectral positions, at which the RFID curves shown in figure 8.3 are extracted. 115

8.3. Normalized time profiles of CARS intensities of neat toluene extracted at 507 cm^{-1} (black squares), 1000 cm^{-1} (red circles), 1019 cm^{-1} (green triangles) of toluene over the probe delay $\Delta\tau_{Pr}$, as indicated by the color-coded arrows in the 2D-CARS spectrum shown in figure 8.2 (b). The corresponding fit curves (solid lines) to a single exponential RFID model (equation (3.33)) are also shown. For comparison, the normalized CARS time profile is shown for an exemplary NR region extracted at 600 cm^{-1} (gray diamonds). 116

9.1. Schematics of index-matched PMMA wedge sample system for E-CARS experiments. 120

9.2. Dektak height profiles of a PMMA wedge before (black curve) and after (red curve) being embedded in ZnI_2 solution for approximately 4 h showing a slope of $(160 \pm 12)\, nm/\mu m$. 122

9.3. Measured normalized F-CARS spectra of pure ZnI_2 solution (blue curve) and of PMMA (green curve, offset by 1). Both spectra were normalized by the same NR-reference CARS spectrum. 123

9.4. Comparison of the E-CARS spectrum of a 224-nm thin PMMA layer (green curve), the spontaneous Raman spectrum of thick PMMA (black curve), and the $Im(\chi^{(3)})$-spectrum of thick PMMA reconstructed from the F-CARS spectrum shown in figure 9.3 (magenta curve). The spectra are scaled to the amplitude of the C-H stretching vibration at 2924 cm^{-1} and are offset by 100 arbitrary units each. Additionally, the unnormalized F-CARS raw spectrum of pure ZnI_2 solution is shown (blue curve), scaled to match the the spectral shape of the E-CARS spectrum in the NR spectral region. 126

9.5. Comparison of $Im(\chi^{(3)})$ amplitude (green curve) of PMMA at 2924 cm^{-1} reconstructed from measured F-CARS spectra with the independently recorded dektak height profile (blue curve) of the same wedge as a function of position x. The inset shows the zoom in into the thinnest part of the PMMA wedge. The horizontal dashed line indicates the saturation value of the $Im(\chi^{(3)})$ amplitude at large x-positions. 127

9.6. E-CARS spectra of the 224 nm thick (red curve) and the 352 nm thick (black curve) PMMA wedge. The spectra are offset by 100 CCD-counts for better clarity. 128

9.7. (a) 2D representation of the measured background-corrected E-CARS spectra versus x-position (thickness) of the PMMA wedge sample. The E-CARS intensity is color-coded. The white lines are a guide to the eye representing the maxima for an oscillation with a thickness periodicity of $\frac{\lambda_{AS}}{2n}$ predicted by theory [14]. (b) E-CARS intensity profiles over the x-position (thickness) at 1124 cm^{-1} (blue curve) and 2924 cm^{-1} (green curve) extracted along the horizontal lines marked by the corresponding arrows shown in (a). For comparison, a simulated E-CARS intensity profile for a sphere (red curve) taken from reference [56] is also shown. Both E-CARS profiles at 1124 cm^{-1} are offset by 7 $a.u.$ for better clarity. The vertical dashed black line marks the zero-thickness position. 129

9.8. Fourier-transform of the oscillatory part of the E-CARS intensity profile over wedge thickness at 2924 cm^{-1} shown in figure 9.7 (b). The black arrow indicates the peak corresponding to an oscillation thickness period of 232 nm. 130

A.1. Simulated SC spectra averaged over 150 single pulse spectra for varying seed pulse length T_{FWHM} and constant average input power of 550 mW. For simulation details see section 5.1. 134

A.2. (a) Auto-fluorescence spectrum measured in the exine of a single daisy pollen grain upon 808 nm excitation. (b) 2PF spectra of FAD and LipDH adapted from reference [75]. The inset in (a) shows the dependence of the pollen auto-fluorescence intensity (black squares) on the incident average pump power in a log-log representation together with the linear fit (red curve) to the data. The horizontal dashed black lines are a guide to the eye indicating the spectral peak position at 510 nm. 135

List of Symbols

α	Attenuation in the PCF
α_P	Linear polarizability of the sample
β	Effective refractive index
β_1	Inverse group velocity
$\lvert\beta_2\rvert$	Group velocity dispersion
Γ_r	Half width at half maximum of the Raman resonance at Ω_r
γ	Nonlinear coefficient of PCF
$\Delta\mathbf{k}_{FWM}$	Wave vector mismatch due to material dispersion
Δk_{NL}	Wave vector mismatch due to nonlinear contributions of SPM and XPM
Δk_{CARS}	Wave vector mismatch for CARS due to material dispersion
δ_r	Detuning from the Raman resonance at Ω_r
ϵ	Extinction coefficient
κ	Effective phase mismatch
λ	Wavelength
λ_{center}	Center wavelength of few-cycle pulse
λ_{min}	Minimum wavelength in SC simulations
λ_{Seed}	Seed wavelength
ν_{AS}	Anti-Stokes frequency
ν_P	Pump frequency
ν_S	Stokes frequency

ρ_r	Depolarization ratio of the Raman resonance at Ω_r
τ_P	Pulse length of few-cycle pulse
τ_{Pr}	Probe pulse time delay
ϕ_{AS}	Anti-Stokes phase
ϕ_{CARS}	CARS phase
ϕ_{Idler}	Idler phase
ϕ_P	Pump phase
ϕ_S	Stokes phase
ϕ_{Seed}	Seed phase
ϕ_{SFG}	SFG phase
ϕ_{Signal}	Signal phase
ϕ_{Stokes}	Stokes phase
$\chi^{(2)}(\nu)$	Second order nonlinear susceptibility
$\chi^{(3)}(\nu)$	Third order nonlinear susceptibility
$\chi^{(3)}_{1111}$	Third order nonlinear susceptibility with all electric fields linearly polarized along the same direction
$\chi^{(3)}_{NR}$	Non-resonant part of $\chi^{(3)}$
$\chi^{(3)}_{obj}$	$\chi^{(3)}$ of the sample object
$\chi^{(3)}_{r}$	Resonant part of $\chi^{(3)}$ of the Raman resonance at Ω_r
$\chi^{(3)}_{solv}$	$\chi^{(3)}$ of the surrounding solvent
$\Omega_{Idler,Max}$	Angular frequency where maximum idler is generated through FWM
$\Omega_{Signal,Max}$	Angular frequency where maximum signal is generated through FWM
ω	Angular frequency
ω_0	Angular optical seed center frequency
ω_{AS}	Angular anti-Stokes frequency
ω_{CARS}	Angular CARS frequency
ω_{Idler}	Angular idler frequency
ω_P	Angular pump frequency
ω_S	Angular Stokes frequency
ω_{Seed}	Angular seed frequency

ω_{SFG}	Angular SFG frequency
ω_{Signal}	Angular signal frequency
ω_{Stokes}	Angular Stokes frequency

A	Amplitude of the PCF input pulse
A_{NR}	Amplitude of the non-resonant sample response
$A_{r,1111}$	Amplitude of Raman resonance at frequency Ω_r
A_r^{aniso}	Amplitude of Raman resonance at frequency Ω_r
A_T	Amplitude of the PCF input pulse
A_{UVVIS}	UVVIS Absorbance of a material
$\tilde{A}'$	Complex spectral envelope of the pulse in the fiber
c	Speed of light in vacuum
c_{con}	Molar concentration of a molecular sample
d	Thickness of the sample
D	Material dispersion
D_{obj}	Diameter of microscopic sample sphere
dT	Temporal grid step size in SC simulations
E	Electrical field strength
E_{CARS}	CARS electric field
E_{Idler}	Idler beam electric field
$\mathbf{E}_P$	Pump electric field vector
$\mathbf{E}_S$	Stokes electric field vector
E_{Signal}	Signal beam electric field
E_{Stokes}	Stokes beam electric field
$F_{\Delta k}$	Phase matching function
Fl	Measured 2PF intensity
Fl_{corr}	Corrected 2PF intensity
f_{rep}	Pulse train repetition rate
g_{FWM}	FWM gain

$\hbar\Omega$	Energy of an exemplary vibrational resonance
I_0	Incident light intensity
I_1	Transmitted light intensity
I_{2PF}	Two-photon induced fluorescence time averaged photon flux
$I_{Fluorescence}$	Fluorescence intensity
I_{Fluo}	Fluorescence intensity
$I_{anti-Stokes}$	Spontaneous anti-Stokes Raman signal intensity
I_{CARS}	CARS signal intensity
$I_{CARS,ref}$	CARS signal intensity of the NR reference
I_{CARS}	CARS signal intensity of the sample
I_{SFG}	SFG signal intensity
I_{Idler}	Idler beam intensity
I_P	Pump beam intensity
I_{Signal}	Signal beam intensity
I_{Stokes}	Spontaneous Stokes Raman signal intensity
$\mathbf{k}_{AS}$	Anti-Stokes wave vector
$\mathbf{k}_{Idler}$	Idler wave vector
$\mathbf{k}_P$	Pump wave vector
$\mathbf{k}_S$	Stokes wave vector
$\mathbf{k}_{Seed}$	Seed wave vector
$\mathbf{k}_{Signal}$	Signal wave vector
k_{SR}	Proportionality factor including the experimental detection efficiency
$\hat{L}$	Complex linear operator
L_D	Dispersion length
L_{NL}	Nonlinear length
n	Linear refractive index
$\tilde{n}$	Total refractive index
n_2	Nonlinear-index coefficient

P_0	Optical peak power of incident pulse
$P^{(2)}$	Second order nonlinear polarization
$\mathbf{P}^{(3)}_{Idler}$	Third order nonlinear polarization vector
$\mathbf{P}^{(3)}_{CARS}$	Third order nonlinear polarization vector at the CARS frequency
P_P	Time averaged excitation power
$R(T')$	Raman response of the nonlinear medium
S	Detected interferometric CARS Signal
S_{CARS}	Normalized CARS intensity
T	Time in the conmoving frame in the fiber
T_0	Temporal width of the PCF input pulse
$T_{2,r}$	Dephasing time of the vibrational resonance r
T'	Integration variable equivalent to T
T_{FWHM}	FWHM of pulse intensity profile
$T_{or,r}$	Rotational correlation time of the vibrational resonance at frequency Ω_r
T_{sample}	Sample temperature
T_{Seed}	Seed pulse length
T_{width}	Time window width for SC simulations
t	Time
t_2	Integration variable equivalent to t
y_0	CARS signal intensity background
z	Propagation length inside the fiber
$\mathfrak{F}$	Symbol for the Fourier transformation

Statement of Authorship

This Ph.D. thesis is the result of my own work. Published or unpublished work of others is credited to the author in the text. Except where references are made, the thesis contains no material published elsewhere or extracted in whole or in part from a thesis presented by me for another degree or diploma.

. . . .

(Place, date) (Signature, Stefan Gomes da Costa)

Curriculum Vitae

Personal information

- Full Name: Stefan Gomes da Costa
- Date of Birth: 19.01.1984 in Saarbrücken, Germany
- Nationality: German

Education

- Ph.D. student at Universität Stuttgart, 3. Physikalisches Institut (08.2010 - 07.2015)
- Short Term Scientific Mission (COST) at Bar-Ilan University, Ramat Gan, Israel (05.2014)
- Dipl. Phys. degree, Universität Stuttgart, Germany (09.2003 - 07.2010)
- Dipl. Phys. studies, University of Oslo, Norway (08.2007 - 12.2007)

Professional

- Application Scientist at WITec GmbH, Ulm, Germany (since 08.2016)

Publication List to Date

- G. Tempea, H. Wan, S. Gomes da Costa, H. B. De Aguiar, and A. Volkmer. Nonlinear optical microscopy with few-cycle laser pulses. In OSA Technical Digest (online), pages JM2O.4, San Jose, California, 2013. Optical Society of America.

- S. Scherer, E. Wollrab, L. Codutti, T. Carlomagno, S. Gomes da Costa, A. Volkmer, A. Bronja, O. J. Schmitz, and A. Ott. Chemical analysis of a "Miller-Type" complex prebiotic broth: Part II: Gas, oil, water and the oil/water-interface. Origins of Life and Evolution of Biospheres, 47(4):381- 403, 2016.